University of Nottingham

UK | CHINA | MALAYSIA

Heat Transfer and Fluid Flow Analysis in Double-tube Heat Exchangers with Novel Self-join Winglet Vortex Generators

Jiajie Feng

Thesis submitted to The University of Nottingham,

Malaysia Campus

for the degree of Doctor of Philosophy

September 2025

Abstract

Heat exchangers are crucial in industrial applications, as improving their working performance can significantly reduce carbon emissions and promote economic development. The improvement of heat exchangers can be achieved through heat transfer enhancement technologies, which aim to optimize heat transfer or minimize flow resistance. Among various enhancement techniques, winglets can induce multi-longitudinal vortices to improve heat transfer under lower pressure drop conditions. However, previous studies pay less attention to the variation of vortex interaction. Furthermore, unlike the tube side, the shell side has two walls that influence fluid flow and vortex interactions. Therefore, a novel self-join winglet vortex generator is proposed to investigate the variation mechanism of vortex interactions on both the tube and shell sides. In this work, ANSYS Fluent software is used to conduct a steady simulation of the effect of winglet structure and arrangement on the variation of vortex structures. Meanwhile, experimental studies of thermal performance are conducted to verify the reliability of numerical models and to summarize the heat transfer and fluid flow characteristics. Results indicate that boundary vortices contribute to enhance mixing uniformity of fluid flows. Furthermore, the dissipation intensity of boundary vortices increases with increasing included angles. As the curved ratio increases, the disturbance distribution in the high-speed region shifts toward the boundary layer, because the variation of curved ratio adjusts the region of vortex development. Due to wall limitations, the movement distance of boundary vortices increases. Compared with plain tubes, the Nusselt number increases by 1.90-2.32 times and 1.40-2.20 times in circular and annular tubes, respectively, while the friction factor increases by 2.23-5.10 times and 2.64-3.91 times in circular and annular tubes, respectively. The maximum thermal enhancement factor reaches 1.63 and 1.52 in the circular and annular tube, respectively. The novel winglet exhibits significant improvement in heat transfer and flow structure. These findings provide valuable guidance for the efficient application of novel winglet vortex generators in heat exchangers, thereby providing strategies to enhance working performance and improve flow fields on both tube and shell sides.

Acknowledgement

The four years spent pursuing my PhD degree have been an extremely wonderful journey in my life. I am honored to express my most sincere gratitude in this acknowledgement to all those who contributed to this thesis.

I would like to give special thanks to my supervisor, Prof. Yousif, for his patience, advice and guidance from the beginning of this research, as well as encouraging me to explore more of the wonderful aspects of fluid mechanics.

I gratefully acknowledge my co-supervisor, Associate Prof. Khai Ching, for his valuable advice, guidance, and supervision. I am very thankful that he made time to provide me with useful suggestions regarding numerical simulation and academic writing, which significantly aided my work progress.

Many special thanks go to Prof. Baiman Chen for his valuable advice and financial support for part of this research. I also thank Dongguan University of Technology (DGUT) for sponsoring my PhD studies for four years.

I would also like to thank Dr. Zi-Yian Lim for the academic enlightenment he gave me throughout these years. I deeply appreciate the assistance he provided, especially in teaching me how to conduct academic research more effectively.

To my friends and fellow PhD colleagues, thank you very much for your endless support and encouragement over all these years. Thank you for your companionship and the wonderful memories we created throughout this learning process.

Lastly, I would like to convey my special thanks to my family for their unwavering support and encouragement. Without their unconditional love and investments in my life, I would be capable of far less.

Table of Contents

Abstract 1

Acknowledgement 2

Table of Contents 3

List of publications 6

List of figures 7

List of tables 13

Nomenclature 14

Chapter 1: Introduction 16

1.1 Background and significance 16
1.2 Research problem and questions 16
1.3 Aim and objectives 17
1.4 Thesis outline 18

Chapter 2: Literature Review 20

2.1 The development of heat transfer enhancement technology 20
2.2 Passive techniques 20
2.2.1 Special-shaped tube 21
2.2.2 Special-shaped wall 23
2.2.3 Special-shaped inserter 27
2.3 Development of winglet applications 30
2.3.1 Applications in fin-and-tube heat exchangers or rectangular channels 31
2.3.2 Applications in tubes with twisted tapes or flat plates 36
2.3.3 Applications in plain tubes 38
2.4 Double-tube heat exchangers 43
2.5 Longitudinal vortex 44
2.5.1 The structure of longitudinal vortex 44
2.5.2 The interaction of longitudinal vortex 46
2.6 Research gap 49

Chapter 3: Methodology 51

3.1 Research methods 51
3.2 Flow chart 51
3.3 Fundamental theory 55
3.3.1 Basic heat transfer theory 55
3.3.2 Secondary flow intensity and vorticity field theory 57
3.4 Numerical simulation 61
3.4.1 Basic assumption 61
3.4.2 Governing equation 62
3.4.3 Numerical calculation method 63

3.4.4 Near-wall treatment 63
3.4.5 Boundary conditions 64
3.5 Experimental verification 65
3.5.1 Experimental setup 65
3.5.2 Data reduction and uncertainty calculation 69
3.5.3 Reliability verification of experiment setup 71
Chapter 4: Heat transfer and fluid flow analysis in circular tubes with novel self-join winglets **73**
4.1 Introduction 73
4.2 Physical model 73
4.3 Numerical model verification 75
4.3.1 Grid independence test 75
4.3.2 Verification of turbulent model 76
4.4 Fluid flow analysis 77
4.5 Heat transfer analysis 83
4.6 Flow and thermal characteristics analysis 86
4.7 Empirical correlations for *Nu* and *f* 89
4.8 Comparisons with previous work 90
4.9 Similarity analysis 91
4.10 Chapter conclusion 94
Chapter 5: The optimization of the flow field in circular tubes equipped with modified winglet structures **96**
5.1 Introduction 96
5.2 Physical model 96
5.3 Optimization mechanism 98
5.4 Effect of lift angles on heat transfer and fluid flow 100
5.5 Effect of curved ratio on heat transfer and fluid flow 107
5.6 Chapter conclusion 111
Chapter 6: Heat transfer and fluid flow analysis in annular tubes with traditional delta winglets **113**
6.1 Introduction 113
6.2 Physical model 113
6.3 Numerical model verification 115
6.3.1 Grid independence test 115
6.3.2 Verification of turbulent model 117
6.4 Flow field analysis 117
6.5 Thermal field analysis 125
6.6 Flow and thermal characteristics analysis 128
6.7 Kinetic energy analysis 132
6.8 Chapter conclusion 136
Chapter 7: Heat transfer and fluid flow analysis in annular tubes with novel

self-join winglets **138**
7.1 Introduction 138
7.2 Physical model 138
7.3 Vortex interactions and wall limitations 140
7.4 Disturbance and uniformity of flow fields 144
7.5 Flow and thermal characteristics analysis 152
7.6 Empirical correlations for *Nu* and *f* 155
7.7 Chapter conclusion 156
Chapter 8: Conclusion and future work **158**
8.1 Conclusion 158
8.2 Future work 159
References **161**

List of publications

Journal papers

[1] J.J. Feng, C.P. Teh, K.C. Ng, J.C. Jen-Haw, D. Xiao, Y.A. Abakr, A. Chan, B. Chen, Heat transfer and fluid flow analysis in circular tubes with multi-delta-winglets vortex generators, Int. Commun. Heat Mass Transfer 159 (2024) 108267. https://doi.org/10.1016/j.icheatmasstransfer.2024.10

[2] J.J. Feng, K.C. Ng, Y.A. Abakr, A. Chan, B. Chen, Experimental and numerical investigation on heat transfer and fluid flow in annular tubes with delta winglets, Appl. Therm. Eng. 278 (2025) 127369. https://doi.org/10.1016/j.applthermaleng.2025.1273

Chinese patents

[1] CN111707113B, A double-tube heat exchanger with an axial vane swirler under reverse flow, 2nd inventor, invention patent, granted.

[2] CN112944960B, Swirling turbulator and heat exchange tube structure, 1st inventor, invention patent, granted.

[3] CN112944959B, Swirling turbulator and heat exchange tube structure, 1st inventor, invention patent, granted.

[4] CN112682905B, A liquid-replenishing air conditioning system, control method, computer equipment and terminal, 3rd inventor, invention patent, granted.

[5] CN112902299B, Heat exchange tube assembly, heat exchanger and air conditioner, 3rd inventor, invention patent, granted.

List of figures

Figure 2.1 Schematic of elliptic tubes. (Luo et al., 2021 [19]) 21
Figure 2.2 Schematic of twisted tubes. (Jafari et al., 2017 [18]) 22
Figure 2.3 Schematic of flat tubes. (Saadeldin et al., 2025 [31]) 23
Figure 2.4 Schematic of rib tubes. (Naphon et al., 2006 [33]) 24
Figure 2.5 Schematic of groove tubes. (Zheng et al., 2016 [34]) 25
Figure 2.6 Schematic of corrugated tubes. (Pethkool et al., 2011 [35]) 26
Figure 2.7 Schematic of dimpled tubes. (Xie et al., 2022 [36]) 26
Figure 2.8 Schematic of conical inserters. (Zheng et al., 2017 [38]) 28
Figure 2.9 Schematic of twisted tapes. (Esmaeilzadeh et al., 2014 [40]) 29
Figure 2.10 Schematic of axial vane swirlers. (Ahmadvand et al., 2009 [41]) 30
Figure 2.11 Winglet applications in rectangular channels. (Promvonge et al., 2022 [62]) 31
Figure 2.12 Winglet applications in fin-and-tube heat exchangers. (Torii et al., 2002 [75]) 32
Figure 2.13 The secondary velocity vectors in rectangular channels: (a) CFD; (b) CFU (Kim and Yang, 2002 [76]). 32
Figure 2.14 Secondary velocity vector at different locations (a) CFD, (b) CFU, and (c) mixed type (Ke et al., 2019 [77]). 33
Figure 2.15 Pictorial diagram and punched holes (Zhou and Feng, 2014 [81]). 34
Figure 2.16 Twisted tapes with twin delta wings (Eiamsa-ard, 2013 [100]) 36
Figure 2.17 Louvered V-shaped winglets (Promvonge et al., 2022 [97]) 37
Figure 2.18 Delta winglets installed on a ring and smoke flow visualization (Xu et al., 2018 [110]). 39
Figure 2.19 Punched rectangular winglets (Wang et al., 2022 [113]). 39
Figure 2.20 The configuration and flow structure of self-connected winglets (Zheng et al., 2022 [20]). 40
Figure 2.21 Winglet structure and streamline distribution: (a) Overall flow direction; (b) Case 4; (c) Case 5; (d) Case 6 (Wu et al., 2024 [114]). 41

Figure 2.22 Schematic of double-tube heat exchangers: (a) Parallel flow; (b) Counter flow (Li et al., 2022 [11]).....43
Figure 2.23 Vortex structure: (a) Transverse vortex (Hu et al., 2022 [136]), (b) Longitudinal vortex (Jacobi and Shah, 1995 [137]). 45
Figure 2.24 Vortex structure induced by delta winglet vortex generators (Torii et al., 1994 [139]).....46
Figure 2.25 Comparison of velocity vectors (a) and contour plot of *Se* (b) on the cross sections (Song et al., 2016 [142]). 48
Figure 3.1 Flow chart of whole research progress. 52
Figure 3.2 The details of characteristics research. 53
Figure 3.3 The details of mechanism research. 54
Figure 3.4 The details of optimization research. 54
Figure 3.5 The experiment setup of the tube side: (a) schematic; (b) the position of testing points. 67
Figure 3.6 The experiment setup of the shell side: (a) schematic; (b) the position of testing points. 68
Figure 3.7 The real picture of the experiment system. 68
Figure 3.8 Verification of experimental reliability: (a) tube sides; (b) shell sides. 72
Figure 4.1 Details of winglet structure and arrangement in different views. 74
Figure 4.2 The grids of circular tubes with novel self-join winglet vortex generators. 75
Figure 4.3 Grid independence test for overall *Nu* and *f*. 76
Figure 4.4 The profiles of overall *Nu* and *f* predicted by numerical models compared with the experiment data from case A1: (a) *Nu* versus *Re*; (b) *f* versus *Re*.....76
Figure 4.5 Streamlines at different cross sections for case A1 at *Re* = 7577. 78
Figure 4.6 Streamlines of different cross sections at *Re* = 7577 in different cases: (a) case A2; (b) case A3; (c) case A4; (d) case A5; (e) case A6; (f) case A7. 79
Figure 4.7 Velocity magnitude contours at *Re* = 7577 in different cases: (a) case A1; (b) case A2; (c) case A3; (d) case A4; (e) case A5; (f) case A6; (g) case A7. 81
Figure 4.8 *TKE* contours at *Re* = 7577 in different cases: (a) case A1; (b) case A2; (c)

case A3; (d) case A4; (e) case A5; (f) case A6; (g) case A7.....82
Figure 4.9 Axial distributions of *Se* at *Re* = 7577 across different cases.....83
Figure 4.10 Temperature contours at different cross sections for case A1 at *Re* = 7577. 84
Figure 4.11 Temperature contours of different cross sections at *Re* = 7577 in different cases: (a) case A2; (b) case A3; (c) case A4; (d) case A5; (e) case A6; (f) case A7. ...85
Figure 4.12 The contours of surface local Nusselt number at *Re* = 7577 in case A1. .86
Figure 4.13 The effects of different cases on heat transfer for different *Re*: (a) *Nu*; (b) Nu/Nu_0.....87
Figure 4.14 The effects of different cases on fluid flow for different *Re*: (a) *f*; (b) f/f_0. 88
Figure 4.15 The variations of *TEF* with different *Re* across different cases.....89
Figure 4.16 Comparisons of the predicted *Nu* and *f* with experimental data: (a) *Nu*; (b) *f*. 90
Figure 4.17 Comparisons of *TEF* between the previous and present work. 91
Figure 4.18 Similarity analysis: (a) ΔT_{sc} versus *Re*; (b) ΔP_{sc} versus *Re*. 94
Figure 5.1 Modified design of novel self-join winglet vortex generators. 97
Figure 5.2 The variations of velocity magnitude behind the winglet vortex generators. (Case B1: β = 30 °, α_v = 60 °, *CR* = 0.67). 99
Figure 5.3 The variations of velocity magnitude and streamlines in various cross sections. (Case B1: β = 30 °, α_v = 60 °, *CR* = 0.67). 100
Figure 5.4 The variations of velocity magnitude in cross section of *z* = 290 mm for various cases: (a) B4; (b) B5; (c) B6; (d) B7; (e) B8; (f) B9. 101
Figure 5.5 *TKE* contours at *Re* = 7577 in different cases: (a) case B4; (b) case B5; (c) case B6; (d) case B7; (e) case B8; (f) case B9. 102
Figure 5.6 The variations of temperature in cross section of *z* = 290 mm. 103
Figure 5.7 Variation in *Se* axial distribution: (a) cases B4 - B9; (b) different *Re* in cases B4 and B7. 104
Figure 5.8 The effects of different cases on heat transfer for different *Re*: (a) *Nu*; (b) Nu/Nu_0. 105

Figure 5.9 The effects of different cases on fluid flow for different *Re*: (a) *f*; (b) f/f_0. 106
Figure 5.10 The variations of *TEF* with different *Re* across different cases..... 107
Figure 5.11 The variations of velocity magnitude in cross section of z = 290 mm. .. 107
Figure 5.12 *TKE* contours at *Re* = 7577 in different cases: (a) case B1; (b) case B2; (c) case B3. 108
Figure 5.13 The variations of temperature in cross section of z = 290 mm..... 109
Figure 5.14 Variation in *Se* axial distribution: (a) cases B1 – B3; (b) different *Re* in cases B1. 109
Figure 5.15 The effects of different cases on heat transfer for different *Re*: (a) *Nu*; (b) Nu/Nu_0. 110
Figure 5.16 The effects of different cases on fluid flow for different *Re*: (a) *f*; (b) f/f_0. 111
Figure 5.17 The variations of *TEF* with different *Re* across different cases..... 111
Figure 6.1 Schematic diagram: (a) the details of winglet arrangements and structures; (b) real photographs of tubes with winglet vortex generators. 114
Figure 6.2 Grid generation in the fluid domain. 116
Figure 6.3 Grid independence test for overall *Nu* and *f*. 116
Figure 6.4 Verification of turbulent model for overall *Nu* and *f*. 117
Figure 6.5 Cross sections at different locations. 119
Figure 6.6 Vortex structures for cases C1 and C6: (a) streamlines at different cross sections; (b) iso-surface of Q criterion overlapped with velocity magnitude contours. ($Q = 2/s^2$, *Re* = 2304) 119
Figure 6.7 Streamlines at the cross-section located at z/d_c = 2.29 for various cases. 120
Figure 6.8 The contours of *TKE* at *Re* = 2304 for various cases. 121
Figure 6.9 3D streamlines with velocity magnitude and *TKE* contours at z/d_c = 1.71 in different cases: (a) case C1; (b) case C6; (c) case C7. 123
Figure 6.10 Variation in *Se* axial distribution: (a) various cases (b) different *Re*. 125
Figure 6.11 Temperature contours at various cross sections..... 126
Figure 6.12 Temperature contours at z/d_c = 0.57 for different cases. 127

Figure 6.13 The contours of surface local Nusselt number in different cases: (a) case C1; (b) case C6; (c) case C7. 128
Figure 6.14 Influence of various cases on heat transfer: (a) *Nu* vs. *Re* (b) Nu/Nu_0 vs. *Re*. 129
Figure 6.15 Influence of various cases on fluid flow: (a) *f* vs. *Re* (b) f/f_0 vs. *Re*. 130
Figure 6.16 Variations of *TEF* with different *Re*: (a) present work (b) previous work. 132
Figure 6.17 Energy distributions at $z/d_c = 2.29$ in the transverse direction at *Re* = 2304: (a) *TKE*; (b) ε. 133
Figure 6.18 Energy distributions in the axial direction at *Re* = 2304: (a) *TKE*; (b) ε. 135
Figure 6.19 Energy distributions in the axial direction at different *Re*: (a) *TKE*; (b) ε. 136
Figure 7.1 The details of winglet configurations in various views. 139
Figure 7.2 Streamlines at different cross sections for case D1 at *Re* = 2304. 140
Figure 7.3 Streamlines of different cross sections at *Re* = 2304 in different cases: (a) case D2; (b) case D3; (c) case D4; (d) case D5; (e) case D6; (f) case D7. 142
Figure 7.4 The iso-surface of Q criterion overlapped with velocity magnitude contours ($Q = 2/s^2$, *Re* = 2304): (a) case D1; (b) case D2; (c) case D3; (d) case D4; (e) case D5; (f) case D6; (g) case D7. 143
Figure 7.5 Variation in *Se* axial distribution: (a) various cases (b) different *Re*. 144
Figure 7.6 The contours of *TKE* at *Re* = 2304 for various cases ($x = 0$, $z = 262$ mm): (a) case D1; (b) case D2; (c) case D3; (d) case D4; (e) case D5; (f) case D6; (g) case D7. 146
Figure 7.7 Energy distributions in the axial direction at *Re* = 2304: (a) *TKE*; (b) ε. . 147
Figure 7.8 Energy distributions in the axial direction at different *Re*: (a) *TKE*; (b) ε. 148
Figure 7.9 Temperature contours at various cross sections. 149
Figure 7.10 The contours of velocity and temperature at $z = 274$ mm in different cases: (a) case D1; (b) case D2; (c) case D3; (d) case D4; (e) case D5; (f) case D6; (g) case

D7.....150
Figure 7.11 The contours of surface local Nusselt number in different cases. 152
Figure 7.12 Influence of various cases on heat transfer: (a) *Nu* vs. *Re* (b) Nu/Nu_0 vs. *Re*.
.....153
Figure 7.13 Influence of various cases on fluid flow: (a) *f* vs. *Re* (b) f/f_0 vs. *Re*.....154
Figure 7.14 Variations of *TEF* with different *Re*. 155
Figure 7.15 Comparisons of the predicted *Nu* and *f* with experimental data: (a) *Nu*; (b)
f. 156

List of tables

Table 2.1 Winglet applications in rectangular channels or fin-and-tube heat exchangers for heat transfer enhancement. 35
Table 2.2 Winglet applications in tubes with twisted tapes or flat plates for heat transfer enhancement. 37
Table 2.3 Winglet applications in plain tubes for heat transfer enhancement..... 42
Table 3.1 The uncertainty values of measured parameters in this work. 70
Table 4.1 Specification of the physical model. 74
Table 5.1 Specification of the physical model. 97
Table 6.1 Specification of the physical model. 114
Table 6.2 Details of grid independence test. 116
Table 7.1 The specifications of physical models. 139

Nomenclature

A	Heat transfer surface area [m^2]
$A^{'}$	Cross-section area [m^2]
BR	Blockage ratio [-]
C	Slope coefficient [-]
CR	Curved ratio [-]
CFD	Common-flow-down [-]
CFU	Common-flow-up [-]
c_p	Specific heat capacity [KJ/(kg·K)]
D	Outside diameter of tubes [m]
De	Se in curved tubes [-]
d	Internal diameter of tubes [m]
d_c	Characteristic diameter [m]
f	Friction factor [-]
f/f_0	Friction factor ratio [-]
H_c	Curved height [m]
H	Winglet height [m]
h	Heat transfer coefficient [$W/(m^2·K)$]
I	Electric current [A]
I_t	Turbulent intensity [%]
$\boldsymbol{J}$	Vorticity flux [1/s]
$\boldsymbol{J}^n_{ABS}$	Mean absolute vorticity flux in mainstream direction [1/s]
L	Pipe length [m]
L_{win}	Winglet length [m]
L_r	Ring length [m]
l	Length of heat transfer surface [m]
$\dot{m}$	Mass flow rate [kg/s]
Nu	Nusselt number [-]
Nu/Nu_0	Nusselt number ratio [-]
n	Velocity exponent [-]
P	Pitch [-]
ΔP	Pressure drop between the inlet and outlet [Pa]
ΔP_{sc}	Pressure drop similarity coefficient
PN	winglets pairs number [-]
Pr	Prandtl number [-]
Q	Heat transfer rate [W]
Q_h	Heat transfer rate between the fluid and tube wall [W]
q	Heat flux [W/m^2]
R_w	Wall thermal resistance [$(m^2·K)/W$]
Re	Reynolds number [-]
S	Symmetric part of the second invariant of the velocity gradient tensor [-]
Se	Secondary flow intensity [-]
Sw	Se in tubes with twisted tapes [-]
T	Temperature [K]
$T^{'}$	Ratio of temperature difference
$\Delta T^{'}$	Temperature difference between wall and bulk temperature
ΔT	Temperature difference [K]
ΔTm	Logarithmic mean temperature difference between hot and cold

	fluids [K]
ΔT_{sc}	Temperature difference similarity coefficient
TEF	Thermal enhancement factor [-]
TKE	Turbulent kinetic energy [m^2/s^2]
Us	Secondary flow velocity [m/s]
U	Voltage [V]
u	Fluid velocity [m/s]
$\dot{V}$	Volume flow rate [m^3/s]
x	Transverse distance [-]
z	Axial distance [-]

Greek letters

α	Attack angle [°]
α_v	Included angle [°]
β	Lift angle [°]
δ	Winglet thickness [m]
δ_r	Ring thickness [m]
ε	Turbulent dissipation rate [m^2/s^3]
k	Turbulent kinetic energy [m^2/s^2]
λ	Thermal conductivity [W/(m·K)]
μ	Dynamic viscosity [Pa·s]
ν	Kinematic viscosity [kg/(m·s)]
ρ	Density [kg/m³]
Ω	Antisymmetric part of the second invariant of the velocity gradient tensor [-]

Subscripts

e	System
f	Fluid
i	Inlet
o	Outlet
ov	Overall
w	Wall
0	Plain tube
1	Fluid 1
2	Fluid 2

Chapter 1: Introduction

1.1 Background and significance

Over the past 30 years, energy consumption has gradually increases alongside industrial production and scientific development [1]. As essential industrial equipment, heat exchangers are widely used in fields such as refrigeration, chemical engineering, and food processing [2]. This is especially true in the chemical industry, where heat exchangers account for approximately 20 % to 40 % of the total equipment investment [3]. Hence, improving the working efficiency of heat exchangers is of great significance for industrial development [4].

As the main component of heat exchangers, heat exchange tubes can be optimized through heat transfer enhancement methods. Compared with traditional heat transfer methods, enhanced heat transfer technology can achieve better thermal performance [5]. Based on power sources, heat transfer enhancement techniques can be categorized into active, passive, and compound methods. Furthermore, passive techniques are widely used due to their ease of operation and low cost. Considering these advantages, this thesis concentrates on passive techniques.

1.2 Research problem and questions

Based on previous studies about winglet vortex generators, novel self-join winglet structures are proposed in this work. This study aims to provide novel insights for efficient applications of winglets in heat exchangers. The goal is to enhance the working performance while lowering both manufacturing costs and pressure drop. For more details about the winglet structures in this work, it can be referred to the literature review section.

Currently, the flow theory has not fully explained the generation and interaction of longitudinal vortices induced by winglets in circular and annular tubes. The similarity correlation between structural parameters and flow field characteristics is crucial for

summarizing and understanding the longitudinal vortex effect. Additionally, revealing the variation mechanism of vortex interaction helps offer valuable guidance for improving mixing uniformity and flow disturbance. Consequently, the heat transfer and fluid flow mechanisms in tubes enhanced by novel self-join winglets are investigated numerically and experimentally in this work. Based on these mechanisms, a parametric study is performed to propose optimization strategies for winglet designs and vortex structures. Furthermore, the further development of novel winglet designs has the potential to balance manufacturing costs and working performance. Thus, the following research problem and questions are proposed.

Research problem:

What is the effect of vortex interactions induced by novel self-join winglet vortex generators on heat transfer and fluid flow in the tube and shell sides of double-pipe heat exchangers?

Research questions:

A. What is the optimal flow structure induced by novel self-join winglet structures in tube and shell sides?
B. What is the mechanism by which vortex interactions induced by novel self-join winglet structures affect heat transfer and fluid flow in the tube and shell sides?
C. How can the flow structure and novel winglet design be optimized in the tube and shell sides?

1.3 Aim and objectives

To address the research problem and questions, the research aim and objectives are proposed. Furthermore, a detailed statement is provided in this section.

Research aim:

To reveal the effect of vortex interactions induced by novel self-join winglet vortex generators on heat transfer and fluid flows in the tube and shell sides of double-pipe heat exchangers.

Research objectives:

A. To summarize the heat transfer and pressure drop characteristics and obtain the optimal flow structure induced by novel self-join winglet structures in the tube and shell sides.
B. To understand the vortex interaction and vortex flow behaviors in the tube and shell sides fitted with novel self-join winglets.
C. To perform parametric studies and propose strategies for optimizing the flow structures and novel winglet designs in circular and annular tubes.

1.4 Thesis outline

The thesis consists of 8 chapters. The following provides a brief description of each chapter.

Chapter 1 presents the background, motivation, research problem and questions, aim and objectives, and the outline structure of this thesis.

Chapter 2 provides a detailed review, including various passive techniques, the development of winglets applications, and flow mechanisms concerning longitudinal vortex flows.

Chapter 3 presents the methodology of this thesis, including fundamental theory, numerical simulation, and experimental verification.

Chapter 4 explores the effects of vortex interactions induced by novel self-join winglet vortex generators on heat transfer and fluid flow in circular tubes. Furthermore, optimization strategies are developed through similarity analysis. Moreover, similarity equations relating structural parameters to flow field characteristics are obtained.

Chapter 5 reveals the optimization mechanism of boundary vortices for heat transfer and fluid flow within circular tubes.

Chapter 6 investigates the flow behavior and heat transfer characteristics in annular tubes with traditional delta winglet structures. Furthermore, the variation mechanism of flow disturbance and turbulent dissipation within annular tubes equipped with delta winglets is revealed.

Chapter 7 demonstrates the optimization effect of the novel self-join winglets on flow fields within annular tubes. Furthermore, optimization insights for the application of novel winglet designs within annular tubes are proposed.

Chapter 8 concludes this thesis and proposes future work directions.

Chapter 2: Literature Review

2.1 The development of heat transfer enhancement technology

Heat transfer enhancement technology significantly improves the working performance of heat exchangers and provides considerable economic benefits [6-11]. With the advances in computational fluid dynamics, research on heat transfer enhancement technology has progressed substantially. The time required for investigating heat exchangers has been effectively reduced. Currently, improving the heat transfer performance of heat exchangers has become the primary focus of heat transfer enhancement technology.

Bergles [12] clearly categorized heat transfer enhancement technology into active and passive techniques [9, 10, 13]. The distinction between these techniques depends on whether external power sources are used. Active techniques include wall vibration [14], fluid vibration [15], and the application of electric fields [16], among others. Passive techniques include rough surfaces [17], special designed tubes [18, 19], and inserted vortex generator [20], etc. In engineering systems, passive techniques are generally preferred over active ones due to their simpler operation and lower cost. Furthermore, Bergles [12] classified heat transfer enhancement technology into three different modes. The first mode focuses on surface treatments, such as rough surfaces[17] and surfaces fitted with fins [21]. The second mode primarily involves special configurations inserted into or modifications to the entire tube structure, such as twisted tape inserts [22], corrugated tubes [23], and fluted tubes [24]. The last mode is compound heat transfer enhancement technology [10], which combines two or more heat transfer techniques, such as ribbed tubes fitted with helical tapes [25], grooved tubes with twisted tapes [26], and helical screw tapes coupled with rib turbulators [27]. In practical application, compound techniques typically achieve better heat transfer effects than single techniques, though they increase the complexity of heat exchangers [10].

2.2 Passive techniques

2.2.1 Special-shaped tube

When fluid flows through straight circular tubes or rectangular tubes, large radial velocity is not induced. Consequently, the heat transfer effect remains weak. The tube geometry can be modified through mechanical processing. The secondary flows generated by such modified tubes can extend the flow path, while simultaneously thinning the boundary layer thickness, thereby enhancing heat transfer performance. Common special-shaped tubes include elliptic tubes, twisted tubes, and flat tubes, among others.

The shape of elliptic tubes is more compact than that of circular tubes. The structure of traditional elliptic tubes can be further optimized through twisting and extrusion. The schematic of the elliptic tubes is shown in Figure 2.1. Li et al. [28] experimentally and numerically studied the heat transfer and flow resistance of elliptic tubes with alternating axes. The results indicate that the heat transfer performance of elliptic tubes is approximately 84 %-134 % higher than that of straight elliptic tubes. The combination of the *k*-ε model and wall function yields a friction factor in turbulent flow that closely matches the experimental data. Furthermore, the multiple vortices induced by elliptic tubes with alternating axis enhance the synergy intensity between velocity and temperature fields. The elliptic structure can promote vortex generation within tubes, thereby improving the heat transfer performance. Compared with other passive techniques, elliptic tubes exhibit lower sweep resistance along the entire flow path. Furthermore, optimizing the elliptic structure can introduce swirl momentum that is suitable for the flow path. Despite these advantages, the manufacturing cost of elliptic tubes is higher than that of most passive techniques. It is obvious that elliptic tubes are not suitable for heat exchangers under conventional working conditions.

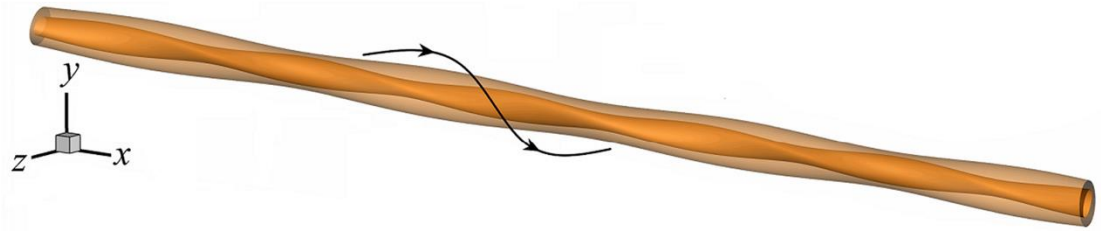

Figure 2.1 Schematic of elliptic tubes. (Luo et al., 2021 [19])

Twisted tubes are the optimal choice for enhancing the heat transfer performance of high-viscosity fluid flows without significantly increasing pressure drop. The schematic of the twisted tubes is shown in Figure 2.2. Yan et al. [29] conducted an experimental study on the heat transfer performance of epoxy resin in horizontal twisted tubes. The results show that the aspect ratio has a more significant impact on heat transfer and pressure drop characteristics than the twisted ratio. While twisted tubes are structurally similar to elliptic tubes, their primary difference lies in the cross-sectional geometry. Obviously, the resulting flow patterns differ accordingly. However, the overall flow path remains consistent along the axial direction. Notably, the manufacturing cost of twisted tubes is comparable to that of elliptic tubes.

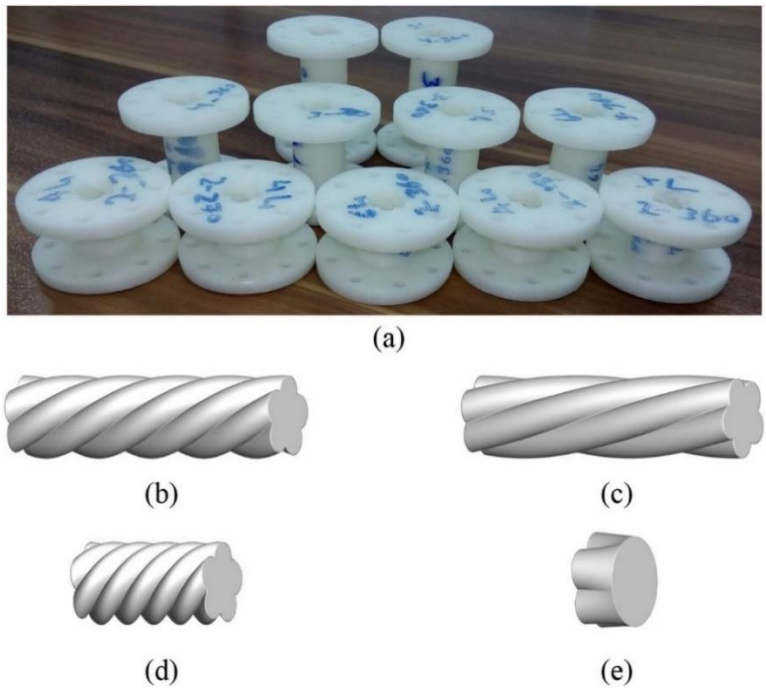

Figure 2.2 Schematic of twisted tubes. (Jafari et al., 2017 [18])

Flat tubes are widely used in industrial applications due to their higher integration and miniaturization capabilities. The schematic of the flat tubes is shown in Figure 2.3. Safikhani and Abbassi [30] conducted numerical simulations on five different flat tubes to study the effect of flatness on flow characteristics and heat transfer in nanofluid flows. The numerical simulations of nanofluids are performed using two phase mixture model

by FORTRAN programming language. The results indicate that heat transfer and wall shear stress increase with flatness. The shape of a flat tube resembles that of an elliptical tube. For a given perimeter, a flat tube has a smaller flow area compared to a circular tube. Consequently, the flow velocity within the flat tube is higher, resulting in better heat transfer performance than that of a circular tube.

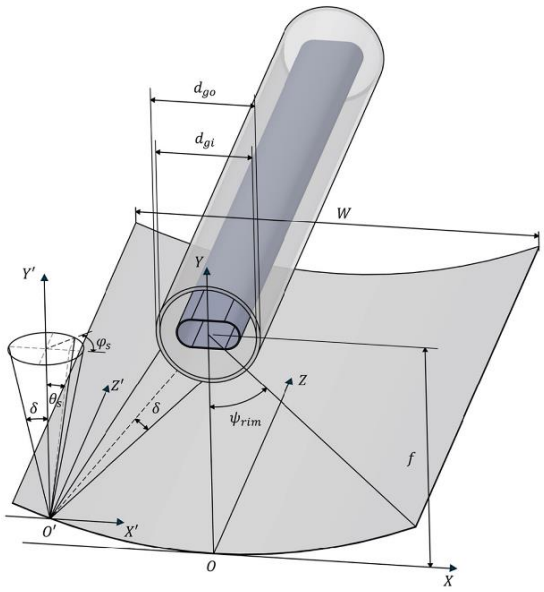

Figure 2.3 Schematic of flat tubes. (Saadeldin et al., 2025 [31])

2.2.2 Special-shaped wall

Modifying the shape of heat transfer surfaces can effectively enhance turbulent intensity and reduce thermal resistance. The wall shape is typically processed through casting, hot rolling, cold machining, sintered coiled wire mesh, electrochemical corrosion, etc. Porous structures, ribs, grooves, zigzag surfaces, etc. are formed on the inner wall. These modifications induce vortices of varying intensity in flow separation regions, disrupting the development of the boundary layer.

Rib tubes are manufactured by extruding toothed ribs on the inner or outer walls of metal circular tubes. Most investigations are conducted numerically due to the complicated manufacturing process and higher processing costs. The schematic of the rib tubes is shown in Figure 2.4. Zheng et al. [32] numerically studied the flow pattern and heat transfer in ribbed tubes using the SST *k-ω* model. The enhanced wall treatment

which blends the viscous sub-layer formulation and the logarithmic layer formulation are used for the near-wall treatments for fluid velocity and temperature fields. Compared with fluid flows induced by a single vortex, those induced by multiple vortices in V-type ribbed tubes demonstrate better heat transfer performance. The mechanism of heat transfer enhancement by traditional ribs relies on flow separation and reattachment. This effect is well illustrated by transverse ribs, which induce a two-dimensional flow pattern. During heat transfer from the wall to the fluid, the temperature in the core region remains lower than that at the wall. Therefore, heat transfer can be enhanced when colder, higher-momentum fluid from the core region is brought into the boundary layer. In other words, when secondary flow occurs, both the velocity and thermal boundary layers become thinner at the wall where the core fluid impinges, resulting in augmented heat transfer in that region.

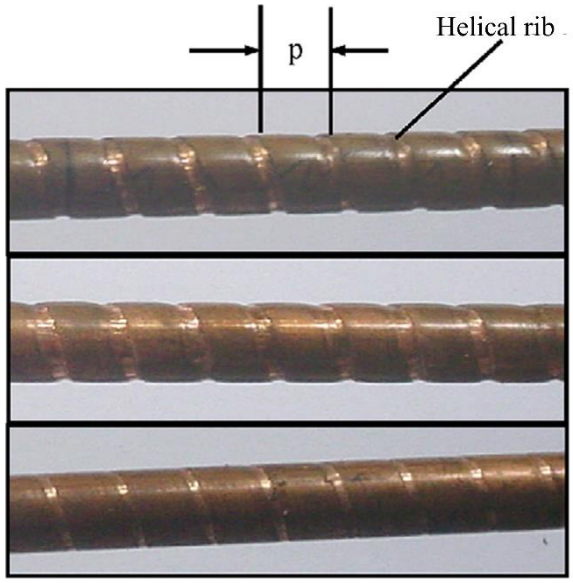

Figure 2.4 Schematic of rib tubes. (Naphon et al., 2006 [33])

Groove tubes are manufactured by machining toothed grooves into the tube wall. The schematic of the groove tubes is shown in Figure 2.5. Zheng et al. [34] numerically studied the turbulent flow characteristics and heat transfer performance of discontinuous groove tubes. The numerical results calculated by the SST k-ω model are much closer to the experimental data than those obtained by other comparable models. Furthermore, the grooves effectively generate longitudinal vortices that disturb fluid

flow between the boundary layer and core region. Compared to the straight grooves, inclined grooves can not only improve the heat transfer rate, but also reduce the irreversibility of the heat transfer and flow process. Furthermore, the discontinuous groove structure exhibits better comprehensive heat transfer performance than the discontinuous rib structure. Although it provides higher heat transfer performance and enhances mixing between the boundary layer and the core region, its machining cost remains a significant challenge.

Figure 2.5 Schematic of groove tubes. (Zheng et al., 2016 [34])

Corrugated tubes can induce local jet flows that disrupt boundary layer development, thereby enhancing heat transfer. The schematic of the corrugated tubes is shown in Figure 2.6. Pethkool et al. [35] experimentally investigated the enhancement effect of helical corrugated tubes on single-phase turbulent convective heat transfer. The results show that compared with plain tubes, the average heat transfer rate increases by 123 %-232 %, while the friction factor increases by 46 %-93 %. The structure of corrugated tubes is similar to that of ribbed and grooved tubes. Their main difference lies in the tip of the protrusion, which is narrower in corrugated tubes than in the other two types. This geometry facilitates the generation of secondary flow. However, the secondary flow induced by corrugated tubes typically takes the form of a single vortex, which is often insufficient to bring a larger volume of cool fluid from the core region into the boundary layer. Many previous studies have overlooked a detailed analysis of the flow field and its impact on overall and local heat transfer distribution. Optimization of the flow field can start with modifying the tip geometry of the protrusion or adjusting the arrangement of the protrusions.

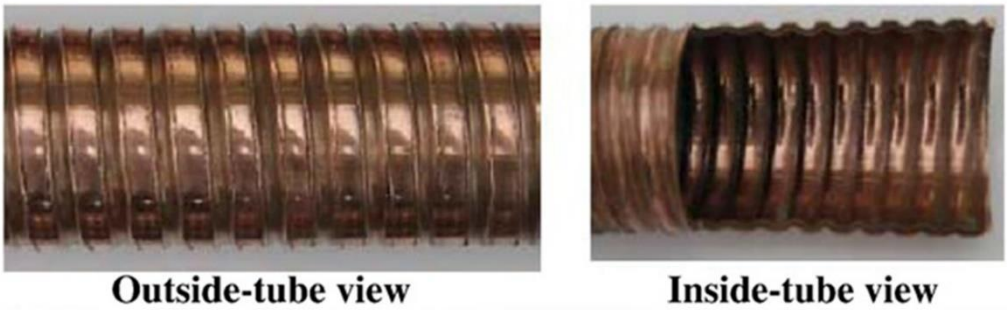

Figure 2.6 Schematic of corrugated tubes. (Pethkool et al., 2011 [35])

Dimpled tubes are manufactured with spherical or ellipsoidal pits or bulges on the tube wall. The schematic of the dimpled tubes is shown in Figure 2.7. Xie et al. [36] proposed novel helical dimpled tubes and numerically investigated their heat transfer characteristics and flow pattern. The realizable k–ε turbulence model with enhanced wall function have a good prediction for the fluid flow in dimpled tube. Furthermore, to capture the flow structures around the dimples, finer cells with prism layers are generated in the tube wall vicinity. The results show that vortices induced by helical dimples enhance fluid mixing between the core region and boundary layer. The thermal performance of helical dimpled tubes is 120 %-270 % higher than that of plain tubes. Helical dimples can improve flow mixing, disrupt the boundary layer, and generate periodic jet flows and transverse flows, thereby offering superior thermohydraulic performance. These three mechanisms can explain the flow phenomenon in dimpled helical tubes: separated flow and accelerated velocity ahead of the dimpled surface, transverse flow and vortices formed behind the dimples, and reattachment of separated flow on the tube wall. Compared with the flow in ribbed and groove tubes, the flow structure in dimpled tubes is more complex, indicating significant potential for further optimization.

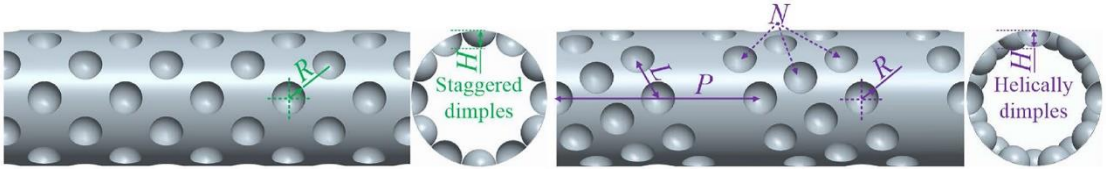

Figure 2.7 Schematic of dimpled tubes. (Xie et al., 2022 [36])

2.2.3 Special-shaped inserter

When fluid flows through special-shaped inserters, its flow direction changes radially. The local or global swirling flows and secondary flows induced by these inserters enhance fluid mixing and disrupt thermal boundary layer development. Special-shaped inserters offer advantages of easy manufacturing and low maintenance costs. Several common types of special-shaped inserters are introduced in this section.

Conical inserters can induce jet flows that scour the tube wall, accelerating near-wall fluid flow and reducing the temperature gradient. These inserters can enhance heat transfer at local regions in tubes without significantly increasing flow resistance. The schematic of the conical inserters is shown in Figure 2.8. Promvonge [37] investigated the flow and heat transfer characteristics of conical-ring inserters in tubes. Experimental results demonstrate a 197 - 333 % improvement in heat transfer performance compared to plain tubes, though with a substantial increase in flow resistance. The installation and machining of conical inserts are relatively straightforward. They can be mounted on a central rod and fitted directly into tubes. Additionally, the geometry of the conical insert can be optimized through various parameters and shape designs. To reduce flow resistance, the primary optimization directions include adopting streamlined forms and introducing perforations. The generation of longitudinal vortices also remains a key consideration, requiring a balance between minimizing flow resistance and enhancing vortex intensity. Undoubtedly, conical inserts hold considerable potential for improving the heat transfer performance of heat exchangers in the future.

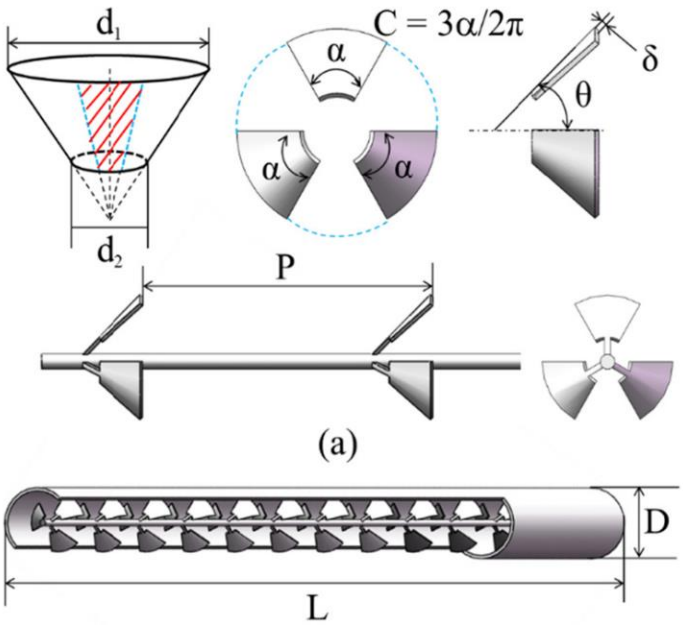

Figure 2.8 Schematic of conical inserters. (Zheng et al., 2017 [38])

Twisted tapes are typically manufactured by twisting metal sheets into an axially rotating configuration. A significant drawback of traditional twisted tapes is their substantial flow resistance. The schematic of the twisted tapes is shown in Figure 2.9. Samruaisin et al. [39] investigated the thermal enhancement characteristics of regularly spaced twisted tapes. The RNG *k-ε* model is performed to model the turbulent flow region. These modified twisted tapes effectively reduce pressure drop while maintaining heat transfer performance. The primary mechanism by which twisted tapes enhance heat transfer is through improved fluid mixing, driven by swirling flow and centrifugal forces. In addition, the curvature of the tape effectively increases the flow path length and heat transfer area. Owing to their lower pressure drop, short twisted tapes are the optimal choice for insertion into tubes. However, it is clear that twisted tapes will remain a preferred option for tube insertion in the future, provided the overall system pressure drop can be effectively reduced.

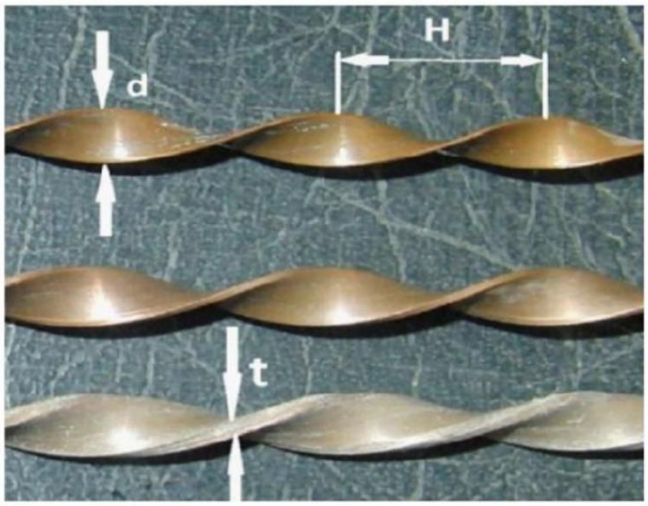

Figure 2.9 Schematic of twisted tapes. (Esmaeilzadeh et al., 2014 [40])

The flow structure induced by axial vane swirlers consists of a single tornado-like vortex structure. The schematic of the axial vane swirlers is shown in Figure 2.10. Ahmadvand et al. [41] conducted an experimental and numerical investigations of steady-state heat transfer and fluid flow characteristics in tubes equipped with axial-vane swirlers. Time-averaged governing equations are solved numerically and RSM model is applied as the turbulence model. Their results demonstrate that the local heat transfer decay rate increases with vane angle. Depending on vane angle, the overall Nusselt number enhancement is found from 50 % to 110 %, while friction factor increases by the range of 90 – 500 %. Swirlers are used as insert devices to enhance heat transfer in tubes. Currently, most research focuses on swirlers inserted in single tubes. Not only is the relevant literature limited, but studies on their application in full heat exchangers are also scarce. Axial-vane swirlers, in particular, show great potential for use in heat exchangers because they can readily redirect the flow into a helical pattern, occupy minimal space inside the tube, and do not extend outside the tube. Earlier work predominantly addressed heat transfer enhancement using twisted-tape and jet-injection swirl generators. Despite the design and installation advantages of axial-vane swirlers, they have not yet been thoroughly investigated for improving heat transfer performance. Moreover, the swirl intensity of axial-vane swirlers can be controlled more easily, especially in double-pipe heat exchangers, as their structure is

better suited to the geometry of the heat exchange tubes.

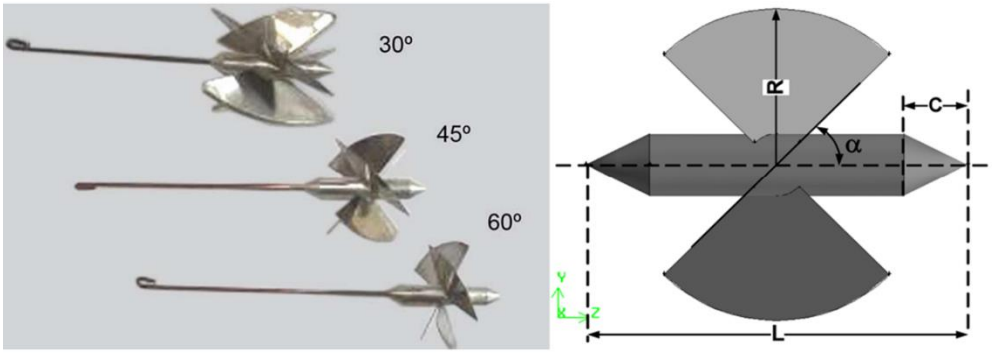

Figure 2.10 Schematic of axial vane swirlers. (Ahmadvand et al., 2009 [41])

In addition to the typical special-shaped inserters introduced above, other configurations including baffles [42], elliptic inserters [43, 44], wire coils [45-50], and inserted rings [51-54] have also drawn research attention. Furthermore, numerous novel inserters have been investigated [55-60].

2.3 Development of winglet applications

Winglets are initially employed on aircraft wings to delay turbulent boundary layer separation under adverse pressure gradients. Biswas et al. [61] pioneered winglet research through numerical and experimental investigations of delta winglets in rectangular channels, examining thermal transfer and flow dynamics. Their simulations identify three vortex types: main, corner, and induced vortices. Results demonstrate that delta winglets can significantly enhance heat exchanger performance. Among tube inserts, winglet vortex generators attract particular attention due to their small configurations and associated low pressure drop [9, 62]. Winglets show strong potential for improving heat exchanger performance. Vortex generation occurs through flow separation at winglet tips, followed by flow roll-up due to the lower pressure on the winglet's back side. This process generates secondary flows rather than modifying the mainstream [63]. Furthermore, winglets can induce multi-longitudinal vortices to optimize heat transfer [20, 64, 65]. The optimization mechanism involves generating the steady vortex structure, but not all winglet configurations can achieve it. The heat exchanger design, flow characteristics, and winglet geometry are key factors

influencing the vortex structure.

Most previous studies on winglet applications have focused on fin-and-tube heat exchangers or rectangular channels, with comparatively fewer investigations examining heat transfer in plain tubes. Two primary challenges emerge when applying winglets in tubular systems. First, pressure drop reduction and installation simplification present technical hurdles. Second, multiple parameters including pitch ratio, blockage ratio, attack angles significantly influence longitudinal vortex size and strength. Therefore, based on distinct flow field characteristics, winglet applications have evolved along three main development pathways: i) fin-and-tube heat exchangers or rectangular channels, ii) tubes with twisted tapes or flat plates, and iii) plain tubes.

2.3.1 Applications in fin-and-tube heat exchangers or rectangular channels

In earlier studies, winglet vortex generators are widely applied in rectangular channels [66-68] (Figure 2.11) and fin-and-tube heat exchangers [69-71] (Figure 2.12), yielding more in-depth findings on mechanisms compared to studies on heat transfer within tubes [72-74].

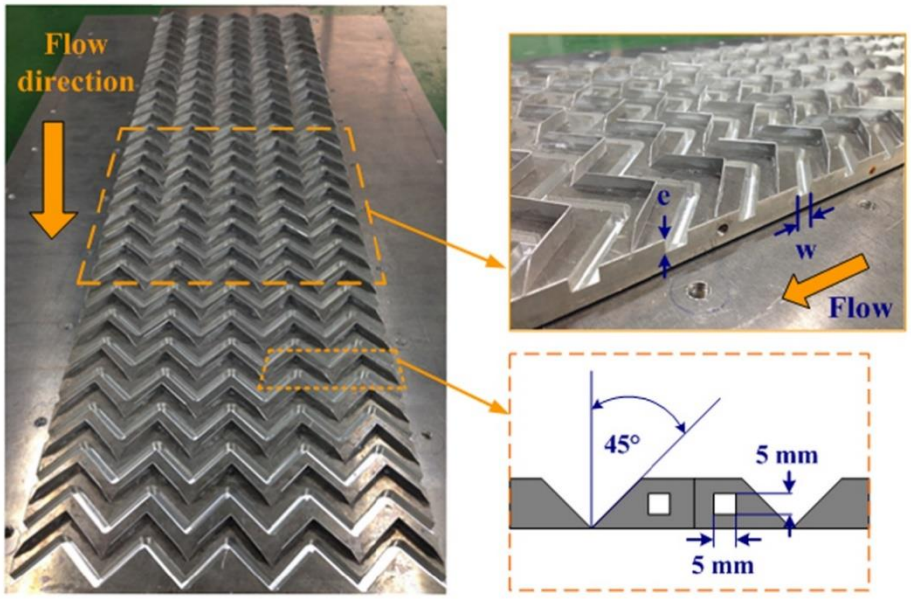

Figure 2.11 Winglet applications in rectangular channels. (Promvonge et al., 2022 [62])

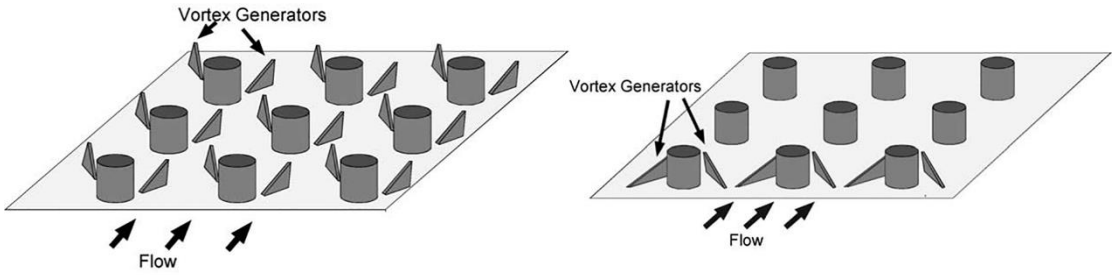

Figure 2.12 Winglet applications in fin-and-tube heat exchangers. (Torii et al., 2002 [75])

Kim and Yang [76] experimentally investigate heat transfer characteristics and vortex interactions of embedded counter-rotating vortex pairs. Their results demonstrate that in common-flow-down (CFD) configurations, vortex-boundary layer interactions are more intense than inter-vortex interactions within a single pair. In contrast, common-flow-up (CFU) cases exhibit the opposite behavior (Figure 2.13). The CFD configurations show superior heat transfer performance relative to CFU cases, largely because vortex interactions are weaker in the former. While CFU cases enhance fluid mixing in the mainstream direction, vortex intensity diminishes due to inter-vortex interactions. Furthermore, the spacing between winglets within a pair constitutes a critical design parameter.

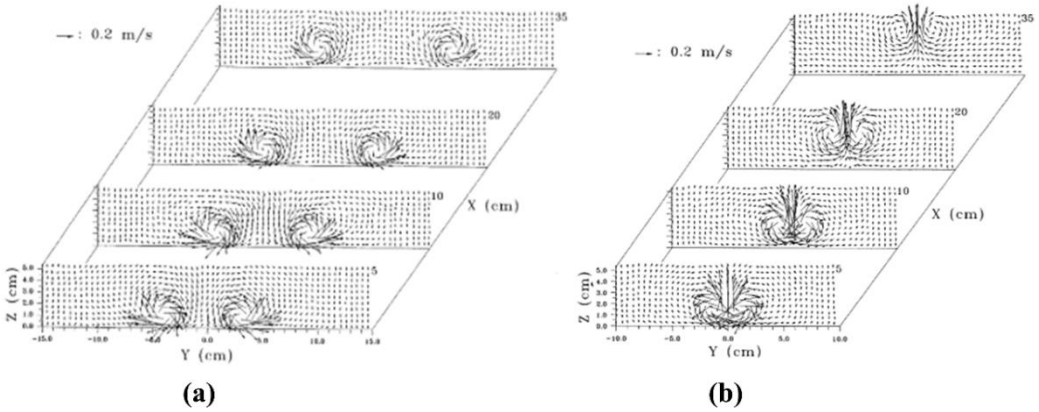

Figure 2.13 The secondary velocity vectors in rectangular channels: (a) CFD; (b) CFU (Kim and Yang, 2002 [76]).

Ke et al. [77] analyzed the dynamic behaviors of longitudinal vortices induced by wall interactions using the “method of images” (Figure 2.14). The high-resolution advection

scheme is selected in ANSYS CFX software. It is a bounded second-order upwind biased discretization. Their results demonstrate that channel height and aspect ratio are the two dominant factors influencing arrangement effectiveness. This finding explains the inconsistent heat transfer performance observed in previous studies comparing CFD and CFU configurations. Specifically, the impact of any single structural variable on vortex interaction varies across different channels or fin-and-tube heat exchangers. Currently, there exists limited research examining similarity relationships between flow characteristics and structural variables in diverse flow fields. Systematic similarity analysis could offer new insights into the fundamental consistency of vortex interaction mechanisms across varying flow fields.

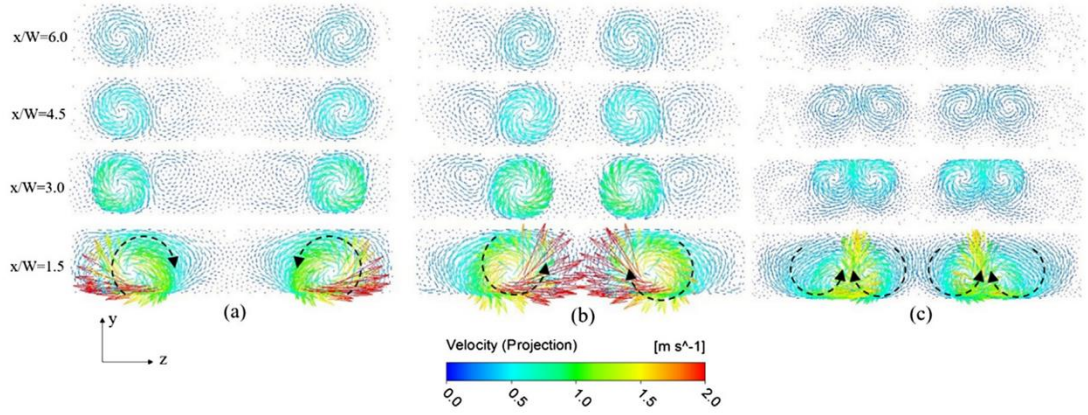

Figure 2.14 Secondary velocity vector at different locations (a) CFD, (b) CFU, and (c) mixed type (Ke et al., 2019 [77]).

Wu et al. [78] numerically investigated the thermal performance of fluid flow in channels with multiple rows of winglet vortex generators using the SST k-ω model. The delta-winglet vortex generators introduce irregular regions, and the Y-block method is used to deal with blocks in regions adjacent to the vortex generators to ensure mesh quality. Their results demonstrate that pitch ratios below 4 and height ratios under 1/12 prove ineffective for heat transfer enhancement. Proper winglet arrangement can significantly improve thermal mixing and secondary flow diffusion. Furthermore, strengthening secondary flows is not the only consideration for enhancing heat transfer. Song et al. [79] developed an enhanced wavy delta winglet design and numerically

evaluated the effects of attack angle, central angle, and arrangement on heat transfer and fluid flow in fin-and-tube heat exchangers. The combination of RNG k-ε model and enhanced wall treatment is adopted for numerical calculations. Their analysis reveals that wavy delta winglets generate longitudinal vortices that strengthen secondary flow intensity. Under the optimum parameter, the Nusselt number of wavy delta winglet is enhanced by 44.87 %, while friction factor is also increased by 47.31 % compared to plain fin. An appropriate winglet arrangement achieves a maximum thermal enhancement factor (*TEF*) of 1.29.

Tian et al. [80] numerically compared overall performance in channels equipped with delta and rectangular winglet pairs. The computational domain is discretized by non-uniform grids, with fine grids in channel region and coarse grids in the extended region. Their results demonstrate that delta winglet pairs exhibit superior overall performance compared to rectangular configurations. Zhou and Feng [81] experimentally investigated flat and curved vortex generators, both with and without punched holes, in rectangular channels. (Figure 2.15). The findings reveal that curved winglets achieve better thermal performance owing to their larger fin area and streamlined design. The introduction of holes improves thermal performance while reducing flow resistance across all cases, though hole positioning shows minimal impact on flow resistance characteristics.

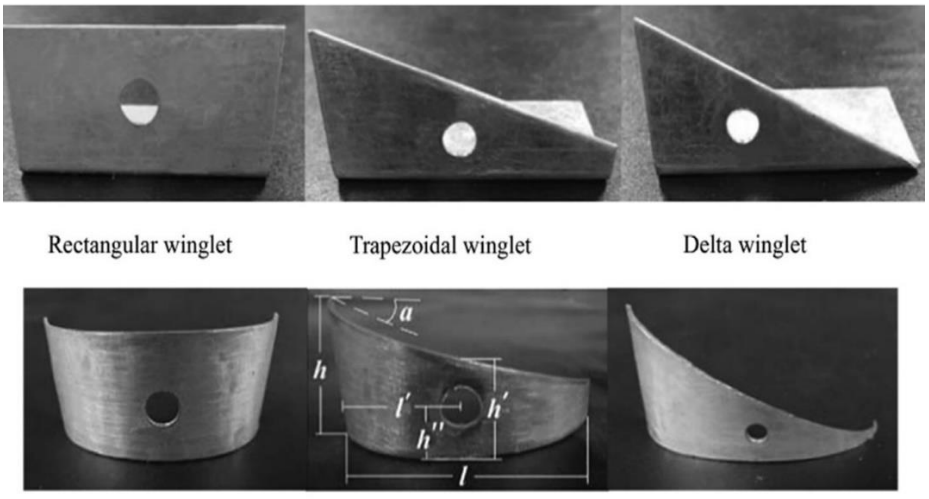

Figure 2.15 Pictorial diagram and punched holes (Zhou and Feng, 2014 [81]).

Table 2.1 summarizes winglet applications in rectangular channels or fin-and-tube heat exchangers for heat transfer enhancement. While most previous studies report superior heat transfer performance for CFD configurations compared to CFU cases, some investigations have reported opposing results. These discrepancies suggest that the vortex structures generated by CFD arrangements may not consistently represent the optimal configuration, as their performance can be affected by structural parameters including tube geometry, winglet spacing, and positioning. Moreover, perforations in winglet vortex generators may significantly impact the downstream vortex formation.

Table 2.1 Winglet applications in rectangular channels or fin-and-tube heat exchangers for heat transfer enhancement.

No.	Winglet installation R: rectangular channels F: fit-and-tube heat exchangers	Researchers	Fluid	Research method E: experiment S: simulation
1	R	Kim and Yang [76]	Air	E
2	F	Torii et al. [75]	Air	E
3	F	Chu et al. [82]	Air	S
4	R	Tian et al. [80]	Air	S
5	F	Zhang et al. [83]	Air	E
6	R	Caliskan [84]	Air	E
7	R	Zhou et al. [81]	Air	E
8	R	Behfard and Sohankar [85]	Air	S
9	R	Skullong et al. [86]	Air	E
10	F	Zhang et al. [87]	Air	E
11	R	Fiebig [88]	Air	E & S
12	F	Song et al. [89]	Air	E
13	R	Nandana and Janoske [90]	Air	S
14	R	Ke et al. [77]	Air	S
15	R	Liu et al. [91]	Water	E & S
16	F	Md Salleh et al. [92]	Air	S
17	R	Ali et al. [93]	Water	S
18	R	Jiang et al. [94]	Water	S
19	R	Khoshvaght et al. [95]	Air	E & S
20	R	Zhao et al. [96]	Air	S
21	R	Promvonge et al. [62]	Air	E & S
22	F	Song et al. [70]	Air	S

2.3.2 Applications in tubes with twisted tapes or flat plates

Due to installation issues within tubes, winglets are commonly fitted on flat plates [97, 98] (Figure 2.17) or twisted tapes [99] (Figure 2.16) in earlier studies. However, flat plates and twisted tapes inevitably affect the vortex interaction and increase the pressure drop.

Eiamsa-ard et al. [100] investigated the thermal performance of twin delta-wing twisted tapes (Figure 2.16). Their results demonstrate that the upward wing configuration outperformed position performed both downward and opposed orientations. Twin tapes with 20° upward wing angles achieve the highest *TEF* of 1.26. Sun et al. [101] examined heat transfer characteristics in circular tubes fitted with multiple rectangular winglets using the SST *k-ω* model. The study reports friction factor ratio (f/f_0) ranging from 1.46 to 11.63 and Nusselt number ratio (Nu/Nu_0) between 1.15 to 2.32.

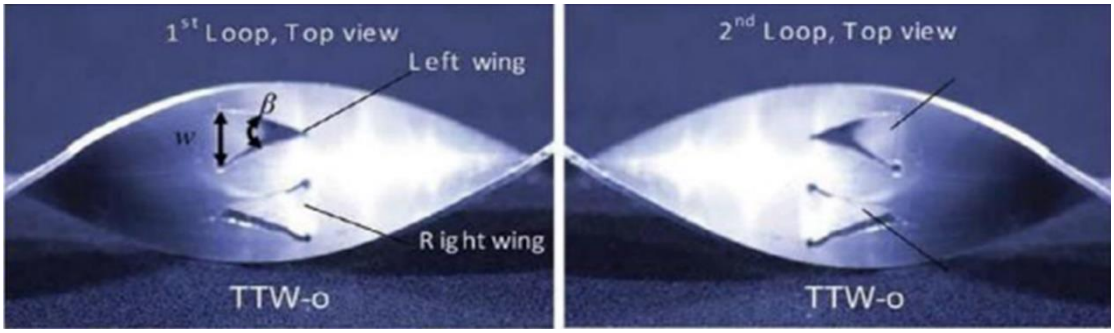

Figure 2.16 Twisted tapes with twin delta wings (Eiamsa-ard, 2013 [100])

Most winglet designs for tubular applications are adapted from those applied in channels or fin-and-tube heat exchangers. The most similar configuration within tubes is the installation of winglets on a flat plate. Promvonge et al. [97] studied thermal performance in circular tubes with louvered V-winglet vortex generators mounted on a flat plate (Figure 2.17). The realizable *k-ε* turbulent model is employed in the computation whilst the SIMPLE algorithm is adopted to handle the velocity-pressure coupling. Their results demonstrate a maximum *TEF* of 2.48, achieved through vortex-induced impingement flows. The primary heat transfer enhancement mechanism is

attributed to impingement jets generated downstream of the fins. Furthermore, perforations on the fin surface can reduce pressure drop. Compared to influencing factors in channels or fin-and-tube heat exchangers, the primary differences in tubes are the wall limitations and vortex interactions.

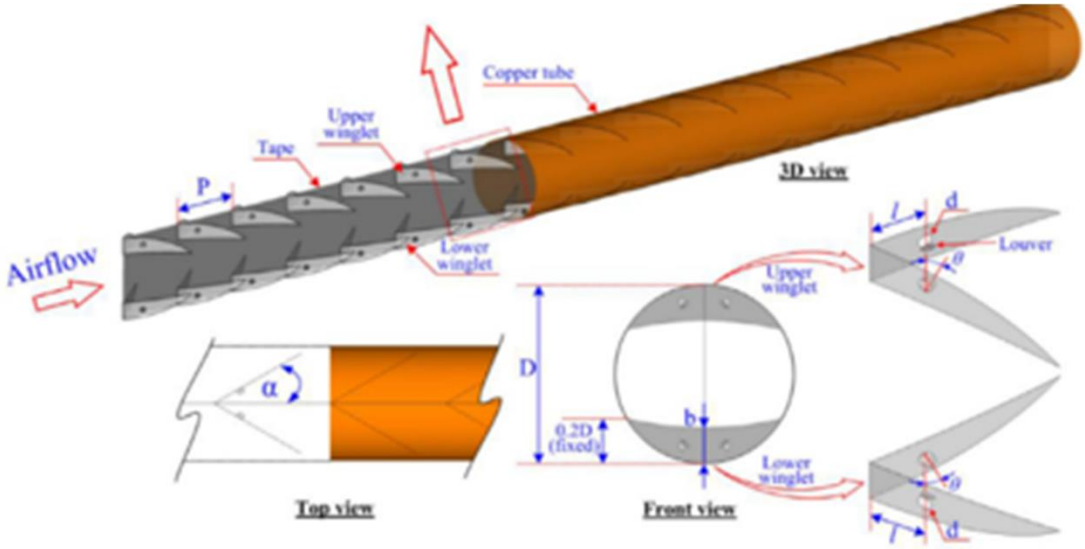

Figure 2.17 Louvered V-shaped winglets (Promvonge et al., 2022 [97])

Table 2.2 summarizes winglet applications in tubes with twisted tapes or flat plates for heat transfer enhancement. The use of twisted tapes in tubes generates higher pressure drop compared to flat plates. Furthermore, the swirling flow induced by twisted tapes may interfere with winglet-induced longitudinal vortices, underscoring the need for structural optimization to balance the intensity between swirling flows and longitudinal vortices. In tubular flow fields with flat plates, the fluid separates into two regions. While this flow division does not disrupt the vortex structure, it may still influence vortex interaction.

Table 2.2 Winglet applications in tubes with twisted tapes or flat plates for heat transfer enhancement.

No.	Winglet installation T: twisted tapes F: flat plates	Researchers	Fluid	Research method E: experiment S: simulation
1	T	Eiamsa-ard et al. [102]	Water	E

2	T	Wongcharee and Eiamsa-ard [103]	Water	E
3	T	Eiamsa-ard et al. [100]	Water	E
4	F	Boonloi and Jedsadaratanachai [104]	Air	S
5	F	Skullong et al. [105]	Air	E
6	F	Lei et al. [106]	Water	S
7	F	Wijayanta et al. [107]	Water	S
8	F	Yaningsih et al. [108]	Water	E
9	F	Promvonge and Skullong [98]	Air	E
10	F	Promvonge et al. [97]	Air	E & S

2.3.3 Applications in plain tubes

Mounting winglets on a ring is an effective method for installing winglets within tubes. However, these rings inevitably introduce additional flow resistance. Furthermore, the optimization with this structure for vortex interactions is limited, as the formed vortex structure does not significantly change with variations in ring structures.

Liang et al. [109] numerically analyze thermal enhancement and flow structures in tubes with varying attack angles, inclination angles, and radial arrangements using the SST k-ω model. The QUICK scheme is employed to discretize the convective terms in governing equations for momentum and energy. Their results demonstrate a maximum Nu/Nu_0 of 1.36. The vortex generators induce both longitudinal and transverse vortices, creating impingement flows and recirculation zones. However, the advantageous flow disturbance effects are offset by detrimental fluid mixing and axial flow development along the tube length. Xu et al. [110] experimentally observed airflow behavior around four winglet vortex generators in tubes (Figure 2.18). Results show that heat transfer and flow resistance increase as blockage ratio and attack angle, but decrease with Reyolds number and pitch ratio. As shown in Figure 2.18, horseshoe vortices form around the vortex generators, while the main longitudinal vortices develop along the top edges of vortex generators. These flow behavior is validated through computational simulations [111].

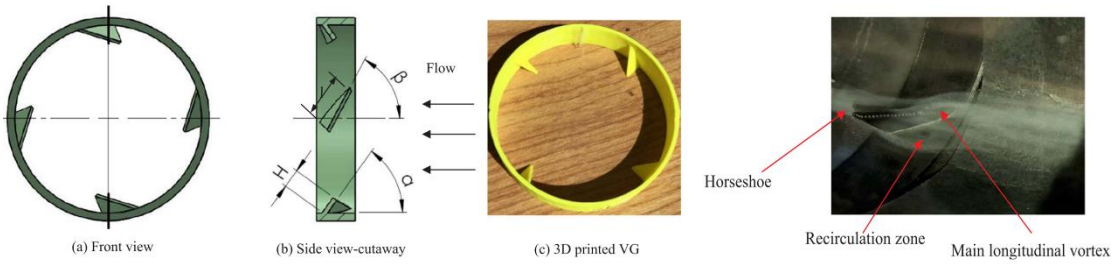

Figure 2.18 Delta winglets installed on a ring and smoke flow visualization (Xu et al., 2018 [110]).

Zhang et al. [112] studied the effects of attack angle and length ratio on the thermal performance in tubes with P-type and V-type rectangular winglet vortex generators using RNG *k*-*ε* model. The results show that P-type configurations generate a single longitudinal vortex, whereas V-type configurations produce multiple longitudinal vortices. Compared to smooth tubes, P-type vortex generators enhance heat transfer rate by 54 %-118 % and increase flow resistance by 152 %-568 %, while V-type vortex generators improve heat transfer by 60 %-118 % and raise flow resistance by 141 %-644 %. Wang et al. [113] conducted combined numerical and experimental studies of the thermal performance of perforated rectangular winglet vortex generators in turbulent flow regimes (Figure 2.19). The vortex generator design incorporates two key features: perforations and rings. This novel design effectively reduces pressure drop while enhancing heat transfer in the circulation regions.

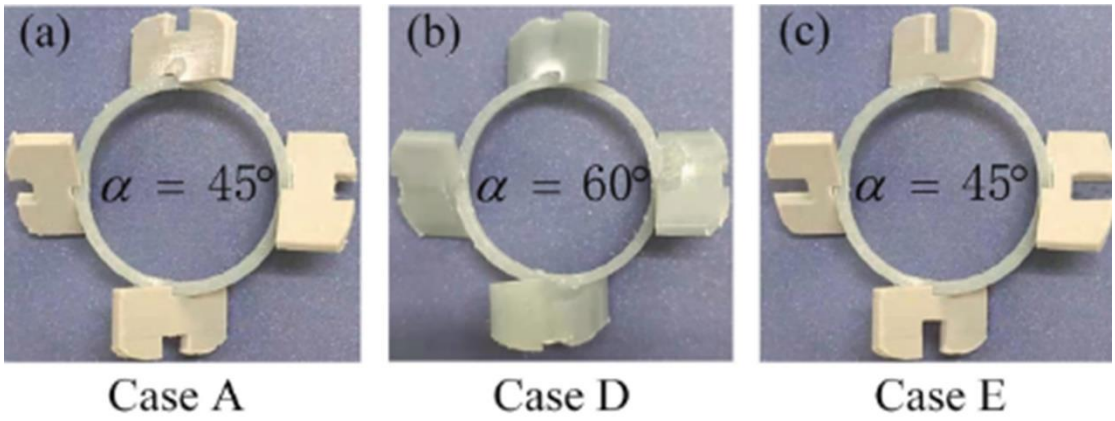

Figure 2.19 Punched rectangular winglets (Wang et al., 2022 [113]).

To address the limitations in vortex interaction optimization, a novel structure that

combines winglets and rings is proposed. Zheng et al. [20] investigated the heat transfer characteristics of turbulent airflow within circular tubes utilizing novel self-join winglets. The Standard *k*-*ε* gives the closest results to the measured data. The findings suggest that this novel structure can significantly improve the fluid mixing while reducing the synergy angle, resulting in stronger vortex flows and more uniform temperature distribution. At a blockage ratio of 0.05 and an included angle of 120 º, the maximum *TEF* reaches 1.27. Figure 2.20 demonstrates the flows behind winglets drive high-temperature fluid from near-wall region to mainstream, while transfer low-temperature fluid from mainstream to near-wall region. This flow behavior contributed to enhance fluid mixing. Winglets and rings are combined into one novel structure to reduce the unnecessary pressure drop, representing a superior alternative to conventional ring structures.

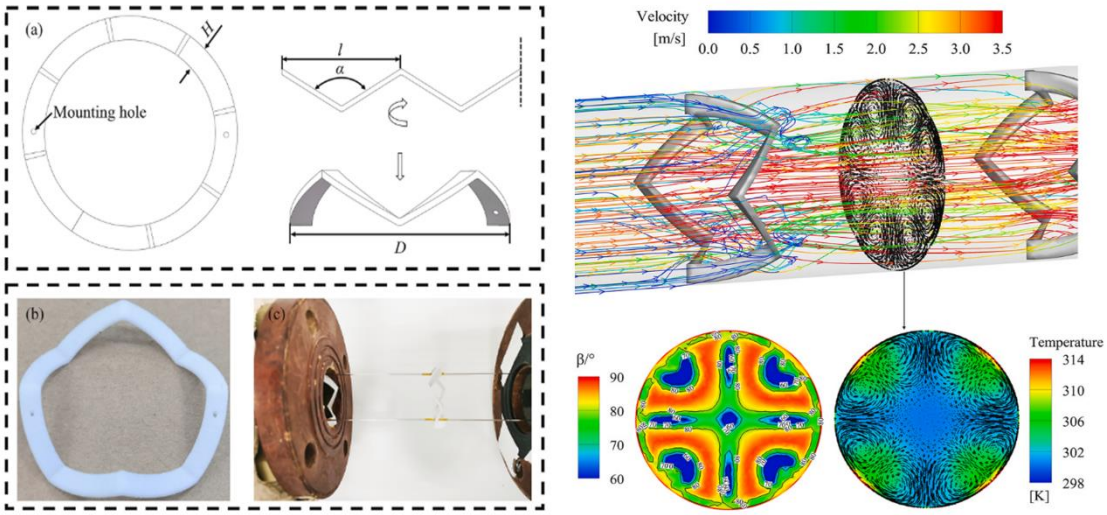

Figure 2.20 The configuration and flow structure of self-connected winglets (Zheng et al., 2022 [20]).

Wu et al. [114] investigated the effect of punching holes on fluid flow and thermal performance within circular tubes equipped with multi-V-winglets vortex generators using the SST *k*-*ω* model (Figure 2.21). It is found that jet flows induced by the holes on the winglet surface impact the recirculation zone and remove stagnant fluid. Furthermore, the existence of punching holes can enhance the overall performance by reducing structural resistance.

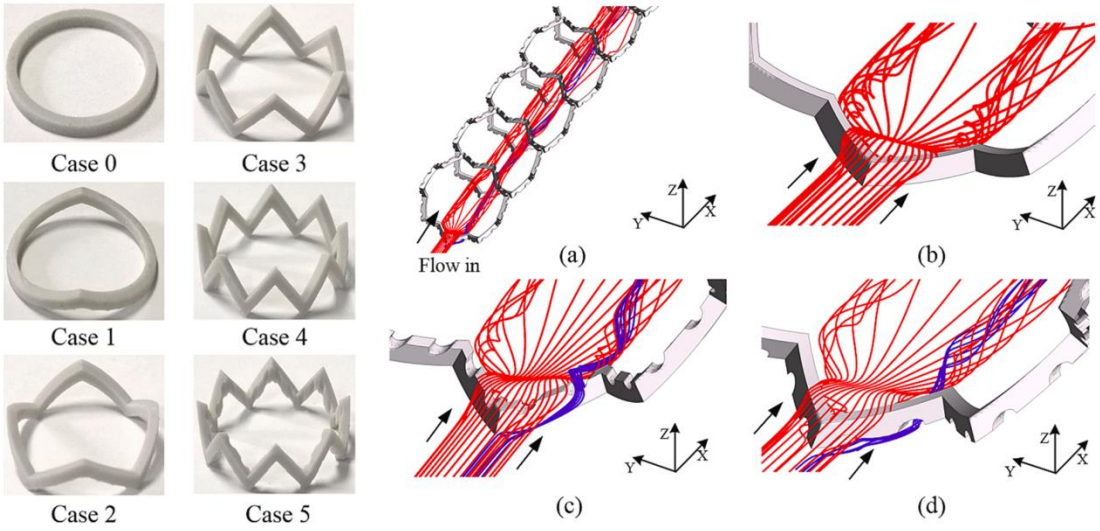

Figure 2.21 Winglet structure and streamline distribution: (a) Overall flow direction; (b) Case 4; (c) Case 5; (d) Case 6 (Wu et al., 2024 [114]).

Based on the configuration of tubular heat exchangers, heat exchange tubes can be categorized as circular or annular. Currently, winglets are primarily applied to the circular tube side of tubular heat exchangers. However, there is a lack of research investigating their potential to enhance heat transfer in annular tubes. Annular tubes, unlike circular tubes, have two walls that influence fluid flow and vortex interactions. Zhang et al. [87] investigated the effect of delta-winglet-pair vortex generators on heat transfer performance on the shell side of heat exchangers with helical fins. Results indicate that heat exchangers with winglets exhibit 16.6 % higher heat transfer performance compared to those without winglets. Among attack angles of 30 º, 45 º, and 60 º, 30 º is the optimal choice when the pressure drop remains constant. Nair et al. [115] conducted numerical and experimental studies on the comprehensive heat transfer performance in annular tubes equipped with angled fins. The ANSYS-Fluent software with the SIMPLEC algorithm and the SST k-ω turbulence model is used to simulate the flow field affected by angled fins. The findings indicate that longitudinal vortices optimize heat transfer with a low impact on the increase in pressure drop. Furthermore, to achieve higher *TEF* values, it is ideal to design heat exchangers with a fin height equal to 20 %−60 % of the gap between the concentric walls.

Table 2.3 summarizes winglet applications in plain tubes for heat transfer enhancement. Winglets have various geometric configurations, including rectangular, delta, and trapezoidal designs. Among these, delta winglets possess the simplest structure and lowest pressure drop characteristics. Delta winglet vortex generators achieve superior heat transfer enhancement at equivalent pressure drop conditions [116]. Furthermore, winglet designs can be categorized as either single-winglet or winglet-pair configurations. The winglet-pair type presents a more efficient longitudinal vortex generator, as it significantly destabilizes flow fields, generates secondary flows, and increases turbulence intensity [117]. This configuration produces counter-rotating vortex pairs that create impinging flows against the tube wall. These impingement flows disrupt boundary layer development while simultaneously enhancing heat transfer performance.

In previous studies of winglet applications in plain circular tubes, the primary focus has been on three aspects: (a) strengthening vortex interaction, (b) reducing flow resistance caused by structure, and (c) weakening recirculation zones. However, these studies have largely overlooked the dynamic variations of vortex interactions. Despite numerous studies conducted on winglet applications, there are still many research questions regarding winglet applications in annular tubes that need to be addressed, particularly concerning the applications of novel winglet structures. The use of winglets on the annular side is crucial for optimizing the overall performance of heat exchangers.

Table 2.3 Winglet applications in plain tubes for heat transfer enhancement.

No.	Winglet configurations	Researchers	Fluid	Research method E: experiment S: simulation
1	Delta winglet pairs	Hatami et al. [118, 119]	Air	E
2	Delta winglets	Xu et al. [111]	Air	S
3	Delta winglets	Liang et al. [109]	Air	S
4	Delta winglets	Xu et al. [110]	Air	E
5	Delta winglet pairs	Zhai et al. [120, 121]	Air	E
6	Delta winglets	Islam et al. [122]	Air	E

7	Rectangular winglets	Sun et al. [101]	Air	E & S
8	Rectangular winglets (Parallel and V-shape)	Zhang et al. [112]	Air	E & S
9	Rectangular winglets on serrated rings	Singh et al. [123]	Air	E & S
10	Curved winglets	Sun et al. [65]	Air	E & S
11	Punched winglets	Wang et al. [113]	Air	E & S
12	Punched winglets	Wang et al. [74]	Air	E & S
13	Multi-V-winglet vortex generators	Zheng et al. [20]	Air	E & S
14	Multi-V winglet vortex generators	Wu et al. [114]	Water	E& S

2.4 Double-tube heat exchangers

Double-tube heat exchangers find extensive applications across multiple energy sectors including solar energy [124], combustion systems [125], geothermal energy [126, 127], anti-scaling and descaling processes [128, 129], waste heat recovery [130], air conditioning [131], and phase-change latent heat energy storage [132, 133]. Their structural robustness, operational flexibility, and exceptional adaptability make them essential components in numerous heat transfer system [134]. The schematic of the double-tube heat exchangers is shown in Figure 2.22.

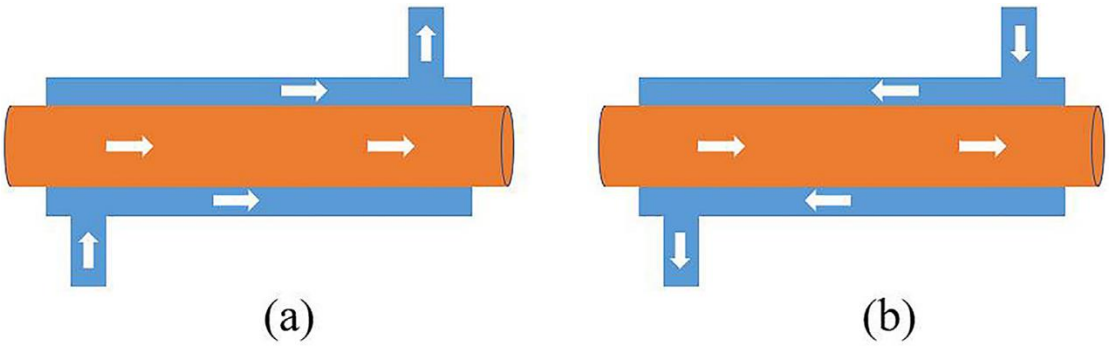

Figure 2.22 Schematic of double-tube heat exchangers: (a) Parallel flow; (b) Counter flow (Li et al., 2022 [11])

As recuperative heat exchangers, double-tube designs employ solid walls to separate and facilitate heat transfer between two media, with the internal tube wall serving as the primary heat transfer surface. Heat transfer enhancement methods in these

exchangers fall into two main categories: (a) tube-side modifications using internal fins or special-shaped inserts (particularly twisted tapes), and (b) shell-side enhancements through external fins or rib baffles. These exchangers are particularly suited for high-temperature, high-pressure applications due to their compact diameter and cost-efficient sealing requirements. However, these exchangers require more space than other heat exchanger types. Furthermore, these exchangers are typically employed for smaller-scale applications because of their higher space occupancy cost. Current research on fluid flows and heat transfer in double-tube heat exchangers primarily focuses on industrial applications. These studies simultaneously aim to improve thermal performance while minimizing pressure drop.

From both economic and installation perspectives, special-shaped inserts represent the most practical solution for enhancing thermal performance in double-tube heat exchangers. The vortex generation mechanisms vary significantly with different insert geometries, resulting in distinct advantages and disadvantages for fluid flow manipulation in each configuration.

2.5 Longitudinal vortex

2.5.1 The structure of longitudinal vortex

Longitudinal vortex flows, one of the typical secondary flows, is a rotating motion around the axis. The generation of longitudinal vortices necessarily involves accompanying transverse vortices. Transverse vortices are two-dimensional with axes perpendicular to the mainstream direction, while longitudinal vortices are three-dimensional with axes parallel to the mainstream direction [135]. Figure 2.23 illustrates the structural differences between transverse [136] and longitudinal [137] vortex flows. Karman vortex streets generated by the flow around cylindrical structures and flows created by externally swept configurations both represent transverse vortex phenomena. In contrast, longitudinal vortices form behind protrusions, such as delta winglets, delta wings, and rectangular winglets. When assessing combined heat transfer and flow resistance, longitudinal vortex generators demonstrate superior overall thermal

effectiveness compared to transverse vortex generators [138].

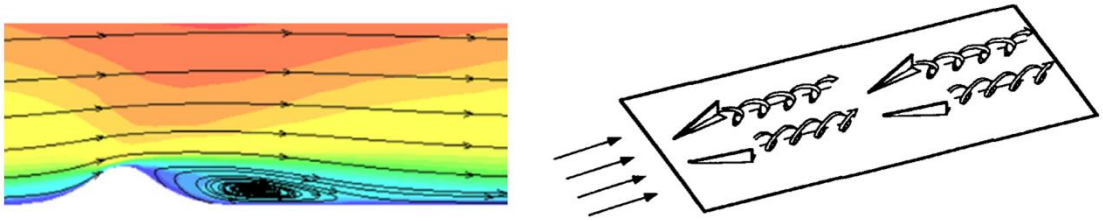

(a) (b)

Figure 2.23 Vortex structure: (a) Transverse vortex (Hu et al., 2022 [136]), (b) Longitudinal vortex (Jacobi and Shah, 1995 [137]).

The mechanisms behind heat transfer enhancement by longitudinal vortex flows can be summarized as the result of separation vortices and flow instability in the thermal boundary layer. In addition to strengthening periodic separation of fluid flows, wake recovery, and laminar flow development, longitudinal vortex flows also disrupt fully developed boundary layers. While their magnitudes are smaller than those of the mainstreams, longitudinal vortex flows exert a significant influence on heat transfer and flow structure. Since vortices are induced only by solid surfaces and do not dissipate into the fluid, longitudinal vortex can propagate over significant distances in fluid flow, often extending tens of times the height of vortex generators. Torii et al. [139] investigated the vortex structure induced by delta winglets. Using rotating probe technology, they measured tail vortices induced by delta winglets on a flat plate. Results conclude that the longitudinal vortex induced by delta winglets consist of the main vortex, corner vortex, and induced vortex, as shown in Figure 2.24. Both the main vortex and corner vortex exhibit high-intensity longitudinal vortex, playing a significant role in enhancing fluid disturbance and convective heat transfer.

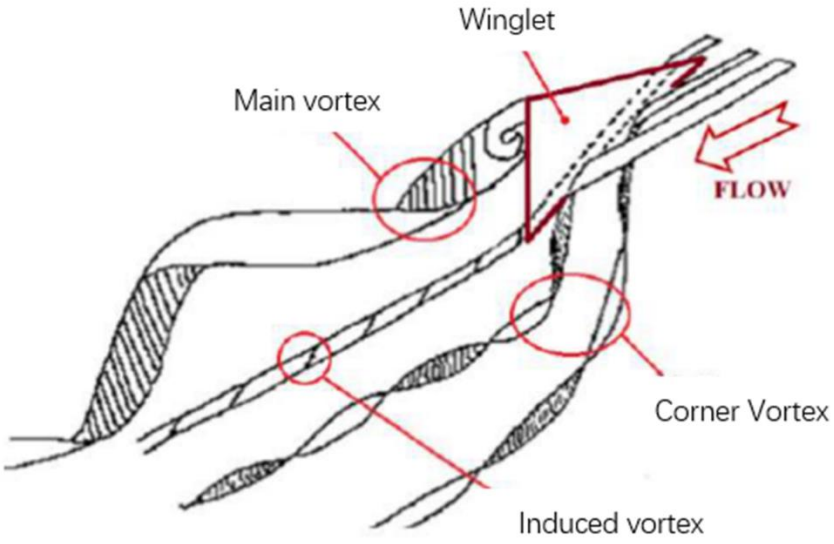

Figure 2.24 Vortex structure induced by delta winglet vortex generators (Torii et al., 1994 [139]).

Longitudinal vortex generators are initially proposed by Schubauer and Spangenberg [140]. Subsequently, Johnson and Joubert [141] conducted a pioneering study on heat transfer in circular tubes equipped with delta winglets, laying the foundation for the application of longitudinal vortex generators to enhance heat transfer. Longitudinal vortex can be generated through various passive methods, such as dimpled tubes, winglets, and groove tubes. The primary challenge in applying longitudinal vortex to heat exchangers is selecting optimal parameters to control the vortex structure. These parameters, such as blockage ratio, attack angle, and pitch ratio, influence vortex intensity, decay rate, and pressure loss.

2.5.2 The interaction of longitudinal vortex

Numerous investigations into longitudinal vortices have primarily concentrated on their applications, resulting in a relative scarcity of quantitative research on longitudinal vortex interactions [142-144]. In past studies concerning longitudinal vortex flows, there has been a lack of consistent explanations for the observed variation trends in heat transfer and pressure drop across different cases.

Eibeck [145] experimentally studied the effect of longitudinal vortices induced by delta wings on heat transfer in turbulent boundary layers. The results indicate that weak longitudinal vortex flows have little effect on heat transfer, whereas strong longitudinal vortex flows notably enhance it. Vortex intensity emerges as a pivotal factor in augmenting heat transfer. Wendt et al. [146] conducted experimental investigations into the structure and development of longitudinal vortices in turbulent boundary layers. The distance between vortex generators influenced the development of longitudinal vortices. The merging of adjacent longitudinal vortices with opposite rotation directions weakened longitudinal vortex intensity, a finding consistent with Song et al. [142]. However, this weakening of longitudinal vortex intensity does not necessarily diminish their heat transfer performance. The distance of vortex interaction is the primary factor affecting average vortex intensity. Yang et al. [147] conducted a numerical analysis to investigate the influence of vortex pairs on the heat transfer performance in rectangular channels. To analyze the vortices produced by the vortex generator, the pseudo-compressibility method is introduced into the Navier-Strokes equation of a three-dimensional unsteady, incompressible viscous flow. Results show that vortices in CFD cases enhance heat transfer more effectively than those in CFU cases. However, the inconsistency across all results arises from the fact that thermal performance is ultimately influenced by the distance of vortex interaction.

Gentry and Jacobi [148] experimentally investigated the interaction between longitudinal vortices and boundary flow in channels with delta wing vortex generators. The results show that mainstream is transported by longitudinal vortices to the boundary layer, effectively reducing its thickness. Moreover, vortex pairs gradually separate when near-wall vortices are transported downstream, yet the vortices remain close to the wall. The possible reason is that the vortex intensity is insufficient to move the vortices away from the wall. Zhu et al. [149] defined a staggered coefficient to approximate longitudinal vortex interaction within fin-and-tube heat exchangers featuring with delta winglets. In previous studies, most results have been summarized through qualitative analyses, with few quantitative analyses addressing longitudinal

vortex interaction. Salviano et al. [150] noted that longitudinal vortex interaction affects both the Colburn factor and friction factor, yet they provided limited explanation on this phenomenon.

Song et al. [142] numerically simulated the interaction of two counter-rotating longitudinal vortices in plate-fin heat exchangers with two rows of delta winglets. The effect of the transversal distance between vortex generators on vortex intensity and vortex interaction is quantitatively analyzed. The governing equations and boundary conditions are transformed into computational space and discretized by the control volume method in a collocated grid system. The results indicate that counter-vortex interaction reduces the average intensity of longitudinal vortices. However, this does not necessarily lead to a decrease in heat transfer performance. The flow region formed between adjacent counter-rotating longitudinal vortices enhances heat transfer. Moreover, arranging vortex generators with zero transverse distance should be avoided due to serious longitudinal vortex interaction (Figure 2.25).

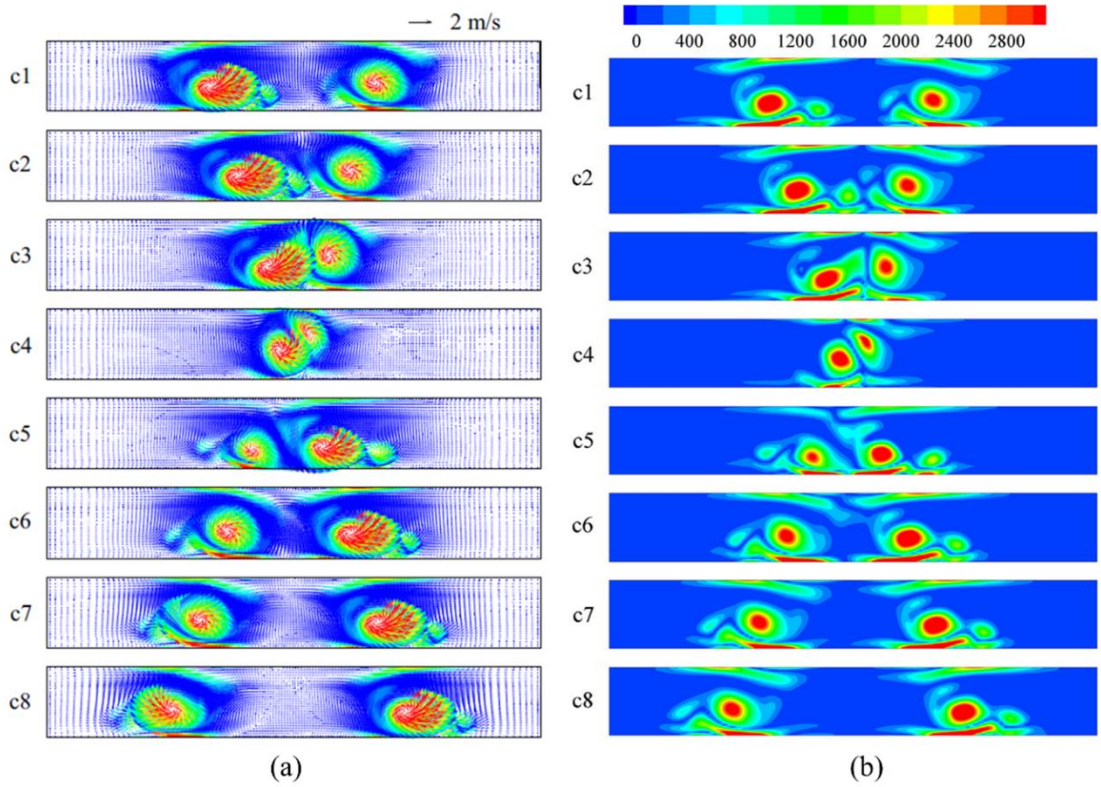

Figure 2.25 Comparison of velocity vectors (a) and contour plot of *Se* (b) on the cross sections (Song et al., 2016 [142]).

Song et al. [143] defined secondary flow intensity (*Se*) to quantitatively study longitudinal vortex intensity in plate-fin heat exchangers with longitudinal vortex generators. They employed a FORTRAN code to obtain numerical results and investigated the effect of transverse distance on longitudinal vortex interaction in detail. Results show that longitudinal vortex interaction is related to the transverse distance of vortex generators. Meanwhile, non-ideal transverse distances between vortex generators must be avoided. Song and Tagawa [144] subsequently quantitatively studied the effect of transverse distance between vortex generators on longitudinal vortex interaction and heat transfer performance. They obtained numerical results by solving the fully three-dimensional elliptic Navier-Stokes equations in a body-fitted coordinate system. The results indicate that co-rotating longitudinal vortex interaction is less affected by the transverse distance between vortex generators, while counter-rotating longitudinal vortex interaction plays a dominant role. At the highest Reynolds number, the maximum differences in longitudinal vortex intensity, *Nu*, and *f* enhancements for different transverse distances are 34.0 %, 33.9 %, and 18.5 %, respectively. The studies conducted by Song et al. [142-144] provide new insights into longitudinal vortex interaction. When longitudinal vortex interaction is weakened, the intensity of both co-rotation and counter-rotation longitudinal vortices increases. Furthermore, longitudinal vortex interaction does not always negatively impact heat transfer.

2.6 Research gap

Based on the literature review, this section summarizes the research gap, which is classified into the following two parts,

(a) Flow fields in tube sides with winglets

Previous studies primarily focus on strengthening the vortex interaction, reducing flow resistance caused by structure, and weakening the recirculation zones. However, the dynamic variations of vortex interactions are not fully

understood. The present work aims to provide novel insights into optimizing vortex interaction in tubes equipped with winglets.

(b) Flow fields in annular sides with winglets

Most studies on the application of winglets focus on rectangular channels, fin-and-tube heat exchangers, and circular tubes. However, despite the numerous studies conducted on winglet applications, there are still many research questions concerning the heat transfer potential of winglet applications in annular tubes that need to be addressed. The use of winglets on the annular side is crucial for optimizing the overall performance of heat exchangers.

Therefore, a novel self-join winglet vortex generator is proposed to investigate the variation mechanism of vortex interactions on both the tube and shell sides of heat exchangers.

Chapter 3: Methodology

3.1 Research methods

In previous studies of heat transfer enhancement technology, research methods are divided into numerical simulation and experimental verification. Experiment work includes proposing reasonable experimental schemes, building experimental setups, and collecting experiment data. Thus, it often requires significant financial resources and time throughout the entire process. With the development of computer technology, numerical simulation is widely applied in various studies. The fundamental theories of numerical simulation are numerical heat transfer and computational fluid dynamics. Physical phenomena are reproduced by solving flow fields in time and space. Numerical simulation can replace some experimental work that is impossible or difficult to complete. However, simulation has some limitations. When combined with experimental verification, it will help to validate the accuracy of the numerical model and ensure numerical results are reliable within the error range. Therefore, numerical simulation and experimental verification are selected as the research methods for this study.

3.2 Flow chart

The entire research progress is shown in Figure 3.1. Research aim and objectives are determined based on the research problem and questions in this study, respectively. Each research component is interrelated and progressively developed. Additionally, the content regarding characteristics, mechanism, and optimization will be described in detail. As shown in Figure 3.2, heat transfer and pressure drop characteristics are evaluated in the characteristics research part. The numerical model and experiment setup remain identical throughout this investigation. The details of the mechanism research are presented in Figure 3.3. Mechanism analysis is conducted using secondary flow intensity theory and compares the variations of vortex structures. Finally, reasonable descriptions of the affecting mechanisms are obtained to complete the mechanism research progress. After completing the characteristics and mechanism

research, the optimization research is conducted as illustrated in Figure 3.4. The optimization step involves optimizing the flow structure and novel winglet design in circular and annular tubes, respectively. The optimization approach is based on findings from the mechanism research part. Ultimately, this will complete the entire research process.

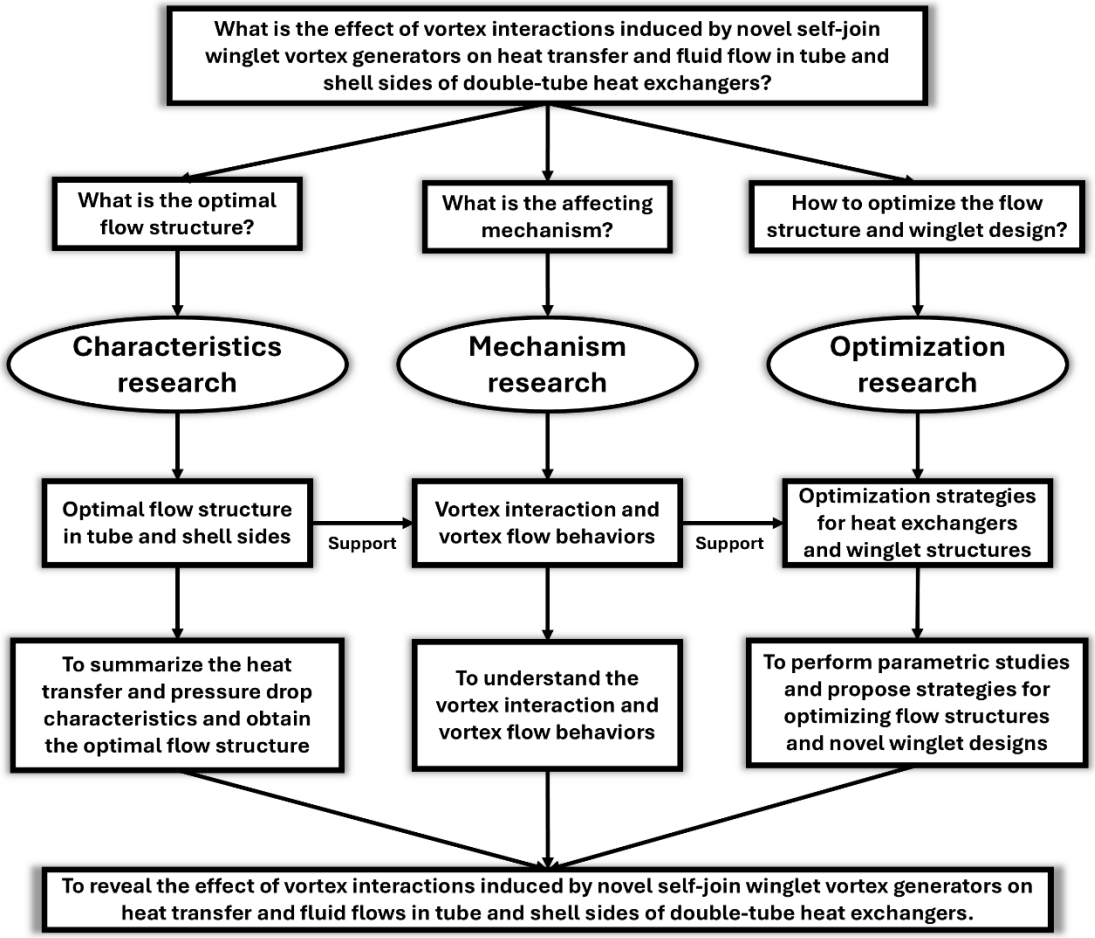

Figure 3.1 Flow chart of whole research progress.

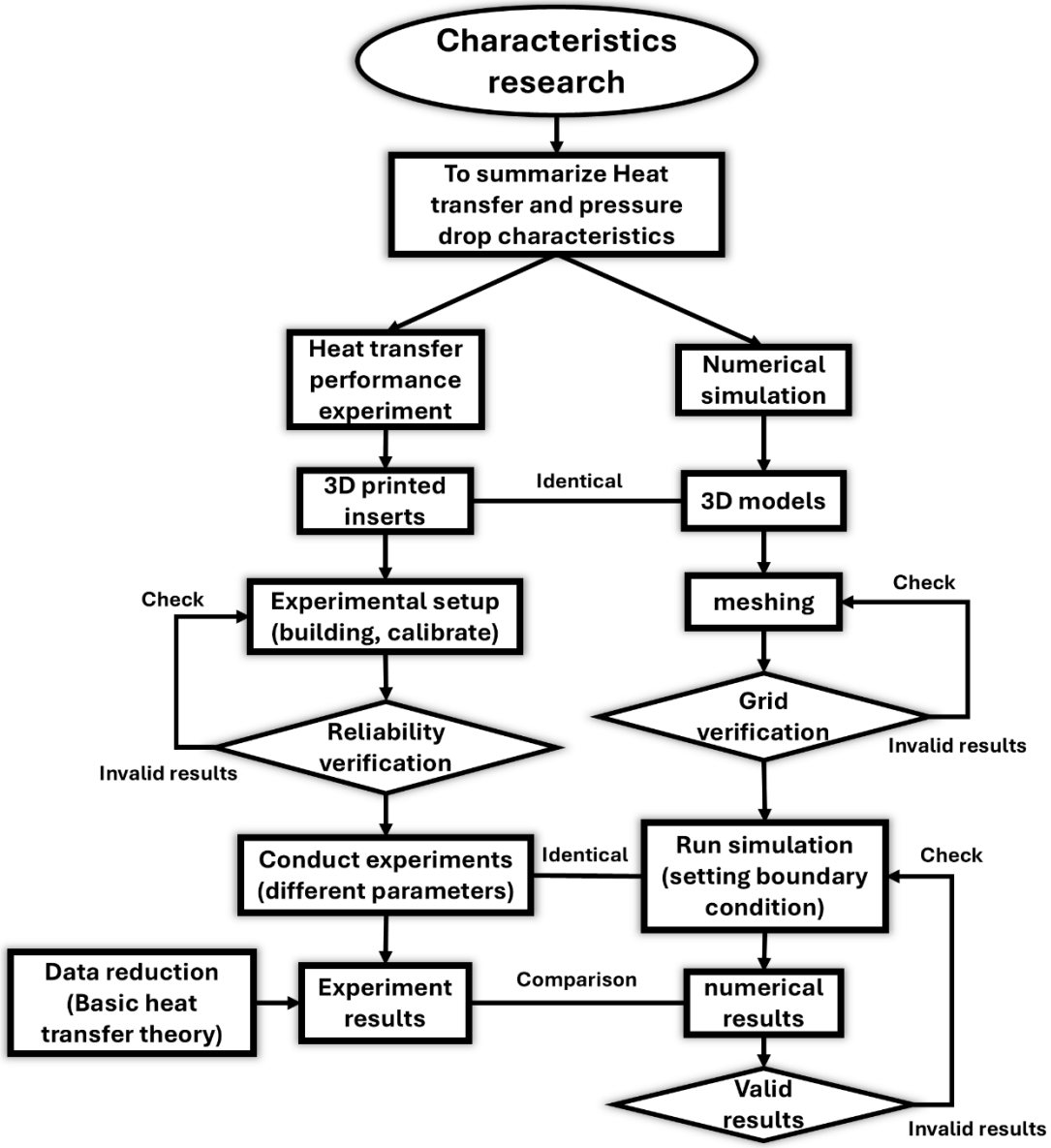

Figure 3.2 The details of characteristics research.

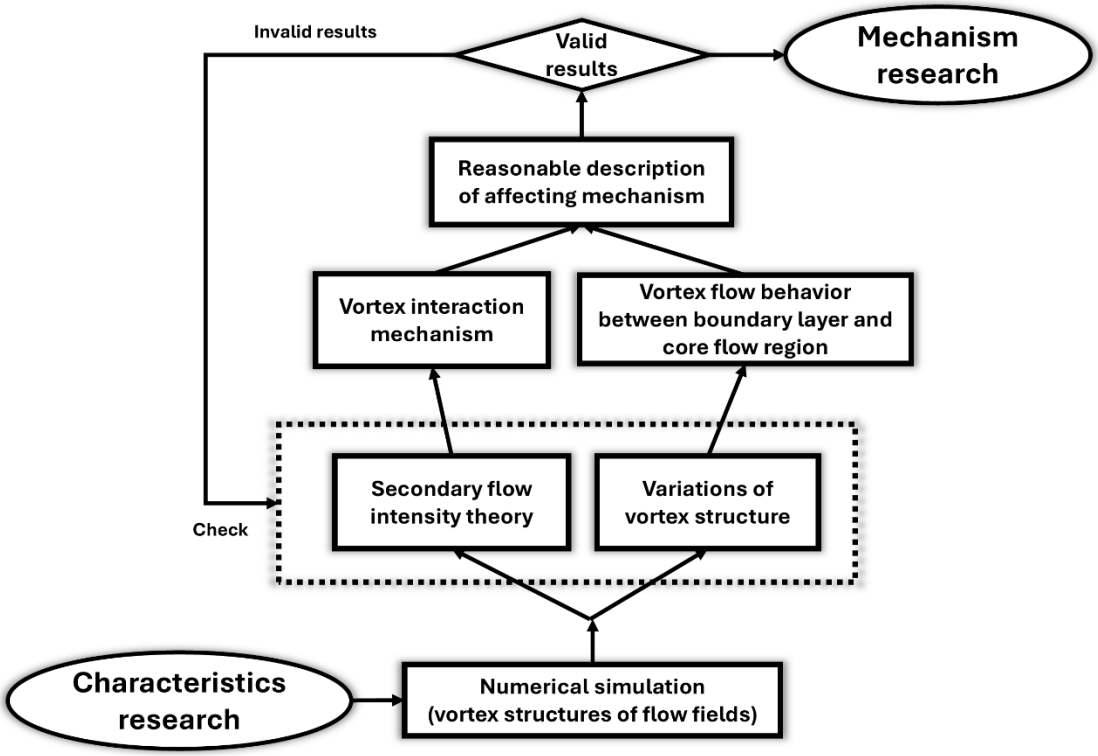

Figure 3.3 The details of mechanism research.

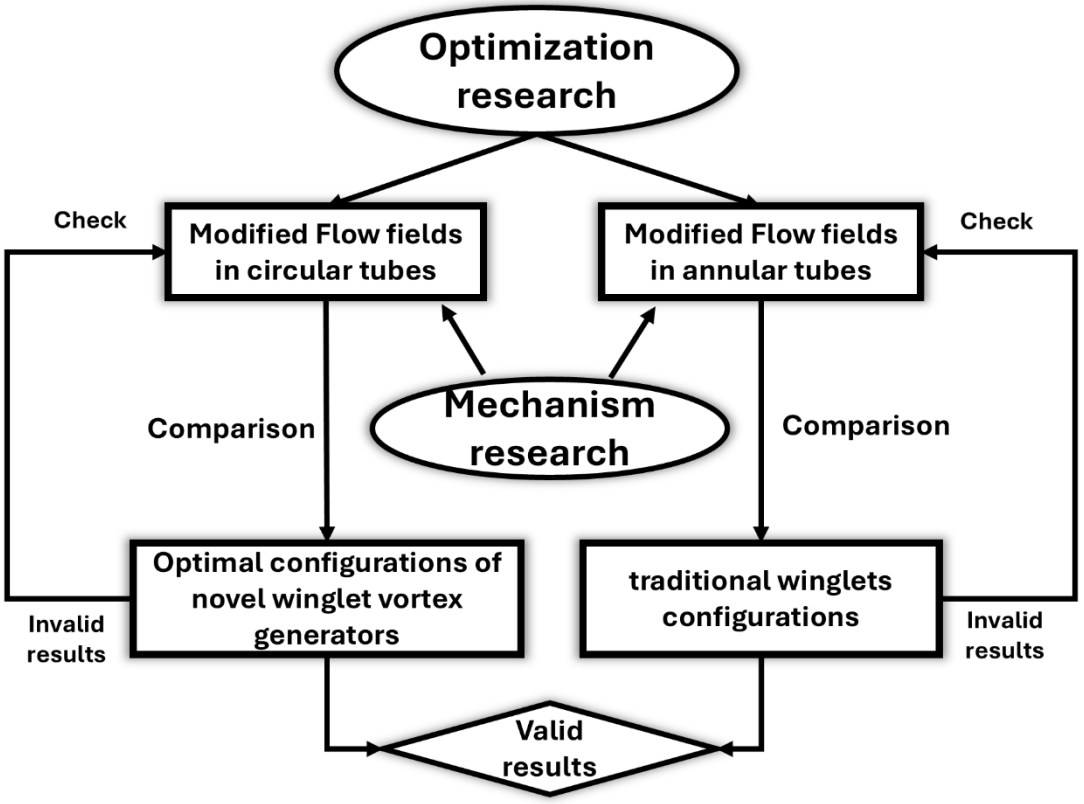

Figure 3.4 The details of optimization research.

3.3 Fundamental theory

3.3.1 Basic heat transfer theory

3.3.1.1 Newton's law of cooling

The earliest basic theory for convective heat transfer was proposed by Newton in 1701. Then, a classic formula, known as Newton's cooling formula, is proposed. This formula defines the heat transfer coefficient, a fundamental physical quantity. Later, the basic concept of strengthening heat transfer is established based on three aspects: increasing the temperature difference between hot and cold fluids, increasing the overall heat transfer coefficient, and increasing the heat transfer surface area.

The heat from hot fluid is transferred through conduction and convection to cold fluid in double-tube heat exchangers. The overall heat transfer rate (Q_{ov}) is calculated by the following equation:

$$Q_{ov} = h_{ov} A \Delta T_m \tag{3.1}$$

where h_{ov} is overall heat transfer coefficient, A is heat transfer surface area, and ΔT_m is logarithmic mean temperature difference between hot and cold fluids.

(a) Increasing ΔT_m

The temperatures of hot and cold fluids vary along the heat transfer surface in heat exchangers. The ΔT_m depends on the flow modes of both the cold and hot fluids. When the inlet and outlet temperatures of the heat exchanger are constant, the ΔT_m for counter flow is the largest, while that for parallel flow is the smallest.

(b) Increasing A

The common method of increasing A is to modify the heat transfer surface shape, such as using the special-shaped tubes and special-shaped walls. Ribbed tubes, grooved tubes, finned surface, and corrugated tubes can enhance the heat transfer performance.

(c) Increasing h_{ov}

The h_{ov} is affected by many factors, including wall thermal conductivity, physical

properties of the fluid (such as thermal conductivity, viscosity, density, and specific heat capacity), flow types (laminar and turbulent), and the shape and size of the heat transfer surface. To improve convective heat transfer capacity, the temperature gradient near the wall should be increased. Inhibiting or disrupting the development of the thermal boundary layer enhances heat transfer in tubes.

3.3.1.2 Thermal enhancement factor

Webb [151] proposed a method to evaluate the performance enhancement of enhanced tubes compared with plain tubes. The benefit is defined as the ratio of heat transfer between enhanced tubes and plain tubes, while the cost is defined as the ratio of flow resistance. The *TEF* equation proposed by Webb is widely adopted by researchers. Under identical pumping power conditions, the *TEF* is calculated using the following equation,

$$TEF = \frac{Nu/Nu_0}{(f/f_0)^{1/3}} \tag{3.2}$$

where *Nu* is Nusselt number, *f* is friction factor, and the subscript "0" presents plain tube.

3.3.1.3 Wilson plots

Following Wilson's [152] work, the Wilson plot method has been widely employed to establish relationships between temperature differences and heat flux on both tube and shell sides of heat exchangers. This approach eliminates the need for difficult and costly measurements of wall temperatures in heat exchangers.

It is assumed that the fluid temperatures are uniform, the surface areas on both sides are equal, and the wall thermal resistance is known and remains constant. The Wilson plot method is described as follows,

The overall temperature difference between fluid 1 and fluid 2, ΔT_{ov}, is given by

$$\Delta T_{ov} = \Delta T_1 + \Delta T_w + \Delta T_2 \quad (3.3)$$

where ΔT_1 and ΔT_2 are the fluid-to-wall temperature differences on each side and ΔT_w is the temperature difference across the wall.

The definitions of heat transfer coefficient (h) and wall thermal resistance (R_w) are given by

$$h_1 = \frac{q}{\Delta T_1} \quad (3.4)$$

$$h_2 = \frac{q}{\Delta T_2} \quad (3.5)$$

$$h_{ov} = \frac{q}{\Delta T_{ov}} \quad (3.6)$$

$$R_w = \frac{\Delta T_w}{q} \quad (3.7)$$

where q is the heat flux.

Equation (3.3) can be written,

$$\frac{1}{h_{ov}} = \frac{1}{h_1} + R_w + \frac{1}{h_2} \quad (3.8)$$

The above equation is typically interpreted as summing thermal resistances to determine the overall thermal resistance. In reality, the formulation involves defining both resistance and corresponding temperature differences.

It is assumed that the velocity of fluid 2 varies while the flow parameters on side 1 remain constant. For side 2, it is known that Nu is proportional to $Re^n Pr^m$. Then,

$$h_2 = C u_2^n \quad (3.9)$$

where C is the slope coefficient, u is fluid velocity, and n is velocity exponent.

Equation (3.8) can be written,

$$\frac{1}{h_{ov}} = (\frac{1}{h_1} + R_w) + \frac{u_2^{-n}}{C} \quad (3.10)$$

3.3.2 Secondary flow intensity and vorticity field theory

3.3.2.1 Vorticity and vorticity flux

The motion of fluid elements can be divided into translational, deformation, and rotational motion. Fluid motion constitutes vortex flow when the rotational angular velocity vector is nonzero. Vorticity originates from the velocity gradient in the flow

field, which is directly affected by the inherent shear stress of viscous fluid. Therefore, the vorticity field represents an inherent characteristic of viscous fluids [153]. Vorticity serves as the most fundamental physical quantity describing various vortex phenomena. Furthermore, all vortexes represent collections of vorticities. The vorticity field constitutes the vector field corresponding to the velocity field. Vortex field, or vorticity field or angular velocity field, also exist in swirling flow field. The vorticity field is defined as the curl of the fluid velocity $\boldsymbol{V}$ (u, v, w).

$$\omega = \nabla \times \boldsymbol{V} = \omega_x \boldsymbol{i} + \omega_y \boldsymbol{j} + \omega_z \boldsymbol{k} = \begin{vmatrix} \boldsymbol{i} & \boldsymbol{j} & \boldsymbol{k} \\ \frac{\partial}{\partial x} & \frac{\partial}{\partial y} & \frac{\partial}{\partial z} \\ u & v & w \end{vmatrix} \tag{3.11}$$

$$\omega_x = \frac{\partial w}{\partial y} - \frac{\partial v}{\partial z} \tag{3.12}$$

$$\omega_y = \frac{\partial u}{\partial z} - \frac{\partial w}{\partial x} \tag{3.13}$$

$$\omega_z = \frac{\partial v}{\partial x} - \frac{\partial u}{\partial y} \tag{3.14}$$

Vorticity follows the vorticity continuity equation,

$$\nabla \cdot \boldsymbol{\omega} = \frac{\partial \omega_x}{\partial x} + \frac{\partial \omega_y}{\partial y} + \frac{\partial \omega_z}{\partial z} = 0 \tag{3.15}$$

The sum of vorticity over any open surface **A** in the flow field is called the vorticity flux through surface $\boldsymbol{A}$ [153],

$$\boldsymbol{J} = \int_A \boldsymbol{\omega} \cdot d\boldsymbol{A} \tag{3.16}$$

The definition of vorticity is as follows,

$$\boldsymbol{J} = \int_A \boldsymbol{\omega} \cdot d\boldsymbol{A} = \int_A \nabla \times \boldsymbol{V} \cdot d\boldsymbol{A} \tag{3.17}$$

According to Stokes' theorem:

$$\oint_L \boldsymbol{V} \cdot d\boldsymbol{l} = \int_A \nabla \times \boldsymbol{V} \cdot d\boldsymbol{A} \tag{3.18}$$

The line integral of the velocity V of the closed curve L at a certain time in flow field is the velocity circulation $\boldsymbol{\Gamma}$ along the closed curve,

$$\boldsymbol{\Gamma} = \oint_L \boldsymbol{V} \cdot d\boldsymbol{l} \tag{3.19}$$

Thus, the vorticity flux **J** through any open surface **A** is equal to the velocity circulation $\boldsymbol{\Gamma}$ along the closed curve $\boldsymbol{L}$ surrounding the surface $\boldsymbol{A}$,

$$\boldsymbol{J} = \int_A \boldsymbol{\omega} \cdot d\boldsymbol{A} = \oint_L \boldsymbol{V} \cdot d\boldsymbol{l} = \boldsymbol{\Gamma} \tag{3.20}$$

The velocity circulation $\boldsymbol{\Gamma}$ is related not only to the velocity direction in the flow field, but also to the direction of the circulation around **L** during integration. Based on right-hand rule, the counterclockwise circle direction is the positive direction. Therefore, the vorticity flux through the open surface is positive or negative in the cases of multiple vortexes with different rotation directions on the same surface.

Vorticity flux through a closed surface,

$$\boldsymbol{J} = \oint_A \boldsymbol{\omega} \cdot d\boldsymbol{A} \tag{3.21}$$

According to the Gaussian divergence theorem,

$$\oint_A \boldsymbol{\omega} \cdot d\boldsymbol{A} = \int_V \nabla \cdot \boldsymbol{\omega} d\boldsymbol{V} = 0 \tag{3.22}$$

According to equation (3.15), the divergence of vorticity **ω** is zero. Therefore, the vorticity flux through the closed surface is zero. The vorticity flux field is the passive field.

3.3.2.2 Secondary flow intensity

When boundary fluid flows are affected by transverse pressure, they move in a direction parallel to the boundary layer. Due to their lower velocity, the fluid near the boundary layer moves more than that farther away. Then, fluid flows become superimposed on the mainstreams. This flow pattern is called a secondary flow. In other words, a secondary flow is the accompanying flow of the mainstream. Secondary flow is ubiquitous in nature. Secondary flows exist in rotating machines, convex and concave surfaces, curved rivers, curved tubes, boundary layers on solid surfaces, the atmosphere, oceanic motions, etc.

The studies of longitudinal vortex motion aim to understand the generation, development, decay, and interaction of longitudinal vortices. Based on these studies, longitudinal vortex motion is effectively controlled [154]. Since a longitudinal vortex is a typical secondary flow, secondary flow intensity can be used to describe

longitudinal vortices. The quantitative parameters of secondary flow intensity (*Se*) are vorticity flux (***J***), mean absolute vorticity flux ($\boldsymbol{J}_{ABS}^{n}$) [155-157], *Se* in tubes with twisted tapes (*Sw* number) [158], *Se* in curved tubes (*De* number) [159], and *Se* number [160]. Due to the limitation of the *Sw* and *De* numbers, the two parameters are only suitable for describing secondary flow intensity of twisted tapes and helical circular tubes, respectively. When vorticity components with different directions exist on a curved surface, they cancel each other out. Therefore, the vorticity flux cannot reflect the true vorticity intensity passing through the surface. However, the rotational angular velocity of longitudinal vortices is obtained through the vorticity field. When vorticity direction is not considered, equation (3.16) is modified to calculate the absolute vorticity through the open surface,

$$\mathbf{J}_{\mathrm{ABS}}^{\mathrm{n}}{}' = \int_A |\omega^n| \cdot d\boldsymbol{A} \tag{3.23}$$

where $\boldsymbol{J}_{ABS}^{n}{}'$ is the sum of absolute vorticity flux through the curved surface. However, $\boldsymbol{J}_{ABS}^{n}{}'$ can only reflect the vorticity present on this surface but cannot reflect the intensity of vorticity on this surface. Since a longitudinal vortex is closely related to vorticity component in the mainstream direction, the secondary flow intensity must be related to the vorticity intensity.

Vorticity intensity is described by the mean absolute vorticity per unit curved surface. Therefore, the vorticity flux on the cross section does not cancel itself out because of flow direction,

$$\mathbf{J}_{\mathrm{ABS}}^{\mathrm{n}} = \frac{1}{A}\int_A |\omega^n| \cdot d\boldsymbol{A} \tag{3.24}$$

where $\boldsymbol{J}_{ABS}^{n}$ is the mean absolute vorticity flux in the mainstream direction, which reflects the mean angular velocity of longitudinal vortices around the *x* axis. The results [155-157] show that $\boldsymbol{J}_{ABS}^{n}$ is correlated with secondary flows.

3.3.2.3 Secondary flow intensity and its physical significance

Since the vorticity component along the mainstream direction represents the angular velocity of the fluid rotating around the axis parallel to the mainstream direction, $\boldsymbol{J}_{ABS}^{n}$

represents the mean angular velocity of the fluid rotating around the axis parallel to the mainstream direction. The $\boldsymbol{J}_{ABS}^{n}$ is multiplied by the characteristics diameter (d_c) and divided by the dynamic viscosity (μ) to obtain the dimensionless *Se* [160],

$$Se = \frac{\rho d_c U_s}{\mu} \tag{3.25}$$

$$U_s = d_c \mathbf{J}_{\mathrm{ABS}}^{\mathrm{n}} \tag{3.26}$$

where ρ is the fluid density and U_s is the velocity of the fluid around the x-axis (secondary flow velocity). *Se* and the Reynolds number (*Re*) have similar equations, which represent the ratio of inertial force to viscous force. However, the physical meaning of the two parameters is different. *Re* reflects the fluid flows of the mainstream, and *Se* reflects the fluid flow of secondary flow.

Song et al. [160-162] studied the application of typical longitudinal vortex flows in channels of flat/circular heat exchangers fitted with vortex generators, such as twisted-elliptic tubes, twisted-square tubes, and twisted-tapes-inserted tubes. The results show that *Se* overcomes the limitations of *Sw* and *De* number applications. Because $\boldsymbol{J}_{ABS}^{n}$ is a dimensional parameter, its rules do not have the disadvantage of portability. The universal applicability of *Se* for describing secondary flow intensity is confirmed.

3.4 Numerical simulation

3.4.1 Basic assumption

The fluid flow in vortex tubes is a complex three-dimensional rotating flow. The heat transfer between the fluid and the tube wall is unstable. Therefore, the following assumptions are proposed for vortex flows in tubes to simplify the physical phenomena,

(a) Fluid flows in tubes are incompressible and steady.
(b) The wall is non-slip and impermeable.
(c) The thermal radiation effect is not considered.
(d) Except for the heat transfer surface, all other surfaces are adiabatic.
(e) The fluid flow in tubes is fully developed turbulent flow.

3.4.2 Governing equation

Based on the theoretical guide of ANSYS Fluent 2022R1 [163], the governing equations for continuity, momentum, energy, turbulent kinetic energy (k), and turbulent dissipation rate (ε) are as follows:

Continuity equation:

$$\frac{\partial \overline{u_i}}{\partial x_i} = 0 \tag{3.27}$$

Momentum equation:

$$\frac{\partial}{\partial x_j}\left(\rho \overline{u_i}\overline{u_j}\right) = \rho \overline{F_i} - \frac{\partial \bar{p}}{\partial x_i} + \frac{\partial}{\partial x_j}\left(\mu \frac{\partial \overline{u_i}}{\partial x_j} - \rho \overline{u_i' u_j'}\right) \tag{3.28}$$

Energy equation:

$$\begin{aligned} &\overline{u_j}\frac{\partial}{\partial x_j}\left[\frac{\rho}{2}\left(\overline{u_\iota}\overline{u_\iota} + \overline{u_\iota' u_\iota'}\right)\right] + \overline{u_j}\frac{\partial}{\partial x_j}\left(\bar{p} - \rho \overline{F_\iota}\right) + \frac{\partial}{\partial x_j}\overline{u_j'\left(p' + \frac{\rho}{2}\overline{u_\iota' u_\iota'}\right)} \\ &\quad = \mu \frac{\partial}{\partial x_j}\left[\overline{u_\iota}\left(\frac{\partial \overline{u_\iota}}{\partial x_j} + \frac{\partial \overline{u_j}}{\partial x_\iota}\right)\right] + \frac{\partial}{\partial x_j}\left[\overline{u_\iota}\left(-\rho \overline{u_\iota' u_j'}\right)\right] + \mu \frac{\partial}{\partial x_j}\overline{u_\iota'\left(\frac{\partial u_\iota'}{\partial x_j} + \frac{\partial u_j'}{\partial x_\iota}\right)} \\ &\quad - \mu\left(\frac{\partial \overline{u_\iota}}{\partial x_j} + \frac{\partial \overline{u_j}}{\partial x_\iota}\right)\frac{\partial \overline{u_\iota}}{\partial x_j} - \mu \overline{\frac{\partial u_\iota'}{\partial x_j}\left(\frac{\partial u_\iota'}{\partial x_j} + \frac{\partial u_j'}{\partial x_\iota}\right)} \end{aligned} \tag{3.29}$$

where, $\overline{u_\iota}$ is Reynolds average velocity component, p is pressure, u_i' is fluctuation velocity, $\overline{F_\iota}$ is mass force.

The k and ε equations in RNG k-ε model are as follows,

k equation:

$$\frac{\partial}{\partial x_i}(\rho k u_i) = \frac{\partial}{\partial x_j}\left(\alpha_k \mu_{eff}\frac{\partial k}{\partial x_j}\right) + \mu_t\left(\frac{\partial u_i}{\partial x_j} + \frac{\partial u_j}{\partial x_i}\right)\frac{\partial u_i}{\partial x_j} - \beta g_i \frac{\mu_t}{Pr_t}\frac{\partial T}{\partial x_i} - \rho\varepsilon \tag{3.30}$$

where $\mu_{eff} = \mu + \mu_t$ and $\mu_t = \rho C_\mu \frac{k^2}{\varepsilon}$

ε equation:

$$\frac{\partial}{\partial x_i}(\rho \varepsilon u_i) = \frac{\partial}{\partial x_j}\left(\alpha_\varepsilon \mu_{eff}\frac{\partial \varepsilon}{\partial x_j}\right) + C_{1\varepsilon}\frac{\varepsilon}{k}\left[\mu_t\left(\frac{\partial u_i}{\partial x_j} + \frac{\partial u_j}{\partial x_i}\right)\frac{\partial u_i}{\partial x_j} - C_{3\varepsilon}\beta g_i \frac{\mu_t}{Pr_t}\frac{\partial T}{\partial x_i}\right] - C_{2\varepsilon}^* \rho \frac{\varepsilon^2}{k}$$

(3.31)

where $C_{2\varepsilon}^{*} = C_{2\varepsilon}\frac{C_{\mu}\eta^{3}(1-\eta/\eta_{0})}{1+\beta\eta^{3}}$, $\eta = \left(2S_{ij}S_{ij}\right)^{0.5}\frac{k}{\varepsilon}$, and $S_{ij} = \frac{1}{2}\left(\frac{\partial u_i}{\partial x_j} + \frac{\partial u_j}{\partial x_i}\right)$

In the above two equations, ρ is density, u_i is velocity component, α_k and α_ε are the reciprocals of effective turbulent Prandtl number for turbulent kinetic energy and dissipation rate, respectively. μ_t is turbulent viscosity, β is thermal expansion coefficient, g_i is acceleration, Pr_t is Prandtl Number, T is temperature, $C_{1\varepsilon}$, $C_{2\varepsilon}$ and $C_{3\varepsilon}$ are model constants, and S_{ij} is average strain rate. According to the help file of ANSYS Fluent 2022R1, it is determined that $\alpha_k = \alpha_\varepsilon \approx 1.393$, $C_\mu = 0.0845$, $Pr_t = 0.7179$, $C_{1\varepsilon} = 1.42$, $C_{2\varepsilon} = 1.68$, $C_{3\varepsilon} = 1.3$, $\beta = 0.012$, and $\eta_0 = 4.3$.

3.4.3 Numerical calculation method

Among numerical calculation methods, Reynolds time-averaged method and the scale analysis method are widely used. The Reynolds time-averaged method has a time-homogenizing effect on transient pulsations. Transient Navier-Stoke equations are not directly calculated. It aims to superpose the turbulent time-averaged flow and the transient pulsation time-average flow. The scale analysis method has higher requirements for meshing, especially for high grid density near the wall. The scale analysis method is usually more suitable for analyzing transient and strongly separated flows. Therefore, the Reynolds time-average method is suitable for this study based on computational cost.

3.4.4 Near-wall treatment

In the vertical direction of the near-wall boundary, the fluid flow velocity gradually approaches the mainstream velocity. The boundary layer inevitably affects fluid flow and heat transfer. In most actual engineering applications, near-wall treatment is widely used for capturing fluid flows in boundary layers. To reduce calculation time, near-wall grids should be as large as possible. However, to closely reproduce actual physical phenomena, dense near-wall grids are required. Hence, combining near-wall treatment with solving turbulent equations can balance solution accuracy and computational cost.

Among near-wall treatment methods, the scalable wall function and the enhanced wall treatment are widely used. For the scalable wall function, the nodes of the first layer grid are positioned in a fully developed turbulence region. The boundary between the viscous sublayer and the wall is uniform. This avoids the discontinuity of near-wall grid size caused by an increase in grid density. The enhanced wall treatment is a combination of the two-layer solution of the low Reynolds number model and the enhanced wall function. If the near-wall grids are sufficiently dense and y^+ equals 1, the enhanced wall treatment uses the two-layer model to solve the ε equation; when the first layer of grids is placed in the turbulent regions, the enhanced wall function is used to connect the wall physical quantities with those in the turbulent regions.

Therefore, to better capture the fluid flow within the boundary layer, the enhanced wall treatment method is adopted in this thesis.

3.4.5 Boundary conditions

ANSYS Fluent 2022R1 is used to perform 3D steady-state simulations of flow behavior and heat transfer within tubes with various winglets. Since the focus of this work is the heat transfer and fluid flow within tube and shell sides, the settings of the isothermal surface and the inlet boundary condition are as follows,

(a) Simulations of tube sides:

The shell side is treated as an isothermal surface of 300 K, while the inlet boundary condition is set as velocity-inlet at 323 K.

(b) Simulations of shell sides:

The tube side is treated as an isothermal surface of 323 K, while the inlet boundary condition is set as velocity-inlet at 300 K.

The outlet boundary condition is set as pressure-outlet. Gradients are calculated using the Green-Gauss Node-Based discretization approach. The turbulent kinetic energy,

turbulent dissipation rate, and energy are discretized using the second-order upwind scheme, while the momentum and pressure are discretized through QUICK and PRESTO! schemes, respectively. The remaining walls are treated as adiabatic, and all surfaces are subject to a no-slip condition. The residual criterion of the energy equation is set to 10^{-9}, while those of other equations are set to 10^{-6}. The pressure-velocity coupling is achieved using Coupled algorithm. The RNG k-ε model utilized in this work is derived from the Navier-Stokes equations using the renormalization group method, according to [163]. Compared to the standard k-ε model, it provides improved performance in predicting vortex flows due to its consideration of the effects of vortices on turbulent flows. The flow fields in this work can be accurately captured by the RNG k-ε model, since the longitudinal vortex flows within tube and shell sides have swirling characteristics. The specification method of turbulent model is set as intensity and hydraulic diameter conditions. The hydraulic diameter is set to 21 mm. The turbulent intensity (I_t) is calculated as follows,

$$I_t = 0.16(Re)^{-1/8} \tag{3.32}$$

3.5 Experimental verification

3.5.1 Experimental setup

Based on research objectives of this work, two experimental setups are built: one for the tube side and the other for the shell side, to investigate the effect of novel self-join winglets on heat transfer and pressure drop characteristics in circular and annular tubes, respectively.

(a) Experimental setup of the tube side

The experiment system includes a hot-water system (tube side), a cold-water system (shell side), a double-pipe heat exchanger, and two data acquisition systems, as shown in Figure 3.5 (a). The heat exchanger consists of an inlet section (250 mm), an outlet section (250 mm), and a test section (1000 mm) [164]. The vortex generators are fixed on two stainless steel rods (0.8 mm diameter) along the tubes. The hot and cold water within the heat exchanger is sourced from a hot thermostat bath (LPS-50, customized

style by Changzhou LP-instrument Co., Ltd.) and a water tank (tap water), respectively. The hot-water pump (maximum volume flow rate of 17 L/min) is a built-in circulating pump of the hot thermostat bath. The maximum volume flow rate of the cold-water pump (ORS-16G, Henger Pump Industry Co., Ltd.) is 150 L/min. Volume flow rates are measured using plastic rotor flowmeters (LZS-20D, Yuyao Yuanda Flow Meter Co., Ltd.) and controlled by valves and bypass systems, consisting of a non-return valve and a ball valve. Hot and cold water exchange heat through a double-pipe heat exchanger. The materials of the tube and shell sides are copper and PVC, respectively. To prevent excessive heat loss, high-density polyethylene cotton is wrapped around the heat exchanger. Inlet and outlet temperatures of both the tube and shell sides are measured using PT100 sensors (JLGKWZP, Jiangsu Lingong Electric Co., Ltd.). Pressure drop on the tube side is measured using a differential pressure transmitter (MIK-2051, Hangzhou Meacon Automation Technology Co., Ltd.). The positions of the testing points are shown in Figure 3.5 (b). The Isolated 4-port USB to RS485 Converter (YN-861, Yuning Technology Co., Ltd.) and temperature data acquisition module (DAM-PT04, Beijing Juying Electronic Co., Ltd.) are used to transmit the pressure drop and temperature data to the computer, respectively. After passing through the outlet of the heat exchanger, the hot water is returned to the hot thermostat bath, while the cold water is drained away.

(b) Experimental setup of the shell side

The heat transfer and pressure drop characteristics of fluid flow within annular tubes are studied using a system similar to that used in circular tubes. As shown in Figure 3.6 (a), hot water flows through the inner copper tube, while cold water flows through the outer PVC tube. To study the specific effects of winglets on annular tubes, acrylic water tanks are added to the system to eliminate swirl effects at the inlet and outlet. The heat exchanger is wrapped in high-density polyethylene insulation to minimize heat loss. Furthermore, waterproof tape is applied to the inner tube inside the acrylic water tank. The flow rate is regulated using main and bypass valves. PT100 sensors and differential pressure transmitters are used to measure temperature and pressure drop, respectively.

The data is transferred to a computer via data acquisition elements. The positions of testing points are shown in Figure 3.6 (b). The heat exchanger includes a 250 mm inlet section, a 600 mm test section, a 250 mm outlet section, and two 250 mm tube sections placed within acrylic water tanks.

The real picture of the experiment system is shown in Figure 3.7. When the relative variation of the collected data is less than 1 %, it can be considered that the flow system is in a steady state. After the flow system reaches the steady-state condition, each run of data acquisition lasts for 30 min. Furthermore, the computer records data every 5 s.

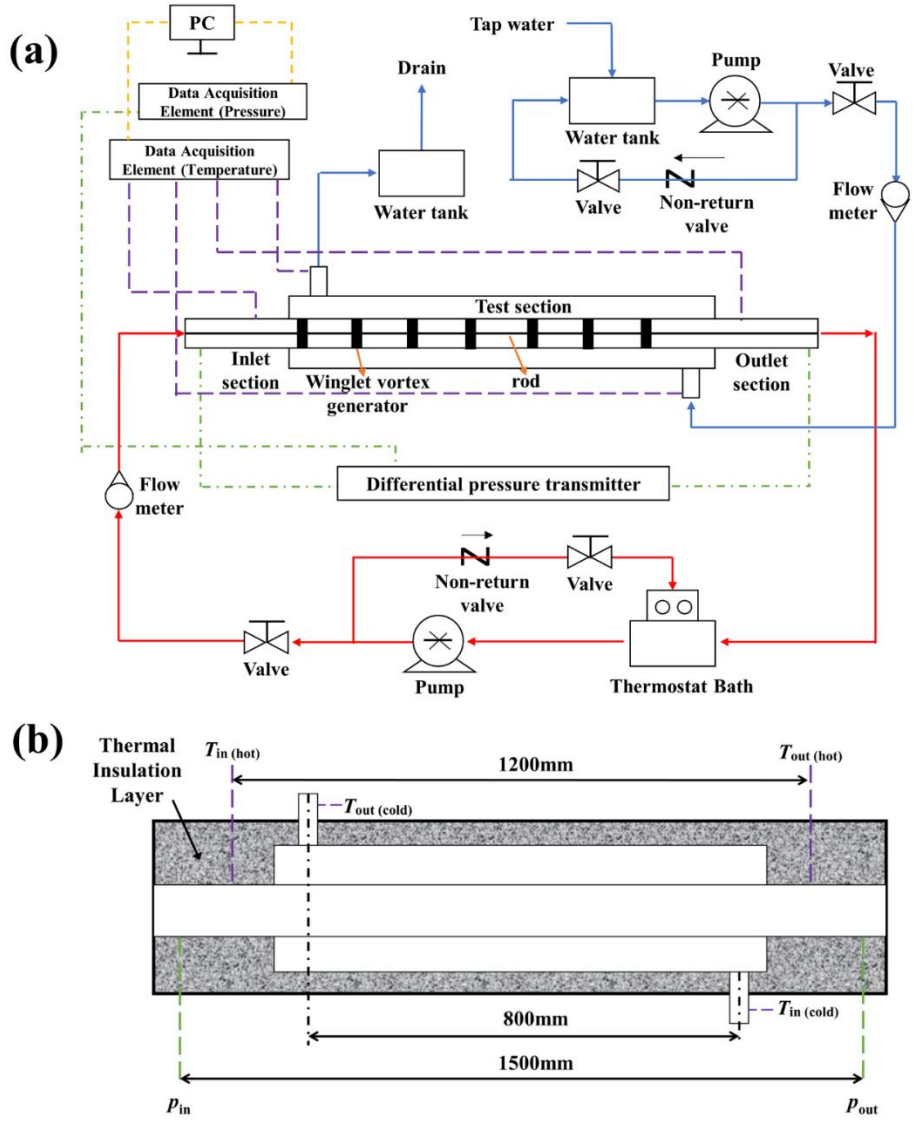

Figure 3.5 The experiment setup of the tube side: (a) schematic; (b) the position of testing points.

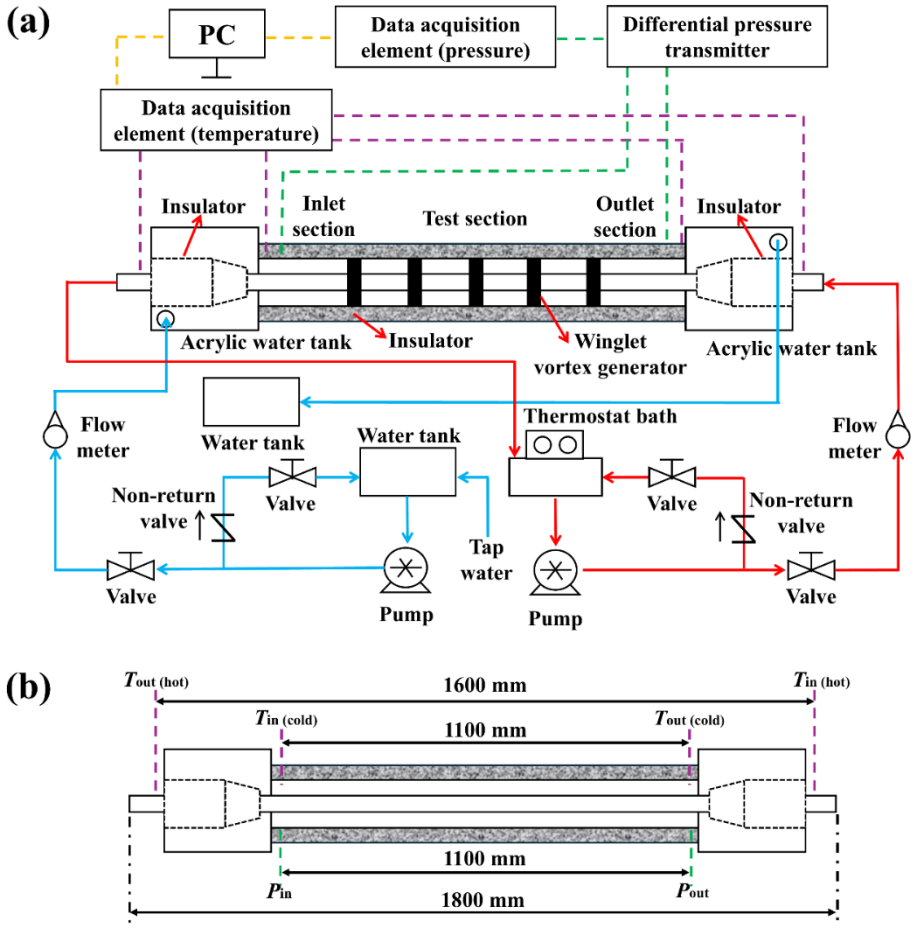

Figure 3.6 The experiment setup of the shell side: (a) schematic; (b) the position of testing points.

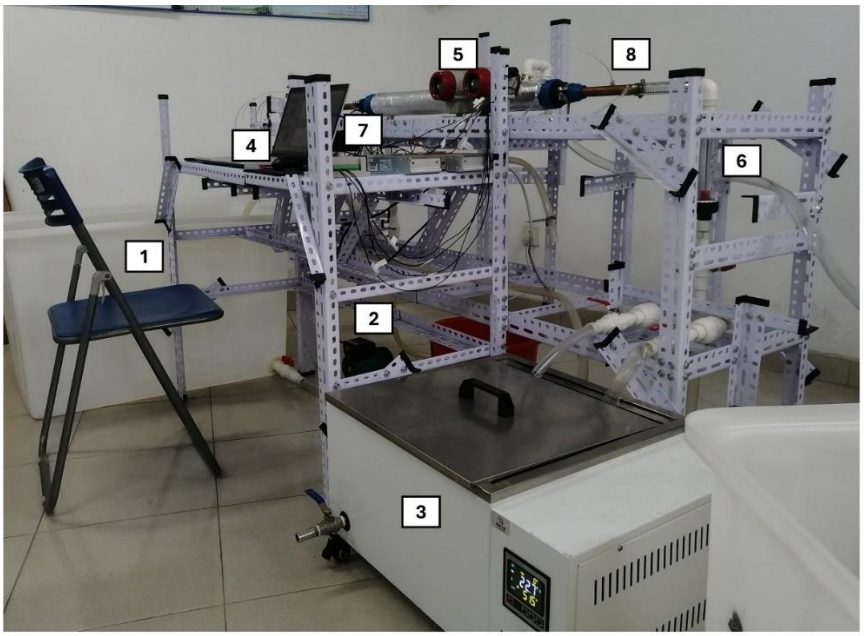

1. Water tank 2. Pump 3. Thermostat bath 4. PC 5. Differential Pressure Transmitter
6. Flow meter 7. Data acquisition element 8. PT100 sensors

Figure 3.7 The real picture of the experiment system.

3.5.2 Data reduction and uncertainty calculation

Water is used as the working fluid in experiments investigating heat transfer and pressure drop characteristics in this work. The flow rate of the experimental systems are as follows,

(a) Experiments on tube sides:

The hot water flow rates range from 250 L/h to 900 L/h, corresponding to *Re* range of 7577 to 27,276. To maintain the wall temperature of the tube side stable, the flow rate of cold water on the shell side is kept constant at 800 L/h.

(b) Experiments on shell sides:

A constant hot water flow rate of 800 L/h is controlled to maintain a stable temperature of the inner tube wall. The cold water flow rate ranges from 400 to 1300 L/h, corresponding to *Re* = 2304–7488.

Data processing and uncertainty calculation are carried out as follows,

$$Re = \frac{ud_c}{\nu} \tag{3.33}$$

where ν is the kinematic viscosity.

The friction factor (f) is calculated as,

$$f = \frac{2d_c \Delta p}{L\rho u^2} \tag{3.34}$$

where ΔP is the pressure drop between the inlet and outlet, L is pipe length.

It is assumed that the heat loss is negligible,

$$Q_{ov} = Q_f = c_p \dot{m} \Delta T_{io} \tag{3.35}$$

where Q_f is heat transfer rate of fluid, c_p is specific heat capacity, $\dot{m}$ is mass flow rate, and ΔT_{io} is temperature different between inlet and outlet.

Due to difficulties in measuring wall temperature, the Wilson plot method is used to

calculate the h of the heat transfer surface, as shown in section 3.3.1.3. Hence, the Nu can be calculated as follows,

$$Nu = \frac{hd_c}{\lambda} \tag{3.36}$$

where λ is thermal conductivity.

The heat from the hot thermostat bath, Q_e, is calculated as follows,

$$Q_e = UI \tag{3.37}$$

where U is the voltage, and I is the electric current.

The heat loss is calculated as follows,

$$Q_{loss} = Q_e - Q_f \tag{3.38}$$

The heat loss from the experimental system to the environment is about 4 %–8 %, which means that the heat loss in this system is acceptable.

The uncertainty values of measured parameters in this work are detailed in Table 3.1. The uncertainty assessment for Nu, f, and Re is conducted according to [114], and these parameters are calculated as follow,

$$\frac{\Delta Nu}{Nu} = [(\frac{\Delta h}{h})^2 + (\frac{\Delta d}{d})^2]^{0.5} \tag{3.39}$$

$$\frac{\Delta h}{h} = [\left(\frac{\Delta Q_f}{Q_f}\right)^2 + \left(\frac{\Delta d}{d}\right)^2 + \left(\frac{\Delta L}{L}\right)^2 + (\frac{\Delta(\Delta T_m)}{\Delta T_m})^2]^{0.5} \tag{3.40}$$

$$\frac{\Delta Q_f}{Q_f} = [(\frac{\Delta u}{u})^2 + (\frac{\Delta(\Delta T)}{\Delta T})^2]^{0.5} \tag{3.41}$$

$$\frac{\Delta f}{f} = [\left(\frac{\Delta u}{u}\right)^2 + \left(\frac{\Delta d}{d}\right)^2 + \left(\frac{\Delta L}{L}\right)^2 + (\frac{\Delta(\Delta P)}{\Delta P})^2]^{0.5} \tag{3.42}$$

$$\frac{\Delta Re}{Re} = [(\frac{\Delta u}{u})^2 + (\frac{\Delta d}{d})^2]^{0.5} \tag{3.43}$$

Based on equations (3.39)-(3.43), the calculated uncertainties for Nu, f, and Re are 4.06%, 4.03%, and 4.03%, respectively.

Table 3.1 The uncertainty values of measured parameters in this work.

Parameters	Absolute uncertainty	Relative uncertainty
Internal diameter of tubes (d)	± 0.1 mm	
Pipe length (L)	± 1 mm	
Temperature (T)		± 0.1%
Pressure drop (ΔP)		± 0.1%
Volume flow rate ($\dot{V}$)		± 4%

3.5.3 Reliability verification of experiment setup

To assess the reliability of the experiment setup, the heat transfer and fluid flow characteristics within plain tubes are compared with empirical correlations proposed by Gnielinski for *Nu*, and by Filonenko for *f*.

Gnielinski *Nu*-correlation [165],

$$Nu_0 = \frac{(f_0/8)(Re-1000)Pr}{1+12.7(f_0/8)^{1/2}(Pr^{2/3}-1)} \tag{3.44}$$

Filonenko *f*-correlation [166],

$$f_0 = (1.82lnRe - 1.64)^{-2} \tag{3.45}$$

Figure 3.8 (a) shows that the maximum deviations of the experiment system for *Nu* and *f* in the tube side are 12.5 % and 11.6 %, respectively, when compared with the Gnielinski and Filonenko correlations. All other deviation values for *Nu* and *f* are below 10 %. As shown in Figure 3.8 (b), the *Nu* and *f* values in the shell side exhibit maximum deviations of 13.6 % and 10.8 %, respectively, relative to the Gnielinski [34] and Filonenko [33] correlations. Deviations of *Nu* and *f* below 10 % account for 80 % and 90 %, respectively. The experimental measurements from both systems exhibit reasonable agreement with empirical correlations, demonstrating the reliability of these two experimental setups.

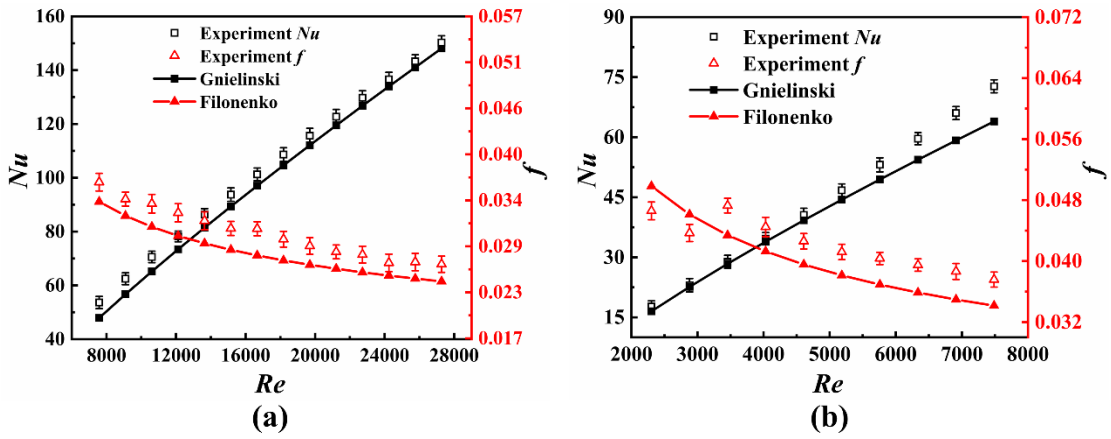

Figure 3.8 Verification of experimental reliability: (a) tube sides; (b) shell sides.

Chapter 4: Heat transfer and fluid flow analysis in circular tubes with novel self-join winglets

4.1 Introduction

This chapter aims to provide novel insights into optimizing vortex interaction in circular tubes equipped with novel self-join winglets. Furthermore, establishing a similarity correlation between structural parameters and flow field characteristics is crucial for guiding the design of winglet structures and optimizing the flow fields. Consequently, the heat transfer and fluid flow in circular tubes equipped with novel self-join winglets are numerically and experimentally investigated in this chapter. Specifically, the research content in this chapter is divided into three parts: (i) investigating the influence of novel self-join winglet configurations on heat transfer and fluid flow characteristics with *Re* ranging from 7577 to 27,276, (ii) studying the fluid mechanisms in flow fields affected by various winglet configurations, and (iii) obtaining similarity correlations between structural parameters and flow characteristics in various flow fields.

4.2 Physical model

The physical models in this chapter are designed based on the self-join winglet vortex generators [20]. Considering the superior performance of the delta winglet structure, novel self-join winglet vortex generators are proposed (Figure 4.1). The physical model specifications are given in Table 4.1. The positive projection plane of the vortex generator features a noncircular design, attributed to the addition of the lift angle β. 3D printing is employed to manufacture the physical model using polylactic acid material due to its favorable thermal properties and mechanical strength. In this chapter, the structural variables include the blockage ratio ($BR = H/d_c$ = 0.10, 0.15, and 0.20), winglet pairs number (PN= 4, 5, 6), and the included angle (α_v = 60 °, 90 °, and 120 °).

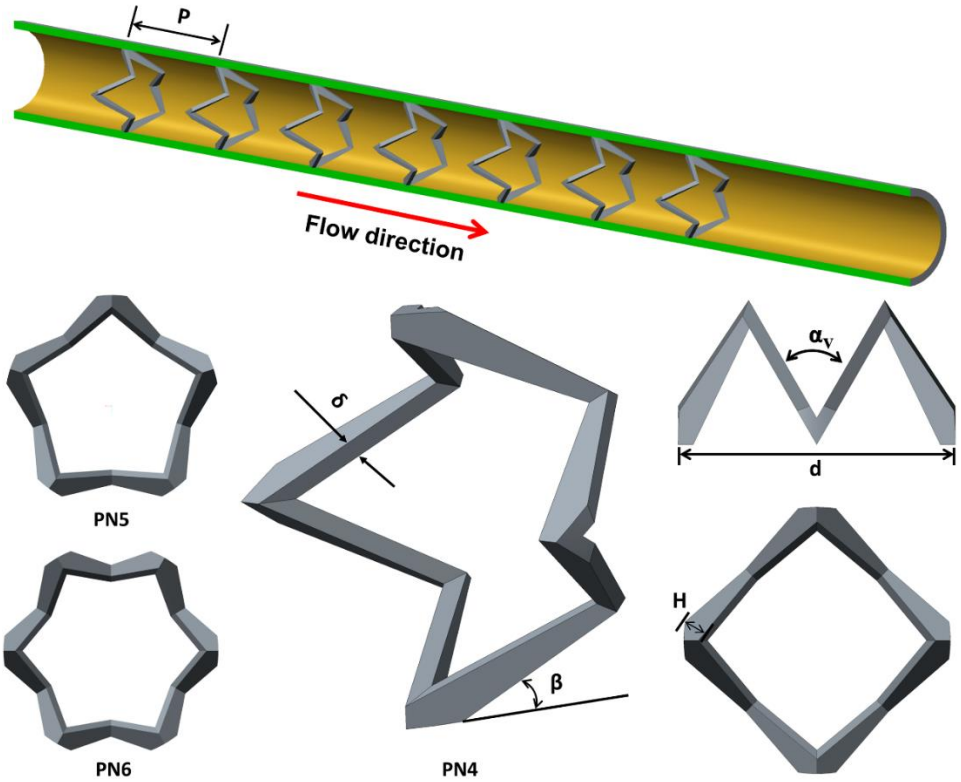

Figure 4.1 Details of winglet structure and arrangement in different views.

Table 4.1 Specification of the physical model.

Specification	Dimension
Included angle (α_v)	60 °, 90 °, 120 °
Internal diameter of tubes (d)	21 mm
Outside diameter of tubes (D)	25 mm
Characteristics diameter (d_c)	21 mm
Winglet height (H)	2.1 mm, 3.2 mm, 4.2 mm
Winglet thickness (δ)	1 mm
Lift angle (β)	30 °
Pitch (P)	143 mm
Number of winglet vortex generators	7
Case A1	$PN = 4$, $BR = 0.10$, $\alpha_v = 60$ °
Case A2	$PN = 4$, $BR = 0.10$, $\alpha_v = 90$ °
Case A3	$PN = 4$, $BR = 0.10$, $\alpha_v = 120$ °
Case A4	$PN = 4$, $BR = 0.15$, $\alpha_v = 60$ °

Case A5	$PN = 4$, $BR = 0.20$, $\alpha_v = 60$ °
Case A6	$PN = 5$, $BR = 0.10$, $\alpha_v = 60$ °
Case A7	$PN = 6$, $BR = 0.10$, $\alpha_v = 60$ °

4.3 Numerical model verification

4.3.1 Grid independence test

The numerical model is generated using the method of extracting fluid domain. The meshing software is ANSYS ICEM 2022R1. To improve grid quality and reduce computation time, both tetrahedron and hexahedron grids are employed to discretize the entire computational domain (Figure 4.2). The contact nodes on both interfaces between the tetrahedron and hexahedron zones are kept as closely aligned as possible. Furthermore, the domains consisting of hexahedron grids are discretized into O-block structures. A grid independence test is conducted with five different cell numbers: 319642, 897740, 1464720, 2050594, and 2687763 (Figure 4.3). The variations in overall *Nu* and *f* are less than 0.17% and 0.87%, respectively, when the number of cells exceeds 1464720. Therefore, numerical models with 1464720 cells are chosen for fluid domain calculations in tube sides.

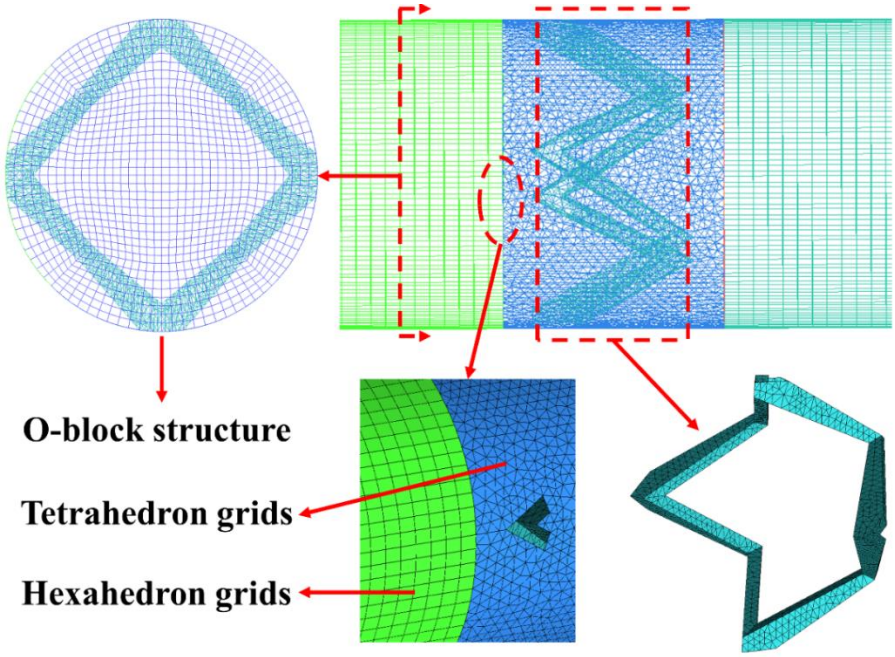

Figure 4.2 The grids of circular tubes with novel self-join winglet vortex generators.

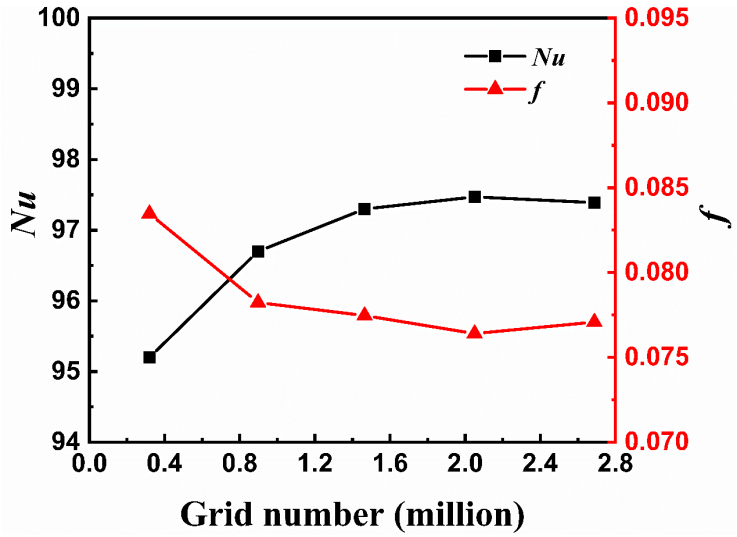

Figure 4.3 Grid independence test for overall *Nu* and *f*.

4.3.2 Verification of turbulent model

Figure 4.4 displays the profiles of overall *Nu* and *f* predicted by five turbulent models compared with the experiment data from case A1. The maximum deviations of overall *Nu* (*f*) are 16.5% (39.4%), 3.9% (2.9%), 7.9% (4.3%), 5.8% (3.5%), and 12.9% (12.9%) for the Standard k-ε, RNG k-ε, Realizable k-ε, Reynolds stress, and SST k-ω models, respectively. Therefore, the numerical data from the RNG k-ε model is in good agreement with the experiment data. RNG k-ε model is used for numerical simulations in tube sides.

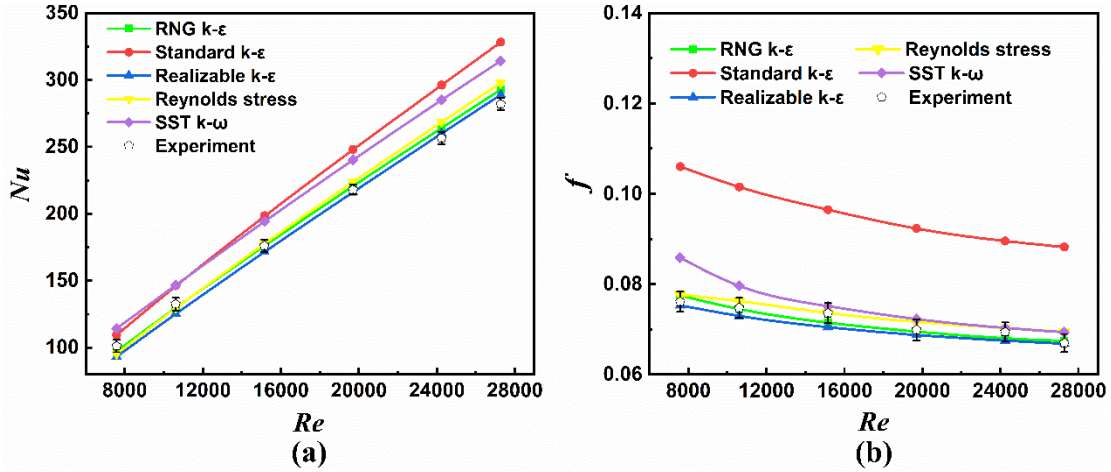

Figure 4.4 The profiles of overall *Nu* and *f* predicted by numerical models compared with the experiment data from case A1: (a) *Nu* versus *Re*; (b) *f* versus *Re*.

4.4 Fluid flow analysis

This section analyzes the variations of vortex structures, velocity magnitude and *TKE* contours, and the axial distribution of *Se* in various cases at *Re* = 7577, aiming to understand the effect of vortex interaction on fluid flows.

Figure 4.5 depicts the streamlines at different cross sections for case A1 at *Re*=7577. Figure 4.5 (k) displays various cross sections used in Chapters 4 and 5. Figure 4.5 (a) illustrates that the flow region within tubes is equally divided into four parts because the fluid passes through the front of the vortex generator. It is evident from Figure 4.5 (b) that the number of longitudinal vortex pairs is twice that of the earlier designs [20, 65, 112, 114]. The connected positions between winglet pairs are closer to the core region within tubes due to the lift angles. In other words, the space for the development of longitudinal vortices near the boundary layer increases. Therefore, the longitudinal vortex pairs near the tube wall are successfully induced by the winglets. However, Figure 4.5 (b) and (e) depict that the vortex pairs are disrupted due to the constraints of the tube wall, preventing them from fully developing and weakening their vortex intensity. Simultaneously, the vortex pairs near the core region expand towards the tube wall, exerting pressure on the vortex pairs near the tube wall. Subsequently, the vortex pairs maintain steady development, as shown in Figure 4.5 (e)-(h), indicating that vortex interaction has a better effect on vortex development along the tube. Finally, the vortex pairs gradually dissipate, as illustrated in Figure 4.5 (i) and (j).

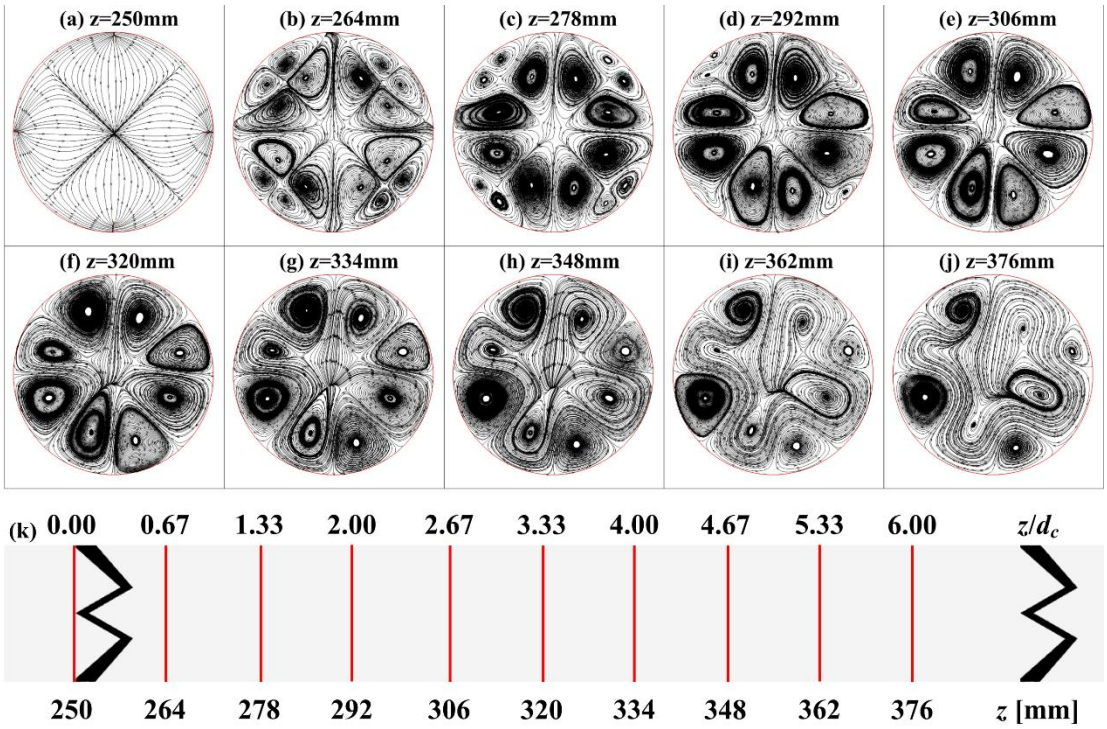

Figure 4.5 Streamlines at different cross sections for case A1 at *Re* = 7577.

To analyze the fluid flow characteristics in different cases, two typical cross sections (z = 264 mm and 334 mm) are selected. Figure 4.6 displays the streamlines at different cross sections for cases A2 through A7 at *Re*=7577. As observed in Figure 4.6 (a) and (b), compared to case A1, the dissipation intensity of the vortex pairs near the tube wall at z = 264 mm is increased with increasing α_v due to enhanced vortex interaction. In other words, a larger α_v reduces the space for vortex development near the boundary layer and enhances the vortex intensity of vortex pairs near the core region. Subsequently, the vortex pairs at z = 334 mm exhibit steady development similar to that observed in case A1. However, the size of vortex pairs near the core region decreases slightly as *BR* increases, as depicted in Figure 4.6 (c) and (d) at z = 264 mm, because an increase in winglet height reduces the space available for vortex development near the core region. The vortex structure near the core region becomes more concentrated as *BR* increases at z = 264 mm, indicating an enhancement in the disturbance intensity of fluid flows within tubes. However, the development of vortex near the core region is limited. As depicted in Figure 4.6 (c) and (d) at z = 334 mm, the vortex structure in case A5 becomes disrupted due to serious vortex interaction. This indicates that the

disturbance caused by higher *BR* negatively affects fluid flows within tubes. Similarly, an increase in *PN* is detrimental to fluid flows within tubes, as shown in Figure 4.6 (e) and (f). Compared to case A1, the vortex structures in cases A6 and A7 are prematurely dissipated at z = 334 mm. This indicates that the vortex interaction in cases A6 and A7 is more serious than that observed in case A1. Compared to case A1 at z = 264mm, the size of a single vortex pair near the core region decreases due to the increase in *PN*. The intensity of a single vortex pair is insufficient to counteract the negative effects of disturbances near the boundary layer. It can be concluded that the presence of vortex pairs near the boundary layer hinders the development of the vortex structure near the core region in cases A6 and A7.

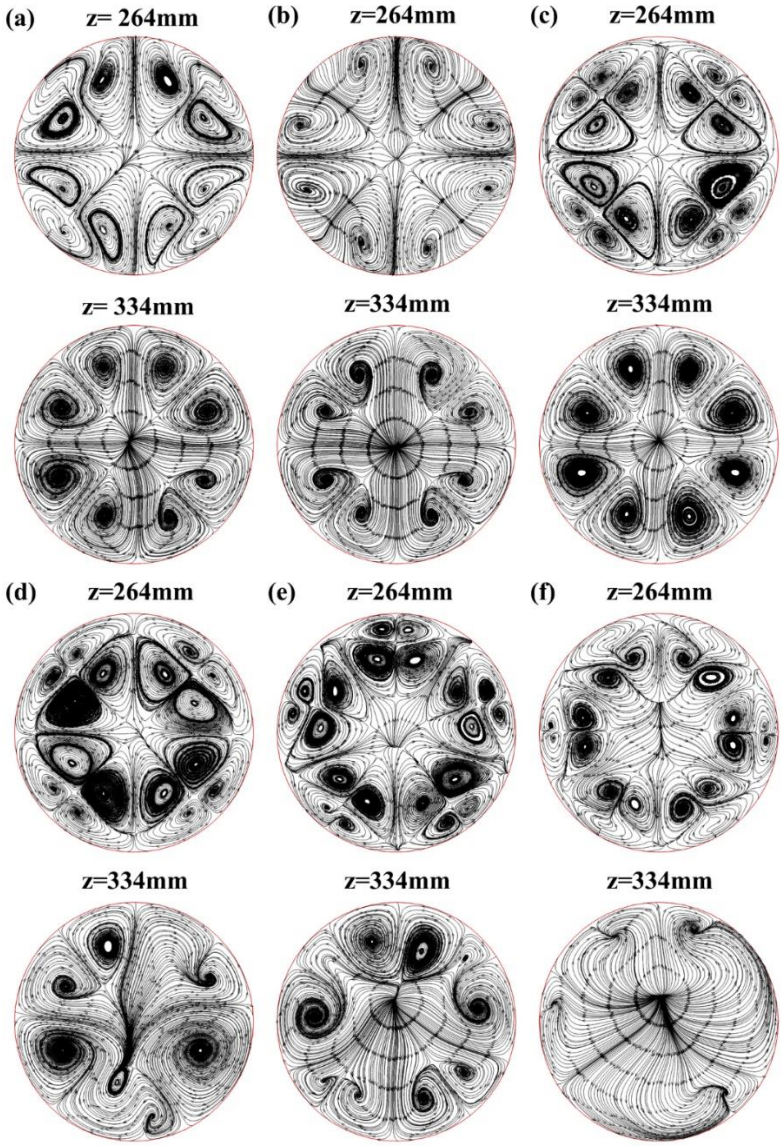

Figure 4.6 Streamlines of different cross sections at *Re* = 7577 in different cases: (a)

case A2; (b) case A3; (c) case A4; (d) case A5; (e) case A6; (f) case A7.

Figure 4.7 shows velocity magnitude contours at Re = 7577 in different cases. As illustrated in Figure 4.7 (a)-(c), the high-speed area within tubes increases with the increasing α_v. It is concluded that vortex pairs near the boundary layer are beneficial for enhancing the mixing uniformity of fluid flows within tubes. However, the high-speed area within tubes decreases with the increase of BR, as shown in Figure 4.7 (a), (d), and (e). Furthermore, the high-speed area becomes concentrated in the core region with increasing BR. Based on the analysis of Figure 4.6 (c) and (d), this is the result of the available space for vortex development near the core region decreases. As a result, the vortex pairs near the core region do not fully develop, and the fluid is confined to a smaller area, disturbing the flow field. Consequently, the vortex pairs are easily constrained and disrupted. With the increase in PN, the high-speed area becomes concentrated in the core region, as shown in Figure 4.7 (a), (f), and (g). This indicates that vortex pairs, lacking sufficient vortex intensity, do not fully disturb the flow field due to the presence of vortex pairs near the boundary layer. Figure 4.8 displays turbulent kinetic energy (TKE) contours at Re = 7577 in different cases. Figure 4.8 (a)-(c) illustrate that, compared to cases A2 and A3, the disturbance of the flow field in case A1 is significantly more uniform due to the presence of stronger vortex pairs near the boundary layer. Consequently, with the increase of α_v, the vortex intensity is significantly enhanced in the region from z = 250 mm to z = 278 mm. Similarly, the TKE is also enhanced in the region from z = 250 mm to z = 320 mm with the increase of BR, as depicted in Figure 4.8 (a), (d), and (e). However, the vortex interaction becomes severe due to the adverse development of the vortex structure in the core region. It can be observed in Figure 4.8 (f) and (g) that the distribution of TKE is less uniform than that in case A1, thus confirming the analysis of velocity magnitude distribution in case A6 and case A7.

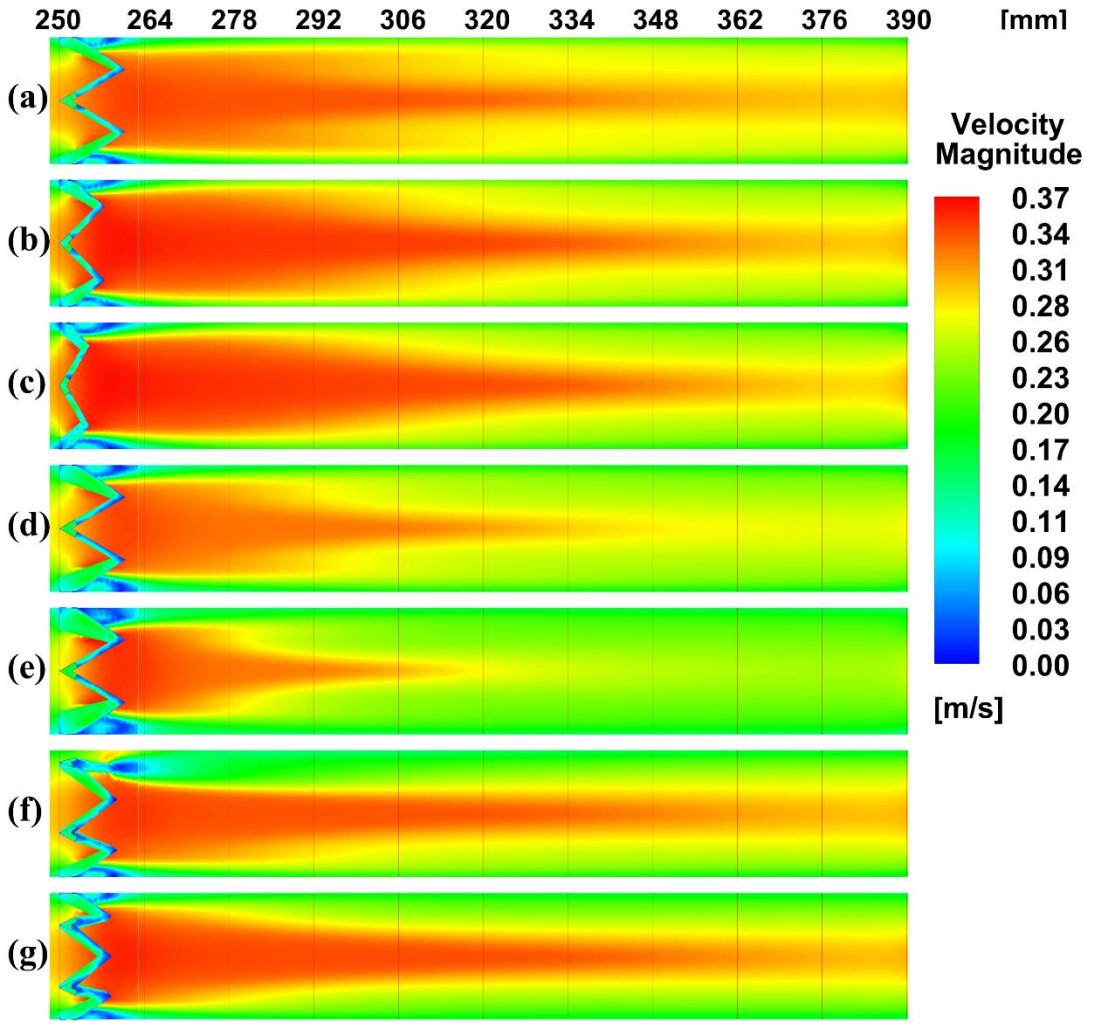

Figure 4.7 Velocity magnitude contours at *Re* = 7577 in different cases: (a) case A1; (b) case A2; (c) case A3; (d) case A4; (e) case A5; (f) case A6; (g) case A7.

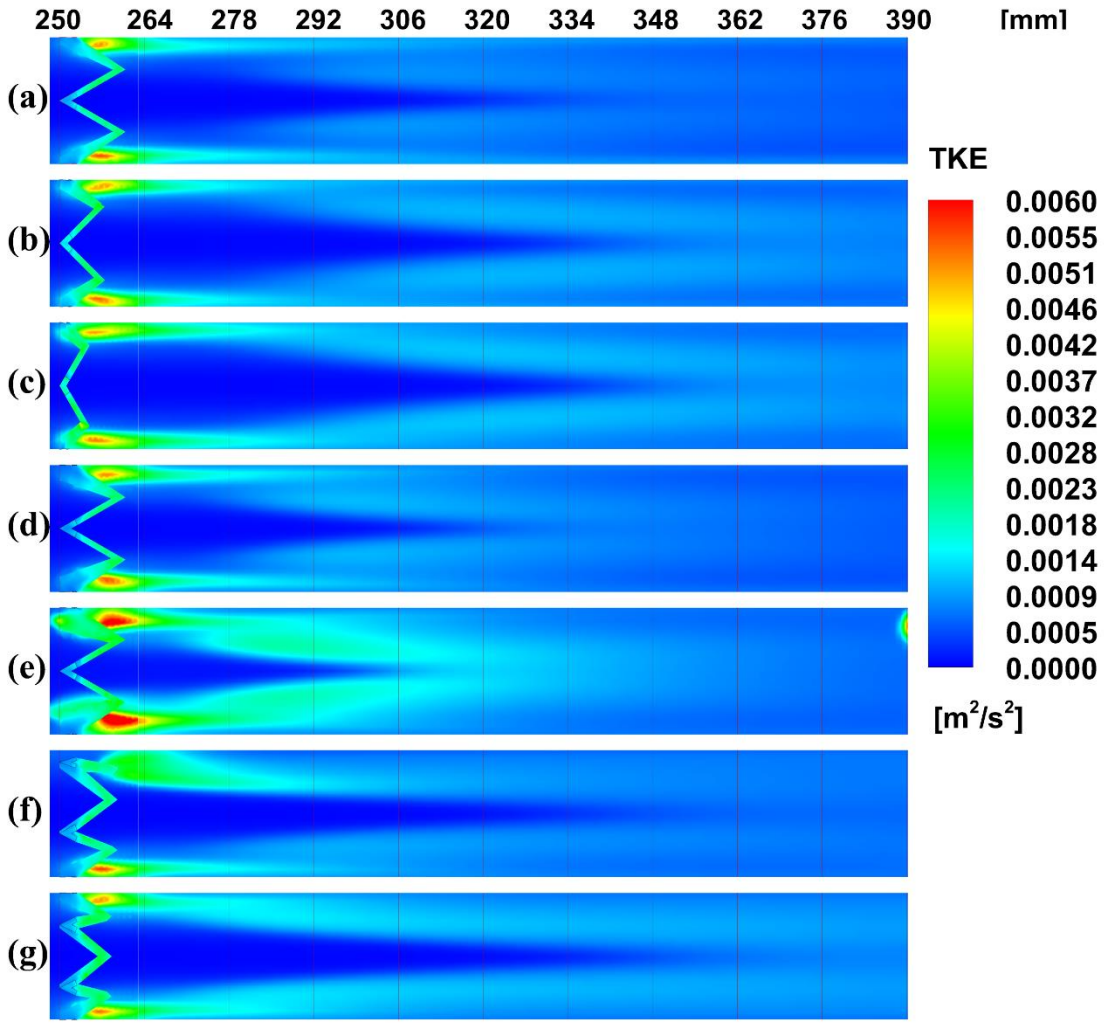

Figure 4.8 *TKE* contours at *Re* = 7577 in different cases: (a) case A1; (b) case A2; (c) case A3; (d) case A4; (e) case A5; (f) case A6; (g) case A7.

Figure 4.9 shows the axial distributions of *Se* at *Re* = 7577 across different cases. Due to the induction of vortex in the region from z = 250 mm to z = 264 mm, *Se* sharply increases in this region. In the region from z = 264 mm to z = 390 mm, *Se* decreases until it stabilizes due to vortex interaction and dissipation. Compared with other cases, *Se* in case A5 is the highest because the vortex pairs near the core region become more concentrated with the increase of *BR*. The reduction in the interaction region between two vortex pairs indicates that vortex interaction becomes more serious. Furthermore, *Se* in case A5 is not the highest from z = 306 mm to z = 390 mm. Based on the analysis in Figure 4.7 and Figure 4.8, most of the vortex energy is counteracted by the vortex interaction. Similarly, this reversal also occurs in case A6 and case A7. In the region

from z = 250 mm to z = 264 mm, *Se* in case A6 and case A7 is higher than that in case A2. However, in the region from z = 264 mm to z = 390 mm, the reversal appears. This can be explained by the destruction of the vortex structure, as shown in Figure 4.6 (e) and (f). In the region from z = 250 mm to z = 264 mm, *Se* in case A6 and case A7 is lower than that in case A4 and case A5 due to the limitation of the single vortex size. While *Se* in case A2 and case A3 is lower than that in other cases in the region from z = 250 mm to z = 264 mm, the flow field variation remains stable, as indicated in Figure 4.6 (a) and (b). Compared with case A2 and case A3, case A1 exhibits higher *Se*. This is due to the vortex interaction of vortex pairs near the boundary layer, resulting in more uniform mixing within tubes.

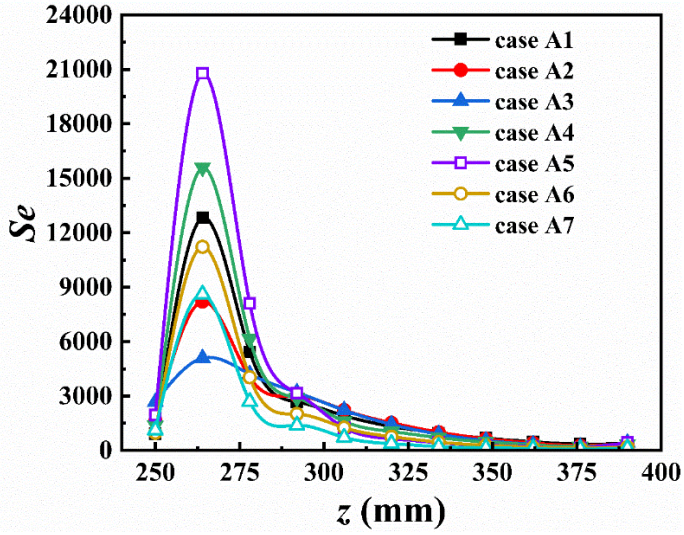

Figure 4.9 Axial distributions of *Se* at *Re* = 7577 across different cases.

4.5 Heat transfer analysis

This section analyzes temperature contours and the axial distribution of the local surface *Nu* in various cases at *Re* = 7577, aiming to understand the effect of vortex interaction on heat transfer.

Figure 4.10 displays the temperature contours at different cross sections for case A1 at *Re* = 7577. At the cross-section of z = 250 mm, 264 mm, 278 mm, and 292 mm, the temperature ranges near the boundary layer are 322.08 K-323 K, 321.46 K-322.38 K, 320.85 K-322.08 K, and 320.54 K-321.77 K, respectively. With vortex interaction near

the boundary layer, as depicted in Figure 4.5 (a)-(d), the temperature gradient near the boundary layer increases along the axial distance. However, the temperature remains uniform in the core region, consistent with core flow theory [167]. Furthermore, in Figure 4.10 (e)-(j), it is evident that the temperature gradient in the core region gradually increases along the axial distance due to the steady development of vortex pairs near the core region. Consequently, the area of the temperature region at 323 K gradually decreases along the axial distance. The gradual variation in temperature gradient from the boundary layer to the core region is attributed to vortex disturbance. This phenomenon enhances heat transfer and fluid mixing between the core region and boundary layer.

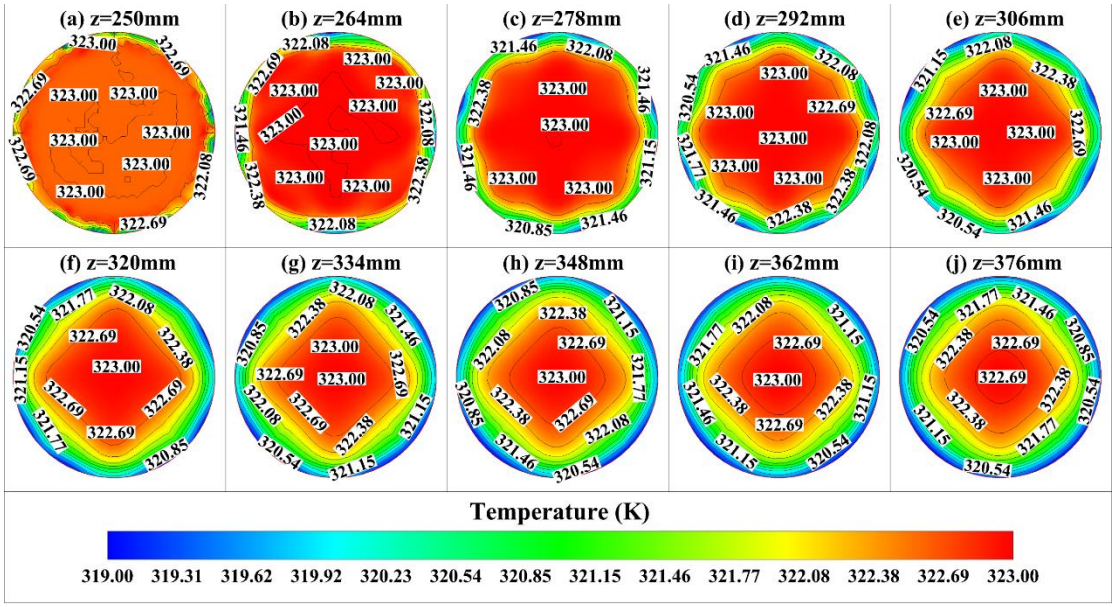

Figure 4.10 Temperature contours at different cross sections for case A1 at *Re* = 7577.

To analyze the heat transfer characteristics in different cases, two typical cross sections (z = 264 mm and 334 mm) are selected. Figure 4.11 displays the temperature contours of different cross sections for *Re* = 7577, ranging from case A2 to case A7. Figure 4.11 (a) to (f) show that the variation range of temperature gradient in the core region and boundary layer is similar to that in case A1, as water flow has a higher specific heat capacity compared to airflow under the same heat load. The temperature range across the entire cross-section is 0.2-0.4 times that of airflow [20]. Hence, the temperature gradient remains steady across cases A1 to A7, suggesting that water is suitable for

winglet tubes requiring a smaller temperature difference. However, the heat transfer rate is contingent upon the flow fields induced by winglets, leading to varying temperature distributions across cross-sections in each case. Figure 4.11 (a) and (b) reveal a progressively more significant gradient variation in temperature distribution as α_v increases, indicating a strong vortex intensity compared to that in case A1. Figure 4.6 (a) and (b) also explain the reason for this gradient variation. In contrast, the significant gradient variation in temperature distribution is not observed in Figure 4.11 (c) and (d). As shown in Figure 4.6 (c) and (d), higher *BR* negatively affects fluid flows within tubes. Furthermore, the situation in case A6 and case A7 mirrors that in case A4 and case A5.

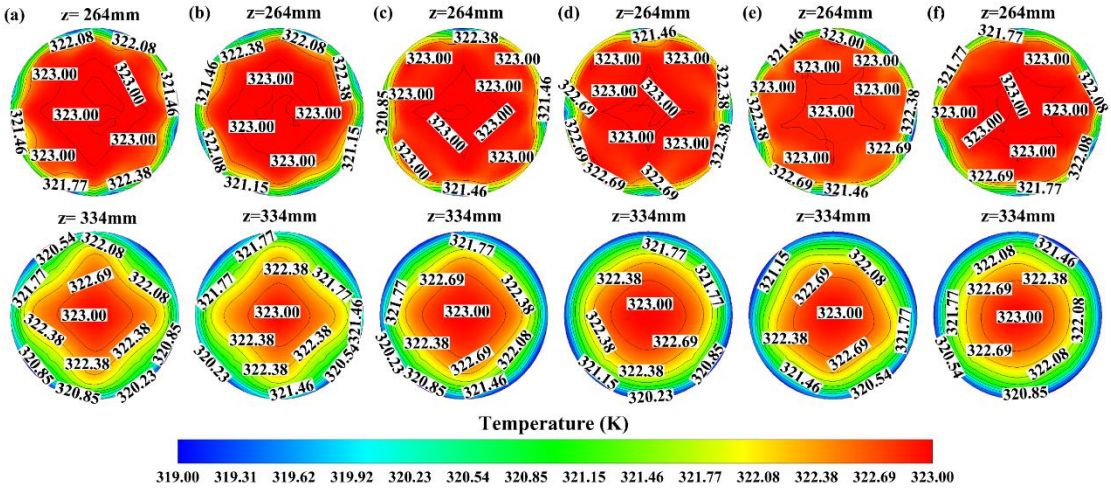

Figure 4.11 Temperature contours of different cross sections at *Re* = 7577 in different cases: (a) case A2; (b) case A3; (c) case A4; (d) case A5; (e) case A6; (f) case A7.

Figure 4.12 displays the contours of the surface local Nusselt number at *Re* = 7577 in case A1. The local *Nu* distribution in region A ranges from 128 to 176, which represents the highest values compared to other regions within the tubes. This is attributed to the intense and complex flow field existing before the formation of longitudinal vortices, as depicted in the cross-section at *z* = 250-264 mm in Figure 4.8 (a). In region B, where the longitudinal vortices have just formed, the vortex disturbance is significant compared to other regions along the tubes, with a specific emphasis on the vortex disturbance in region C. Moreover, it is important to note that the vortex pairs near the

boundary layer enhance heat transfer in region C, as depicted in Figure 4.5 (b) and (c). However, the heat transfer intensity observed in region C is not sustained beyond it due to the dissipation of vortex pairs near the boundary layer. While the heat transfer in region B is weaker than that in region A, the flow field and vortex interaction remain relatively stable. Furthermore, the steady vortex interaction in region B helps to maintain a stable intensity of vortex interaction along the tubes. The disturbance caused by vortices in region D to the heat transfer surface is more significant than that behind region C due to the presence of an impinging stream in region D. Compared with the heat transfer at z = 250-393 mm behind region B, the local Nu values decrease to 64-96 at z = 1108-1251 mm. This indicates a decrease in heat transfer intensity along the tubes by 25 % to 33 %, reflecting steady variations in the local heat transfer within the flow field of the tubes.

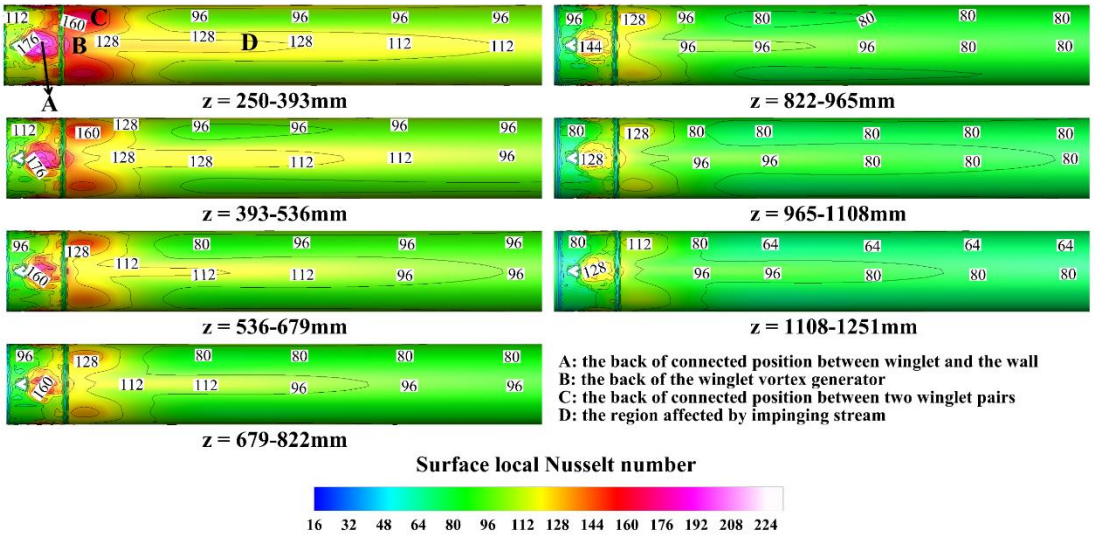

Figure 4.12 The contours of surface local Nusselt number at Re = 7577 in case A1.

4.6 Flow and thermal characteristics analysis

This section analyzes the variations of Nu, Nu/Nu_0, f, f/f_0, and TEF in various cases at different Re values, aiming to summarize the heat transfer and pressure drop characteristics of flow fields.

Figure 4.13 (a) displays the Nu variations within tubes with winglets. Nu increases with rising Re due to the high turbulence intensity. Furthermore, the Nu difference between

each case also increases with the increasing *Re*, indicating that *Nu* is sensitive to structural variation at high *Re* due to enhanced vortex interaction. *Nu* value in case A5 is the highest, consistent with the analysis in Figure 4.6 (d), where the vortex structure is more concentrated compared to other cases. Consequently, the turbulent disturbance is the strongest in the region from $z = 250$ mm to $z = 292$ mm, as depicted in Figure 4.9. However, the *Nu* difference between each case is not significant due to the constraints of tube diameter and winglet size. In this work, the highest *Nu* value is twice that reported by Zheng et al [20]. Figure 4.13 (b) illustrates the variations of the Nu/Nu_0 within tubes with winglets. *Nu* is increased by 1.90-2.32 times compared with plain tubes. The Nu/Nu_0 values increase to 106.2 % and 108.0 % of those in case A1 as α_v increases, respectively. Furthermore, with the increase in *BR*, the Nu/Nu_0 values are 103.5 % and 110.0 % of those in case A1, respectively. Similarly, as *PN* increases, the Nu/Nu_0 values are 101.9 % and 103.8 % of those in case A1, respectively. Nu/Nu_0 decreases nonlinearly as *Re* increases, indicating that vortex interaction and disturbance become more dominant at lower *Re*. At high *Re*, the impact of flow disturbance outweighs that of vortex interaction. Consequently, the potential for enhancing heat transfer by increasing *Re* is gradually diminished compared to plain tubes.

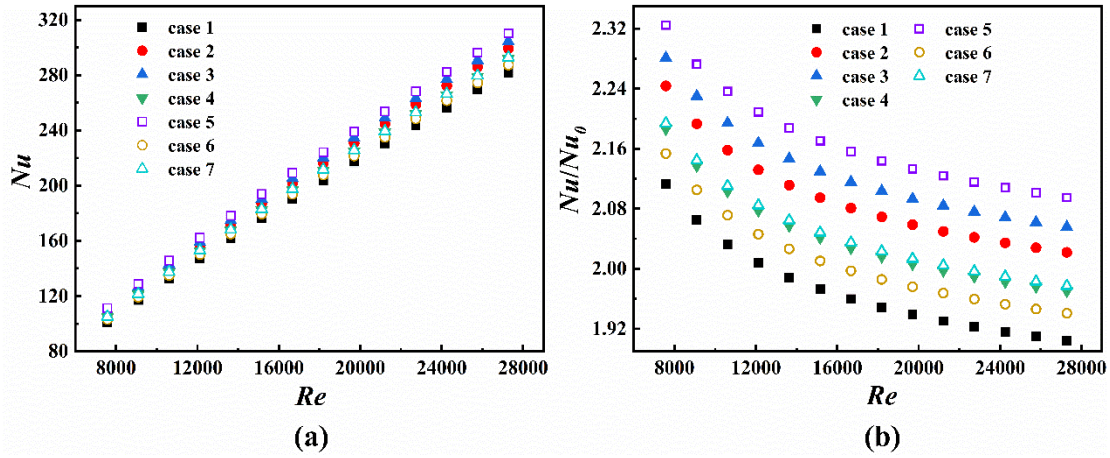

Figure 4.13 The effects of different cases on heat transfer for different *Re*: (a) *Nu*; (b) Nu/Nu_0.

Figure 4.14 illustrates the influence of novel self-join winglet vortex generators in different cases on fluid flow, represented by *f* and f/f_0. Figure 4.14 (a) indicates that

increasing *Re* results in a decrease in *f* across all cases. A larger α corresponds to higher *f* values, attributed to serious vortex interaction near the boundary layer. Furthermore, an increase in *BR* leads to a significant rise in *f*, attributed to intensified fluid flows and the destruction of vortex structures. Similarly, the impact of higher *PN* resembles that of a larger α_v. However, the main factor contributing to higher *f* in case A6 and case A7 is the destruction of vortex structures. In this work, the highest *f* value is 0.13 times that reported by Zheng et al [20]. As shown in Figure 4.14 (b), the f/f_0 exhibits an increasing trend with increasing *Re*. This suggests that high *Re* does not exhibit a better effect on fluid flow compared to that within plain tubes. The *f* is increased by 2.23-5.10 times compared with plain tubes. The f/f_0 values increase to 115.3 %-119.7 % and 127.5 %-131.9 % of those in case A1 as α_v increases, respectively. Furthermore, the f/f_0 values range from 127.3 % to 133.2 % and 175.0 % to 184.4 % of those in case A1 as *BR* increases, respectively. Similarly, with increasing *PN*, the f/f_0 values range from 105.2 % to 109.1 % and 113.8 % to 118.6 % of those in case A1, respectively. While large α_v, *BR*, and *PN* can significantly enhance heat transfer performance, they also result in increased pressure loss. Therefore, achieving a balance between pressure drop and enhanced heat transfer is essential when selecting the appropriate structural parameters.

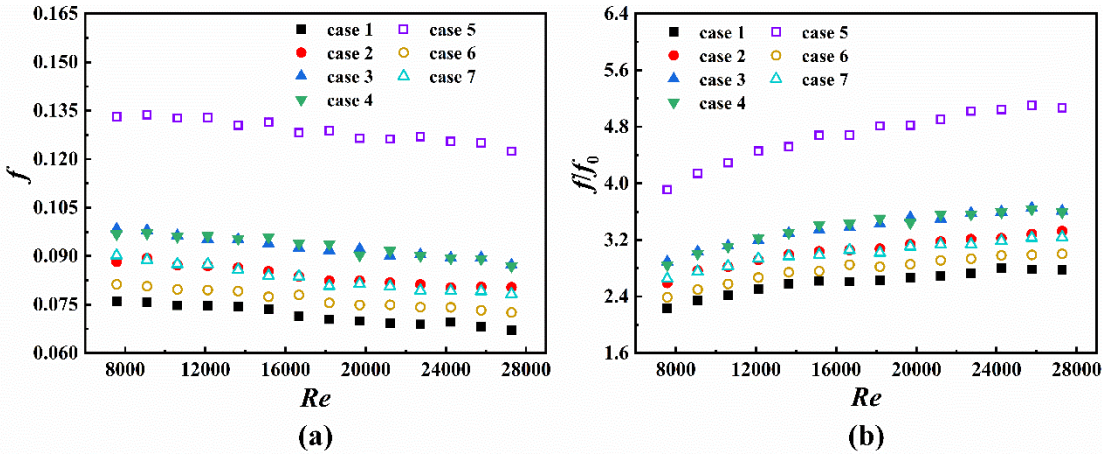

Figure 4.14 The effects of different cases on fluid flow for different *Re*: (a) *f*; (b) f/f_0.

Figure 4.15 displays the variations of *TEF* with different *Re* across different cases. A decreasing trend in *TEF* is observed as *Re* increases, attributed to significantly increased flow resistance at higher *Re*. Furthermore, *TEF* tends to be higher with lower values of

BR and *PN*, implying that lower *BR* and *PN* contribute to better overall thermal performance due to reduced flow resistance. The best *TEF*, 1.63, is observed in case A2, suggesting that a lower α_v does not necessarily demonstrate better comprehensive performance. Furthermore, the lowest *TEF* of 1.24 is observed in case A5. While this value exceeds 1, it can be attributed to the balanced pressure drop induced by winglet vortex generators, relative to the limited intensification of heat transfer.

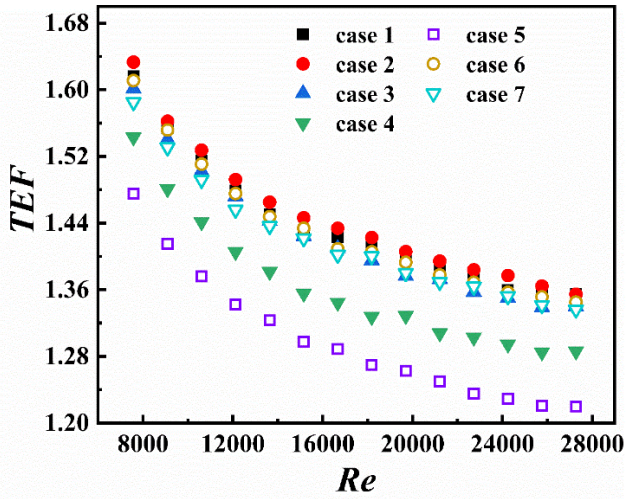

Figure 4.15 The variations of *TEF* with different *Re* across different cases.

4.7 Empirical correlations for *Nu* and *f*

Figure 4.16 compares the predicted *Nu* and *f* values from the correlations with the experimental data. The predicted *Nu* and *f* are obtained through the equation fitting function of Origin software. The maximum deviations are 6.6 % and 6 % for *Nu* and *f*, respectively. Therefore, the predicted data are in good agreement with the experimental data. The predicted results are valuable for guiding the design and optimization of novel winglet structures in the future. The correlations and constraints are provided as follows,

$$Nu=0.02688Re^{0.90814}BR^{0.10643}PN^{0.07035}(1+\alpha_v\pi/180)^{0.19578}+8.20506 \quad (4.1)$$

$$f=0.58746Re^{-0.20344}BR^{2.18696}PN^{1.37492}(1+\alpha_v\pi/180)^{2.09617}+0.05581 \quad (4.2)$$

where $7577 \le Re \le 27276$, $0.10 \le BR \le 0.20$, $4 \le PN \le 6$, and $60\ ^\circ \le \alpha_v \le 120\ ^\circ$.

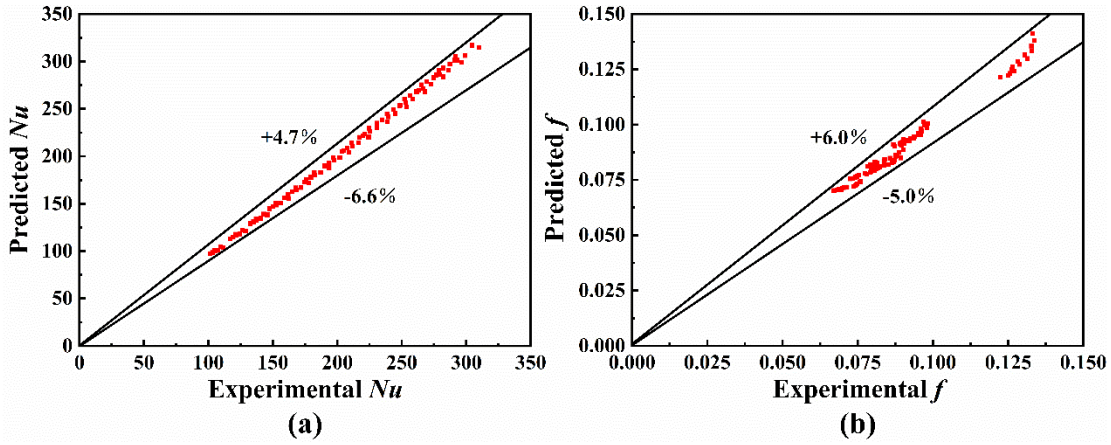

Figure 4.16 Comparisons of the predicted *Nu* and *f* with experimental data: (a) *Nu*; (b) *f*.

4.8 Comparisons with previous work

Figure 4.17 compares the *TEF* between the previous and present works. In this work, the winglets demonstrate superior performance in enhancing thermal performance compared to novel self-join winglets [20], protruded baffle bundles [168], delta winglet pairs [120], punched V-shape winglets [73], multiple rectangular winglets [101], grooved channels [169], curved wings [65], and torus rings [53]. It is found that the *TEF* of helical dimples [36] is significantly higher than that achieved in this work. While the heat transfer enhancement achieved with the winglet vortex generators in present work is significant, there is still potential for further improvement. Moreover, it is important to note that the *TEF* depicted in Figure 4.17 decreases as *Re* increases. The difference lies in the variation of the decreasing trend, suggesting that the vortex variation in the flow field is the key influencing factor.

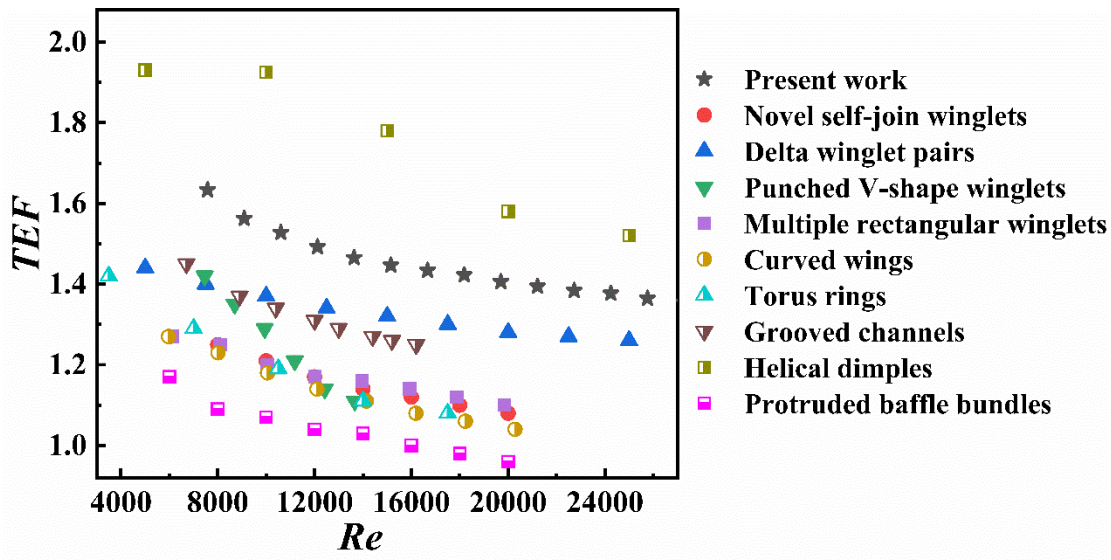

Figure 4.17 Comparisons of *TEF* between the previous and present work.

4.9 Similarity analysis

Compared to experimental work, numerical methods are widely utilized in earlier studies due to their strengths in time and cost saving. However, designing a 3D model, discretizing fluid domain, and solving numerical cases still require considerable time. Furthermore, limitations exist regarding boundary conditions and numerical assumptions. Therefore, both experimental work and numerical simulation remain insufficient for optimizing flow structures. Establishing a similarity correlation between structural parameters and flow field characteristics is crucial for guiding the design of vortex generators and optimizing the flow fields to enhance heat transfer within tubes. To investigate the correlation between flow state and optimized parameters, the similarity analysis is defined as follows:

$$\dot{V}=A' u \tag{4.3}$$

where A' is cross-section area.

$$\dot{m}=\rho \dot{V} \tag{4.4}$$

$$A'=\pi d^2/4 \tag{4.5}$$

$$Q_h=hA\Delta T' \tag{4.6}$$

where Q_h is the heat transfer rate between the fluid and tube wall; $\Delta T'$ is

temperature difference between wall and bulk temperature.

It is assumed that the heat loss is negligible,

$$Q_h = Q_f \tag{4.7}$$

$$A = \pi dl \tag{4.8}$$

where l is the length of the heat transfer surface.

Combining equations (3.33) and (4.3) yields the following equation,

$$Re = \dot{V}d / A'\nu \tag{4.9}$$

Combining equations (4.4), (4.5), and (4.9) yields the following equation,

$$Re = 4\dot{m} / \rho\pi d\nu \tag{4.10}$$

Combining equations (3.35), (4.6), (4.7), and (4.8) yields the following equation,

$$\dot{m} = h\pi dl\Delta T' / c_p \Delta T_{io} \tag{4.11}$$

Combining equations (3.36), (4.10), and (4.11) yields the following equations,

$$\mathrm{Re} = \frac{4\lambda l}{\rho c_p \nu d} \cdot \frac{\Delta T'}{\Delta T} \cdot \mathrm{Nu} \tag{4.12}$$

where $\Delta T'/\Delta T$ can be defined as the ratio of temperature difference (T'), Nu is represented by the empirical correlation (e.g. equation (4.1)).

It is assumed that flow structures in two flow fields are similar. Hence,

$$Re_1 = Re_2 \tag{4.13}$$

By combining equations (4.12) and (4.13), the similarity correlation of heat transfer characteristics between two flow fields is obtained,

$$\frac{T_1'}{T_2'} = \frac{\rho_1}{\rho_2} \cdot \frac{c_{p1}}{c_{p2}} \cdot \frac{\nu_1}{\nu_2} \cdot \frac{\lambda_2}{\lambda_1} \cdot \frac{d_1}{d_2} \cdot \frac{l_2}{l_1} \cdot \frac{Nu_2}{Nu_1} \tag{4.14}$$

Temperature difference similarity coefficient (ΔT_{sc}) is defined as the following equation,

$$\Delta T_{sc} = T_1' / T_2' \tag{4.15}$$

Combining equations (3.33)and (3.34) yields the following equation,

$$Re=(2d^3\Delta P/L\rho fv^2)^{0.5} \tag{4.16}$$

where f is represented by the empirical correlation (e.g. equation (4.2)).

Combining equations (4.13) and (4.16) yields the following equation,

$$\left(\frac{\Delta P_1}{\Delta P_2}\right)^{0.5}=\left(\frac{\rho_1}{\rho_2}\right)^{0.5}\cdot\frac{v_1}{v_2}\cdot\left(\frac{d_2}{d_1}\right)^{1.5}\cdot\left(\frac{L_1}{L_2}\right)^{0.5}\cdot\left(\frac{f_1}{f_2}\right)^{0.5} \tag{4.17}$$

Pressure drop similarity coefficient (ΔP_{sc}) is defined as the following equation,

$$\Delta P_{sc}=(\Delta P_1/\Delta P_2)^{0.5} \tag{4.18}$$

With the optimal *TEF* as the selecting standard, case A2 is compared with previous works, including self-join winglets [20], inclined winglets [170], rectangular winglets [101], delta winglet pairs [121], perforated conical strip [171], V-finned twisted tapes [172], helical dimples [36], and inclined vortex rings [52]. Figure 4.18 (a) shows the variation in similarity of temperature differences between the present and previous works. As *Re* increases, ΔT_{sc} gradually increases, implying that the present work exhibits dependence on *Re* variations compared to previous works. Moreover, it is important to note that the variation in temperature differences is significant among the winglet-type cases. This indicates that the enhancement effect of longitudinal vortices induced by winglets on heat transfer increases gradually with increasing *Re*, with a specific emphasis on the delta-winglets case. Therefore, the delta-winglets case can serve as a standard for optimizing the heat transfer performance of novel winglet vortex generators. Furthermore, the ΔT_{sc} values for the self-join-winglets and inclined-winglets cases are around 1, indicating that the overall temperature difference is similar to that in the present work. Therefore, these two cases can serve as reference models for designing the winglet configurations and optimizing the temperature fields in present work. Figure 4.18 (b) shows the variation in similarity of pressure drop between the present and previous works. With the increase in *Re*, the variations of ΔP_{sc} values in most cases are not significant. However, the ΔP_{sc} values of helical-dimples case

decrease significantly. The main reason is that the transverse flows induced by dimples on the wall surface are quite different from the longitudinal vortex flows induced by other tube inserts. The helical-dimples case can serve as a reference for enhancing disturbance intensity. However, the temperature difference variation in the helical-dimples case is lower than that in present work, as shown in Figure 4.18 (a). This suggests that in addition to optimizing fluid flow, it is also necessary to consider enhancing heat transfer intensity. Hence, the temperature difference of the flow field in present work can serve as a reference for the helical-dimples case. The ΔP_{sc} values of self-join-winglets and inclined-winglets cases are lower than those of the non-winglet-type cases, indicating that the variation of fluid flow is more stable compared to the present work. While the overall variation in temperature fields for these two cases is similar to that in present work, there remains potential for improving flow disturbance in this work.

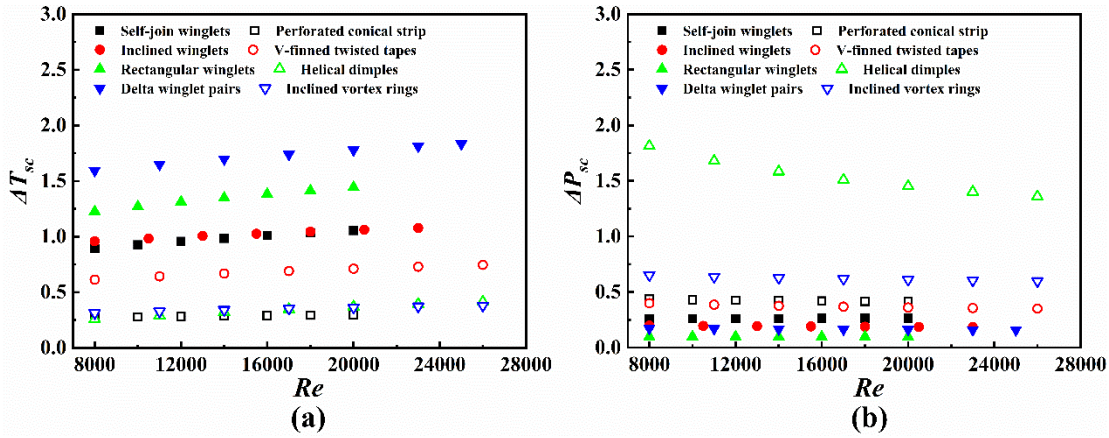

Figure 4.18 Similarity analysis: (a) ΔT_{sc} versus Re; (b) ΔP_{sc} versus Re.

4.10 Chapter conclusion

In this chapter, the design of self-join winglet vortex generators is modified to optimize the vortex interaction within tubes. Experimental measurements and numerical simulations are conducted to investigate the effect of blockage ratio (BR), winglet pairs number (PN), and included angle (α_v) on heat transfer and fluid flow in circular tubes with winglets. Furthermore, similarity equations between structural parameters and flow field characteristics are obtained. The key findings in this chapter are as follows:

(1) The number of vortex pairs is twice that of previous designs. Longitudinal vortices near the tube wall are induced by winglets because of lift angles.

(2) The vortex pairs near the tube wall contribute to enhancing the mixing uniformity of fluid flows in tubes. Furthermore, the dissipation intensity of the vortex pairs near the tube wall is increased with increasing α_v. Higher values of *BR* and *PN* adversely affect fluid flows in tubes.

(3) Nusselt number and friction factor are increased by 1.90-2.32 and 2.23-5.10 times, respectively, compared with plain tubes.

(4) The maximum thermal enhancement factor (*TEF*) reaches 1.63 when $BR = 0.10$, $PN = 4$, and $\alpha_v = 90$ °, suggesting that a lower α_v does not necessarily demonstrate better comprehensive performance. Furthermore, the lowest *TEF* reaches 1.24 when $BR = 0.20$, $PN = 4$, and $\alpha_v = 60$ °. While this value exceeds 1, it can be attributed to the balanced pressure drop induced by winglet vortex generators, relative to the limited intensification of heat transfer.

(5) Similarity analysis indicated that the variation in temperature differences is significant among the winglet-type cases. Furthermore, the delta-winglets case can serve as a standard for optimizing the heat transfer performance of novel winglet vortex generators. The variation of fluid flow in self-join-winglets and inclined-winglets cases is more stable compared to the present work. While the overall variation in temperature fields for these two cases is similar to that in present work, there remains potential for improving flow disturbance in this work.

Chapter 5: The optimization of the flow field in circular tubes equipped with modified winglet structures

5.1 Introduction

As shown in Chapter 4, the dissipation rate of vortices near the tube wall is crucial for longitudinal vortex development and for optimizing the flow field within circular tubes. The boundary vortices help delay the destruction of flow fields induced by longitudinal vortices. Furthermore, these vortices contribute to the uniformity of temperature fields. Based on this mechanism, this chapter aims to optimize the vortex interaction of boundary vortices in circular tubes equipped with novel self-join winglet vortex generators, while also providing optimization strategies for improving uniformity in heat transfer and fluid flow. Consequently, the optimization mechanism and flow behavior in circular tubes equipped with modified winglet designs are numerically and experimentally investigated in this chapter. Specifically, the research content presented in this chapter is divided into three parts: (i) revealing the optimization mechanism of flow fields influencing by modified winglet designs, (ii) investigating the effect of curved height and lift angle on heat transfer and fluid flow, and (iii) summarizing the heat transfer and fluid flow characteristics of optimized flow fields under *Re* ranging from 7577 to 27,276.

5.2 Physical model

The optimization design of winglet structures in this chapter can be based on variation mechanism of boundary vortices. In this chapter, the optimization variables include lift angles (β = 30 °, 45 °, and 60 °), included angles (α_v = 60 °, 90 °, 120 °), curved ration ($CR = H_c/d_c$ = 0.67, 1.33, and 2.00). The physical model is shown in Figure 5.1. More details of the physical model can be found in Table 5.1. The parameters studied in this chapter are based on the variation mechanism of boundary vortices. These parameters are primarily crucial for adjusting the development space and improving the interaction intensity of boundary vortices. Furthermore, the reasons for selecting the value range of each parameter are outlined below,

(a) For the parameter "β", it is key to generating boundary vortices, as concluded in Chapter 4. Its value ranges from 0 to 90º. The values 30º and 60º present typical growth points within this range, allowing observation of overall variation trends. Since 45º is the median value of the range, it helps reveal the average variation characteristic.

(b) For the parameter "α_v", the selections of this parameter and its value range follow previous studies. The aim is to compare the results with earlier winglet designs.

(c) For the parameter "*CR*", it is chosen because it further adjusts the development space for boundary vortices without significantly increasing the cross-sectional blockage area. The rationale for selecting specific values is the same as that for the parameter "β".

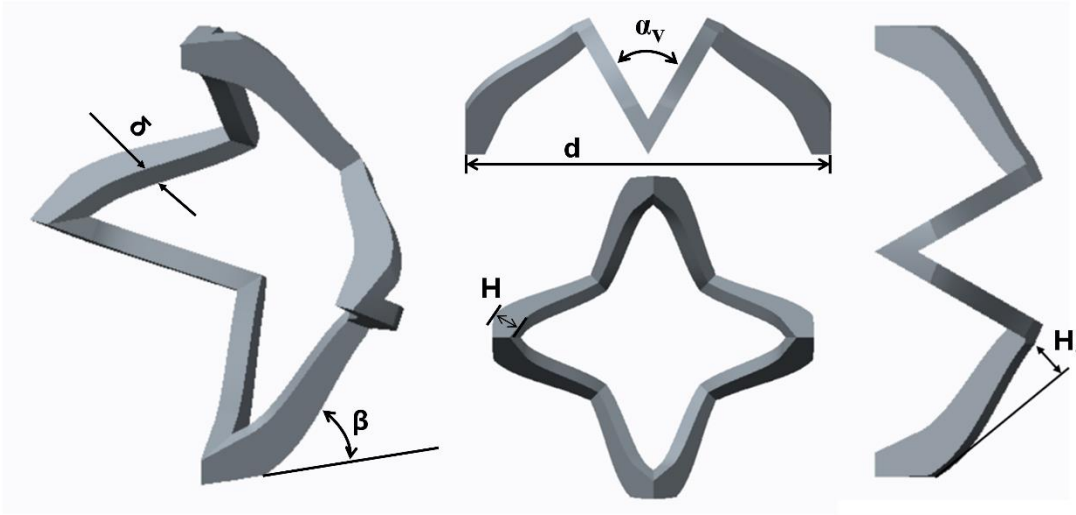

Figure 5.1 Modified design of novel self-join winglet vortex generators.

Table 5.1 Specification of the physical model.

Specification	Dimension
Included angle (α_v)	60 °, 90 °, 120 °
Lift angle (β)	30 °, 45 °, 60 °
Curved ratio (*CR*)	0.67, 1.33, 2.00
Curved height (H_c)	14 mm, 28 mm, 42 mm
Internal diameter of tubes (*d*)	21 mm

Characteristics diameter (d_c)	21 mm
Winglet thickness (δ)	1 mm
Winglet height (H)	2.1 mm
Case B1	β = 30 °, α_v = 60 °, CR = 0.67
Case B2	β = 30 °, α_v = 60 °, CR = 1.33
Case B3	β = 30 °, α_v = 60 °, CR = 2.00
Case B4	β = 45 °, α_v = 60 °, CR = 0
Case B5	β = 45 °, α_v = 90 °, CR = 0
Case B6	β = 45 °, α_v = 120 °, CR = 0
Case B7	β = 60 °, α_v = 60 °, CR = 0
Case B8	β = 60 °, α_v = 90 °, CR = 0
Case B9	β = 60 °, α_v = 120 °, CR = 0

5.3 Optimization mechanism

To further verify the optimization mechanism on flow variations induced by boundary vortices, the flow fields behind the winglet vortex generators are analyzed in detail in this section.

Figure 5.2 shows the variations of velocity magnitude behind the winglet vortex generators. The maximum value of velocity magnitude is 0.3 m/s, which is 81.08 % of that in case A1, as shown in Figure 4.7 (a). Furthermore, the average velocity magnitude is lower than that in case A1. The velocity variation range of core region in case B1 is between 0.24 m/s- 0.3 m/s, while that in case A1 is between 0.28 m/s- 0.37m/s. The adjustment in velocity variation is stable for optimized flow fields. It indicates that the curved height significantly affects the uniformity of the flow fields in circular tubes. Meanwhile, the area of high-speed region (red part) is also reduced compared to case A1, suggesting that the intensity of flow disturbance is reduced. Achieving a reasonable balance between uniformity and disturbance is crucial for the optimization of the flow field within circular tubes.

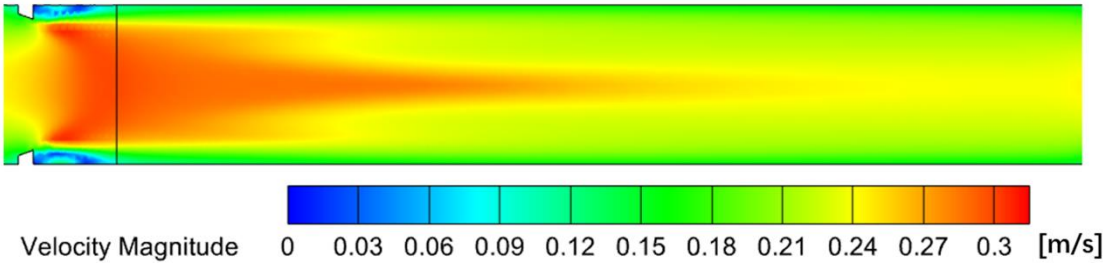

Figure 5.2 The variations of velocity magnitude behind the winglet vortex generators. (Case B1: β = 30 °, α_v = 60 °, CR = 0.67).

Figure 5.3 shows the variations of velocity magnitude and streamlines in various cross sections. Compared with the flow fields in case A1 (shown in Figure 4.5), the development region of boundary vortices is enlarged, indicating that the intensity of boundary vortices increases. Furthermore, the core vortices remain largely unaffected by the boundary vortices. The structures of core vortices remain stable, which is crucial for the steady development of flow fields within circular tubes. In case A1, the boundary vortices completely dissipate at the cross section of z = 306 mm. However, in case B1, the boundary vortices remain in their final dissipative stage at z = 306 mm, demonstrating the movement distance of the boundary vortices increases. Obviously, there remains significant potential for further reducing the dissipation rate of the boundary vortices. As the axial distance increases, the area of high-speed region is reduced, while it concentrates on the core region within circular tubes, which is beneficial by the steady flow fields. At the cross section of z = 264 mm, the velocity variation range in the core region is between 0.24 m/s- 0.3 m/s, while that at the cross section of z = 306 mm is between 0.24 m/s– 0.27 m/s. These results suggest that the boundary vortices play an efficient and stable role in adjusting the uniformity of the velocity in core regions.

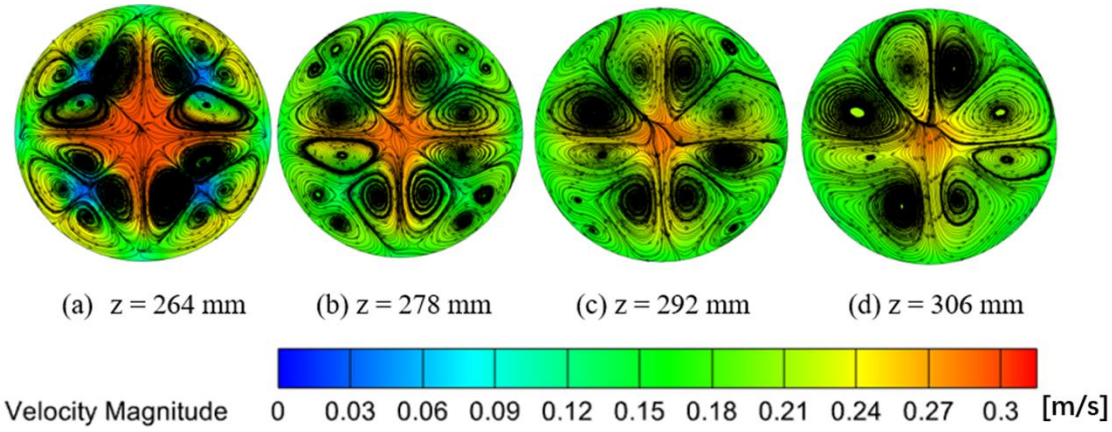

Figure 5.3 The variations of velocity magnitude and streamlines in various cross sections. (Case B1: β = 30 °, α_v = 60 °, CR = 0.67).

5.4 Effect of lift angles on heat transfer and fluid flow

This section analyzes the effect of lift angles on velocity magnitude, *TKE*, temperature, and *Se* in various cases. Furthermore, it summarizes the heat transfer and pressure drop characteristics of flow fields induced by modified lift angles.

Figure 5.4 shows the variations of velocity magnitude in the cross section of z = 290 mm. As the included angle increases, in the core region, the area of the high-speed region increases, while the area of the low-speed region decreases. The disturbance in the core region becomes more uniform rather than concentrated. This indicates that the disturbance intensity of the flow fields is enhanced. However, the vortex interaction is also enhanced, which significantly affects the vortex development. In the boundary region, the velocity variations opposite to those in the core region appear. This suggests that the disturbance energy concentrates in the core region due to the increase in included angles. Furthermore, as the lift angle increases, the area of the high-speed region decreases. The primary reason is that the structural limitations of the winglet structure hinder the development of flow fields in the core region. Meanwhile, the variations in included angles do not significantly affect the influence of lift angles. Furthermore, the boundary area of the high-speed region increases as the included angle increases, indicating that an adjustment in the distribution of the high-speed region.

This enhances the uniformity of the flow fields and improves heat and mass transfer between the core region and the boundary layer. Moreover, the uniformity of the low-speed region (blue region) is crucial for maintaining the uniformity of the flow fields.

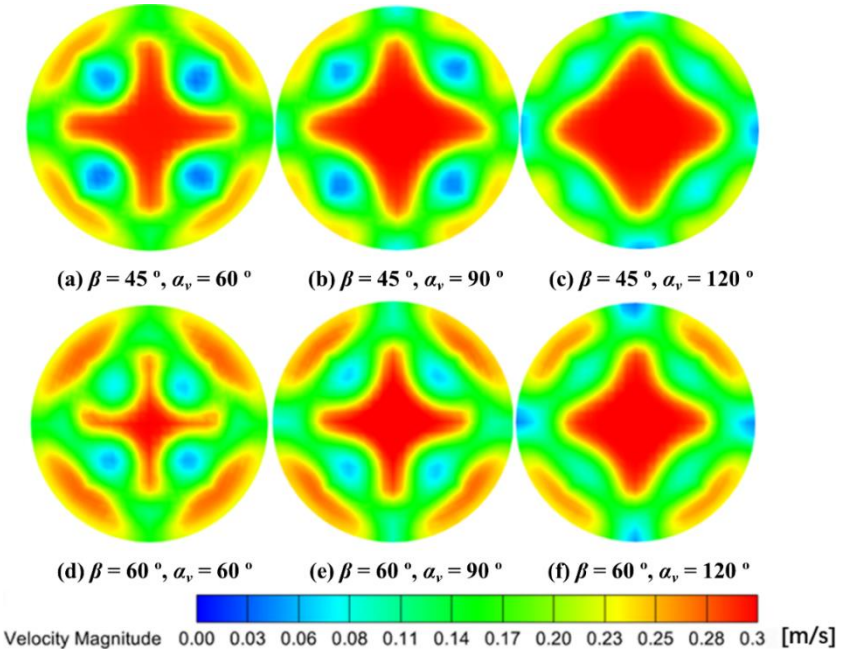

Figure 5.4 The variations of velocity magnitude in cross section of z = 290 mm for various cases: (a) B4; (b) B5; (c) B6; (d) B7; (e) B8; (f) B9.

Figure 5.5 displays the *TKE* contours at *Re* = 7577 for different cases. As shown in Figure 5.5 (a), (b), and (c), as the included angle increases, the region with *TKE* values between 0-0.0005 m^2/s^2 expands. This clearly has a detrimental effect on the overall disturbance in the core region, as most of the space in the core region is not utilized efficiently. However, this disturbance mode is beneficial for the downstream flows. Furthermore, the disturbance intensity in the region near the vortex generators increases due to structural limitations. For the upstream flows, case B4 represents a suitable disturbance mode when β is 45 °. As show in Figure 5.5 (d), (e), and (f), when β increases to 60 °, the region with *TKE* values between 0-0.0005 m^2/s^2 decreases. The adjustment in life angle improves the disturbance pattern of the flow fields, thereby the uniformity of the flow fields is improved. Furthermore, the disturbance intensity in the region near the vortex generators increases significantly with increasing β. However, when the β is 60 °, the difference between high-disturbance and low-disturbance regions

becomes particularly significant, suggesting that further improvements in overall uniformity are possible for this disturbance mode. Establishing a reasonable balance between included angles and lift angles is crucial for adjusting the uniformity of the flow fields.

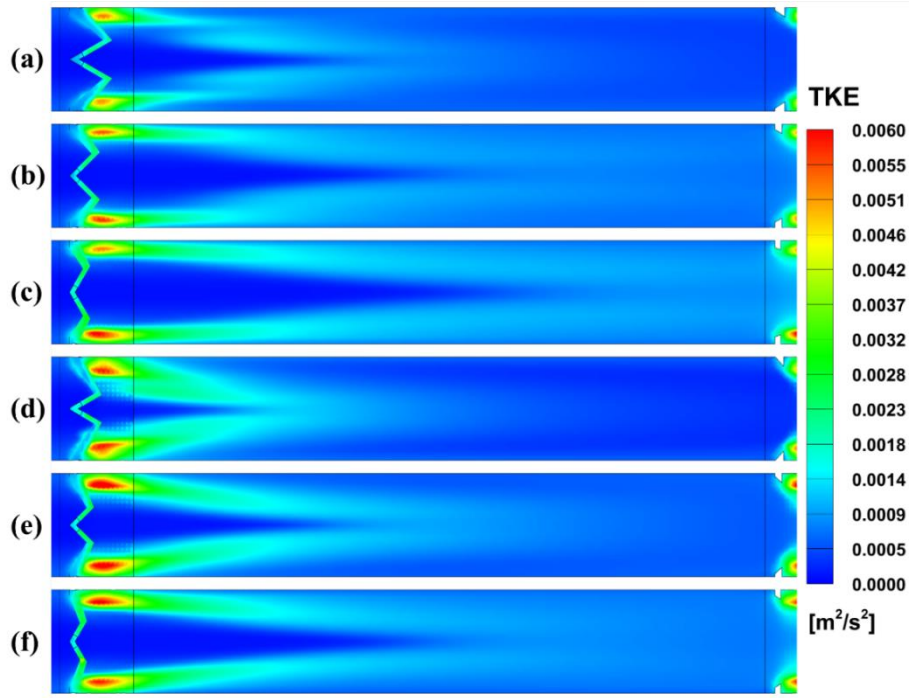

Figure 5.5 *TKE* contours at *Re* = 7577 in different cases: (a) case B4; (b) case B5; (c) case B6; (d) case B7; (e) case B8; (f) case B9.

Figure 5.6 shows the variations of temperature in the cross section of z = 290 mm. As the included angle increases, the high-temperature region becomes more concentrated, and the temperature gradient becomes more uniform. However, as the lift angle increases, the regional distribution effect is more significant than that caused by increasing included angles. This flow characteristic is suitable for local heat transfer disturbance. Therefore, it is concluded that increasing the included angle improves the uniformity of the flow fields, while increasing the lift angle enhances the regional disturbance. Furthermore, the variations of temperature range are around 320-323 K, which is consistent with the previous studies concerning the temperature variations of water flows. Compared with case A1, increasing both included angle and lift angle are beneficial for the uniformity of heat transfer and fluid flows.

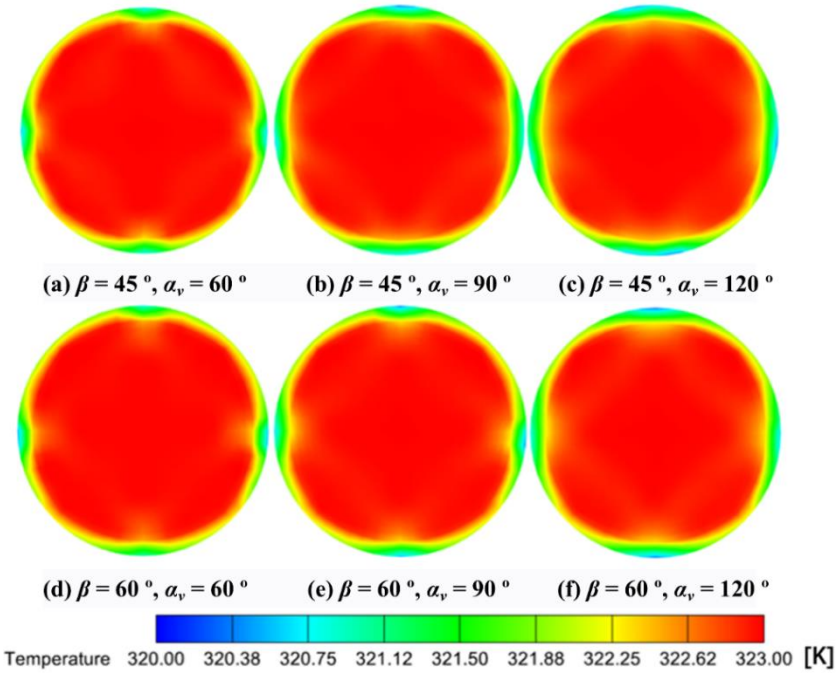

Figure 5.6 The variations of temperature in cross section of z = 290 mm.

Figure 5.7 demonstrates the variation in *Se* axial distribution for different cases and *Re*. As shown in Figure 5.7 (a), the *Se* peak values appear at the crosse section of z/d_c = 0.67 due to the steady vortex structure initially generated around this location. The vortex gradually dissipates downstream of the vortex generators. As the included angle increases, the *Se* values decrease, primarily because the disturbance intensity decreases in the core region, consistent with the analysis in Figure 5.5. Furthermore, before the cross section of z/d_c = 2.00, the *Se* values also decrease as the lift angle increases. The steady vortex structure maintains the effect of the winglet structure. However, the *Se* variations demonstrate an opposite trend after the cross section of z/d_c = 2.00, as the uniformity of the flow field increases until reaching the reversal point, which can also be observed in Figure 5.5. This indicates that the increasing lift angle is suitable for enhancing the flow disturbance in the downstream section of the tubes. Furthermore, after the cross section of z/d_c = 2.00, the *Se* differences between small and large lift angles increase as the included angle decreases, suggesting that the adjustment of included angles is beneficial for enhancing the effect of lift angles. However, in cases B6 and B9, this flow phenomenon appears after the cross section of z/d_c = 4.00,

demonstrating that only when the included angle is appropriately applied does it show a significant enhancement effect on lift angles. As shown in Figure 5.7 (b), the *Se* difference between small and large lift angles increases as *Re* increases. The effect of increasing *Re* enhances the effect of lift angles. For the effect of small lift angles, the effect of flow disturbance weakens with increasing *Re*, while for the effect of large lift angles, the effect of flow disturbance remains nearly constant with increasing *Re*.

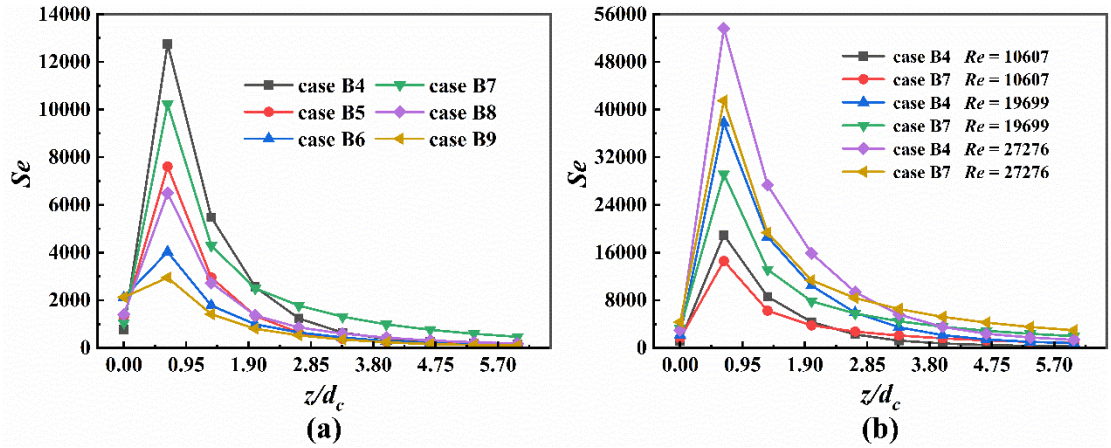

Figure 5.7 Variation in *Se* axial distribution: (a) cases B4 - B9; (b) different *Re* in cases B4 and B7.

Figure 5.8 shows the effects of different cases on heat transfer at different *Re*. As shown in Figure 5.8 (a), *Nu* increases with increasing *Re* due to the stronger flow disturbance. Furthermore, the *Nu* differences between different cases becomes more significant. However, the difference is particularly significant between cases B6 and B4. From the analysis in Figure 5.7, a reasonable value of included angle can enhance the effect of lift angles. When the included angle is between 90 ° and 120 °, the heat transfer enhancement effect is significant due to the adjustment of flow disturbance. As shown in Figure 5.8 (b), case B6 exhibits the highest Nu/Nu_0 value, while case B4 shows the lowest one. Furthermore, the difference between other cases is not significant, suggesting that the effect of large lift angle is not significant for enhancing the heat transfer due to the overall uniformity of flow disturbance. As *Re* increases, the Nu/Nu_0 values decrease.

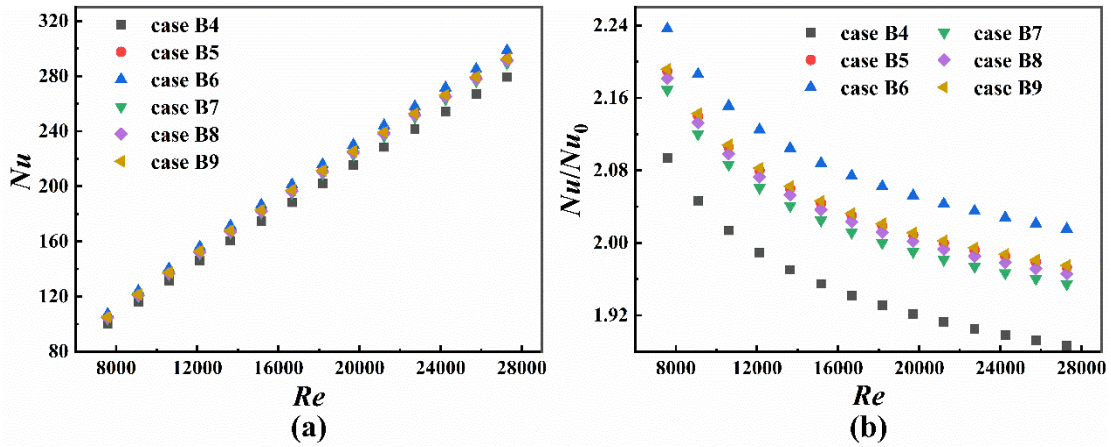

Figure 5.8 The effects of different cases on heat transfer for different *Re*: (a) *Nu*; (b) *Nu*/*Nu*0.

Figure 5.9 demonstrates the effects of different cases on fluid flow at different *Re*. As shown in Figure 5.9 (a), the *f* values decrease with increasing *Re* due to the stronger power input to the flow system. Case B4 not only demonstrates the minimum heat transfer capacity, but also shows the minimum flow resistance. This characteristic is attributed to the advantages and disadvantages of the structures. However, case B8 exhibits the highest *f*/*f*0 values among all cases, which is inconsistent with this characteristic resulting from the structures. The vortex interaction is the primary affecting factor. This means that an included angle of 90 º is the turning point at which the influence of the lift angle becomes significant. Figure 5.9 (b) demonstrates an increasing *f*/*f*0 trend with increasing *Re*. Under the influence of high *Re*, the optimization effect on flow resistance weakens. Consistent with the differences and variations among the various cases in Figure 5.9 (a), these results indicate that the actual contribution of vortex interaction to the flow resistance follows a consistent pattern.

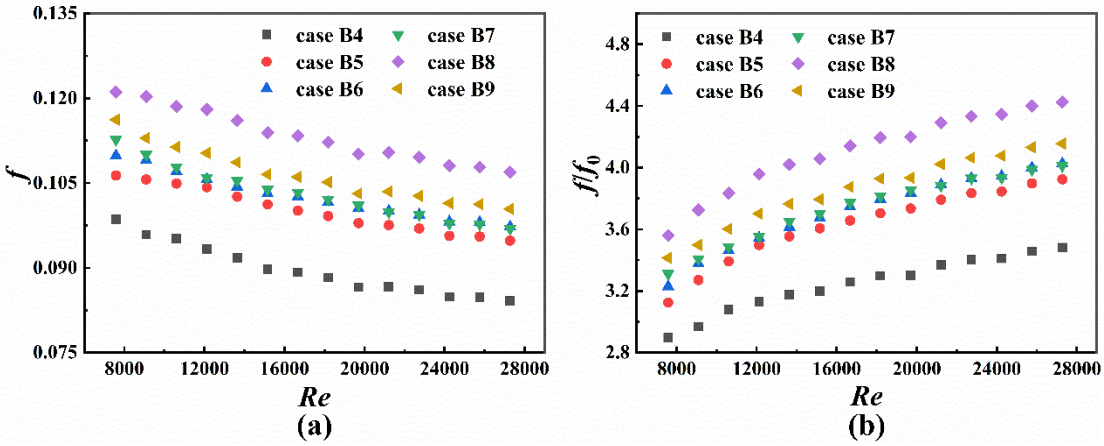

Figure 5.9 The effects of different cases on fluid flow for different *Re*: (a) *f*; (b) f/f_0.

Figure 5.10 displays the variations of *TEF* with different *Re* across different cases. As shown in Figure 5.10, case B6 exhibits the highest *TEF* value of 1.51, while case B8 shows the lowest *TEF* value of 1.20. All the *TEF* values exceed 1, which means that the optimized structures have an impact on the overall working performance. When the lift angle is 45 °, the *TEF* values increase with the included angle. The primary reason is that the Nu/Nu_0 and f/f_0 values follow the same variation trend, as shown in Figure 5.8 and Figure 5.9. This indicates that heat transfer and fluid flow in cases with lift angle of 45 ° are primarily affected by the structural disturbance induced by the included angle. However, at 60 ° lift angles, the *TEF* values first decrease and then increase as the included angle rises. Case B8 shows the lowest *TEF* values compared to cases B7 and B9. The increase in lift angles expands the development area of the boundary vortices, thereby adjusting the vortex interaction between the boundary and core vortices. The intensity of flow disturbance increases with lift angle, as shown in Figure 5.5. A significant difference in disturbance uniformity is observed between cases B5 and B8. The overall disturbance uniformity of flow field in case B8 is weaker than that in case B5, indicating that vortex interaction becomes serious as the included angle approaches 90 °, reducing the overall flow field optimization effectiveness. Furthermore, the f/f_0 values in cases B7 - B9 also reflect this trend (Figure 5.9 (b)), further indicating that the flow field in case B8 requires optimization in terms of vortex interaction.

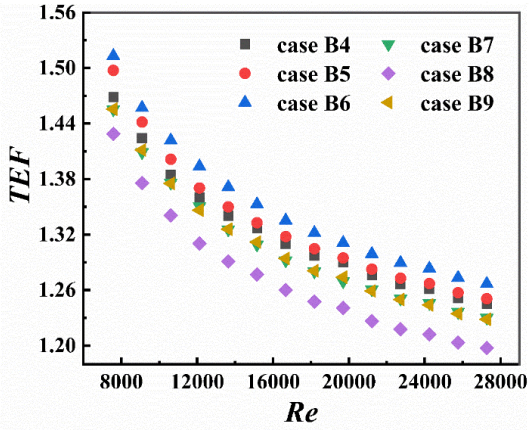

Figure 5.10 The variations of *TEF* with different *Re* across different cases.

5.5 Effect of curved ratio on heat transfer and fluid flow

This section analyzes the effect of curved ratio on velocity magnitude, *TKE*, temperature, and *Se* in various cases. Furthermore, it summarizes the heat transfer and pressure drop characteristics of flow fields induced by modified curved ratio.

Figure 5.11 shows the variations of velocity magnitude in the cross section of z = 290 mm. As the curved ratio increases, the disturbance distribution in the high-speed region shifts toward the boundary layer. The area of the high-speed region decreases significantly in a regional pattern. The reason is that the variations in curved height adjust the region of vortex development, demonstrating that it is more beneficial for heat transfer and fluid flow. Furthermore, the low-speed region decreases as the curved ratio increases. In other words, velocity distribution within the flow field becomes more uniform with increasing curved ratio.

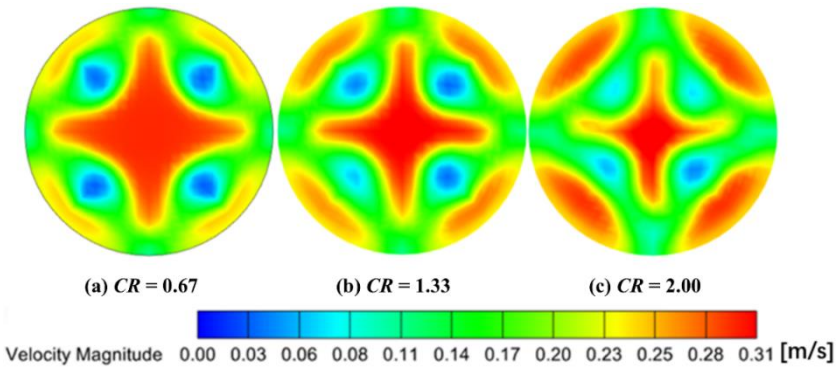

Figure 5.11 The variations of velocity magnitude in cross section of z = 290 mm.

Figure 5.12 shows the *TKE* contours at *Re* = 7577 in different cases. As shown in Figure 5.12, the flow disturbance in the core region strengthens as the curved ratio increases. However, the variation in flow disturbance appears upstream of the tube. For downstream of the tubes, the disturbance intensity does not vary significantly as the curved ratio increases. There is still room for improvement in the adjustment of overall uniformity of the flow disturbance within the flow fields. Increasing the curved ratio can enhance heat transfer. However, it is not beneficial for reducing the flow resistance. The included angles and lift angles are the key affecting factors for improving the flow disturbance. Furthermore, the strongest disturbance region in each case appears near the winglet vortex generators. Creating holes on the winglet vortex generators represents a potential future optimization direction.

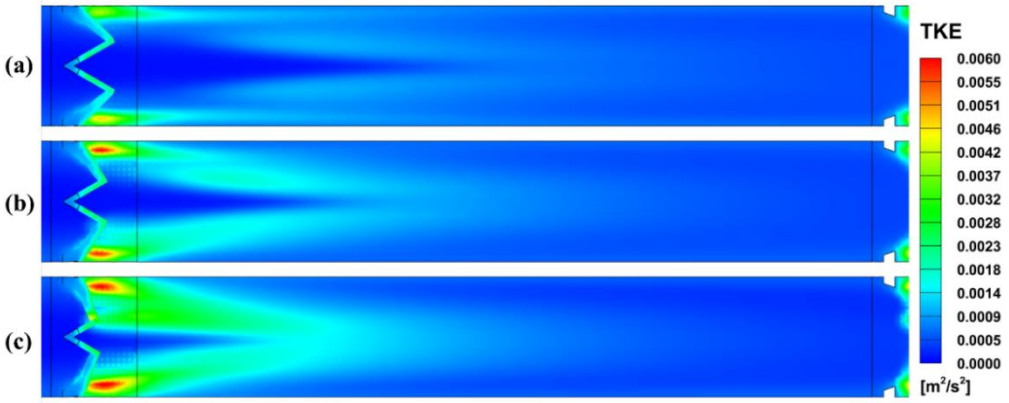

Figure 5.12 *TKE* contours at *Re* = 7577 in different cases: (a) case B1; (b) case B2; (c) case B3.

Figure 5.13 displays the variations of temperature in the cross section of *z* = 290 mm. As shown in Figure 5.13, as the curved ratio increases, the temperature distribution becomes more regionally concentrated, indicating that the heat transfer in local regions is significantly affected by the variations of curved ratio. Furthermore, the intensity of vortex interaction becomes more serious, suggesting that serious vortex interaction affects the development of vortex structures. Furthermore, regional disturbances are detrimental to the uniformity of temperature disturbances.

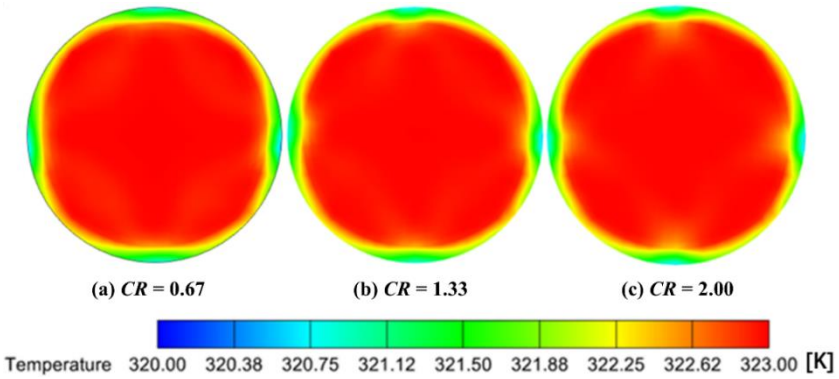

Figure 5.13 The variations of temperature in cross section of z = 290 mm.

Figure 5.14 displays the variation in *Se* axial distribution for different cases and *Re*. As shown in Figure 5.14 (a), the *Se* peak value decreases as *CR* increases due to serious vortex interaction. Furthermore, the increasing trend of *Se* values shows no significant variation among various cases, primarily because vortex interaction also varies gradually. However, after the cross section of z/d_c = 2.00, the variation trend in *Se* values among various cases no longer follows this characteristics pattern concerning vortex interaction variations, as it becomes dependent on the disturbance uniformity of the flow field. Case B3 exhibits the highest *Se* value after the cross section of z/d_c = 2.67. It suggests that large curved ratio is suitable for enhancing the uniformity of flow disturbance downstream of the tubes. As shown in Figure 5.14 (b), the *Se* values increase with increasing *Re* due to stronger power input. Furthermore, as *Re* increases, the variation differences between various cases gradually decreases, indicating that the effect of high-*Re* flow is weaker than low-*Re* effects.

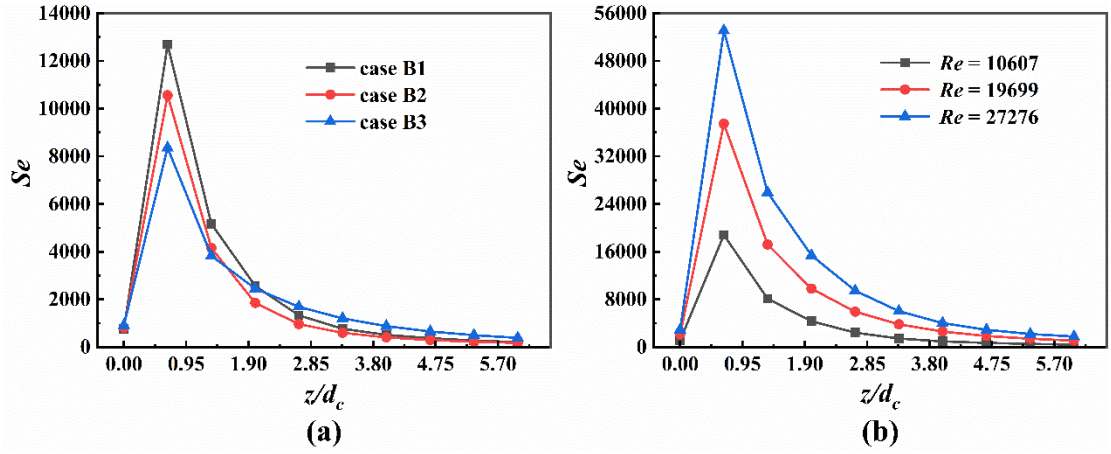

Figure 5.14 Variation in *Se* axial distribution: (a) cases B1 – B3; (b) different *Re* in

cases B1.

Figure 5.15 demonstrates the effects of different cases on heat transfer for different *Re*. As shown in Figure 5.15 (a), case B3 exhibits the highest *Nu* values among various cases. The primary reason is consistent with the analysis in Figure 5.12. Furthermore, serious vortex interactions in case B3 also exhibit significant variations in *Nu* differences among various cases. As shown in Figure 5.15 (b), compared with plain tubes, the *Nu* improvement in case B3 is significant due to serious vortex interaction. Furthermore, *Nu* values of case B2 and B1 is nearly the same, indicating that case B2 has potential for further optimization.

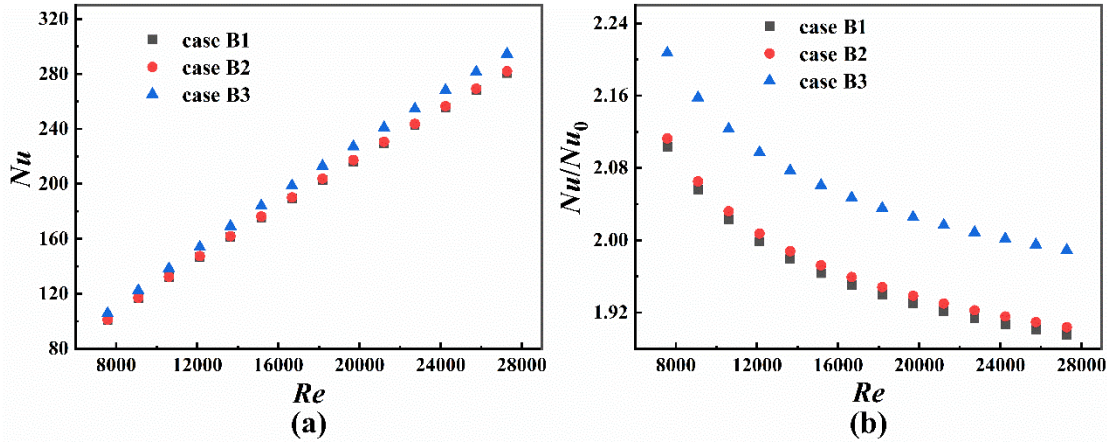

Figure 5.15 The effects of different cases on heat transfer for different *Re*: (a) *Nu*; (b) Nu/Nu_0.

Figure 5.16 shows the effects of different cases on fluid flow for different *Re*. As shown in Figure 5.16 (a), the *f* values increase as *CR* increases due to increased structural resistance. However, the variation trend of *f* differences is not consistent with that of the *Nu* differences, as shown in Figure 5.15. This indicates that flow resistance primarily depends on the blockage structure, while heat transfer depends on the vortex interaction induced by various flow structures. As shown in Figure 5.16 (b), compared with plain tubes, f/f_0 values increase as *Re* increases. However, the increasing trend gradually weakens as the effect of *Re* dominates over structural variables.

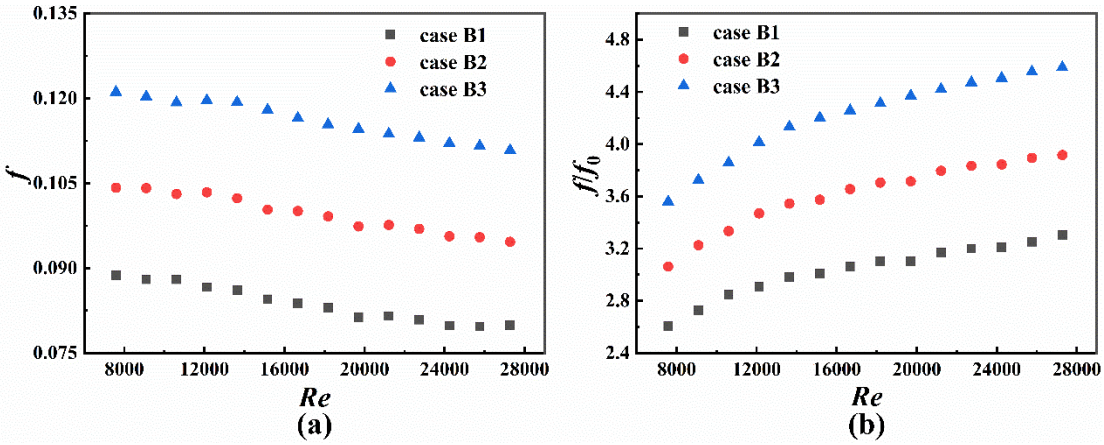

Figure 5.16 The effects of different cases on fluid flow for different *Re*: (a) *f*; (b) *f*/*f*$_0$.

Figure 5.17 displays the variations of *TEF* at different *Re* for different cases. As shown in Figure 5.17, case B1 exhibits the highest *TEF* value of 1.53, while case B3 shows the lowest *TEF* value of 1.20. The variation range of *TEF* is similar to that observed in cases with varying lift angles and included angles, indicating that these structural variables have optimization potential when considering their combined effects. However, the increasing trend for case B2 is weaker than that for case B1. This suggests that the vortex interaction in case B2 requires future optimization.

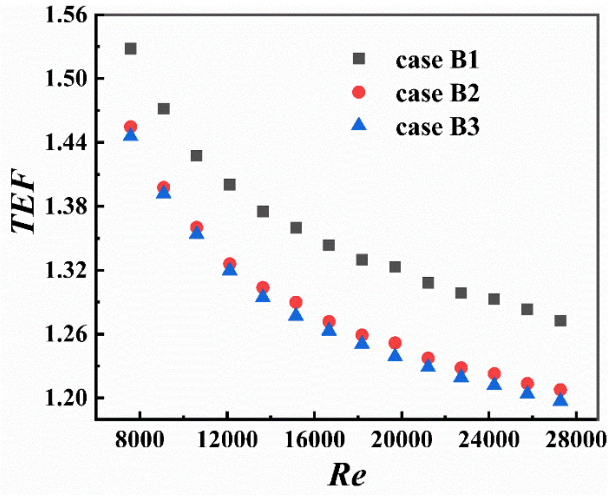

Figure 5.17 The variations of *TEF* with different *Re* across different cases.

5.6 Chapter conclusion

In this chapter, the vortex interaction of boundary vortices is optimized to improve the uniformity of heat transfer and fluid flow in circular tubes. The effects of curved ratio

(*CR*), lift angle (β), and included angle (α_v) on heat transfer and fluid flow are experimentally and numerically investigated for circular tubes with modified winglet designs. Furthermore, the optimization mechanism of flow fields influenced by modified winglet designs is revealed. The key findings from this chapter are as follows:

(1) Compared with the flow fields in case A1, the development region of boundary vortices is enlarged, indicating that the intensity of boundary vortices increases. Furthermore, the core vortices remain largely unaffected by the boundary vortices, and the movement distance of the boundary vortices increases.
(2) When the lift angle is 60 º, the difference between high-disturbance and low-disturbance regions becomes particularly significant, suggesting that further improvements in overall uniformity are possible for this disturbance mode. Establishing a reasonable balance between included angles and lift angles is crucial for adjusting the uniformity of the flow fields.
(3) Increasing the included angle improves the uniformity of the flow fields, while increasing the lift angle enhances the regional disturbance.
(4) As the curved ratio increases, the disturbance distribution in the high-speed regions shifts toward the boundary layer, and velocity distribution within the flow field becomes more uniform with increasing curved ratio.
(5) Case B1 exhibits the highest *TEF* value of 1.53, while case B3 shows the lowest *TEF* value of 1.20. The variation range of *TEF* is similar to that observed in cases with varying lift angles and included angles, indicating that these structural variables have optimization potential when considering their combined effects. Achieving a reasonable balance between uniformity and disturbance is crucial for the optimization of the flow field within circular tubes.

Chapter 6: Heat transfer and fluid flow analysis in annular tubes with traditional delta winglets

6.1 Introduction

This chapter aims to explore the vortex interaction and the wall limitation, thereby providing valuable guidance for efficient winglet applications in annular tubes. Furthermore, the cases studied in this chapter serve as the comparative cases for the applications of novel self-join winglets in annular tubes. Consequently, numerical simulations and experimental measurements are conducted to investigate fluid flow and heat transfer within annular tubes fitted with delta winglets. Specifically, the present work consists of three parts: (i) analyzing the effect of delta winglets on pressure drop and heat transfer characteristics within annular tubes across a *Re* range of 2304–7488, (ii) exploring the flow mechanism within annular tubes influenced by different winglet structures, and (iii) revealing the variation mechanism of flow disturbance and turbulent dissipation within annular tubes equipped with delta winglets based on energy variations.

6.2 Physical model

Winglet models are designed in a delta shape for superior performance [78, 122, 173]. For easier installation, delta winglets are combined with circular rings using 3D printing techniques with polylactic acid. The specifications of physical models are given in Table 6.1. Figure 6.1 shows the details of winglet configurations in various views. The research variables include attack angle (α = 30 º, 45 º, and 60 º), blockage ratio ($BR = H/d_c$ = 0.20, 0.30, and 0.40), configuration (parallel and V-shaped type), and flow direction (upstream and downstream). Regarding the rationale for parameter selection in this chapter, because winglet applications in annular tubes have rarely been studied, the parameters and their value ranges are based on previous studies of winglets in circular tubes. The aim is to explore the vortex interaction and the wall limitation, thereby providing valuable guidance for efficient winglet applications in annular tubes.

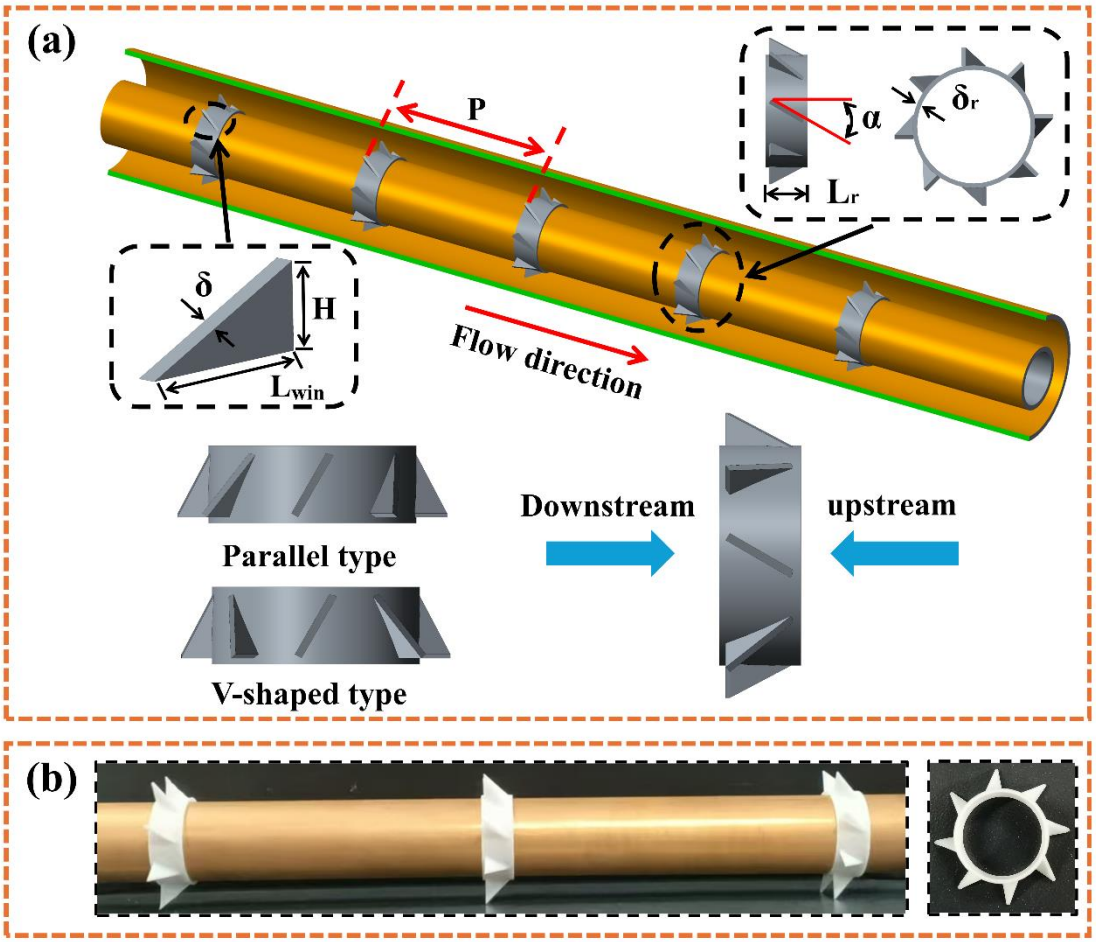

Figure 6.1 Schematic diagram: (a) the details of winglet arrangements and structures; (b) real photographs of tubes with winglet vortex generators.

Table 6.1 Specification of the physical model.

Specification	Dimension
Outer diameter of inner tubes	25 mm
Inner diameter of outer tubes	46 mm
Thickness of inner and outer tubes	2 mm
Characteristics diameter (d_c)	21 mm
Attack angle (α)	30 º, 45 º, 60 º
Winglet height (H)	4.2 mm, 6.3 mm, 8.4 mm
Winglet length (L_{win})	9 mm
Winglet thickness (δ)	1 mm
Ring length (L_r)	10 mm

Ring thickness (δ_r)	1 mm
Pitch (P)	120 mm
Case C1	Parallel, downstream, BR = 0.20, α = 30 º
Case C2	Parallel, downstream, BR = 0.20, α = 45 º
Case C3	Parallel, downstream, BR = 0.20, α = 60 º
Case C4	Parallel, downstream, BR = 0.30, α = 30 º
Case C5	Parallel, downstream, BR = 0.40, α = 30 º
Case C6	V-shaped, downstream, BR = 0.20, α = 30 º
Case C7	V-shaped, upstream, BR = 0.20, α = 30 º

6.3 Numerical model verification

6.3.1 Grid independence test

ANSYS ICEM 2022R1 is used to discretize the fluid domain (Figure 6.2). Considering the complexity of the 3D model of the winglet vortex generators, tetrahedron grids are used to discretize the installation region. Furthermore, since the annular channel has a regular geometric structure, hexahedron grids are employed to discretize it, thereby improving calculation accuracy and reducing the number of grids. The contact nodes on both interfaces between the tetrahedron and hexahedron zones are kept as closely aligned as possible. The boundary layer is refined to improve the accuracy of fluid flow and heat transfer calculations. A grid independence test is performed based on this refinement, with a grid growth ratio of 1.2. Details of the 8 grid sets are summarized in Table 6.2. The effect of the grid number on overall Nu and f is shown in Figure 6.3. When the grid number ranges from 2.37 to 2.74 million, the variations in overall f and Nu are 0.20 % and 0.15 %, respectively, representing the smallest variations among all grid ranges. Furthermore, the average Y^+ is less than 1 when the grid number exceeds 2.00 million, as shown in Table 6.2. Thus, considering both calculation accuracy and computational cost, numerical models with 2.37 million grids are chosen for the subsequent work.

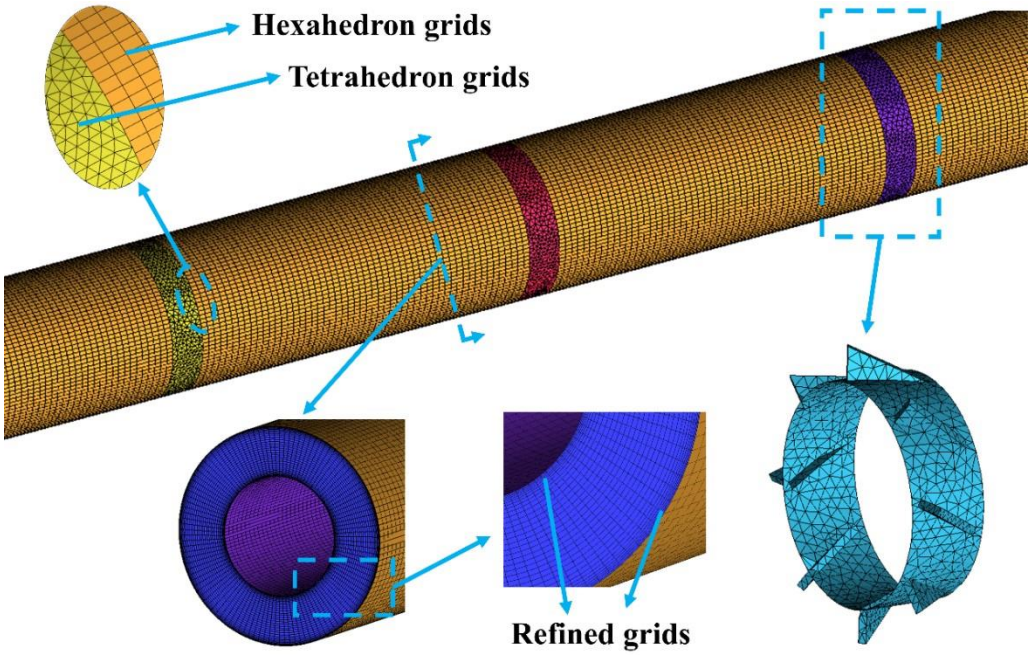

Figure 6.2 Grid generation in the fluid domain.

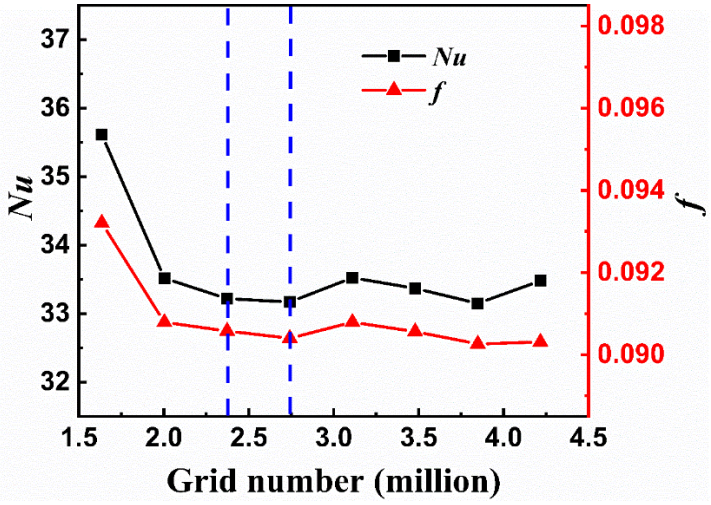

Figure 6.3 Grid independence test for overall *Nu* and *f*.

Table 6.2 Details of grid independence test.

Grid case	1	2	3	4	5	6	7	8
Node number	22	28	34	40	46	52	58	64
Height of first layer grid (mm)	0.5	0.15	0.09	0.03	0.01	2×10^{-3}	4×10^{-4}	8×10^{-5}
Grid number (million)	1.64	2.00	2.37	2.74	3.11	3.48	3.85	4.22

Average Y^+	2.64	0.78	0.47	0.16	0.05	0.01	0.0023	0.00052

6.3.2 Verification of turbulent model

Figure 6.4 displays the validation of the turbulent models for overall *Nu* and *f*. Based on the comparison in Figure 6.4, the maximum deviations of overall *Nu* (*f*) are 5.16 % (3.36 %), 12.07 % (3.40 %), 12.13 % (3.42 %), 5.33 % (7.10 %), and 15.25 % (13.51 %) for RNG k-ε, Standard k-ε, Realizable k-ε, Reynolds stress, and SST k-ω models, respectively. The RNG k-ε model exhibits the highest accuracy among the evaluated turbulent models. Consequently, the RNG k-ε model is adopted for subsequent work.

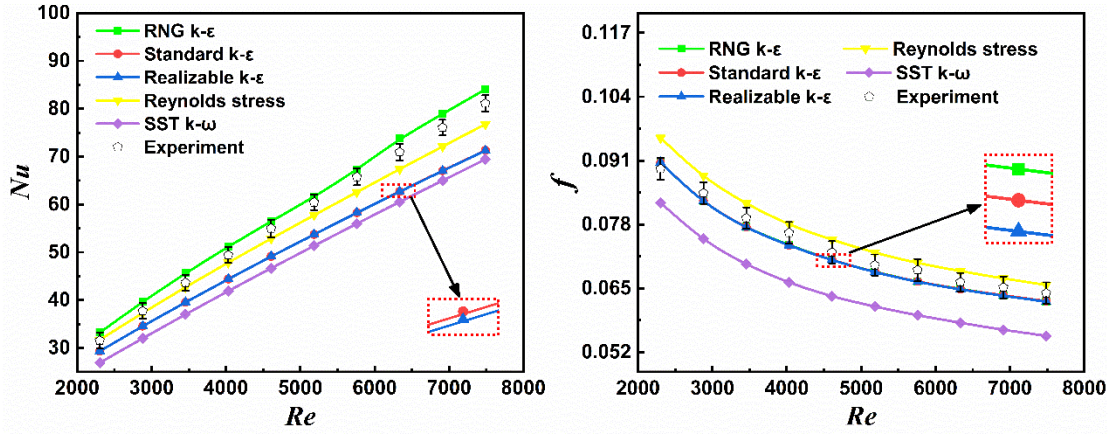

Figure 6.4 Verification of turbulent model for overall *Nu* and *f*.

6.4 Flow field analysis

This section analyzes the variations of vortex structures, velocity magnitude and *TKE* contours, and the axial distribution of *Se* in various cases, aiming to understand the effect of vortex interaction on fluid flows.

Figure 6.5 displays various cross sections used in Chapters 6 and 7. At z/d_c = 0, the cross-section is located at the inlet of the first vortex generator. The streamlines for cases C1 and C6 at various cross-sections are illustrated in Figure 6.6 (a). As shown in case C1 in Figure 6.6 (a), vortices initially form near the inner tube and gradually move away from it, eventually dissipating near the outer tube. This behavior contrasts with previous results [109, 111], suggesting that the radial movement of vortices is primarily

influenced by the installed location of winglets. In case C6, as shown in Figure 6.6 (a), vortices also form near the inner tube. However, a significant difference is the emergence of a stable vortex structure, where vortex pairs do not completely dissipate near the outer tube. This indicates that the vortex interaction induced by V-shaped winglet pairs sustains stable vortex structures movement downstream, which enhances downstream heat transfer and fluid mixing. Therefore, arrangement variables are more effective than structure variables in sustaining stable vortex interactions and flow structures along annular tubes.

The Q-criterion can provide a clear, threshold-based visualization of vortex cores, allows for quantitative comparison of vortex intensity across configurations. By examining the iso-surfaces of a positive Q-value, we can directly observe and measure the variation of longitudinal vortex cores. To identify the vortex core in the flow field, the Q-criterion [66, 78] is introduced using the following equation,

$$Q = 0.5 \times (\|\Omega\|^2 - \|S\|^2) \qquad (6.1)$$

where Ω and S are the antisymmetric and symmetric parts of the second invariant of the velocity gradient tensor, respectively. Physically, a region with Q > 0 indicates where the local rotation rate dominates the strain rate, effectively highlighting vortex cores.

Figure 6.6 (b) demonstrates the iso-surface of the Q criterion [66, 78] overlapped with velocity magnitude contours. Compared with case C1, case C6 exhibits a larger vortex core region under the same Q criterion value. The maximum velocity magnitude within vortex generators is 0.14 m/s, while that behind the vortex generators is in the range of 0.10 - 0.13 m/s. It can be seen that the vortex core in case C6 has higher efficiency in sustaining more disturbance energy. Furthermore, the vortex cores in case C6 remain in a stable state along the tubes. However, the vortex intensity along the tubes in case C1 gradually decreases due to weak vortex interactions. The combination of a large vortex core region and stable vortex interactions have a significant effect on enhancing heat transfer and flow disturbance in flow systems.

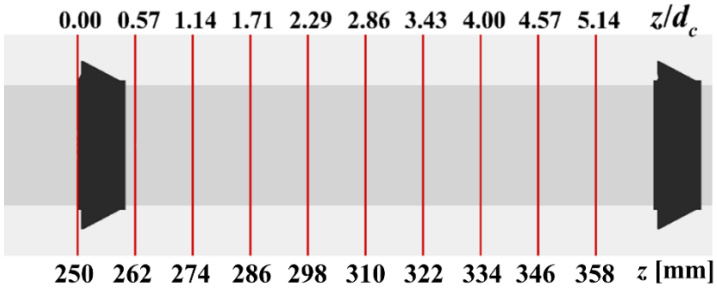

Figure 6.5 Cross sections at different locations.

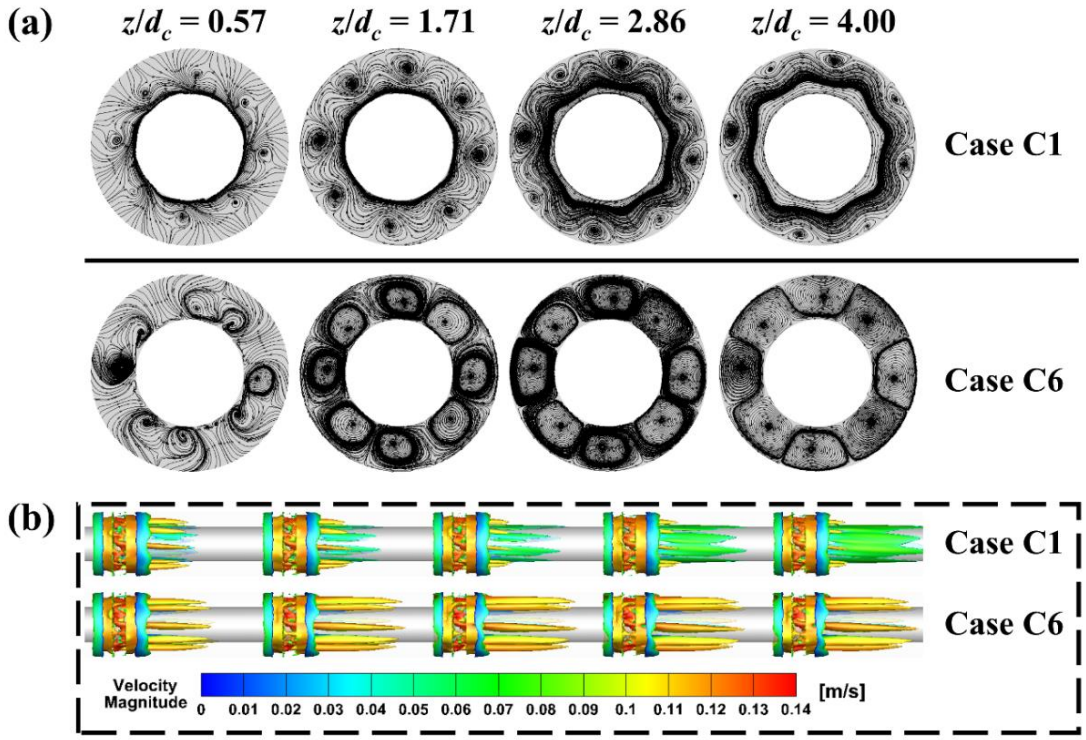

Figure 6.6 Vortex structures for cases C1 and C6: (a) streamlines at different cross sections; (b) iso-surface of Q criterion overlapped with velocity magnitude contours. ($Q = 2/s^2$, $Re = 2304$)

Figure 6.7 displays the streamlines at the cross-section located at $z/d_c = 2.29$ for various cases. With increasing α, vortex intensity increases owing to the expanded transverse projected region of winglets. However, the overall blockage volume of the flow channel remains unchanged, so the development space for vortices is not significantly affected. In contrast, as *BR* increases, the dissipating rate rises due to the growing blockage volume in the flow region. When *BR* reaches 0.40, the downstream vortices almost completely integrate, suggesting that vortex interaction and fluid mixing are adversely

affected when *BR* exceeds 0.30. Vortex interaction is a key factor in maintaining a stable vortex structure, as shown in Figure 6.7 for case C6 and C7. However, the disturbance of vortex pairs in downstream cases are more concentrated than those in upstream cases, suggesting more efficient and balanced vortex interaction in case C7 compared to case C6. In both cases, a stable vortex structure is maintained downstream, which contrasts with the analysis in circular tubes equipped with winglet pairs *[120]*. In annular channels, vortices do not merge into a large vortex, primarily because the annular geometry limits the further expansion of vortex pairs, allowing them to move downstream for longer distances. Furthermore, up-wash flows form toward the inner tube wall between two vortex pairs, while down-wash flows form away from the inner tube wall within a single vortex pair. For the inner tube wall as a heat transfer surface, up-wash flows primarily enhance heat transfer, while down-wash flows primarily promote fluid mixing.

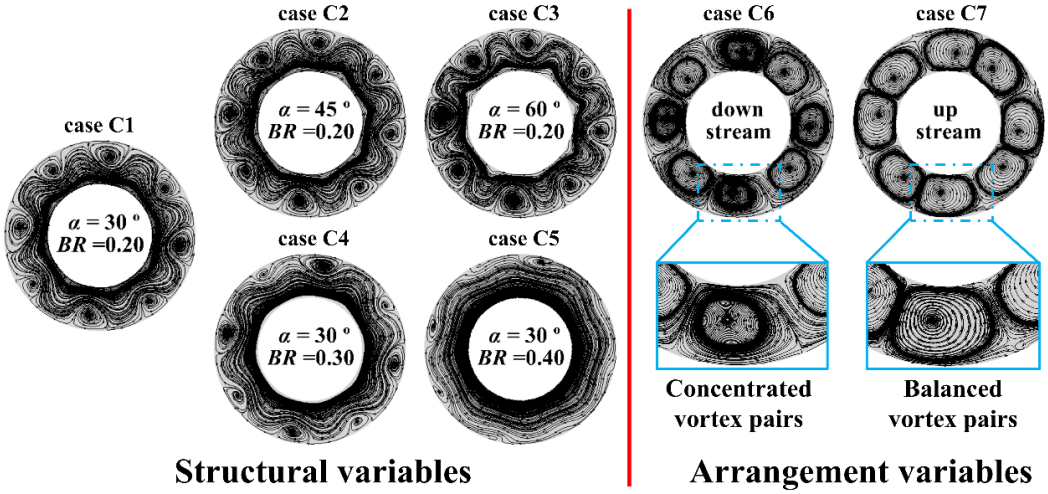

Figure 6.7 Streamlines at the cross-section located at z/d_c = 2.29 for various cases.

The contours of *TKE* for various cases are depicted in Figure 6.8. In longitudinal sections, *TKE* increases with α due to greater disturbance caused by the expanded transverse projected region of winglets. Furthermore, a significant enhancement region appears behind winglet vortex generators, where vortices initially form but have not yet reached their most stable structure, as shown at z/d_c = 0.57 for case C1 in Figure 6.6 (a). Downstream, *TKE* gradually decreases and becomes more uniform as the vortex structure stabilizes. In the cross sections at z/d_c = 0.57, *TKE* near the inner tube wall

gradually enhances from case C1 to C3. However, this strong-disturbance region does not expand significantly in the radial direction, confirming that winglet height plays a crucial role in *TKE* distribution in this region, as shown in Figure 6.8 (cases C4 and C5). As *BR* increases, *TKE* near the inner tube wall also enhances. Moreover, the expansion of *TKE* distribution region in the radial direction is more significant than in cases with increasing α. However, when *BR* reaches 0.30, the radial distribution of *TKE* is already close to the outer tube wall. With further increases in *BR*, *TKE* primarily exhibits significant intensification. Therefore, when *BR* is between 0.20 and 0.30, the distribution of disturbance regions within annular tube is more balanced, consistent with the analysis shown in Figure 6.7 for cases with increasing *BR*. This balanced distribution is beneficial for vortex interaction and fluid mixing. In longitudinal sections, the enhancement of *TKE* with increasing *BR* is less significant than with increasing α, particularly in the disturbance region behind winglets. This is primarily due to serious vortex interactions, which limit further vortex development.

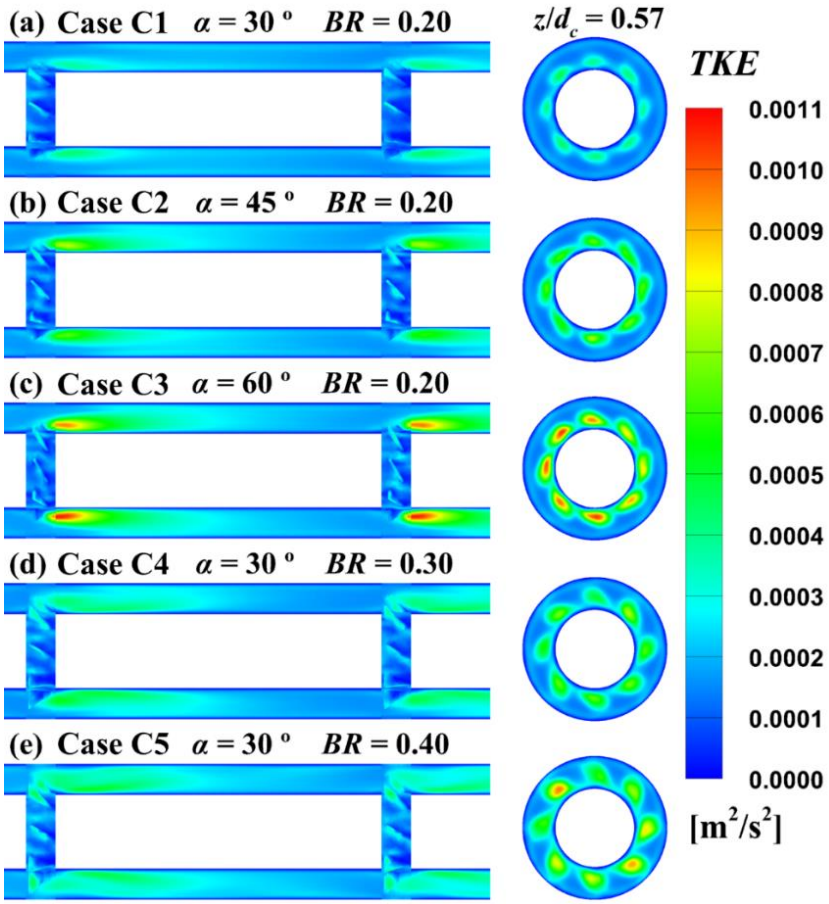

Figure 6.8 The contours of *TKE* at *Re* = 2304 for various cases.

Figure 6.9 displays 3D streamlines with velocity magnitude and *TKE* contours for cases C1, C6, and C7. Compared to cases C6 and C7, the high-*TKE* distribution in case C1 is more uniform due to weaker vortex interaction. As shown in the 3D streamlines in Figure 6.9 (a), adjacent vortices exhibit weak interactions, resulting in a significant velocity gradient within annular tubes, which is unfavorable for fluid mixing. Compared to cases C1 and C6, the velocity distribution in case C7 is entirely regionalized. However, the *TKE* distributions in cases C6 and C7 are both divided into four strong disturbance regions. This is primarily because the disturbance caused by vortex pairs is more concentrated in case C6 than case C7, as shown in the streamlines in Figure 6.7. The high-speed region in case C6 is less affected by vortex pairs, whereas the stronger vortex interaction in case C7 enhances fluid mixing. Furthermore, the vortex pairs in cases C6 and C7 both form behind CFU configurations, consistent with the flow mechanisms described in previous studies [67, 120]. The first difference between cases C6 and C7 is the interaction distance of vortices, as shown in the 3D streamlines in Figure 6.9 (b) and (c). Clearly, vortex interaction is stronger in case C7. The second difference lies in the area of the disturbance region. In case C7, flows transition from sharp to blunt edges, causing the disturbance to extend radially with increasing winglet height. In contrast, in case C6, flows pass from blunt to sharp edges, resulting in more concentrated disturbance. This flow mechanism explains why vortex pairs in case C6 are more concentrated than case C7, as shown in Figure 6.7.

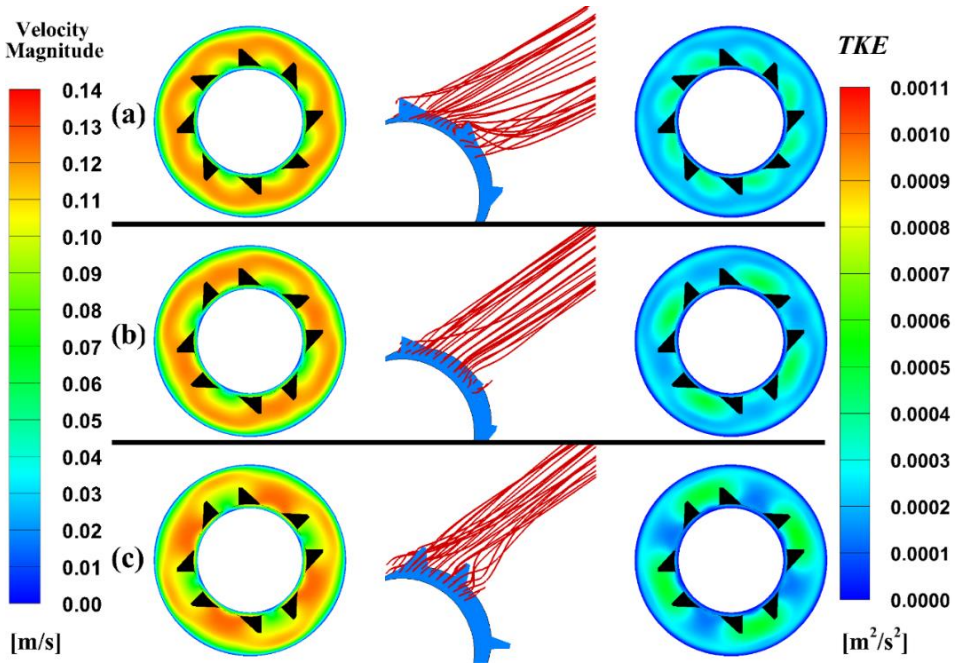

Figure 6.9 3D streamlines with velocity magnitude and *TKE* contours at z/d_c = 1.71 in different cases: (a) case C1; (b) case C6; (c) case C7.

Figure 6.10 (a) presents the variation in *Se* axial distribution at *Re* = 2304 for various cases. In the region of z/d_c = 0 - 0.57, the fluid flows pass through the vortex generators. Since the vortices have not yet fully formed, the *Se* values in this region are primarily influenced by structural blockage. Consequently, *Se* values in cases C4 and C5 are higher than in other cases due to the increased volume blockage of flow channels. However, at z/d_c = 0, *Se* decreases with increasing α, as higher α results in the winglet structure being located further from the cross-section z/d_c = 0. This trend reverses at z/d_c = 0.57 due to the increased transverse blockage caused by higher α. Furthermore, the correlation of *Se* values between case C1 and C6 in this region support this explanation, as they share the same α, *BR*, and flow direction. In this region, due to radially expanding disturbances, the variations in *Se* values for case C7 are the most significant among cases with the same winglet size. For all cases, the peak *Se* value occurs at z/d_c = 0.57, where vortices initially form. As the vortex dissipates, *Se* values decrease. Notably, the downward trends for cases C6 and C7 are more gradual than for other cases from z/d_c = 0.57 to 2.29. Furthermore, from z/d_c = 1.71 to 5.14, *Se* values in cases C6 and C7 are consistently higher than in cases C1, C2, and C3 for the same

winglet size. This indicates that strong vortex interactions provide sufficient vortex intensity to maintain vortex pairs movement downstream in cases C6 and C7. Compared to case C6, *Se* values in case C7 are higher in the region behind vortex generators, particularly from z/d_c = 0.57 to 2.29, confirming the analysis in Figure 6.7 and Figure 6.9. Although case C5 exhibits the highest *Se* values among all cases due to increased volume blockage, cases C6 and C7 are recommended for fluid mixing and heat transfer due to their stable vortex structures. Compared to cases with increasing α, the variation trends of *Se* in cases with increasing *BR* are more significant due to serious vortex interaction, as shown in Figure 6.7. When *BR* increases to 0.30 and 0.40, the growth rates of the peak *Se* values are 67 % and 28 %, respectively. Thus, the positive effect of further increasing *BR* diminishes significantly when *BR* exceeds 0.30. In contrast, the variation trends of *Se* in cases with increasing α are minimal from z/d_c = 1.71 to 5.14, primarily because the development space for vortices is not significantly affected, as shown in Figure 6.7. Consequently, the variations in vortex interaction caused by increasing α are also minor in this region compared to other cases. The only notable difference in this region is that *Se* values decrease as α increases, as larger α induces stronger vortex interactions. The turning point for the positive effect of increasing α occurs at z/d_c = 1.71, suggesting the potential for future optimization of winglet structure design. Figure 6.10 (b) shows the variation in *Se* axial distribution at different *Re*. With the increase in *Re*, the difference between structural and arrangement variables is not significant within the range of z/d_c = 0 - 1.14. Near the cross-section at z/d_c = 1.14, the vortices begin to reach a stable state. This proves that, in the absence of stable vortex disturbance, the *Se* difference is primarily affected by structural blockage. However, in the downstream region starting from z/d_c = 1.14, as *Re* increases from 2880 to 7488, the *Se* difference between case C1 and case C6 increases significantly. This suggests that the disturbance effect caused by the increasing *Re* has a significant influence on enhancing the effect of vortex interaction.

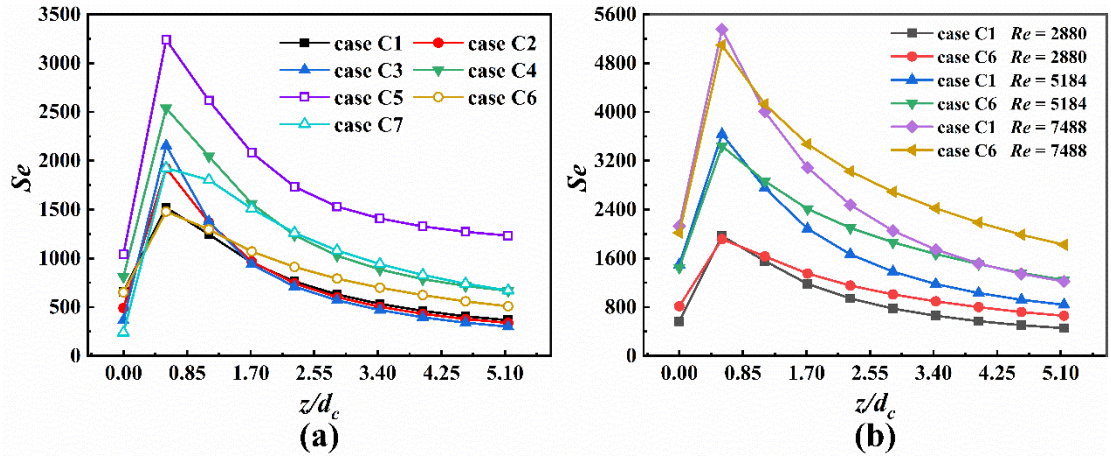

Figure 6.10 Variation in *Se* axial distribution: (a) various cases (b) different *Re*.

6.5 Thermal field analysis

This section analyzes temperature contours and the axial distribution of the local surface *Nu* in various cases, aiming to understand the effect of vortex interaction on heat transfer.

The temperature contours in various cross sections for cases C1 and C6 are shown in Figure 6.11. The high-temperature region extends radially along the tube in case C1, whereas in case C6, it extends regionally. This difference is primarily due to the stable vortex structure in case C6, which enhances fluid mixing and heat transfer. Notably, the temperature near the outer boundary layer increases from 300.0 K to 300.5 K in case C1, compared to an increase from 300.0 K to 301.0 K in case C6. The regional distribution in case C6 enhances energy transfer intensity, reducing the local temperature gradient. Furthermore, the temperature range in the core region is 300.5 - 301.5 K for case C1, and 300.5 K - 303 K for case C6, demonstrating that the overall heat transfer intensity in case C6 is stronger than in case C1.

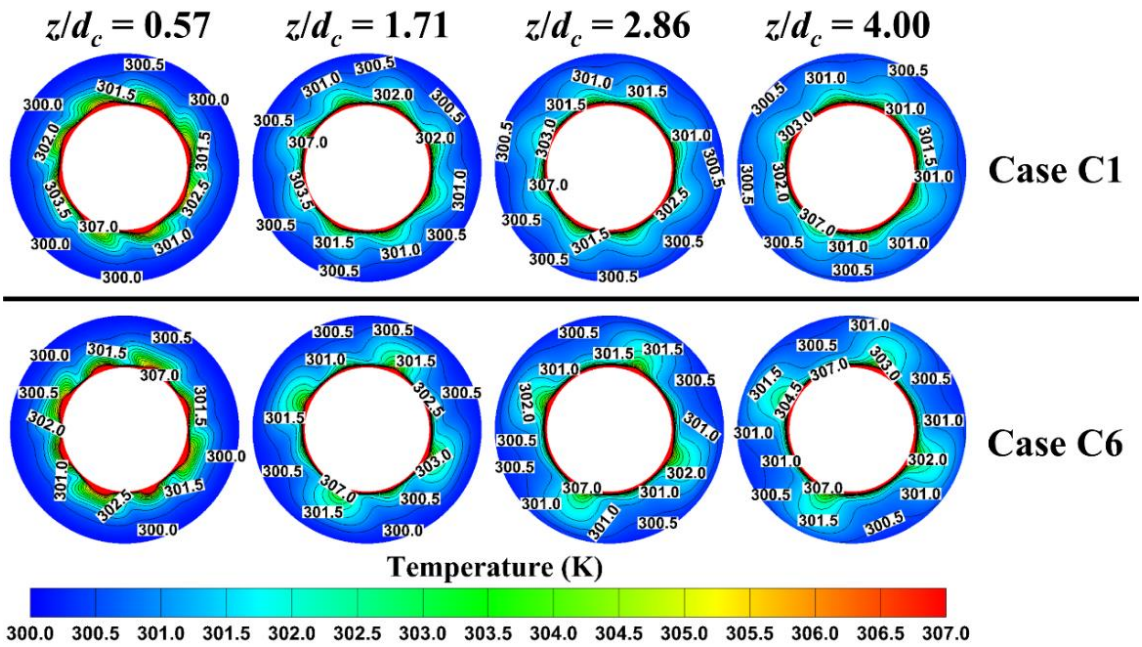

Figure 6.11 Temperature contours at various cross sections.

Figure 6.12 displays temperature contours at z/d_c = 0.57 for different cases. The cross section of z/d_c = 0.57 is located in the significant disturbance region behind winglets, as shown in Figure 6.8. As α increases, the high-temperature distribution expends radially due to greater disturbance. The temperature range in the core region is 300.5 - 301.5 K for case C1, 300.5 - 302.5 K for case C2, and 300.5 - 303.0 K for case C3, indicating that the temperature variation rate does not increase linearly with α. The optimal α value is between 45 º - 60 º. In contrast, cases with increasing *BR* show no significant variation in the radial expansion of high-temperature distribution regions. However, as *BR* increases, the area of high-temperature distribution near the inner boundary layer gradually increases. The is primarily due to increased overall blockage volume, which limits further radial expansion of high-temperature distribution. The temperature range in the core region is 300.5 - 301.5 K for case C4, and 300.5 - 302.0 K for case C5. In comparison to cases C2 and C3, the temperature range for cases C4 and C5 is reduced due to serious vortex interactions.

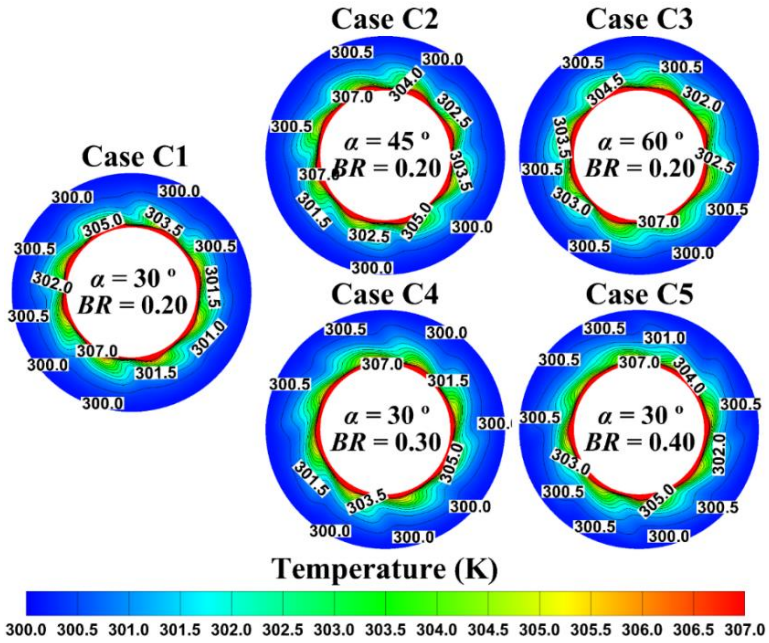

Figure 6.12 Temperature contours at z/d_c = 0.57 for different cases.

Figure 6.13 shows the contours of surface local *Nu* for cases C1, C6, and C7. The local surface *Nu* values in the strong-disturbance region for cases C6 and C7 range from 71 to 90, which is 1.22 - 1.27 times higher than those in case C1. Furthermore, the area of high local surface *Nu* in cases C6 and C7 is larger than in case C1, demonstrating that the impacting up-wash flows induced by arrangement variations enhance fluid mixing and heat transfer, consistent with the conclusions in Figure 6.7. Vortex interaction is the primary factor optimizing vortex disturbance. However, a significant limitation is that the disturbance intensity in the non-impacting regions for cases C6 and C7 is weaker than in case C1, as the surface local *Nu* in these regions is 0.73 - 0.81 times that of case C1. This suggests that further optimization in these non-impacting regions for cases C6 and C7 is required. Compared to case C6, the strong-disturbance region behind the winglet pairs in case C7 is larger and merges into a single region due to closer adjacent vortex pairs, as shown in Figure 6.7. Furthermore, in case C7, a smaller high-disturbance region appears between adjacent high-disturbance regions, with a maximum local *Nu* value of 58, which is 1.81 and 2.23 times higher than in cases C6 and C1, respectively. This enhancement is primarily attributed to stronger vortex interaction in case C7, as shown in the 3D streamlines Figure 6.9 (c). Expanding this

region is crucial for improving heat transfer in non-impacting regions.

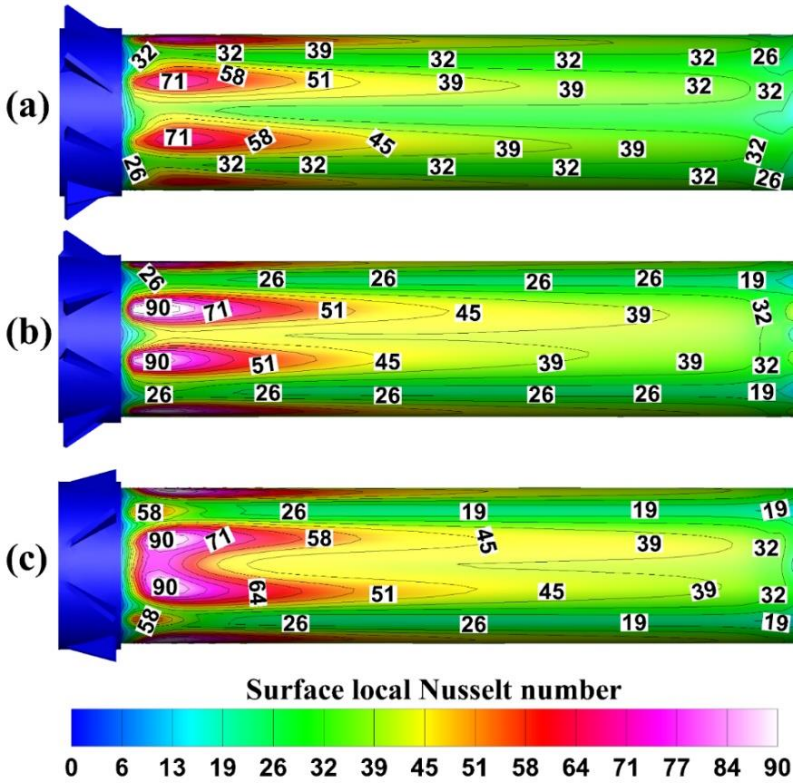

Figure 6.13 The contours of surface local Nusselt number in different cases: (a) case C1; (b) case C6; (c) case C7.

6.6 Flow and thermal characteristics analysis

This section analyzes the variations of Nu, Nu/Nu_0, f, f/f_0, and TEF in various cases at different Re values, aiming to summarize the heat transfer and pressure drop characteristics of flow fields.

Figure 6.14 (a) shows the influence of various cases on Nu at different Re. As Re increases, Nu increases due to stronger flow disturbance. Furthermore, the difference between arrangement cases and case C1 increases more significantly than that between structural cases and case C1 with increasing Re, primarily due to the positive effects of vortex disturbance and stable vortex interactions. For heat transfer induced by structural variations, limitations in winglet size and tube diameter ratio also contribute to the smaller differences. Case C7 exhibits the highest Nu values due to more balanced vortex interactions compared to other cases. The Nu values in cases C4 and C5 are lower than

in cases C2 and C3, consistent with the analysis in Figure 6.12. Significant vortex structure breakdown in cases C4 and C5 weakens radial heat transfer, negatively impacting overall heat transfer in the flow field. Figure 6.14 (b) illustrates the influence of various cases on Nu/Nu_0 at different *Re*. *Nu* increases by 1.27 - 2.15 times compared to plain tubes. The Nu/Nu_0 values in cases C2 and C3 rise to 103.1 % and 105.0 % of case C1, respectively, while in cases C4 and C5, they rise to 101.4 % and 102.7 % of case C1, respectively, demonstrating that the positive effect on heat transfer from increasing *BR* is weaker than that from increasing α. Furthermore, the Nu/Nu_0 values in cases C6 and C7 increase to 108.7 % and 112.2 % of case C1, respectively, indicating that the vortex interaction has a more significant positive effect than structural disturbance in this work. Nu/Nu_0 decreases nonlinearly with increasing *Re*, consistent with the analysis and conclusions for circular tubes [174].

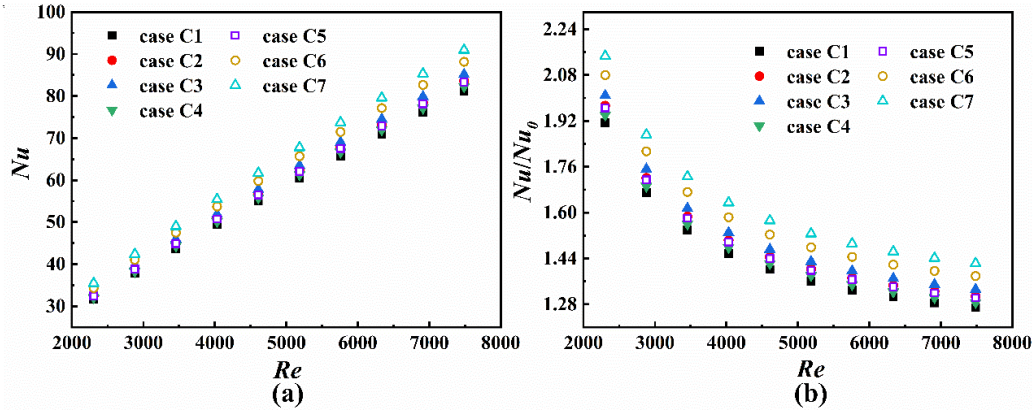

Figure 6.14 Influence of various cases on heat transfer: (a) *Nu* vs. *Re* (b) Nu/Nu_0 vs. *Re*.

Figure 6.15 (a) demonstrates the influence of various cases on *f* at different *Re*. As *Re* increases, *f* decreases due to increased system power. Compared to cases with increasing α, *f* values increase more significantly in cases with increasing *BR*, primarily due to flow channel blockage. The vortex development and fluid flow in cases with increasing *BR* are seriously affected by reduced flow channel volume, leading to higher flow resistance. Among all cases, case C5 demonstrates the highest *f* value, with its nonlinear increase in flow resistance negatively impacting overall system performance. Furthermore, the *f* values for case C6 fall between cases C1 and C2, while those for

case C7 lie between cases C2 and C4, showing lower flow resistance variation due to stable vortex interactions. Case C6 exhibits lower f values than case C7 because its vortex structure is more concentrated, causing weaker flow disturbance. This finding contrasts with previous results within circular tubes [120], Primarily because vortices in case C6 do not merge into a big vortex within annular tubes, avoiding significant pressure drop. Both cases C6 and C7 maintain stable downstream vortex structures, with flow resistance levels being determined by vortex-induced flow disturbances. Figure 6.15 (b) presents the influence of various cases on f/f_0 at different Re. As Re increases, f/f_0 increases, indicating that high Re leads to poorer flow performance compared to plain tubes. The f/f_0 ranges from 1.79 to 1.87 for case C1 and 2.22 to 2.46 for case C5, showing significant flow resistance due to serious vortex interaction. The f/f_0 values for cases C2 and C3 are 104.8 % - 110.2 % and 112.9 % - 121.4 % of case C1, respectively, whereas cases C4 and C5 exhibit higher f/f_0 values of 109.5 % - 116.9 % and 122.6 % - 132.2 % of case C1, confirming that the negative effect of increasing BR on fluid flows is stronger than that of increasing α. The f/f_0 values in cases C6 and C7 increase to 103.2 % - 106.5 % and 108.1 % - 112.0 % of case C1, respectively, suggesting that the negative effect of vortex interaction on fluid flows is not significant, compared with structural disturbance. f increases by 1.79 - 2.46 times compared to plain tubes. Furthermore, f/f_0 reaches 114.4 % - 140.9 % of Nu/Nu_0. This variation trend is optimistic since this trend reported in previous studies [109, 111, 121] is in the range of 90 % - 180.0 %.

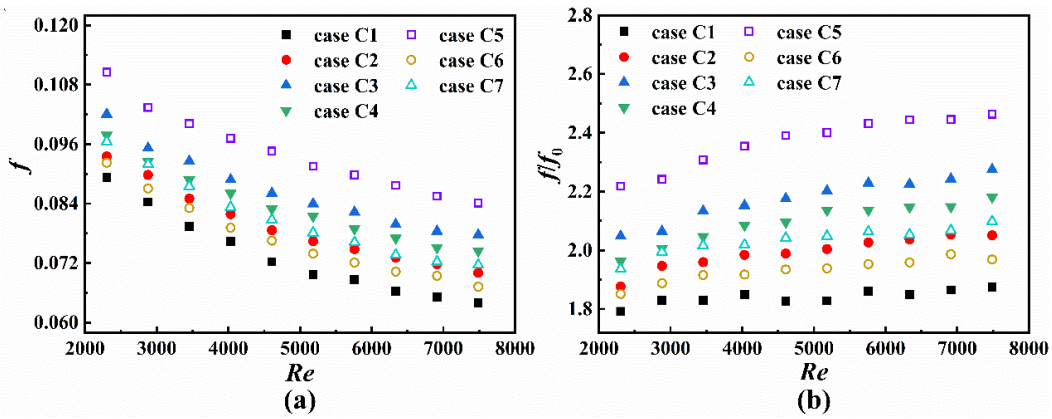

Figure 6.15 Influence of various cases on fluid flow: (a) f vs. Re (b) f/f_0 vs. Re.

As shown in Figure 6.16 (a), the *TEF* demonstrates a decreasing trend with increasing *Re*, as the effect of heat transfer enhancement becomes weaker compared to the effect of increased flow resistance. Arrangement cases exhibit superior *TEF* performance compared to structural cases, attributed to their stable vortex interactions. Furthermore, cases with increasing α achieve higher *TEF* values than those with increasing *BR*, suggesting that the strategy for modifying *BR* is not recommended for heat transfer and fluid flow in annular tubes. When *Re* exceeds 3456, the *TEF* variations with modifying α become insignificant, indicating that the beneficial effect of modifying α is significantly affected by *Re* variations. The design of modifying α demonstrates significant optimization potential. Case C7 achieves the maximum *TEF* of 1.72, while case C5 shows the minimum *TEF* of 0.96. Importantly, 93 % of *TEF* values exceed 1, confirming a well-balanced relationship between heat transfer enhancement and flow resistance increase. Figure 6.16 (b) presents a comparison of *TEF* between the present work and previous studies. The optimal cases from different studies are selected for comparison. In this work, the delta winglets show better performance compared to the helical strip [175] and perforated curve fins [176]. However, the overall performance of angled fins [115], helical surface discs [177], and helical fins with winglets [178] is better than that in this work. While winglets have significant structural advantages in reducing flow resistance, there is still great potential for optimization in heat transfer performance. Among these cases, the *TEF* in the helical surface discs and helical fins with winglets demonstrates a slow decreasing trend with increasing *Re*, which proves that the balance between heat transfer and flow resistance is better than in other cases. These two cases provide valuable references for future optimization.

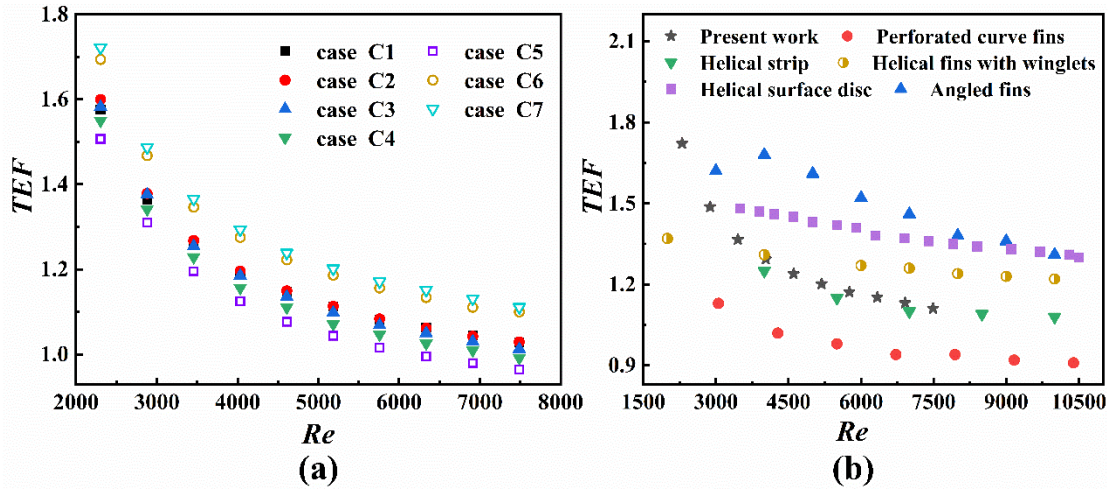

Figure 6.16 Variations of *TEF* with different *Re*: (a) present work (b) previous work.

6.7 Kinetic energy analysis

This section analyzes the energy distribution in various cases, aiming to understand the effect of vortex interaction on *TKE* and ε.

Figure 6.17 (a) presents the *TKE* distributions at z/d_c = 2.29 in the transverse direction at *Re* = 2304. Case C5 demonstrates the highest *TKE* values in the core region among all cases, attributable to serious vortex interactions. The *TKE* values in the core region for case C4 reach 113.1 % - 165.0 % of case C1, while those for case C5 reach 115.0 % - 186.0 % of case C1. When *BR* increases from 0.30 to 0.40, the variation in disturbance intensity in the flow systems is reduced, further confirming that *BR* value is not recommended for exceeding 0.30. Compared to cases with increasing α, cases with increasing *BR* have single-peak trends with peaks near the inner tube wall. This is primarily due to serious vortex interactions near the inner tube wall, as shown in Figure 6.7. Cases C1 and C2 exhibit wavy trends due to vortex disturbance and movement. When α increases to 60 °, the wavy trend gradually transitions to a single-peak trend, indicating that the vortex disturbance is dominant. The *TKE* values in the core region for case C2 reach 108.5 % - 128.6 % of case C1, while those for case C3 reach 113.7 % - 166.1 % of case C1, suggesting that the increase in α significantly enhances the intensity of vortex disturbance. Furthermore, the *TKE* values in the local region for case C6 are higher than those for case C1. This is primarily due to concentrated vortex

structures existing in this local region, as shown in Figure 6.7. These vortex structures are also responsible for the wavy trends in case C6. Therefore, downstream configuration is suitable for enhancing flow disturbance in local regions of annular tubes. In contrast, case C7 exhibits a single-peak trend due to balanced vortex structures. The *TKE* values in the core region for case C6 reach 92.8 % - 112.9 % of case C1, while those for case C7 reach 101.4 % - 144.9 % of case C1. Case C7 demonstrates more significant enhancement in overall system performance compared to case C6. Figure 6.17 (b) shows the ε distributions at $z/d_c = 2.29$ in the transverse direction at $Re = 2304$. All cases exhibit a two-peak trend with peaks near the tube walls, primarily due to the interaction between vortices and tube walls. Consequently, turbulent dissipation intensity near the tube walls is stronger than in other regions. For cases C4 and C5, the ε peak values near the inner tube walls are significantly higher than those near the outer tube walls, resulting from serious vortex interactions, consistent with the analysis in Figure 6.17 (a). The ε peak values for case C4 exceed those for case C5, since case C5 exhibits stronger flow disturbance intensity than case C4. Compared to cases C4 and C5, other cases show insignificant differences in ε peak values between inner and outer wall regions, indicating that flow disturbance and vortex interaction effects remain within reasonable ranges. In the core region, the dissipation intensity level among all cases mirrors the disturbance intensity level, resulting from the dynamic balance between flow disturbance and turbulent dissipation. Minimal ε values occur at $x/d_c = 0.86$ (core region center), confirming reasonable ε distribution in the core region.

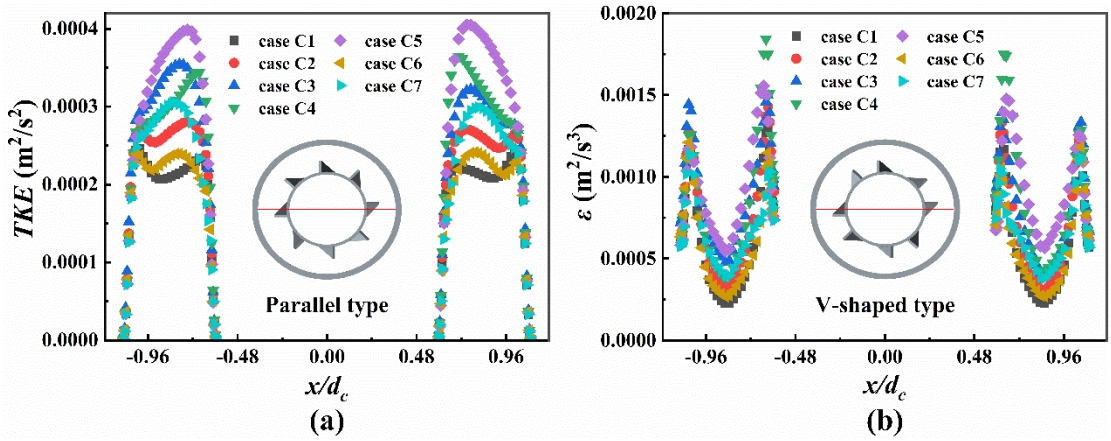

Figure 6.17 Energy distributions at $z/d_c = 2.29$ in the transverse direction at $Re =$

2304: (a) *TKE*; (b) ε.

Figure 6.18 (a) shows the *TKE* distributions in the axial direction at *Re* = 2304. As z/d_c increases, the *TKE* distributions exhibit a trend of first rising and then falling due to vortex generation and dissipation. The *TKE* peak values for cases C4 and C5 occur at z/d_c = 0.67 and 0.57, respectively, while those for other cases appear near z/d_c = 1.10. This indicates that vortices in cases C4 and C5 dissipate earlier, confirming the analysis in Figure 6.7. Case C5 exhibits maximum *TKE* values among all cases due to the most serious vortex interaction. Furthermore, most of the disturbed energy for case C5 is concentrated near z/d_c = 0.57, which is not beneficial for the uniformity of downstream heat transfer and fluid flows. The *TKE* peak value for case C4 reaches 115.1 % and 117.0 % of cases C3 and C7, respectively, suggesting that cases C3 and C7 can serve as alternative strategies to case C4 regarding flow disturbance. This also highlights the significant effect of vortex interaction in case C7 on flow disturbance. The *TKE* peak value for case C3 reaches 189.2 % of case C1, while that for case C2 reaches 132.1 % of case C1. When α increases to 60 º, the increasing trend of *TKE* in the axial direction approaches that in the transverse direction, as shown in Figure 6.17 (a). This indicates that the disturbance stability induced by increasing α is consistent in both transverse and axial spatial dimensions. Compared to case C1, case C6 demonstrates an insignificant enhancement of *TKE* in local regions along the axial direction, primarily due to weakened vortex interaction caused by concentrated vortex structures. Furthermore, The *TKE* peak value for case C7 reaches 165.9 % of case C6, confirming that optimized vortex interaction significantly influences flow disturbance. Figure 6.18 (b) displays the ε distributions in the axial direction at *Re* = 2304. The local figure primarily shows the ε distributions downstream of the winglet vortex generators. Cases C4 and C5 exhibit particularly significant ε variations between z/d_c = 0 and 0.48 (the vortex generator installation region), indicating that the reduction in flow channel volume seriously influences ε values. As z/d_c increases, the ε variation trends for all cases mirror the *TKE* variation trends observed in Figure 6.18 (a) after the fluid flows pass the vortex generators. This demonstrates the dynamic balance in the longitudinal

dimension between flow disturbance and turbulent dissipation.

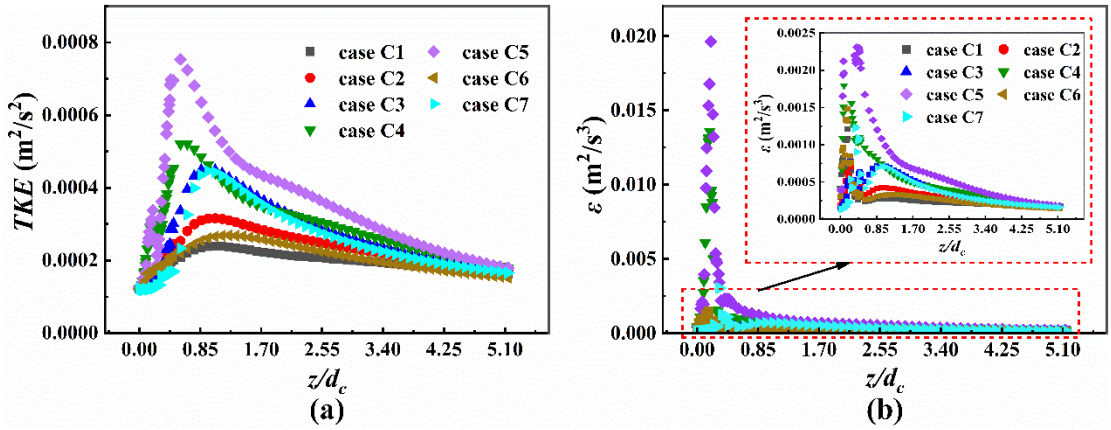

Figure 6.18 Energy distributions in the axial direction at Re = 2304: (a) *TKE*; (b) ε.

Figure 6.19 (a) shows the *TKE* distributions in the axial direction at different *Re*. In the region of z/d_c = 0 - 0.48, the *TKE* peak value for case C1 at *Re* = 5184 reaches 348.9 % of that at *Re* = 2880, while the value at *Re* = 7488 reaches 724.7 % of that at *Re* = 2880, demonstrating that increasing *Re* significantly enhances disturbance energy input. Cases C1 and C6 exhibit similar *TKE* values in the region of z/d_c = 0 - 0.48, indicating that flow disturbance differences are primarily influenced by structural blockage prior to vortex generation, in agreement with the analysis in Figure 6.10 (a). However, the increase in *Re* amplifies the flow disturbance difference downstream of the vortex generators, demonstrating that increased *Re* strengthens vortex interactions within annular tubes. Furthermore, downstream the vortex generators, the *TKE* peak value for case C1 at *Re* = 5184 reaches 329.3 % of that at *Re* = 2880, while the value at *Re* = 7488 reaches 609.8 % of that at *Re* = 2880. Thus, while flow disturbance remains significantly influenced by the positive effect of increasing *Re* on *TKE* enhancement after vortex generation, this effect is weaker than before vortex generation. This weaking primarily results from vortex interaction and dissipation occurring downstream the vortex generators. Figure 6.19 (b) displays the ε distributions in the axial direction at different *Re*. Downstream of the vortex generators, the ε differences between cases C1 and C6 mirror their *TKE* differences as shown in Figure 6.19 (a), confirming that increasing *Re* has little effect on the dynamic balance between flow

disturbance and turbulent dissipation. However, from z/d_c = 0 to 0.48, ε values exhibit a single-peak trend that differs from *TKE* variations due to interactions between fluid flows and vortex generators. Furthermore, before vortex generation, the ε peak value for case C1 at *Re* = 5184 reaches 486.4 % of that at *Re* = 2880, while the value at *Re* = 7488 reaches 1300 % of that at *Re* = 2880, demonstrating that increasing *Re* significantly enhances microscopic mixing intensity in this region compared to mesoscopic mixing. The similar ε values observed for cases C1 and C6 before vortex generation further indicate that dissipation differences in this region are also primarily affected by structural blockage.

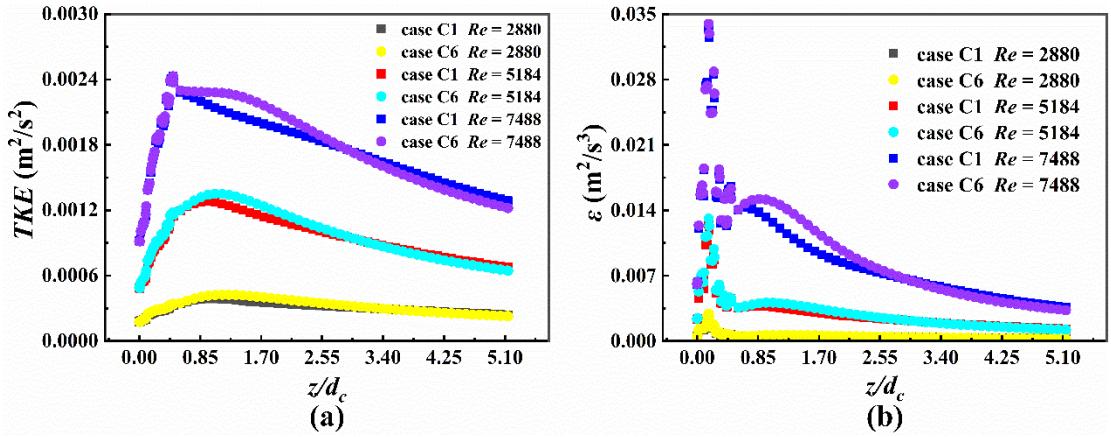

Figure 6.19 Energy distributions in the axial direction at different *Re*: (a) *TKE*; (b) ε.

6.8 Chapter conclusion

In this chapter, delta winglets are installed within annular tubes to explore the flow mechanism. Numerical simulations and experimental verifications are performed to study the influence of attack angle (α), blockage ratio (*BR*), configuration, and flow direction on heat transfer and pressure drop characteristics in annular flow fields with delta winglets. Furthermore, the variation mechanism of flow disturbance and turbulent dissipation within annular tubes equipped with winglets is revealed. The key findings are as follows:

(1) With increasing α, vortex intensity increases owing to the expanded transverse projected region of winglets. In contrast, as *BR* increases, the dissipating rate rises due

to the growing blockage volume in the flow region. Arrangement variables are more effective than structure variables in sustaining stable vortex interactions and flow structures along annular tubes.

(2) Compared to circular tubes, vortices in annular tubes with V-shaped winglet pairs do not merge into a large vortex, primarily because the annular geometry limits the further expansion of vortex pairs, allowing them to move downstream for longer distances. Furthermore, upstream configurations exhibit more efficient and balanced vortex interaction compared to downstream configurations.

(3) The thermal enhancement factor (*TEF*) reaches its maximum value of 1.72 under α = 30 º, *BR* = 0.20 with V-shaped upstream configuration, while the minimum *TEF* reaches 0.96 when α = 30 º, *BR* = 0.40 with parallel downstream configuration. Importantly, 93 % of *TEF* values exceed 1, confirming a well-balanced relationship between heat transfer enhancement and flow resistance increase.

(4) The Nusselt number (*Nu*) and the friction factor (*f*) increase by 1.27 - 2.15 and 1.79 - 2.46 times, respectively, compared to plain annular tubes.

(5) The disturbance stability induced by increasing α is consistent in both transverse and axial spatial dimensions. When *BR* increases from 0.30 to 0.40, the variation in disturbance intensity is reduced, confirming that *BR* value is not recommended for exceeding 0.30. Downstream configuration is suitable for enhancing flow disturbance in local regions of annular tubes, while upstream configuration demonstrates more significant enhancement in overall system performance. Furthermore, increased *Re* strengthens vortex interactions within annular tubes.

Chapter 7: Heat transfer and fluid flow analysis in annular tubes with novel self-join winglets

7.1 Introduction

The boundary vortices induced by novel self-join winglet vortex generators contribute to the uniformity of temperature fields. However, these vortices dissipate faster than core vortices. The wall limitation can serve as a solution to improve the dissipation of boundary vortices. This chapter highlights the superiority of novel self-join winglet vortex generators in optimizing the stability of annular flow fields through a comparison with traditional delta winglets in annular sides and novel self-join winglets in circular sides. It aims to investigate the variation of flow fields induced jointly by boundary vortices and wall limitation, thereby providing valuable guidance for the efficient application of novel self-join winglets in annular sides of heat exchangers. Consequently, the vortex interaction and wall limitation within annular tubes equipped with novel self-join winglets are experimentally and numerically investigated. Specifically, the present work consists of three parts: (i) understanding the combined effect of boundary vortices and annular walls on flow field stability across a *Re* range of 2304–7488, (ii) summarizing the variation characteristics of flow disturbance and heat transfer uniformity within annular tubes influenced by novel self-join winglets, and (iii) obtaining empirical correlations for *Nu* and *f* based on experimental data.

7.2 Physical model

Based on the combined mechanism of boundary vortices and wall limitations, novel self-join winglet vortex generators are applied in annular tubes. Figure 7.1 shows the details of winglet configurations in various views. The specifications of physical models are given in Table 7.1. In this chapter, the structural variables include the blockage ratio ($BR = H/d_c$ = 0.10, 0.15, and 0.20), winglet pairs number (PN = 4, 5, 6), and the included angle (α_v = 60 °, 90 °, and 120 °).

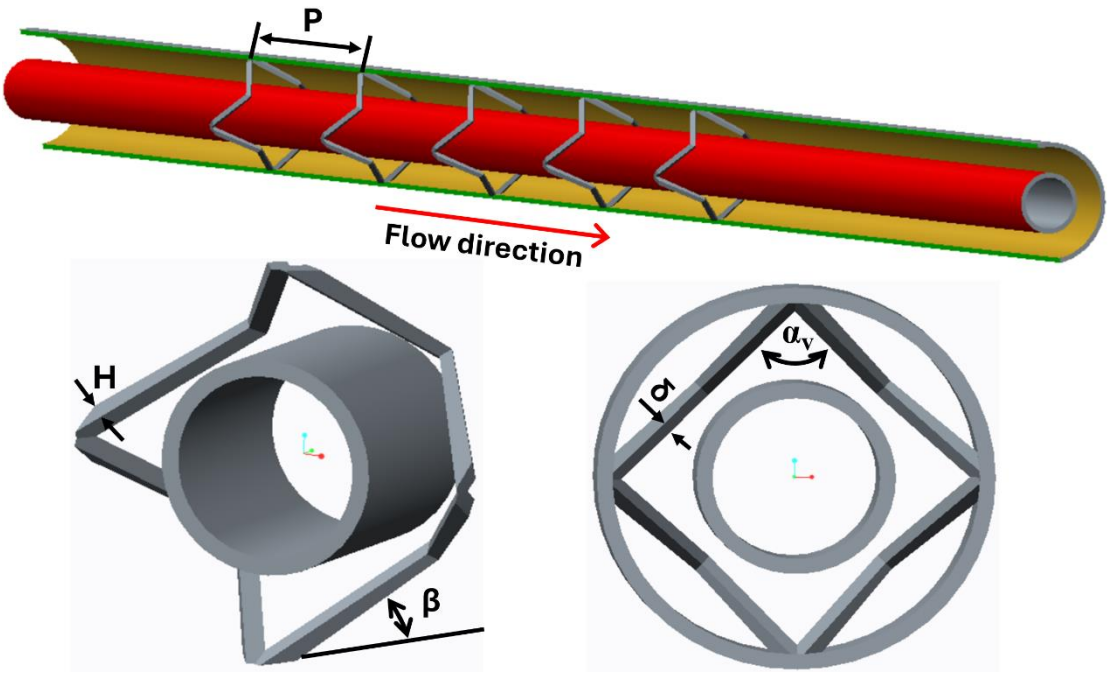

Figure 7.1 The details of winglet configurations in various views.

Table 7.1 The specifications of physical models.

Specification	Dimension
Outer diameter of inner tubes	25 mm
Inner diameter of outer tubes	46 mm
Thickness of inner and outer tubes	2 mm
Characteristics diameter (d_c)	21 mm
Included angle (α_v)	60 °, 90 °, 120 °
Winglet height (H)	2.1 mm, 3.2 mm, 4.2 mm
Winglet thickness (δ)	1 mm
Lift angle (β)	30 °
Pitch (P)	120 mm
Number of winglet vortex generators	5
Case D1	PN = 4, BR = 0.10, α_v = 60 °
Case D2	PN = 4, BR = 0.10, α_v = 90 °
Case D3	PN = 4, BR = 0.10, α_v = 120 °
Case D4	PN = 4, BR = 0.15, α_v = 60 °

Case D5	PN = 4, BR = 0.20, α_v = 60 °
Case D6	PN = 5, BR = 0.10, α_v = 60 °
Case D7	PN = 6, BR = 0.10, α_v = 60 °

7.3 Vortex interactions and wall limitations

This section analyzes the variations of vortex structures, Q criterion contours, and the axial distribution of *Se* in various cases, aiming to understand the combined mechanism of vortex interaction and wall limitations.

Figure 7.2 displays the streamlines at different cross sections for case D1 at Re = 2304. The cross section at z = 250 mm is the beginning of the test section. The flow region is divided into four single parts. As shown in Figure 7.2 (b) - (d), each single part develops two vortex pairs, though these differ from those in circular tubes due to the influence of both inner and outer walls. The size of outer boundary vortex pairs increases with axial distance, while the inner boundary vortex pairs gradually separate under the squeezing force exerted by outer boundary vortex pairs. Eventually, a steady vortex structure forms in the downstream flow field. Compared to circular tubes, the movement distance of boundary vortices increases due to wall limitation. Furthermore, the number of vortex pairs induced by self-join winglets is twice that induced by traditional delta winglets. The flow fields investigated in this chapter significantly demonstrate the combined effect of boundary vortices and wall limitations.

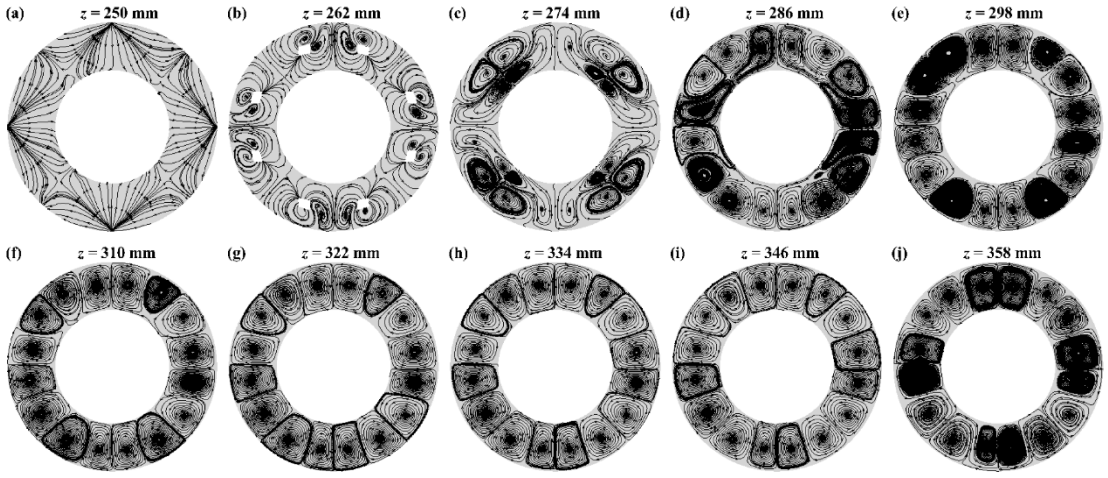

Figure 7.2 Streamlines at different cross sections for case D1 at Re = 2304.

Figure 7.3 shows the streamlines at different cross sections at Re = 2304 for different cases. As shown in Figure 7.3 (a) and (b), as α_v increases, the development space of outer boundary vortices decreases, resulting in an acceleration in the dissipation of the outer boundary vortices. It can be significantly observed that the outer boundary vortices dissipate completely in the downstream flow fields. Furthermore, a larger α_v exhibits stronger inner boundary vortices compared to a smaller α_v. The primary reason is that increasing α_v expands the development space of inner boundary vortices. This indicates that cases of larger α_v are suitable for applications in enhancing vortex disturbance, while cases of smaller α_v are better for improving flow uniformity. However, as shown in Figure 7.3 (c) and (d), the variation mode of vortex pairs remains unchanged as BR increases. Compared to case D1, the advantage in flow uniformity is not significantly affected. It indicates that the effect of increasing BR is primarily on vortex intensity. As show in Figure 7.3 (e) and (f), the number of vortex pairs increases with PN at the cross section of z = 262 mm and 274 mm. However, as PN increases, the dissipation intensity of outer boundary vortices enhances due to the expanded development space of inner boundary vortices. This dissipation mechanism is consistent with that observed in cases of increasing α_v. Furthermore, in the downstream region of the flow fields, the number of vortex pairs equals the number of winglet pairs.

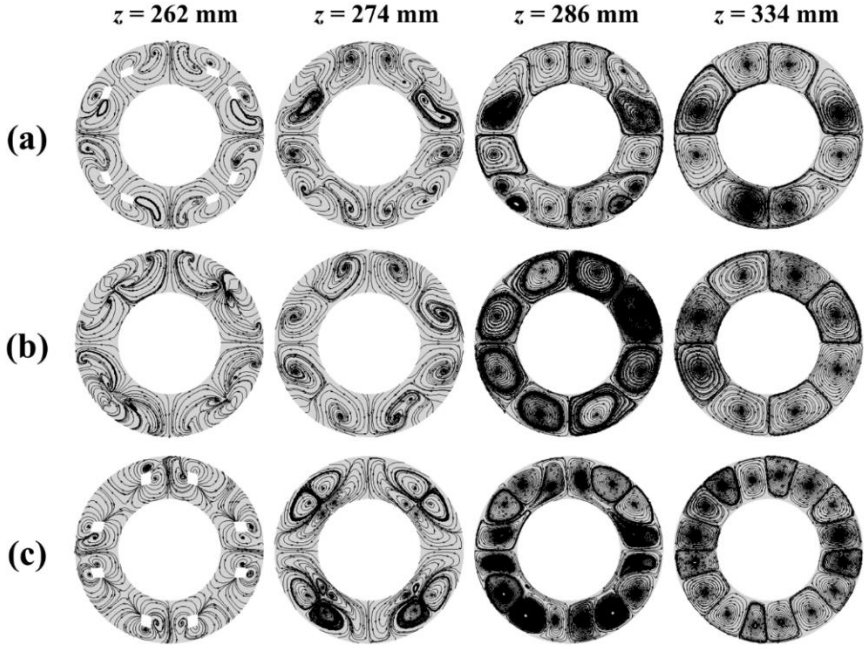

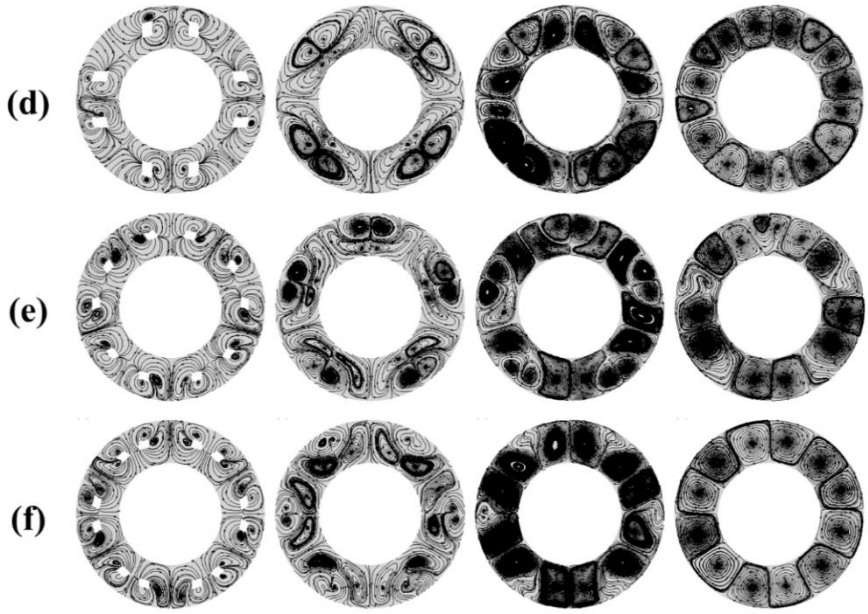

Figure 7.3 Streamlines of different cross sections at *Re* = 2304 in different cases: (a) case D2; (b) case D3; (c) case D4; (d) case D5; (e) case D6; (f) case D7.

Figure 7.4 demonstrates the iso-surface of Q criterion overlapped with velocity magnitude contours. As shown in Figure 7.4 (a)-(c), the size of the vortex core first increases and then decreases as α_v increases, indicating that an α_v of 90 º is a turning point for optimizing vortex interactions. Furthermore, the size of vortex cores in cases with α_v = 90 º increases significantly with axial distance, indicating that the effect of vortex interaction reaches its maximum. As shown in Figure 7.4 (a), (d), and (e), the variation of vortex core size is not significant as *BR* increases, indicating that the effect of increasing *BR* primarily contributes to the vortex intensity. This finding is consistent with the analysis in Figure 7.3 (c) and (d), primarily because the development space of inner and outer boundary vortices is not significantly affected. In the region of vortex generator, the values of velocity magnitude increase as *BR* increases. However, the adjustment of velocity in other regions remains largely unchanged. This suggests that intensity of energy dissipation is stronger in the region of vortex generators than in other regions, representing a potential direction for future optimization. Jet flows induced by holes may be an effective optimization strategy. As shown in Figure 7.4 (a), (f), and (g), case D1 exhibits the largest vortex cores due to stable vortex interactions. Furthermore, as *PN* increases from 4 to 5, the values of velocity magnitude at the region

of vortex generator decrease from 0.14 m/s to 0.12 m/s. When *PN* increases from 5 to 6, velocity magnitude in this region remains within the range of 0.11 m/s to 0.12 m/s, indicating that the impact on energy dissipation intensity is not significant for cases with large *PN*. Among all cases, case D5 exhibits the strongest energy dissipation, while case D3 displays the weakest. This indicates that reductions in the development space of outer boundary vortices play a crucial role in adjusting energy dissipation. Furthermore, the values of velocity magnitude in all cases range from 0.7 m/s and 0.13 m/s downstream of the vortex generators, suggesting considerable potential for optimizing energy balance and vortex interactions.

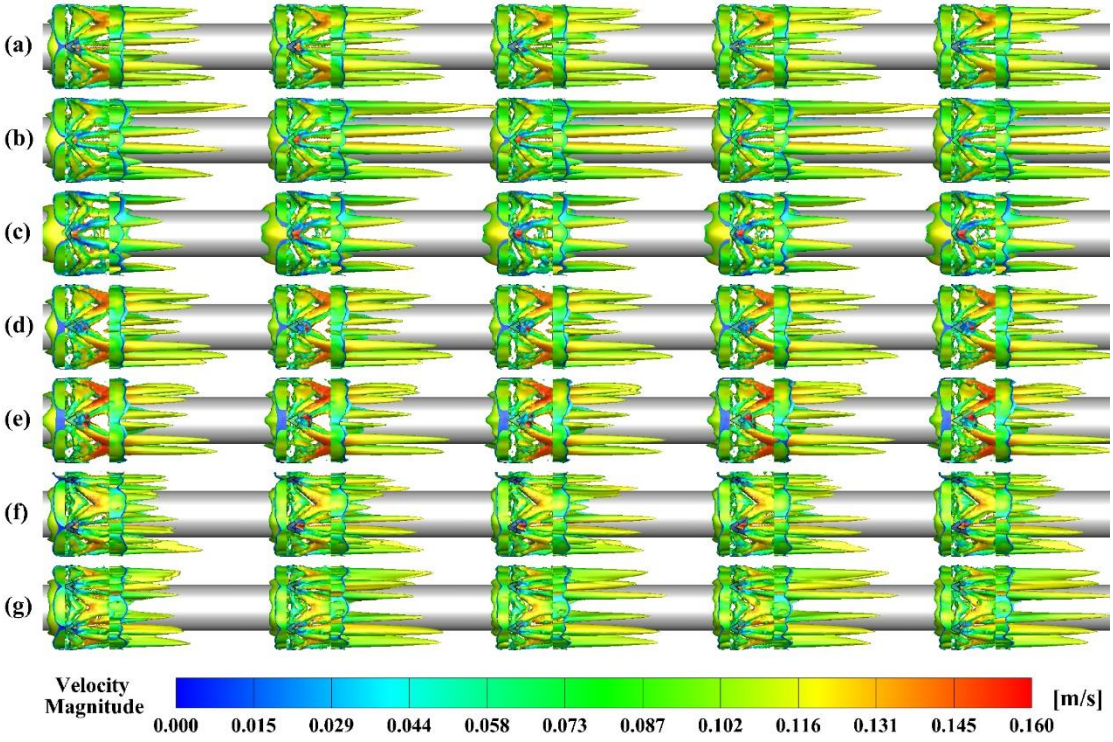

Figure 7.4 The iso-surface of Q criterion overlapped with velocity magnitude contours ($Q = 2/s^2$, $Re = 2304$): (a) case D1; (b) case D2; (c) case D3; (d) case D4; (e) case D5; (f) case D6; (g) case D7.

Figure 7.5 (a) displays the variation in *Se* axial distribution for various cases. As z/d_c increases, all *Se* values show a trend of increasing first and then decreasing due to the variation in vortex interaction. However, the *Se* peak values of cases D1, D4, and D5 occur at larger z/d_c regions compared to other cases. This behavior depends on the structure of winglet vortex generators. As α_v and *PN* increase, the structure of vortex

generators is concentrated near the cross section at $z = 250$ mm. In contrast, the variation in *BR* primarily affects the development space of outer boundary vortices and does not change the regional extent of flow disturbance. It concludes that increasing *BR* plays a more significant role in maintaining the stability of vortex interaction compared to other cases. Furthermore, when *BR* increases to 0.15, the effect of further increasing *BR* on vortex interaction is not significant. Therefore, a *BR* value of 0.15 represents a turning point of further optimization. As *PN* increases, the *Se* peak value rises due to serious vortex interactions between inner and outer boundary vortices. However, downstream of the vortex generators, the *Se* values of case D1 are higher than those of cases D6 and D7, primarily due to the stable vortex interaction in case D1, as shown in Figure 7.2. As α_v increases, the *Se* peak values exhibit a trend of first increasing and then decreasing. The case D3 shows the lowest *Se* peak value among all cases, owing to the dominant disturbance from inner boundary vortices. Therefore, vortex interactions between vortex pairs are crucial for the adjustment of flow disturbances. Figure 7.5 (b) demonstrates the variation in *Se* axial distribution at different *Re*. As *Re* increases, the *Se* values increase linearly, indicating that increasing *Re* does not significantly affect steady vortex interactions.

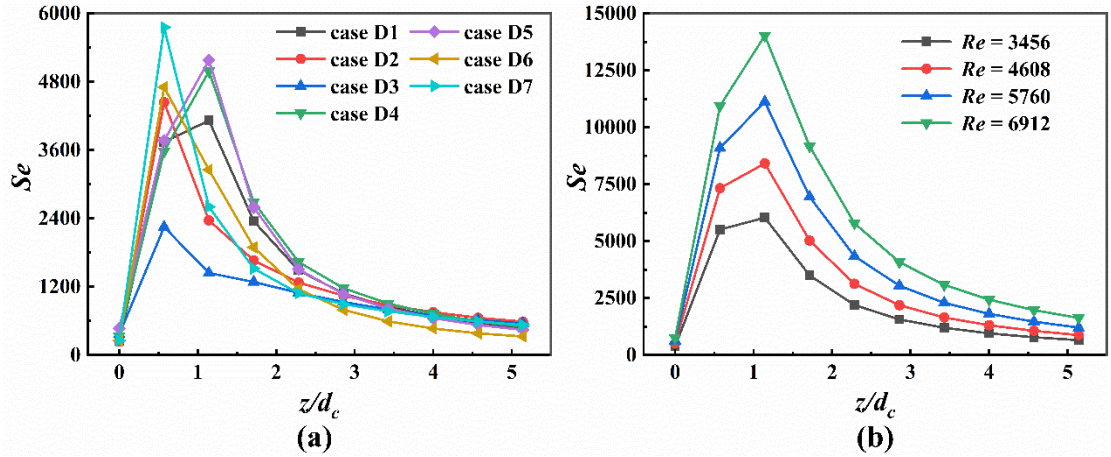

Figure 7.5 Variation in *Se* axial distribution: (a) various cases (b) different *Re*.

7.4 Disturbance and uniformity of flow fields

This section analyzes *TKE* contours, energy distributions, temperature contours, velocity magnitude contours, and surface local *Nu* contours in various cases, aiming to

understand the combined effect of vortex interaction and wall limitations on the disturbance and uniformity of flow fields.

Figure 7.6 shows the contours of *TKE* at *Re* = 2304 for various cases. As α_v increases, the fluid flow becomes concentrated near the inner tube walls, resulting in greater energy dissipation by the vortex generators. The intensity of flow disturbance exhibits a trend of first increasing and then decreasing with increasing α_v, indicating that the α_v of 90 º is the turning point for further optimization. As shown in the cross sections, disturbance energy gradually increases as α_v increases. Furthermore, the flow disturbance shows a uniformity trend when α_v equals 120 º, which is beneficial for the flow disturbance and heat transfer uniformity in downstream sections. When α_v is less than 90 º, the whole disturbance shows a regional distribution. It can be significantly observed that this disturbance mode is helpful for local enhancement, especially for the development of inner boundary vortices. However, the overall uniformity remains crucial for steady vortex dissipation. Furthermore, the disturbance intensity of inner vortex pairs increases as α_v increases, consistent with the analysis in Figure 7.2 and Figure 7.3. As *BR* increases, significant *TKE* variation occurs near the vortex generators due to reduced development space for outer boundary vortices. The *TKE* variations in other regions remain largely unchanged with increasing *BR*, which is consistent with the analysis of Q criterion in Figure 7.4. Furthermore, the flow disturbance in large *BR* cases significantly becomes stronger than that in small *BR* cases. As shown in the cross section, the distribution of flow disturbance remains regional model, indicating that increasing *BR* has no significant impact on the disturbance mode. Furthermore, the enhancement is primarily observed in the vortex interaction region of inner vortex pairs. As *PN* increases, the overall intensity of flow disturbance enhances, consistent with the analysis in Figure 7.5 (a). Similar to cases of increasing *BR*, the disturbance mode maintains regional distribution. The differences between these two increasing variables lie in the disturbance intensity and regional mode. The disturbed region in the cross section increases as *PN* increases. However, the enhancement of disturbance intensity is weaker compared to cases of increasing *BR*. In all cases, stronger flow disturbance

occurs upstream compared to downstream, which is unfavorable for overall uniformity of flow fields.

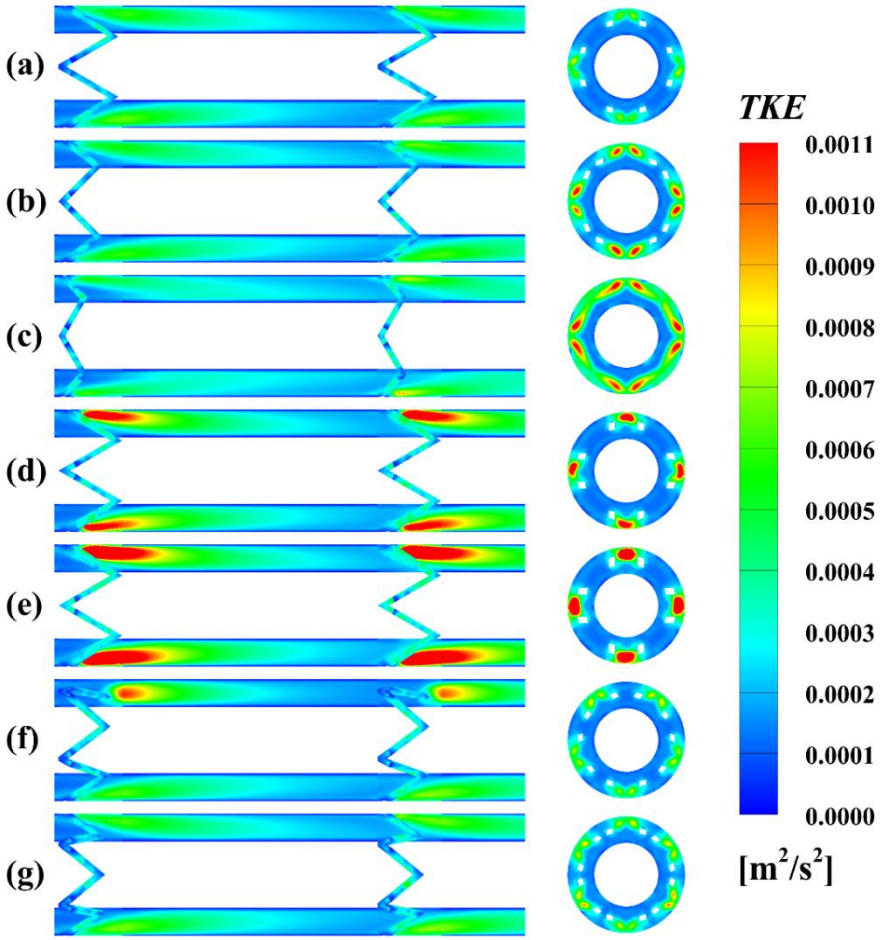

Figure 7.6 The contours of *TKE* at *Re* = 2304 for various cases (x = 0, z = 262 mm): (a) case D1; (b) case D2; (c) case D3; (d) case D4; (e) case D5; (f) case D6; (g) case D7.

Figure 7.7 demonstrates the energy distributions in the axial direction at *Re* = 2304. As show in Figure 7.7 (a), case D5 exhibits the highest *TKE* peak value, while case D3 displays the lowest. The primary reason is that the development space of outer vortex pairs is reduced by a larger *BR* when α_v is 60 º, whereas it is increased by a smaller *BR* when α_v is 120 º. Based on the analysis in Figure 7.5 and Figure 7.6, an α_v of 90 º is the turning point for the overall intensity of flow disturbance. Therefore, the combined effect of a smaller α_v and a larger *BR* on flow disturbance is significant. The *TKE* peak value of case D1 is 128.68 % of that of case D3, while that of case D2 is 130.15 % of

case D3. Furthermore, the *TKE* peak value of case D5 is 293.33 % of that of case D1, while that of case D4 is 180.00 % of case D1. Compared to the effect of α_v, the effect of *BR* on flow disturbance is more significant. When α_v increases from 60 º to 90 º, the increase in *TKE* values is not significant, suggesting that 60 º is the optimal choice when overall heat transfer performance is considered. The *TKE* peak value of case D6 increases to 242.29 % of case D1, while that of case D7 increases to 273.12 % of case D1. It can be concluded that further increasing *PN* has a limited effect. Furthermore, cases D6 and D7 show *TKE* values close to those of case D5, indicating that a *BR* of 0.20 can serve as a substitute for increasing *PN*. As shown in Figure 7.7 (b), case D7 exhibits the maximum ε peak value, while case D3 displays the minimum ε peak value, which is inconsistent with the variation trend of *TKE* peak values. The dissipation intensity of case D5 is lower than that of case D7, owing to the fact that increasing *BR* causes less interference to vortex interactions compared to case D7. Furthermore, the ε values of cases D6 and D7 are not significantly different, suggesting that the energy efficiency of case D7 is higher than that of case D6. The ε variation trend for increasing *BR* and α_v is consistent with the *TKE* variation trend, indicating that the flow fields in cases 1 to 5 are in a state of dynamic balance.

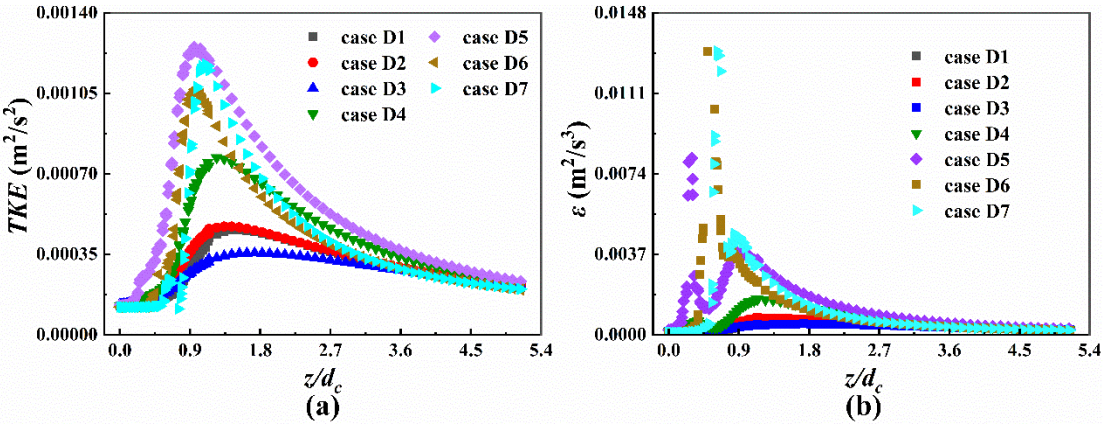

Figure 7.7 Energy distributions in the axial direction at *Re* = 2304: (a) *TKE*; (b) ε.

Figure 7.8 shows the energy distributions in the axial direction at different *Re*. As shown in Figure 7.8 (a), as *Re* increases, the *TKE* values increase due to the increasing input power. The position at which the *TKE* peak value appears moves downstream with

increasing *Re*, primarily because of the increase in disturbance intensity. The *TKE* peak value at *Re* = 4608 increases to 155.37 % of case at *Re* = 3456, that at *Re* = 5760 increases to 195.46 % of case at *Re* = 3456, and that at *Re* = 6912 increases to 217.75 % of case at *Re* = 3456. This means that further increases in *Re* have a diminishing effect on the overall intensity of flow disturbance. As shown in Figure 7.8 (b), the position where the ε peak value appears does not move downstream like *TKE* peak values. The vortex interaction remains the primary factor affecting vortex dissipation. Furthermore, the ε peak value at *Re* = 4608 increases to 221.74 % of case at *Re* = 3456, that at *Re* = 5760 increases to 360.87 % of case at *Re* = 3456, and that at *Re* = 6912 increases to 534.78 % of case at *Re* = 3456. The intensity of vortex dissipations significantly enhances as *Re* increases due to strengthened vortex interactions.

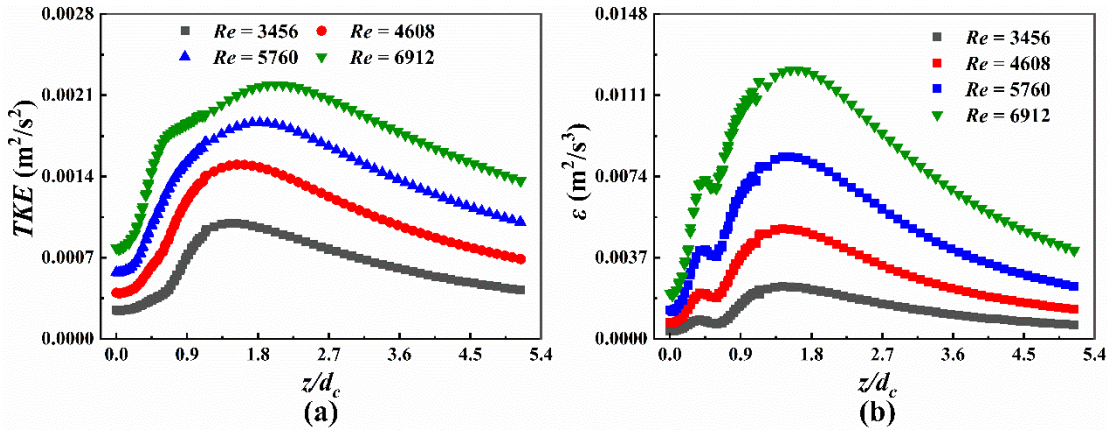

Figure 7.8 Energy distributions in the axial direction at different *Re*: (a) *TKE*; (b) ε.

Figure 7.9 displays the temperature contours at various cross sections. As shown in Figure 7.9 (a) – (d), the temperature distribution shifts from a circular to a regional pattern as the vortex structure gradually achieves a stable state. The four extended regions correspond primarily to the locations of the inner vortex pairs, as illustrated by the vortex structure in Figure 7.2. This indicates that the rotational direction of the vortex pairs is a key factor for optimizing heat transfer uniformity. However, compared to case C6, the temperature distribution in case D1 demonstrates greater uniformity due to additional extended regions associated with inner boundary vortices, as shown in Figure 7.9 (h) – (j). Furthermore, case C6 exhibits a more significant temperature

gradient, as seen in Figure 6.11., whereas case D1 displays a more uniform temperature gradient, which contributes to improved heat transfer uniformity. The temperature range in the core region is 300.5 K–303 K for case C6, while that is 300.5 K–304 K for case D1. It proves that novel self-join winglet structures are crucial for further adjustment in temperature distribution compared to traditional winglet structures. However, both winglet structures result in non-uniform local temperature distribution, indicating a remaining challenge to be addressed.

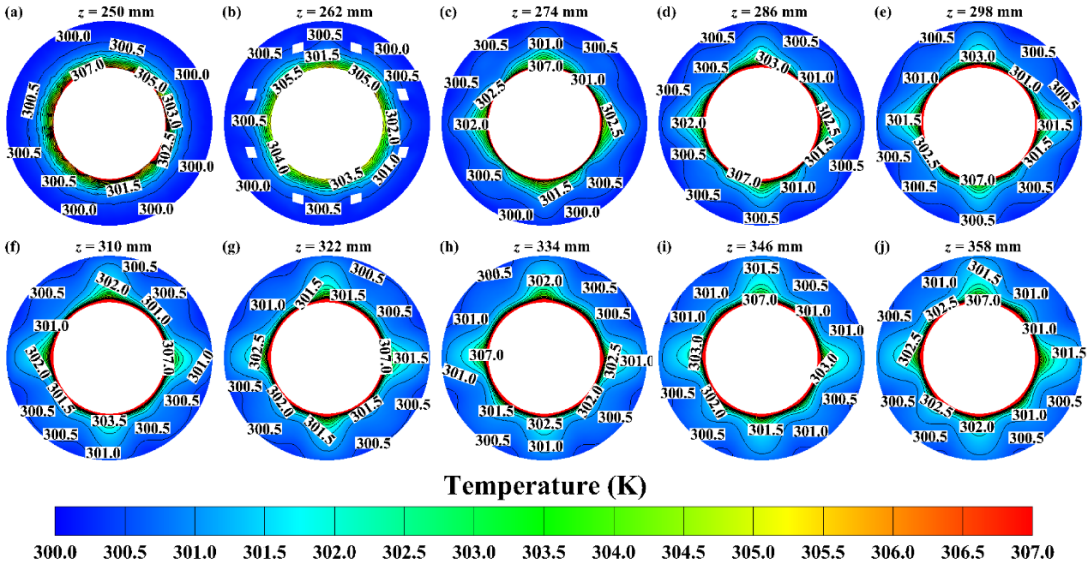

Figure 7.9 Temperature contours at various cross sections.

Figure 7.10 displays the contours of velocity and temperature at z = 274 mm for different cases. As shown in Figure 7.10 (a) – (c), the fluid flow shifts from a regional disturbance mode to a single disturbance mode as α_v increases. The high-velocity region corresponds to the region where vortex interaction occurs, which also explains the distribution of inner and outer vortex pairs. As α_v increases, the disturbance intensity of the outer vortex pairs decreases. However, when α_v is 90 °, the temperature distribution transitions to a single disturbance mode. The weak disturbance from the outer boundary vortices has no significant effect on temperature uniformity. Therefore, the flow intensity of the outer vortex pairs is crucial for improving the uniformity of the flow fields, as shown in Figure 7.10 (a). As shown in Figure 7.10 (a), (d), and (e), the flow intensity of the outer vortex pairs increases with *BR*. This trend can be observed from

the high-velocity distribution of both inner and outer vortex pairs. Due to this trend, the regional intensity of the temperature distribution becomes more significant in high-*BR* cases compared to the low-*BR* case. This further confirms that the disturbance intensity of the outer boundary vortices is crucial for achieving a uniform disturbance mode in the flow fields. As shown in Figure 7.10 (a), (f), and (g), the area of the high-velocity region near the outer boundary layer significantly decreases as *PN* increases. However, when *PN* exceeds 5, the temperature distribution transitions to a single disturbance mode. Furthermore, the area of vortex interaction in the inner vortex pairs does not increase with *PN*, primarily because vortex dissipation is not significant when *PN* exceeds 5, as shown in Figure 7.7 (b). The primary difference between cases D6 and D7 lies in the intensity of flow disturbance. Therefore, to improve the overall working performance of the flow fields, optimization can be achieved based on the effect of *PN* on the adjustment in the disturbance intensity.

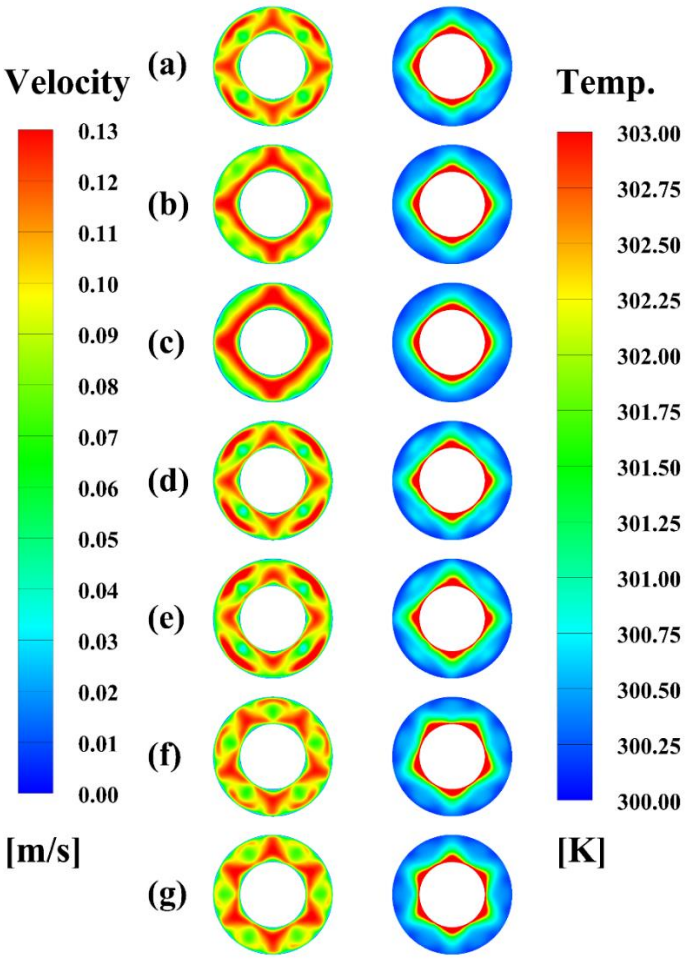

Figure 7.10 The contours of velocity and temperature at z = 274 mm in different

cases: (a) case D1; (b) case D2; (c) case D3; (d) case D4; (e) case D5; (f) case D6; (g) case D7.

Figure 7.11 shows the contours of the surface local Nusselt number for different cases. As α_v increases, the high-*Nu* region around the vortex generator significantly decreases, as the vortex interaction in this region weakens compared to other regions. The primary reason is that the effect of outer vortex pairs on flow disturbance becomes weaker than that of inner vortex pairs. Therefore, the uniformity of the flow field in case D3 is more significant than in cases D1 and D2. Furthermore, the local *Nu* values behind the strong flow disturbance are between 30-55 in case D1, that are between 35-60 in case D2, and that are between 40-55 in case D3. This indicates that the intensity of local heat transfer behind the high-*Nu* region in case D1 exhibits a weaker trend compared to cases D2 and D3, resulting in a more significant overall local surface *Nu* gradient in case D1. As *BR* increases, the area of the high-*Nu* region around the vortex generator expands due to enhanced flow disturbance. Furthermore, compared to cases with increasing α_v, the high-*Nu* regions become closer to each other, which is attributed to stronger vortex interaction induced by higher *BR*. It can be concluded that cases of modified *BR* are suitable for optimizing flow disturbance, while cases of modified α_v are better for improving heat transfer uniformity. Furthermore, the local *Nu* values behind the strong flow disturbance are between 40-60 in case D4, while that are between 40-65 in case D5. It suggests that the overall local surface *Nu* in cases D4 and D5 is higher than in cases D2 and D3, indicating that stronger flow disturbance is crucial for enhancing the overall working performance of heat exchangers. As *PN* increases, the area of the high-*Nu* region around the vortex generator also increases, but its increase is weaker than that in cases with increasing *BR*. Furthermore, the number of strong flow disturbance regions increases in cases D6 and D7 due to increasing winglet pairs. The local *Nu* values behind the strong flow disturbance are between 35-60 in case D6, while that are between 40-60 in case D7, demonstrating that increasing *PN* is helpful for enhancing the intensity of local heat transfer.

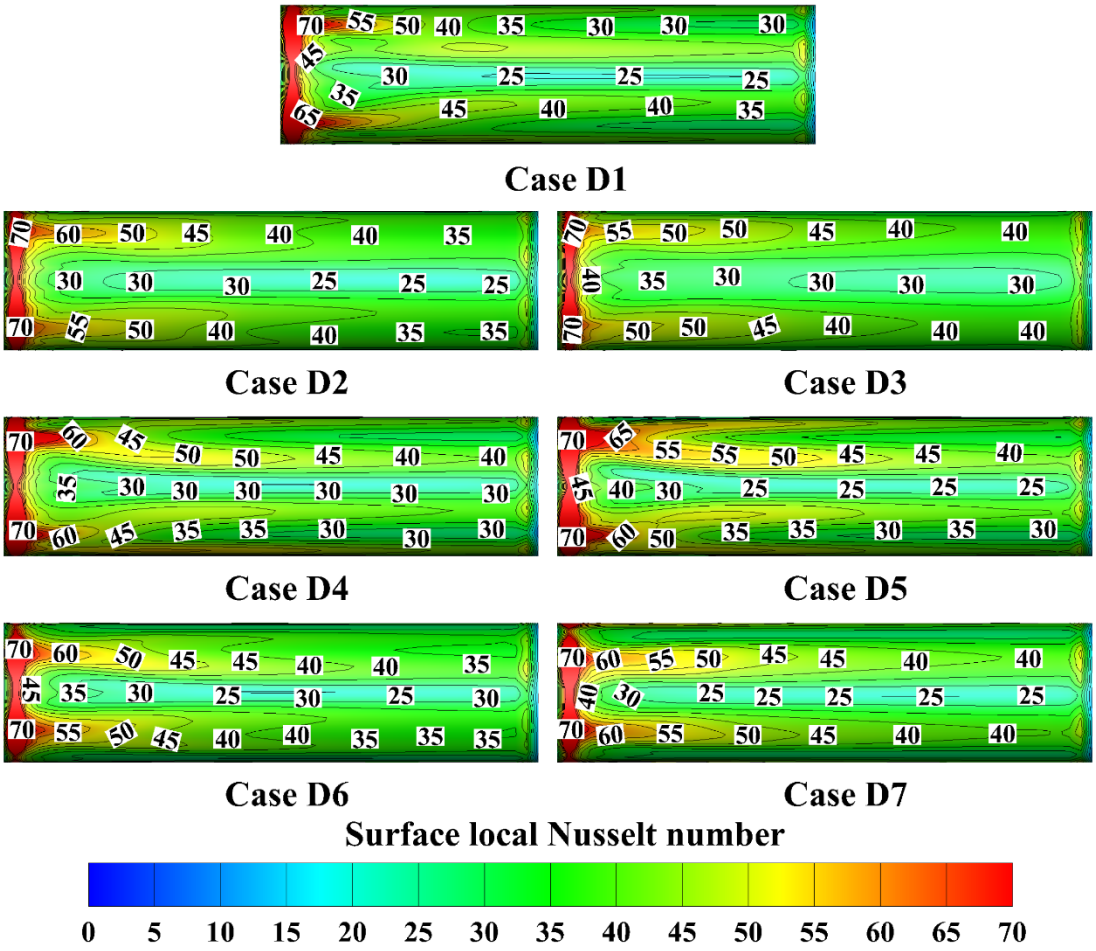

Figure 7.11 The contours of surface local Nusselt number in different cases.

7.5 Flow and thermal characteristics analysis

This section analyzes the variations of *Nu*, Nu/Nu_0, *f*, f/f_0, and *TEF* in various cases at different *Re* values, aiming to summarize the heat transfer and pressure drop characteristics of flow fields.

Figure 7.12 displays the influence of various cases on heat transfer. As shown in Figure 7.12 (a), the *Nu* values show an increasing trend as *Re* increases due to higher turbulence intensity. Compared to novel self-join winglets applied in circular tubes (Figure 4.13), the *Nu* difference between each case becomes smaller, indicating that the *Re* range is a key factor affecting the sensitivity of structural variables. The *Nu* values in case D5 are the highest, consistent with analysis in case A5 in Figure 4.13, suggesting that the effect of modified *BR* is less influenced by wall limitations. Furthermore, the

characteristics diameter used in this chapter is the same as that applied in annular tubes with traditional delta winglets in this work. However, the *Nu* difference between the two types of winglets is not significant due to constraints in winglet size. The highest *Nu* value is 112.0 % of that reported in case C5 in Figure 6.14. As shown in Figure 7.12 (b), the *Nu* values increase by 1.40–2.20 times those of the smooth tube, with both maximum and minimum values lower than those in case C7 (Figure 6.14). It can be concluded that novel self-join winglets have the potential to enhance the contribution of heat transfer in the flow system. The Nu/Nu_0 values increase to 101.9 % and 100.8 % of those in case D1 as α increases, respectively. Furthermore, with the increase in *BR*, the Nu/Nu_0 values are 102.5 % and 104.5 % of those in case D1, respectively. Similarly, as *PN* increases, the Nu/Nu_0 values are 101.0 % and 102.4 % of those in case D1, respectively. The Nu/Nu_0 values decrease nonlinearly as *Re* increases, consistent with the trend in circular tubes equipped with novel self-join winglets. Consequently, compared to smooth tubes, the effect of increasing *Re* on heat transfer enhancement is weaker.

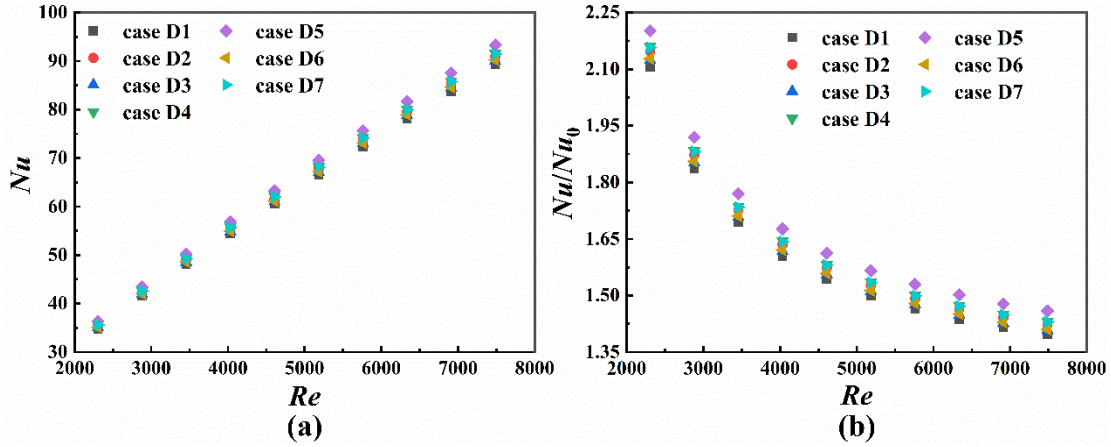

Figure 7.12 Influence of various cases on heat transfer: (a) *Nu* vs. *Re* (b) Nu/Nu_0 vs. *Re*.

Figure 7.13 shows the influence of various cases on fluid flow. As shown in Figure 7.13 (a), the *f* values first increase and then decrease as α_v increases, which is inconsistent with the trend in circular tubes with novel self-join winglets (Figure 4.14). An α_v of 90 ° is the turning point for optimization in annular tubes. Furthermore, the *f* values

increase significantly as *BR* increases due to the augmentation of flow disturbance. Similarly, the variation trend caused by increasing *PN* is the same as that caused by a larger *BR*. However, the difference between these two variables is the intensity of flow disturbance. Cases with modified *PN* are more suitable for improving heat transfer uniformity in flow fields. The highest *f* value is 161.3 % of that reported in case C5 in Figure 6.14. As shown in Figure 7.13 (b), the f/f_0 values exhibit an increasing trend with *Re*, consistent with the detrimental effect of a higher *Re* in circular tubes with novel self-join winglets (Figure 4.14). This suggests that wall limitations have little effect on flow fields induced by a higher *Re*. The *f* values increase by 2.64–3.91 times those of plain tubes. As α_v increases, the f/f_0 values increase to 107.7 %–109.7 % and 102.2 %–104.9 % of those in case D1, respectively. Furthermore, as *BR* increases, the f/f_0 values range from 116.3 % to 119.4 % and 132.6 % to 135.5 % of those in case D1, respectively. Similarly, with increasing *PN*, the f/f_0 values range from 104.3 % to 106.5 % and 111.5 % to 116.1 % of those in case D1, respectively. While large *BR* and *PN* can enhance the heat transfer performance, they also increase pressure loss. In contrast, modified α_v does not exhibit this variation characteristics, suggesting that the variation of α_v can affect the vortex interaction induced by wall limitations.

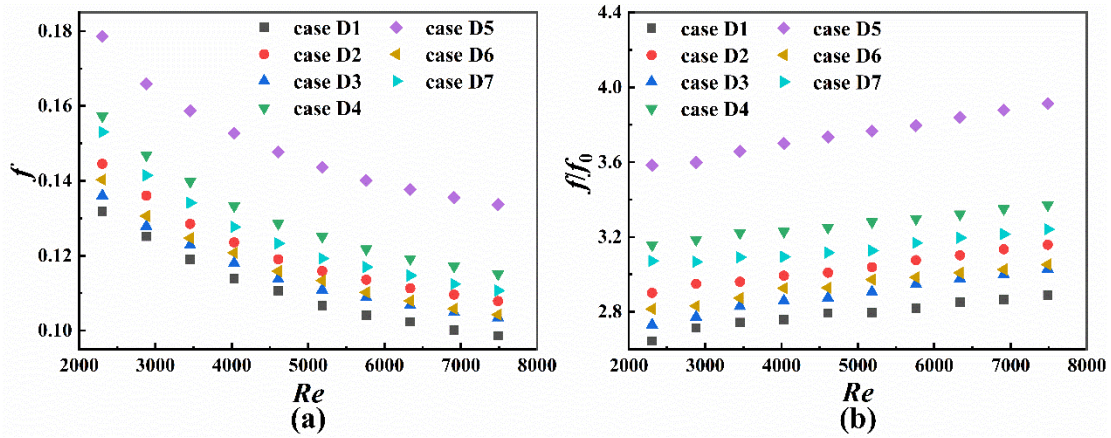

Figure 7.13 Influence of various cases on fluid flow: (a) *f* vs. *Re* (b) f/f_0 vs. *Re*.

Figure 7.14 shows the variations of *TEF* with different *Re*. As shown in Figure 7.14, the *TEF* demonstrates a decreasing trend with *Re*, as the effect of flow resistance is stronger than that of heat transfer. Cases with modified α_v exhibit superior *TEF*

performance compared to cases with modified *BR* and *PN*, due to their effect on vortex interactions induced by wall limitations. Cases D1 and D3 achieve the maximum *TEF* of 1.52, suggesting that the α_v of 60 º and 120 º are the optimal choices for enhancing flow disturbance and improving heat transfer uniformity, respectively. Furthermore, the minimum *TEF* of 0.93 occurs in case D5. While this value is below 1, it remains above 0.9 even under high pressure drop conditions, indicating that cases with modified *BR* hold potential for improving winglet design.

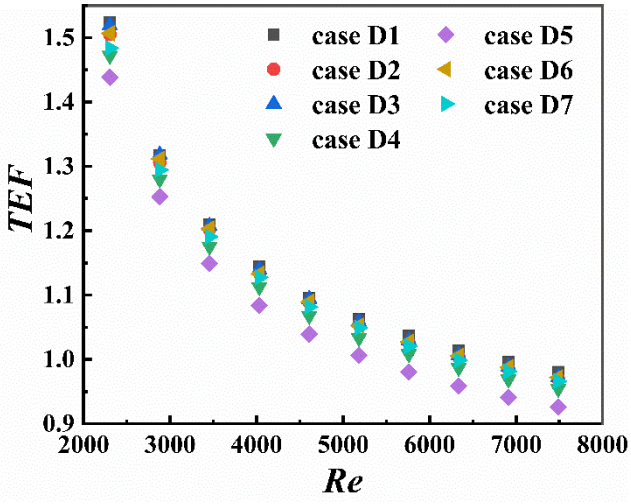

Figure 7.14 Variations of *TEF* with different *Re*.

7.6 Empirical correlations for *Nu* and *f*

Figure 7.15 compares the predicted *Nu* and *f* values from the correlations with the experimental data. The maximum deviations are 1.0 % and 5.5 % for *Nu* and *f*, respectively. Therefore, the predicted data are in good agreement with the experimental data. The predicted results are valuable for guiding the design and optimization of novel winglet structures in the future. The correlations and constraints are provided as follows,

$$Nu=0.07478Re^{0.80003}BR^{0.05853}PN^{0.04772}(1+\alpha_v\pi/180)^{0.02682}+0.00193 \quad (7.1)$$

$$f=3.08199Re^{-0.36467}BR^{0.57571}PN^{0.38096}(1+\alpha_v\pi/180)^{0.18264}+0.03863 \quad (7.2)$$

where $2304 \le Re \le 7488$, $0.10 \le BR \le 0.20$, $4 \le PN \le 6$, and $60\ ° \le \alpha_v \le 120\ °$.

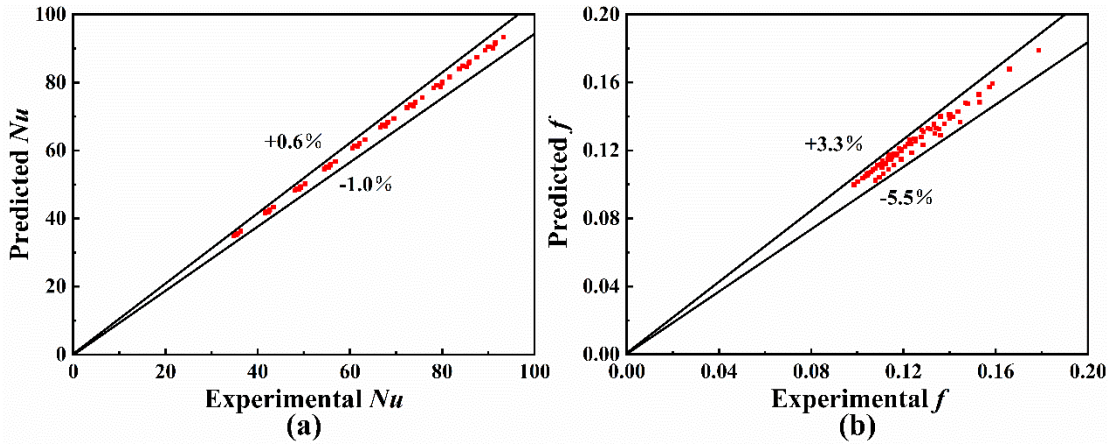

Figure 7.15 Comparisons of the predicted *Nu* and *f* with experimental data: (a) *Nu*; (b) *f*.

7.7 Chapter conclusion

In this chapter, novel self-join winglet vortex generators are applied in annular tubes. The effects of blockage ratio (*BR*), winglet pairs number (*PN*), and included angle (α_v) on heat transfer uniformity and flow disturbance are investigated in annular tubes with novel self-join winglets. Furthermore, empirical correlations for *Nu* and *f* based on experimental data are obtained. The key findings of this chapter are as follows:

(1) Compared to circular tubes, the movement distance of boundary vortices increases because of wall limitation. Furthermore, the number of vortex pairs induced by novel self-join winglets is twice that induced by traditional delta winglets.

(2) As α_v increases, the development space of outer boundary vortices decreases, resulting in an acceleration in the dissipation of the outer boundary vortices. However, the effect of increasing *BR* is primarily on vortex intensity. Furthermore, the dissipation mechanism in cases of increasing *PN* is consistent with that observed in cases of increasing α_v.

(3) Nusselt number and friction factor increase by 1.40–2.20 and 2.64–3.91 times, respectively, compared with the smooth tube.

(4) The maximum thermal enhancement factor reaches 1.52 when *BR* = 0.10, *PN* = 4, and α_v = 60 º or 120 º, suggesting that the α_v of 60 º and 120 º are the optimal choices

for enhancing flow disturbance and improving heat transfer uniformity, respectively. Furthermore, the lowest *TEF* reaches 0.93 when $BR = 0.20$, $PN = 4$, and $\alpha_v = 60$ º. While this value is below 1, it remains above 0.9 even under high pressure drop conditions, indicating that cases with modified *BR* hold potential for improving winglet design.

(5) Cases of larger α_v are suitable for applications in enhancing vortex disturbance, while cases of smaller α_v are better for improving flow uniformity. An α_v of 90 º is a turning point for optimizing vortex interactions.

Chapter 8: Conclusion and future work

8.1 Conclusion

Based on previous studies about winglet vortex generators, novel self-join winglet structures are proposed in this work. This thesis successfully achieves the objectives presented in section 1.3 of Chapter 1. The key conclusions in this thesis are as follows:

Objective 1: To summarize the heat transfer and pressure drop characteristics and obtain the optimal flow structure induced by novel self-join winglet structures in the tube and shell sides.

(1) Compared to smooth tubes, the Nusselt number and friction factor in tube sides increase by 1.90–2.32 and 2.23–5.10 times, respectively, while those in shell sides increase by 1.40–2.20 and 2.64–3.91 times, respectively.

(2) Longitudinal vortices near the tube wall are induced by winglets because of lift angles. Furthermore, the number of vortex pairs induced by novel self-join winglets is twice that induced by traditional delta winglets.

Objective 2: To understand the vortex interaction and vortex flow behaviors in the tube and shell sides fitted with novel self-join winglets.

(1) The vortex pairs near the tube wall contribute to enhancing the mixing uniformity of fluid flows in circular tubes. Furthermore, the dissipation intensity of the vortex pairs near the tube wall is increased with increasing included angle. Higher values of blockage ratio and winglet pairs number adversely affect fluid flows in tubes.

(2) Compared to circular tubes, the movement distance of boundary vortices in annular tubes increases because of wall limitation. As included angle and winglet pair number increases, the development space of outer boundary vortices decreases, resulting in an acceleration in the dissipation of the outer boundary vortices. However, the effect of increasing blockage ratio is primarily on vortex intensity.

Objective 3: To perform parametric studies and propose strategies for optimizing the flow structures and novel winglet designs in circular and annular tubes.

(1) In circular tubes, as curved diameter increases, the disturbed distribution in high-speed region is adjusted to the boundary layer. The reason is the variations of curved diameter adjust the region of vortex development. Increasing the included angle improves the uniformity of the flow fields, while increasing the lift angle enhances the regional disturbance.

(2) In annular tubes, cases of larger included angles are suitable for applications in enhancing vortex disturbance, while cases of smaller included angles are better for improving flow uniformity. An included angle of 90 º is a turning point for optimizing vortex interactions.

This thesis aims to reveal the variation mechanism of vortex interactions induced by novel self-join winglets in circular and annular tubes. These findings provide valuable guidance for enhancing the working performance of heat exchangers, thereby significantly reducing carbon emissions and promoting economic development. Furthermore, these results provide novel strategies for optimizing vortex interactions and winglet designs.

8.2 Future work

Based on current studies about flow fields induced by novel self-join winglet vortex generators, further research is needed in the future. These future studies hold significant potential for improving the heat transfer performance of heat exchangers and can be divided into the following three directions:

(1) Boundary vortex

The boundary vortices induced by novel self-join winglets are crucial for improving the heat transfer uniformity of flow fields. However, in circular tubes, these vortices dissipate more quickly than those near the core region. The flow field in circular

tubes cannot maintain mixing uniformity for a long distance. Therefore, further research is needed to understand how to reduce the dissipation rate of boundary vortices in future work.

(2) Wall limitation

The wall limitation has the advantage of maintaining the mixing uniformity and steady vortex structure. The structural limitations of annular tube walls are key factors for further optimizing vortex interactions. The interaction mechanism between wall and vortex pairs can be better investigated in the future.

(3) Structural optimization

The results from structural variables investigated in this thesis provide valuable guidance for efficient applications of novel winglets in tube and shell sides of heat exchangers. However, the structural and arrangement variables examined in this work remain limited. Consequently, future work should focus on further optimizing the winglet structure.

References

[1] E. Tang, C. Peng, Y. Xu, Changes of energy consumption with economic development when an economy becomes more productive, J. Cleaner Prod. 196 (2018) 788-795.

[2] Y.-L. He, S.-Z. Tang, W.-Q. Tao, M.-J. Li, F.-L. Wang, A general and rapid method for performance evaluation of enhanced heat transfer techniques, Int. J. Heat Mass Transf. 145 (2019) 118780.

[3] Y. Hong, J. Du, S. Wang, S.-M. Huang, W.-B. Ye, Effect of decaying swirl flow on tubular turbulent heat transfer enhancement by using short length helical tapes, Chem. Eng. Res. Des. 138 (2018) 1-12.

[4] T. Pukšec, A. Foley, N. Markovska, N. Duić, Life cycle to pinch analysis and 100% renewable energy systems in a circular economy at sustainable development of energy, water and environment systems 2017, Renewable Sustainable Energy Rev. 108 (2019) 572-577.

[5] M. Sheikholeslami, M. Gorji-Bandpy, D.D. Ganji, Review of heat transfer enhancement methods: focus on passive methods using swirl flow devices, Renewable Sustainable Energy Rev. 49 (2015) 444-469.

[6] P.M. Ligrani, M.M. Oliveira, T. Blaskovich, Comparison of heat transfer augmentation techniques, AIAA J. 41 (3) (2003) 337-362.

[7] C. Maradiya, J. Vadher, R. Agarwal, The heat transfer enhancement techniques and their thermal performance factor, Beni-Suef Univ. J. Basic Appl. Sci. 7 (1) (2018) 1-21.

[8] M.H. Mousa, N. Miljkovic, K. Nawaz, Review of heat transfer enhancement techniques for single phase flows, Renewable Sustainable Energy Rev. 137 (2021) 110566.

[9] M. Veerabhadrappa Bidari, P.B. Nagaraj, G. Lalagi, Influence of different types of vortex generators (VGs) to enhance heat transfer performance in heat exchangers: a review, Int. J. Ambient Energy 43 (1) (2022) 5718-5741.

[10] C. Rajesh Babu, P. Kumar, S. Roy, R. Ganesan, A comprehensive review on compound heat transfer enhancement using passive techniques in a heat exchanger, Mater. Today: Proc. 54 (2022) 428-436.

[11] H. Li, Y. Wang, Y. Han, W. Li, L. Yang, J. Guo, Y. Liu, J. Zhang, M. Zhang, F. Jiang, A comprehensive review of heat transfer enhancement and flow characteristics in the concentric pipe heat exchanger, Powder Technol. 397 (2022) 117037.

[12] A.E. Bergles, ExHFT for fourth generation heat transfer technology, Exp. Thermal Fluid Sci. 26 (2-4) (2002) 335-344.

[13] S.D. Shelare, K.R. Aglawe, P.N. Belkhode, A review on twisted tape inserts for enhancing the heat transfer, Mater. Today: Proc. 54 (2022) 560-565.

[14] W.-Y. Zhang, W.-W. Yang, Y.-H. Jiao, D.-W. Zhang, Numerical study of periodical wall vibration effects on the heat transfer and fluid flow of internal turbulent flow Int. J. Therm. Sci. 173 (2022) 107367.

[15] D. Duan, Y. Cheng, M. Ge, W. Bi, P. Ge, X. Yang, Experimental and numerical study on heat transfer enhancement by flow-induced vibration in pulsating flow, Appl. Therm. Eng. 207 (2022) 118171.

[16] M.M. Ohadi, D.A. Nelson, S. Zia, Heat transfer enhancement of laminar and turbulent pipe flow via corona discharge, Int. J. Heat Mass Transf. 34 (4-5) (1991) 1175-1187.

[17] H. Huang, T. Sun, G. Zhang, M. Liu, B. Zhou, The effects of rough surfaces on heat transfer

and flow structures for turbulent round jet impingement, Int. J. Therm. Sci. 166 (2021) 106982.

[18] M. Jafari, M. Farhadi, K. Sedighi, An experimental study on the effects of a new swirl generator on thermal performance of a circular tube, Int. Commun. Heat Mass Transfer 87 (2017) 277-287.

[19] C. Luo, K.W. Song, T. Tagawa, Heat transfer enhancement of a double pipe heat exchanger by co-twisting oval pipes with unequal twist pitches, Case Stud. Therm. Eng. 28 (2021) 101411.

[20] N. Zheng, K. Zhang, Q. Chen, Z. Sun, Novel self-join winglet vortex generators for enhanced heat transfer of turbulent airflow in round tubes, Int. Commun. Heat Mass Transfer 130 (2022) 105806.

[21] B. Kristiawan, A.I. Rifa'i, K. Enoki, A.T. Wijayanta, T. Miyazaki, Enhancing the thermal performance of TiO_2/water nanofluids flowing in a helical microfin tube, Powder Technol. 376 (2020) 254-262.

[22] W. Li, Z. Yu, Y. Wang, Y. Li, Heat transfer enhancement of twisted tape inserts in supercritical carbon dioxide flow conditions based on CFD and vortex kinematics, Therm. Sci. Eng. Prog. 31 (2022) 101285.

[23] G.G. Cruz, M.A.A. Mendes, J.M.C. Pereira, H. Santos, A. Nikulin, A.S. Moita, Experimental and numerical characterization of single-phase pressure drop and heat transfer enhancement in helical corrugated tubes, Int. J. Heat Mass Transf. 179 (2021) 121632.

[24] L. Wang, D.-W. Sun, P. Liang, L. Zhuang, Y. Tan, Heat transfer characteristics of carbon steel spirally fluted tube for high pressure preheaters, Energy Convers. Manag. 41 (10) (2000) 993-1005.

[25] J. Du, Y. Hong, Experimental investigation on thermal-hydraulic characteristics in a traverse rib tube fitted with regularly spaced helical tapes, Int. J. Heat Mass Transf. 154 (2020) 119726.

[26] Y. Hong, J. Du, S. Wang, Experimental heat transfer and flow characteristics in a spiral grooved tube with overlapped large/small twin twisted tapes, Int. J. Heat Mass Transf. 106 (2017) 1178-1190.

[27] K. Nanan, M. Pimsarn, C. Thianpong, S. Eiamsa-ard, Heat transfer enhancement by helical screw tape coupled with rib turbulators, J. Mech. Sci. Technol. 28 (11) (2015) 4771-4779.

[28] B. Li, B. Feng, Y.-L. He, W.-Q. Tao, Experimental study on friction factor and numerical simulation on flow and heat transfer in an alternating elliptical axis tube, Appl. Therm. Eng. 26 (17-18) (2006) 2336-2344.

[29] W. Yan, X. Gao, W. Xu, C. Ding, Z. Luo, Z. Zhang, Heat transfer performance of epoxy resin flows in a horizontal twisted tube, Appl. Therm. Eng. 127 (2017) 28-34.

[30] H. Safikhani, A. Abbassi, Effects of tube flattening on the fluid dynamic and heat transfer performance of nanofluids, Advanced Powder Technology 25 (3) (2014) 1132-1141.

[31] M.K. Saadeldin, S.Z. Shuja, S.M. Zubair, Optical performance investigation for a parabolic trough collector equipped with an innovative flat tube receiver, Renewable Energy 246 (2025) 122860.

[32] N. Zheng, P. Liu, F. Shan, Z. Liu, W. Liu, Effects of rib arrangements on the flow pattern and heat transfer in an internally ribbed heat exchanger tube, Int. J. Therm. Sci. 101 (2016) 93-105.

[33] P. Naphon, M. Nuchjapo, J. Kurujareon, Tube side heat transfer coefficient and friction factor characteristics of horizontal tubes with helical rib, Energy Convers. Manag. 47 (18-19) (2006) 3031-3044.

[34] N. Zheng, P. Liu, F. Shan, Z. Liu, W. Liu, Heat transfer enhancement in a novel internally grooved tube by generating longitudinal swirl flows with multi-vortexes, Appl. Therm. Eng. 95 (2016) 421-432.

[35] S. Pethkool, S. Eiamsa-ard, S. Kwankaomeng, P. Promvonge, Turbulent heat transfer enhancement in a heat exchanger using helically corrugated tube, Int. Commun. Heat Mass Transfer 38 (3) (2011) 340-347.

[36] S. Xie, Z. Guo, Y. Gong, C. Dong, J. Liu, L. Ren, Numerical investigation of thermal-hydraulic performance of a heat exchanger tube with helical dimples, Int. J. Therm. Sci. 177 (2022) 107530.

[37] P. Promvonge, Heat transfer behaviors in round tube with conical ring inserts, Energy Convers. Manag. 49 (1) (2008) 8-15.

[38] N. Zheng, P. Liu, F. Shan, Z. Liu, W. Liu, Sensitivity analysis and multi-objective optimization of a heat exchanger tube with conical strip vortex generators, Appl. Therm. Eng. 122 (2017) 642-652.

[39] P. Samruaisin, W. Changcharoen, C. Thianpong, V. Chuwattanakul, M. Pimsarn, S. Eiamsa-ard, Influence of regularly spaced quadruple twisted tape elements on thermal enhancement characteristics, Chem. Eng. Process. Process Intensif. 128 (2018) 114-123.

[40] E. Esmaeilzadeh, H. Almohammadi, A. Nokhosteen, A. Motezaker, A.N. Omrani, Study on heat transfer and friction factor characteristics of γ-Al_2O_3/water through circular tube with twisted tape inserts with different thicknesses, Int. J. Therm. Sci. 82 (2014) 72-83.

[41] M. Ahmadvand, A.F. Najafi, S. Shahidinejad, An experimental study and CFD analysis towards heat transfer and fluid flow characteristics of decaying swirl pipe flow generated by axial vanes, Meccanica 45 (1) (2010) 111-129.

[42] P. Promvonge, S. Tamna, M. Pimsarn, C. Thianpong, Thermal characterization in a circular tube fitted with inclined horseshoe baffles, Appl. Therm. Eng. 75 (2015) 1147-1155.

[43] M.E. Nakhchi, M. Hatami, M. Rahmati, Experimental evaluation of performance intensification of double-pipe heat exchangers with rotary elliptical inserts, Chem. Eng. Process. Process Intensif. 169 (2021) 108615.

[44] M.E. Nakhchi, M. Hatami, M. Rahmati, Experimental investigation of performance improvement of double-pipe heat exchangers with novel perforated elliptic turbulators, Int. J. Therm. Sci. 168 (2021) 107057.

[45] F. Xin, M. Yu, W. Liu, Z. Liu, Heat transfer characteristics of enhanced cooling tube with a helical wire under oscillatory flow in Stirling engine, Int. J. Therm. Sci. 168 (2021) 107063.

[46] K. Varun, U.C. Arunachala, Intensification of thermo-hydraulic and exergetic performance by wire matrix and wavy tape: an experimental study, Int. Commun. Heat Mass Transfer 121 (2021) 105124.

[47] L. Syam Sundar, N.T. Ravi Kumar, B.M. Addis, P. Bhramara, M.K. Singh, A.C.M. Sousa, Heat transfer and effectiveness experimentally-based analysis of wire coil with core-rod inserted in Fe_3O_4/water nanofluid flow in a double pipe Ubend heat exchanger, Int. J. Heat Mass Transf. 134 (2019) 405-419.

[48] K. Abdul Hamid, W.H. Azmi, R. Mamat, K.V. Sharma, Heat transfer performance of TiO_2-

SiO_2 nanofluids in a tube with wire coil inserts, Appl. Therm. Eng. 152 (2019) 275-286.

[49] K. Sharifi, M. Sabeti, M. Rafiei, A.H. Mohammadi, L. Shirazi, Computational fluid dynamics (CFD) technique to study the effects of helical wire inserts on heat transfer and pressure drop in a double pipe heat exchanger, Appl. Therm. Eng. 128 (2018) 898-910.

[50] J. Pérez-García, A. García, R. Herrero-Martín, J.P. Solano, Experimental correlations on critical Reynolds numbers and friction factor in tubes with wire-coil inserts in laminar, transitional and low turbulent flow regimes, Exp. Thermal Fluid Sci. 91 (2018) 64-79.

[51] C. Thianpong, K. Yongsiri, K. Nanan, S. Eiamsa-ard, Thermal performance evaluation of heat exchangers fitted with twisted-ring turbulators, Int. Commun. Heat Mass Transfer 39 (6) (2012) 861-868.

[52] P. Promvonge, N. Koolnapadol, M. Pimsarn, C. Thianpong, Thermal performance enhancement in a heat exchanger tube fitted with inclined vortex rings, Appl. Therm. Eng. 62 (1) (2014) 285-292.

[53] S. Chamoli, X. Zhuang, P. Kumar Pant, P. Yu, Heat transfer in a turbulent flow tube integrated with tori as vortex generator inserts, Appl. Therm. Eng. 194 (2021) 117062.

[54] S. Banihashemi, M. Assari, S. Javadi, S. Vahidifar, Turbulent flow thermal characteristics in a pipe with ring insert: an experimental and numerical study, Chem. Eng. Process. Process Intensif. 172 (2022) 108780.

[55] R.K.B. Gallegos, R.N. Sharma, Flags as vortex generators for heat transfer enhancement: gaps and challenges, Renewable Sustainable Energy Rev. 76 (2017) 950-962.

[56] Y. Sun, G. Wen, X. Xiao, B. Ren, N. Yang, L. Zhang, Numerical study on heat transfer and flow characteristics for laminar flow in a circular tube with swirl generators, Trans. Tianjin Univ. 24 (2018) 244-255.

[57] Y. Liang, P. Liu, N. Zheng, F. Shan, Z. Liu, W. Liu, Numerical investigation of heat transfer and flow characteristics of laminar flow in a tube with center-tapered wavy-tape insert, Appl. Therm. Eng. 148 (2019) 557-567.

[58] R. Zarei, K. Razzaghi, F. Shahraki, Experimental characterization of heat transfer enhancement in a circular tube fitted with Koflo Blade™ inline mixer, Chem. Eng. Process. Process Intensif. 166 (2021) 108508.

[59] J.H. Hassan, V.M. Hameed, Evaluate the hydrothermal behavior in the heat exchanger equipped with an innovative turbulator, S. Afr. J. Chem. Eng. 41 (2022) 182-192.

[60] H. Meng, T. Meng, Y. Yu, Z. Wang, J. Wu, Experimental and numerical investigation of turbulent flow and heat transfer characteristics in the Komax static mixer, Int. J. Heat Mass Transf. 194 (2022) 123006.

[61] G. Biswas, K. Torii, D. Fujii, K. Nishino, Numerical and experimental determination of flow structure and heat transfer effects of longitudinal vortices in a channel flow, Int. J. Heat Mass Transf. 39 (16) (1996) 3441-3451.

[62] P. Promvonge, P. Promthaisong, S. Skullong, Experimental and numerical thermal performance in solar receiver heat exchanger with trapezoidal louvered winglet and wavy groove, Sol. Energy 236 (2022) 153-174.

[63] P. Promvonge, T. Chompookham, S. Kwankaomeng, C. Thianpong, Enhanced heat transfer in a triangular ribbed channel with longitudinal vortex generators, Energy Convers. Manag. 51 (6) (2010) 1242-1249.

[64] J. Wang, T. Fu, L. Zeng, F.-S. Lien, G. Chen, Thermal-hydraulic performance in a tube with

punched delta winglets inserts in turbulent flow, Int. J. Therm. Sci. 172 (2022) 107326.
[65] Z. Sun, Q. Chen, N. Zheng, Experimental and numerical studies of intensified turbulent heat transfer in round pipes with curved wing vortex generators, Int. J. Heat Mass Transf. 180 (2021) 121823.
[66] H. Naik, S. Tiwari, H.D. Kim, Flow and thermal characteristics produced by a curved rectangular winglet vortex generator in a channel, Int. Commun. Heat Mass Transfer 135 (2022) 106103.
[67] J. Wang, Y. He, L. Zeng, Z. Liu, C. Li, J. Dou, Thermohydraulic performance intensification in a rectangular channel using punched vortex generators, Int. Commun. Heat Mass Transfer 157 (2024) 107799.
[68] P. Promvonge, S. Sripattanapipat, C. Thianpong, S. Skullong, P. Promthaisong, M.E. Nakhchi, Enhanced thermal effectiveness of square duct with V-type double-baffles: numerical study, Int. Commun. Heat Mass Transfer 157 (2024) 107727.
[69] R. Sharma, D.P. Mishra, L.S. Brar, Performance enhancement of a fin and tube heat exchanger with the novel arrangement of curved winglets using a multi-objective optimization approach, Int. Commun. Heat Mass Transfer 157 (2024) 107804.
[70] K.W. Song, D.L. Hu, Q. Zhang, K. Zhang, X. Wu, L.B. Wang, Thermal-hydraulic characteristic of a novel wavy fin-and-circle tube heat exchanger with concave curved vortex generators, Int. J. Heat Mass Transf. 194 (2022) 123023.
[71] P. Saini, M.P. Shah, Performance evaluation of finned tube heat exchanger using curved wavy delta winglet vortex generators with circular perforations, Int. Commun. Heat Mass Transfer 159 (2024) 108184.
[72] J. Wang, L. Zeng, S. Yu, Y. He, J. Tang, Experimental and numerical investigations of tube inserted with novel perforated rectangular V-shape vortex generators, Appl. Therm. Eng. 249 (2024) 123451.
[73] J. Wang, L. Zeng, Y. He, B. Zhao, P. Chu, Effect of structure parameters on thermal performance of novel punched V-shape VGs for hear exchangers: an experimental approach, Int. Commun. Heat Mass Transfer 155 (2024) 107472.
[74] J. Wang, T. Fu, L. Zeng, F.-S. Lien, H. Wang, X. Deng, A comparative study on thermo-hydraulic performance in a tube with different punched winglets, Int. J. Therm. Sci. 181 (2022) 107772.
[75] K. Torii, K.M. Kwak, K. Nishino, Heat transfer enhancement accompanying pressure-loss reduction with winglet-type vortex generators for fin-tube heat exchangers, Int. J. Heat Mass Transf. 45 (18) (2002) 3795-3801.
[76] E. Kim, J.S. Yang, An experimental study of heat transfer characteristics of a pair of longitudinal vortices using color capturing technique, Int. J. Heat Mass Transf. 45 (16) (2002) 3349-3356.
[77] Z. Ke, C.-L. Chen, K. Li, S. Wang, C.-H. Chen, Vortex dynamics and heat transfer of longitudinal vortex generators in a rectangular channel, Int. J. Heat Mass Transf. 132 (2019) 871-885.
[78] G. Wu, J. Xu, H. Wang, W. Yin, Optimized design of multiple vortex generator rows to enhance thermo-hydraulic performance in fully developed forced convection channel, Int. Commun. Heat Mass Transfer 157 (2024) 107715.
[79] K.W. Song, K. Sun, X.J. Lu, Q.F. Gao, Q.Z. Hou, B.D. Gu, Effect of wavy delta winglet vortex

generators on heat transfer performance of a fin-and-tube heat exchanger, Int. J. Heat Fluid Flow 108 (2024) 109485.

[80] L.-T. Tian, Y.-L. He, Y.-G. Lei, W.-Q. Tao, Numerical study of fluid flow and heat transfer in a flat-plate channel with longitudinal vortex generators by applying field synergy principle analysis, Int. Commun. Heat Mass Transfer 36 (2) (2009) 111-120.

[81] G. Zhou, Z. Feng, Experimental investigations of heat transfer enhancement by plane and curved winglet type vortex generators with punched holes, Int. J. Therm. Sci. 78 (2014) 26-35.

[82] P. Chu, Y.L. He, Y.G. Lei, L.T. Tian, R. Li, Three-dimensional numerical study on fin-and-oval-tube heat exchanger with longitudinal vortex generators, Appl. Therm. Eng. 29 (5-6) (2009) 859-876.

[83] L. Zhang, H. Guo, J. Wu, W. Du, Compound heat transfer enhancement for shell side of doublepipe heat exchanger by helical fins and vortex generators, Heat Mass Transfer 48 (2012) 1113-1124.

[84] S. Caliskan, Experimental investigation of heat transfer in a channel with new winglet-type vortex generators, Int. J. Heat Mass Transf. 78 (2014) 604-614.

[85] M. Behfard, A. Sohankar, Numerical investigation for finding the appropriate design parameters of a fin-and-tube heat exchanger with delta-winglet vortex generators, Heat Mass Transfer 52 (2016) 21-37.

[86] S. Skullong, P. Promvonge, C. Thianpong, M. Pimsarn, Thermal performance in solar air heater channel with combined wavy-groove and perforated-delta wing vortex generators, Appl. Therm. Eng. 100 (2016) 611-620.

[87] L. Zhang, B. Shang, H. Meng, Y. Li, C. Wang, B. Gong, J. Wu, Effects of the arrangement of triangle-winglet-pair vortex generators on heat transfer performance of the shell side of a double-pipe heat exchanger enhanced by helical fins, Heat Mass Transfer 53 (2017) 127-139.

[88] M. Fiebig, Compact heat exchangers: vortex generators, J. Enhanced Heat Transfer 24 (1-6) (2017) 1-28.

[89] K.W. Song, Z.P. Xi, M. Su, L.C. Wang, X. Wu, L.B. Wang, Effect of geometric size of curved delta winglet vortex generators and tube pitch on heat transfer characteristic of fin-tube heat exchanger, Exp. Thermal Fluid Sci. 82 (2017) 8-18.

[90] V. Nandana, U. Janoske, Numerical study on the enhancement of heat transfer performance in a rectangular duct with new winglet shapes, Therm. Sci. Eng. Prog. 6 (2018) 95-103.

[91] H.-L. Liu, C.-C. Fan, Y.-L. He, D.S. Nobes, Heat transfer and flow characteristics in a rectangular channel with combined delta winglet inserts, Int. J. Heat Mass Transf. 134 (2019) 149-165.

[92] M.F. Md Salleh, A. Gholami, M.A. Wahid, Numerical evaluation of thermal hydraulic performance in fin-and-tube heat exchangers with various vortex generator geometries arranged in common-flow-down or common-flow-up, ASME J. Heat Mass Transfer 141 (2) (2019) 021801.

[93] E. Ali, J. Park, H. Park, Numerical investigation of enhanced heat transfer in a rectangular channel with winglets, Heat Transfer Eng. 42 (8) (2020) 695-705.

[94] Y. Jiang, B. Chen, C. Duan, X. Yan, L. Wang, Flow and heat transfer characteristics in square

channel with concave-convex vortex generators based on numerical simulations, Asia-Pac. J. Chem. Eng. 16 (2) (2020) e2601.

[95] M. Khoshvaght-Aliabadi, N. Naeimabadi, F. Nejati Barzoki, A. Salimi, Experimental and numerical studies of air flow and heat transfer due to insertion of novel delta-winglet tapes in a heated channel, Int. J. Heat Mass Transf. 169 (2021) 120912.

[96] Z. Zhao, L. Luo, D. Qiu, S. Wang, Z. Wang, B. Sundén, On the topology of vortex structures and heat transfer of a gas turbine blade internal tip with different arrangement of delta-winglet vortex generators, Int. J. Therm. Sci. 160 (2021) 106676.

[97] P. Promvonge, P. Promthaisong, S. Skullong, Thermal performance augmentation in round tube with louvered V-winglet vortex generator, Int. J. Heat Mass Transf. 182 (2022) 121913.

[98] P. Promvonge, S. Skullong, Thermohydraulic performance and entropy generation in heat exchanger tube with louvered winglet tapes, Int. J. Therm. Sci. 181 (2022) 107733.

[99] P. Promvonge, S. Skullong, Heat transfer in a tube with combined V-winglet and twin counter-twisted tape, Case Stud. Therm. Eng. 26 (2021) 101033.

[100] S. Eiamsa-ard, C. Nuntadusit, P. Promvonge, Effect of twin delta-winged twisted-tape on thermal performance of heat exchanger tube, Heat Transfer Eng. 34 (15) (2013) 1278-1288.

[101] Z. Sun, K. Zhang, W. Li, Q. Chen, N. Zheng, Investigations of the turbulent thermal-hydraulic performance in circular heat exchanger tubes with multiple rectangular winglet vortex generators, Appl. Therm. Eng. 168 (2020) 114838.

[102] S. Eiamsa-ard, K. Wongcharee, P. Eiamsa-ard, C. Thianpong, Heat transfer enhancement in a tube using delta-winglet twisted tape inserts, Appl. Therm. Eng. 30 (4) (2010) 310-318.

[103] K. Wongcharee, S. Eiamsa-ard, Heat transfer enhancement by twisted tapes with alternate-axes and triangular, rectangular and trapezoidal wings, Chem. Eng. Process. Process Intensif. 50 (2) (2011) 211-219.

[104] A. Boonloi, W. Jedsadaratanachai, Flow topology, heat transfer characteristic and thermal performance in a circular tube heat exchanger inserted with punched delta winglet vortex generators, J. Mech. Sci. Technol. 30 (2016) 457-471.

[105] S. Skullong, P. Promvonge, C. Thianpong, M. Pimsarn, Heat transfer and turbulent flow friction in a round tube with staggered-winglet perforated-tapes, Int. J. Heat Mass Transf. 95 (2016) 230-242.

[106] Y. Lei, F. Zheng, C. Song, Y. Lyu, Improving the thermal hydraulic performance of a circular tube by using punched delta-winglet vortex generators, Int. J. Heat Mass Transf. 111 (2017) 299-311.

[107] A.T. Wijayanta, M. Aziz, K. Kariya, A. Miyara, Numerical study of heat transfer enhancement of internal flow using double-sided delta-winglet tape insert, Energies 11 (11) (2018) 3170.

[108] I. Yaningsih, A.T. Wijayanta, T. Miyazaki, S. Koyama, Impact of blockage ratio on thermal performance of delta-winglet vortex generators, Appl. Sci. 8 (2) (2018) 181.

[109] G. Liang, M.D. Islam, N. Kharoua, R. Simmons, Numerical study of heat transfer and flow behavior in a circular tube fitted with varying arrays of winglet vortex generators, Int. J. Therm. Sci. 134 (2018) 54-65.

[110] Y. Xu, M.D. Islam, N. Kharoua, Experimental study of thermal performance and flow

behaviour with winglet vortex generators in a circular tube, Appl. Therm. Eng. 135 (2018) 257-268.

[111] Y. Xu, M.D. Islam, N. Kharoua, Numerical study of winglets vortex generator effects on thermal performance in a circular pipe, Int. J. Therm. Sci. 112 (2017) 304-317.

[112] K. Zhang, Z. Sun, N. Zheng, Q. Chen, Effects of the configuration of winglet vortex generators on turbulent heat transfer enhancement in circular tubes, Int. J. Heat Mass Transf. 157 (2020) 119928.

[113] J. Wang, T. Fu, L. Zeng, F.-S. Lien, X. Deng, Experimental investigation and numerical investigations of heat transfer enhancement in a tube with punched winglets, Int. J. Therm. Sci. 177 (2022) 107542.

[114] X. Wu, T. Fu, J. Wang, L. Zeng, F. Zhang, A comparative study of fluid flow and heat transfer in the tube with multi-V-winglets vortex generators, Appl. Therm. Eng. 236 (2024) 121448.

[115] S.R. Nair, M.K. Tan, Y. Wang, S.N. Kazi, C.S. Oon, The effect of angled fins in generating swirling flows with vortices that augment heat transfer performance in an annular conduit, Int. J. Energy Res. 2023 (2023) 1-23.

[116] S. Ferrouillat, P. Tochon, C. Garnier, H. Peerhossaini, Intensification of heat-transfer and mixing in multifunctional heat exchangers by artificially generated streamwise vorticity, Appl. Therm. Eng. 26 (16) (2006) 1820-1829.

[117] J.X. Zhu, M. Fiebig, N.K. Mitra, Numerical investigation of turbulent flows and heat transfer in a rib-roughened channel with longitudinal vortex generators, Int. J. Heat Mass Transf. 38 (3) (1995) 495-501.

[118] M. Hatami, D.D. Ganji, M. Gorji-Bandpy, Experimental investigations of diesel exhaust exergy recovery using delta winglet vortex generator heat exchanger, Int. J. Therm. Sci. 93 (2015) 52-63.

[119] M. Hatami, D.D. Ganji, M. Gorji-Bandpy, Experimental and thermodynamical analyses of the diesel exhaust vortex generator heat exchanger for optimizing its operating condition, Appl. Therm. Eng. 75 (2015) 580-591.

[120] C. Zhai, M.D. Islam, M.M. Alam, R. Simmons, I. Barsoum, Parametric study of major factors affecting heat transfer enhancement in a circular tube with vortex generator pairs, Appl. Therm. Eng. 153 (2019) 330-340.

[121] C. Zhai, M.D. Islam, R. Simmons, I. Barsoum, Heat transfer augmentation in a circular tube with delta winglet vortex generator pairs, Int. J. Therm. Sci. 140 (2019) 480-490.

[122] M. Islam, A. Nurizki, I. Barsoum, N. Ayish, R. Simmons, Experimental study of heat transfer and flow of delta winglets inline arrays in a tube heat exchanger for enhanced heat transfer, Heat Transfer 50 (4) (2020) 3582-3602.

[123] S. Singh, A. Pandey, H. Kharkwal, Effects of serrated circular ring with rectangular winglets on thermal properties of tube heat exchanger: an experimental and numerical study, Exp. Heat Transfer 33 (6) (2019) 572-585.

[124] O. García-Valladares, N. Velázquez, Numerical simulation of parabolic trough solar collector: improvement using counter flow concentric circular heat exchangers, Int. J. Heat Mass Transf. 52 (3-4) (2009) 597-609.

[125] M. Cavazzuti, E. Agnani, M.A. Corticelli, Optimization of a finned concentric pipes heat exchanger for industrial recuperative burners, Appl. Therm. Eng. 84 (2015) 110-117.

[126] J.D. Templeton, F. Hassani, S.A. Ghoreishi-Madiseh, Study of effective solar energy storage

using a double pipe geothermal heat exchanger, Renewable Energy 86 (2016) 173-181.
[127] S. Kumar, K. Murugesan, Optimization of geothermal interaction of a double U-tube borehole heat exchanger for space heating and cooling applications using Taguchi method and utility concept, Geothermics 83 (2020) 101723.
[128] B.O. Hasan, E.A. Jwair, R.A. Craig, The effect of heat transfer enhancement on the crystallization fouling in a double pipe heat exchanger, Exp. Thermal Fluid Sci. 86 (2017) 272-280.
[129] Y. Lv, K. Lu, Y. Ren, Composite crystallization fouling characteristics ofnormal solubility salt in double-pipe heat exchanger, Int. J. Heat Mass Transf. 156 (2020) 119883.
[130] D.K. Johar, D. Sharma, S.L. Soni, P.K. Gupta, R. Goyal, Experimental investigation and exergy analysis on thermal storage integrated micro-cogeneration system, Energy Convers. Manag. 131 (2017) 127-134.
[131] S. Ghani, S.M.A. Gamaledin, M.M. Rashwan, M.A. Atieh, Experimental investigation of double-pipe heat exchangers in air conditioning applications, Energy and Buildings 158 (2018) 801-811.
[132] Y. Pahamli, M.J. Hosseini, A.A. Ranjbar, R. Bahrampoury, Inner pipe downward movement effect on melting of PCM in a double pipe heat exchanger, Applied Mathematics and Computation 316 (2018) 30-42.
[133] M. Taghilou, A.M. Sefidan, A. Sojoudi, S.C. Saha, Solid-liquid phase change investigation through a double pipe heat exchanger dealing with time-dependent boundary conditions, Appl. Therm. Eng. 128 (2018) 725-736.
[134] M. Omidi, M. Farhadi, M. Jafari, A comprehensive review on double pipe heat exchangers, Appl. Therm. Eng. 110 (2017) 1075-1090.
[135] H.M. Kaci, C. Habchi, T. Lemenand, D.D. Valle, H. Peerhossaini, Flow structure and heat transfer induced by embedded vorticity, Int. J. Heat Mass Transf. 53 (17-18) (2010) 3575-3584.
[136] Q. Hu, X. Qu, W. Peng, J. Wang, Experimental and numerical investigation of turbulent heat transfer enhancement of an intermediate heat exchanger using corrugated tubes, Int. J. Heat Mass Transf. 185 (2022) 122385.
[137] A.M. Jacobi, R.K. Shah, Heat transfer surface enhancement through the use of longitudinal vortices: a review of recent progress, Exp. Thermal Fluid Sci. 11 (1995) 295-309.
[138] H.E. Ahmed, H.A. Mohammed, M.Z. Yusoff, An overview on heat transfer augmentation using vortex generators and nanofluids: approaches and applications, Renewable Sustainable Energy Rev. 16 (8) (2012) 5951-5993.
[139] K. Torri, K. Nishino, K. Nakayama, Mechanism of heat transfer augmentation by longitudinal vortices in a flat plate boundary layer, Trans. Jpn. Soc. Mech. Eng. Ser. B 60 (1994) 997-1004.
[140] G.B. Schubauer, W.G. Spangenberg, Forced mixing in boundary layers, J. Fluid Mech. 8 (1) (1960) 10-32.
[141] T.R. Johnson, P.N. Joubert, The influence of vortex generators on the drag and heat transfer from a circular cylinder normal to an airstream, ASME J. Heat Mass Transfer 91 (1) (1969) 91-99.
[142] K.W. Song, S. Liu, L.B. Wang, Interaction of counter rotating longitudinal vortices and the effect on fluid flow and heat transfer, Int. J. Heat Mass Transf. 93 (2016) 349-360.

[143] K.W. Song, L.B. Wang, Effects of longitudinal vortex interaction on periodically developed flow and heat transfer of fin-and-tube heat exchanger, Int. J. Therm. Sci. 109 (2016) 206-216.

[144] K.W. Song, T. Tagawa, The optimal arrangement of vortex generators for best heat transfer enhancement in flat-tube-fin heat exchanger, Int. J. Therm. Sci. 132 (2018) 355-367.

[145] P.A. Eibeck, J.K. Eaton, Heat transfer effects of a longitudinal vortex embedded in a turbulent boundary layer, ASME J. Heat Mass Transfer 109 (1) (1987) 16-24.

[146] B.J. Wendt, I. Grebert, W.R. Hingst, Structure and development of streamwise vortex arrays embedded in a turbulent boundary layer, AIAA J. 31 (2) (1993) 319-325.

[147] J.S. Yang, J.K. Seo, K.B. Lee, A numerical analysis on flow field and heat transfer by interaction between a pair of vortices in rectangular channel flow, Curr. Appl. Phys. 1 (4-5) (2001) 393-405.

[148] M.C. Gentry, A.M. Jacobi, Heat transfer enhancement by delta-wing vortex generators on a flat plate: Vortex interactions with the boundary layer, Exp. Thermal Fluid Sci. 14 (3) (1997) 231-242.

[149] C. Zhu, H. Liang, D. Sun, L. Wang, Y. Zhang, Numerical study of interactions of vortices generated by vortex generators and their effects on heat transfer enhancement, Numer. Heat Transfer, Part A 50 (4) (2006) 345-360.

[150] L.O. Salviano, D.J. Dezan, J.I. Yanagihara, Optimization of winglet-type vortex generator positions and angles in plate-fin compact heat exchanger: response surface methodology and direct optimization, Int. J. Heat Mass Transf. 82 (2015) 373-387.

[151] R.L. Webb, Principles of Enhanced Heat Transfer, John Wiley & Sons, New York, 1994.

[152] E.E. Wilson, A basis for rational design of heat transfer apparatus, Journal of Fluids Engineering 37 (1915) 47-70.

[153] M. Chen, Fundamentals of viscous fluid mechanics, Higher Education Press, Beijing, China, 1993.

[154] B. Tong, X. Yin, K. Zhu, Theory of Vortex Motion, University of Science and Technology of China Press, Hefei, China, 2009.

[155] K.-W. Song, L.-B. Wang, Relationship between heat transfer intensity and absolute vorticity flux intensity in flat tube bank fin channels with vortex generators, Prog. Comput. Fluid Dyn. 8 (7-8) (2008) 496-502.

[156] L.-M. Chang, L.-B. Wang, K.-W. Song, D.-L. Sun, J.-F. Fan, Numerical study of the relationship between heat transfer enhancement and absolute vorticity flux along main flow direction in a channel formed by a flat tube bank fin with vortex generators, Int. J. Heat Mass Transf. 52 (7-8) (2009) 1794-1801.

[157] K.W. Song, L.-B. Wang, D.-L. Sun, Convective heat transfer and absolute vorticity flux along main flow in a channel formed by flat tube bank fins with vortex generators mounted on both fin surfaces, J. Enhanced Heat Transfer 16 (2) (2009) 123-139.

[158] R.M. Manglik, A.E. Bergles, Heat transfer and pressure drop correlations for twisted-tape inserts in isothermal tubes: Part I laminar flows, ASME J. Heat Mass Transfer 115 (4) (1993) 881-889.

[159] W.R. Dean, J.M. Hurst, Note on the motion of fluid in a curved pipe, Mathematika 6 (1) (1959) 77-85.

[160] K.-W. Song, L.-B. Wang, The effectiveness of secondary flow produced by vortex generators mounted on both surfaces of the fin to enhance heat transfer in a flat tube bank fin heat exchanger, ASME J. Heat Mass Transfer 135 (4) (2013) 041902.
[161] W.-L. Hu, K.-W. Song, Y. Guan, L.-M. Chang, S. Liu, L.-B. Wang, Secondary flow intensity determines Nusselt number on the fin surfaces of circle tube bank fin heat exchanger, Int. J. Heat Mass Transf. 62 (2013) 620-631.
[162] Y.-Y. Chen, K.-W. Song, L.-B. Wang, D.-L. Sun, Comparisons of local experimental results with numerical results of heat transfer enhancement of a flat tube bank fin with vortex generators, Numer. Heat Transfer, Part A 55 (2) (2009) 144-162.
[163] ANSYS Fluent 2022R1 User's Guide, ANSYS Inc., USA, 2022.
[164] I. Firat, S. Karagoz, O. Yildirim, F. Sonmez, Experimental investigation of the thermal performance effects of turbulators with different fin angles in a circular pipe, Int. J. Therm. Sci. 184 (2023) 107969.
[165] V. Gnielinski, New equations for heat and mass transfer in turbulent pipe and channel flow, Int. Chem. Eng. 16 (2) (1976) 359-368.
[166] G.K. Filonenko, Hydraulic resistance in pipes, Teploenergetika 1 (1954) 40-44.
[167] W. Liu, K. Yang, Mechanism and numerical analysis of heat transfer enhancement in the core flow along a tube, Sci. China Ser. E: Technol. Sci. 51 (8) (2008) 1195-1202.
[168] S. Eiamsa-ard, K. Ruengpayungsak, C. Thianpong, M. Pimsarn, V. Chuwattanakul, Parametric study on thermal enhancement and flow characteristics in a heat exchanger tube installed with protruded baffle bundles, Int. J. Therm. Sci. 145 (2019) 106016.
[169] S. Chokphoemphun, S. Hongkong, S. Thongdaeng, S. Chokphoemphun, Experimental study and neural networks prediction on thermal performance assessment of grooved channel air heater, Int. J. Heat Mass Transf. 163 (2020) 120397.
[170] S. Chokphoemphun, M. Pimsarn, C. Thianpong, P. Promvonge, Heat transfer augmentation in a circular tube with winglet vortex generators, Chin. J. Chem. Eng. 23 (4) (2015) 605-614.
[171] S. Chamoli, R. Lu, P. Yu, Thermal characteristic of a turbulent flow through a circular tube fitted with perforated vortex generator inserts, Appl. Therm. Eng. 121 (2017) 1117-1134.
[172] P. Promvonge, Thermal performance in square-duct heat exchanger with quadruple V-finned twisted tapes, Appl. Therm. Eng. 91 (2015) 298-307.
[173] J. Wang, T. Fu, L. Zeng, G. Chen, F.-S. Lien, Numerical and experimental investigations of micro thermal performance in a tube with delta winglet pairs, Micromachines 12 (7) (2021) 786.
[174] J.J. Feng, C.P. Teh, K.C. Ng, J.C. Jen-Haw, D. Xiao, Y.A. Abakr, A. Chan, B. Chen, Heat transfer and fluid flow analysis in circular tubes with multi-delta-winglets vortex generators, Int. Commun. Heat Mass Transfer 159 (2024) 108267.
[175] M.H. Tusar, P.K. Bhowmik, B. Salam, J.U. Ahamed, J.K. Kim, Convective heat transfer and friction factor characteristics of helical strip inserted annuli at turbulent flow, Int. J. Heat Mass Transf. 176 (2021) 121422.
[176] Y. Wang, C.S. Oon, J.-J. Foo, M.-V. Tran, S.R. Nair, F.W. Low, Numerical investigation of thermo-hydraulic performance utilizing clove-treated graphene nanoplatelets nanofluid in an annular passage with perforated curve fins, Results Eng. 17 (2023) 100848.
[177] S. Yadav, S.K. Sahu, Heat transfer augmentation in double pipe water to air counter flow

heat exchanger with helical surface disc turbulators, Chem. Eng. Process. Process Intensif. 135 (2019) 120-132.

[178] L. Zhang, X. Yan, Y. Zhang, Y. Feng, Y. Li, H. Meng, J. Zhang, J. Wu, Heat transfer enhancement by streamlined winglet pair vortex generators for helical channel with rectangular cross section, Chem. Eng. Process. Process Intensif. 147 (2020) 107788.